Precision spectroscopy with ^{40}Ca$^+$ ions in a Paul trap

Dissertation

zur Erlangung des Doktorgrades an der

Fakultät für Mathematik, Informatik und Physik
der Leopold-Franzens-Universität Innsbruck
vorgelegt von

Mag. Michael Chwalla

durchgeführt am Institut für Experimentalphysik

unter der Leitung von
Univ.-Prof. Dr. Rainer Blatt

April 2009

Abstract

This thesis reports on experiments with trapped ^{40}Ca$^+$ ions related to the field of precision spectroscopy and quantum information processing.

For the absolute frequency measurement of the $4s\ ^2S_{1/2} - 3d\ ^2D_{5/2}$ clock transition of a single, laser-cooled ^{40}Ca$^+$ ion, an optical frequency comb was referenced to the transportable Cs atomic fountain clock of LNE-SYRTE and the frequency of an ultra-stable laser exciting this transition was measured with a statistical uncertainty of 0.5 Hz. The correction for systematic shifts of 2.4(0.9) Hz including the uncertainty in the realization of the SI second yields an absolute transition frequency of $\nu_{Ca^+} = 411\,042\,129\,776\,393.2(1.0)$ Hz. This is the first report on a ion transition frequency measurement employing Ramsey's method of separated fields at the 10^{-15} level. Furthermore, an analysis of the spectroscopic data obtained the Landé g-factor of the $3d\ ^2D_{5/2}$ level as g$_{5/2}$=1.2003340(3).

The main research field of our group is quantum information processing, therefore it is obvious to use the tools and techniques related to this topic like generating multi-particle entanglement or processing quantum information in decoherence-free sub-spaces and apply them to high-resolution spectroscopy. As a first realization, the quadrupole moment $\theta(3d, 5/2)$ of the ^{40}Ca$^+$ $3d\ ^2D_{5/2}$ state was measured with especially designed states that are sensitive to electric field gradients but insensitive to the linear Zeeman effect and related noise. Measurements with Ramsey-type experiments could be performed at the sub-Hertz level despite the presence of strong technical noise, yielding $\theta(3d, 5/2)$ =1.82(1) ea_0^2. In addition, the measurement technique was also used in preliminary experiments to determine the linewidth of the narrowband interrogation laser.

While entanglement leads to enhanced signal-to-noise ratios, it is not an essential ingredient for this kind of method. The measurement result obtained with classically correlated but un-entangled states confirms the measured value previously obtained with maximally entangled states. This might be interesting for experiments suffering from short single-atom coherences where experiments with correlated atoms could substantially enhance the coherence time and thus allow for precision spectroscopy with high resolution.

Zusammenfassung

In dieser Arbeit werden Messungen auf dem Gebiet der Präzisionsspektroskopie und Quanteninformationsverarbeitung an gefangenen und Laser-gekühlten ^{40}Ca$^+$ Ionen vorgestellt.

Zur Messung der Absolutfrequenz des $4s\,^2S_{1/2} - 3d\,^2D_{5/2}$-Übergangs von ^{40}Ca$^+$ wurde ein optischer Frequenzkamm auf eine transportable Atomuhr in Form einer Cs-Fontäne stabilisiert und die Frequenz des hochstabilen Anregungslasers relativ zur SI-Definition der Sekunde mit einer statistischen Unsicherheit von 0.5 Hz gemessen. Eine genaue Analyse der systematischen Verschiebungen ergab eine Frequenzkorrektur von 2.4(0.9) Hz, sodaß die absolute Übergangsfrequenz mit ν_{Ca^+} =411 042 129 776 393.2 (1.0) Hz angegeben werden kann. Das entspricht einer relativen Unsicherheit von 2.4×10^{-15} und liegt innerhalb eines Faktors 3 bezüglich der Ungenauigkeit der verwendeten Realisation der SI-Sekunde. Zusätzlich konnten die Spektroskopie-Daten zur Bestimmung des Landé g-Faktors des $D_{5/2}$ Zustandes zu $g_{5/2} = 1.2003340(3)$ genutzt werden.

Zur Demonstration der Anwendbarkeit von Methoden der Quanteninformations-Verarbeitung in der Spektroskopie konnte das Quadrupolmoment des $3d\,^2D_{5/2}$-Niveaus mit Hilfe von speziell für diesen Zweck konstruierten, verschränkten Zuständen bestimmt werden. Dabei wurde ein Bell-Zustand aus magnetischen Unterzuständen des metastabilen $D_{5/2}$-Niveaus erzeugt und die Oszillationsfrequenz unter Verwendung von verallgemeinerten Ramsey-Experimenten als Funktion des elektischen Feldgradienten präzise vermessen. Nach Berücksichtigung von systematischen Effekten ergab sich ein elektrisches Quadrupolmoment von $\theta(3d, 5/2)$ =1.82(1) ea_0^2. Weiters konnte die Linienbreite des Spektroskopie-Lasers mit Hilfe dieser Technik ermittelt werden und demonstriert somit eine weitere Anwendungsmöglichkeit.

Während verschränkte Zustände Messungen bei maximalem Kontrast erlauben, ist diese Eigenschaft für die Meßmethode an sich nicht zwingend erforderlich. Man kann alternativ auch Produktzustände mit klassischen Korrelationen verwenden, allerdings unter einem Kontrastverlust von mindestens 50%. Die Messung des Quadrupolmomentes liefert, wie zu erwarten, ein ähnliches Resultat wie die Messung mit Bell-Zuständen. Damit eröffnen Messungen mit korrelierten Atomen die Möglichkeit von Präzissionsmessungen auch unter ungünstigen Bedingungen mit ansonsten (zu) kurzen Kohärenzzeiten einzelner Atome.

Contents

Figure 1: Aerial image of the technical campus of the University of Innsbruck with the laboratory locations of the Institute of Experimental Physics and of the Institute for Quantum Optics and Quantum Information. The 400 m long optical fiber link between the two buildings is indicated by the yellow line. The image is taken from tiris - Tiroler Rauminformationssystem, the official map server of the Tyrolean government.

Chapter 1

Introduction

From its very beginning until today, mankind was concerned with the measurement of time. Periodic astronomical events fascinated people more than 5000 years ago and incited them to build stone rings like in Stonehenge or to make the artful sky disk of Nebra which is the oldest depiction of the sky worldwide. With these devices people were able to directly observe solstices, equinoxes, and other astronomical phenomena. The first civilizations used periodic astronomical events to predict the times for planting and harvest which was vital for their survival. Therefore, the keeping of time was actually reserved to priests and closely related to religion. Even today we find remnants of the Neolithic or Bronze Age calendar in some of our festival days, although in a christianized form.

As early civilizations developed, the need for joint efforts in many parts of every day life became more important concerning not only farming but also construction work like building of cities, fortresses, or temples just to name a few. This required a division of the day into smaller units. A natural choice was the division of the daylight into twelve hours. Twelve, because this is approximately the ratio between the frequency of the moon's phases and the Earth's orbit. The measurement device for this task: a simple stick where the movement of its shadow cast by the sun can be observed on a clear day - the sundial was invented. However, it has some practical limitations: the most obvious one the fact that it doesn't work at night or on a cloudy day. Another one is that the length of the hour strongly depends on the latitude of the observing site and is additionally subjected to seasonal changes, i. e. hours in summer are longer than in winter. By applying these corrections, modern sundials are able to reach an impressive relative (in-)accuracy of 7×10^{-4}.

Among the oldest and commonly used timekeeping devices for millennia were water clocks and sandglasses. With these devices, time was measured as a function of water or sand flow, respectively. Remarkably, the underlying principle does not depend on the observation of celestial bodies and would also work at night or inside rooms. Furthermore, the length of an hour did not depend on the season in contrast to the case for sundials. The accuracy could be fine-tuned by controlling the water pressure including complex gearing, and some of them became quite sophisticated. The water clocks were calibrated by sundials. Through the centuries, these clocks were used for timing speeches and other

events, times for prayers and masses in church, though never reaching the accuracy of modern clocks.

The first clock which incorporates an oscillatory device depending on its natural resonance frequency, was the pendulum clock. The original concept had been developed by Galileo Galilei when he discovered that a pendulum's oscillation period depends on its length only. Christiaan Huygens, however, was credited as the inventor of the pendulum clock for his design described in 1658. Later refinements reduced the clock errors to below 10 s per day enabling the discovery of variations in sundial time depending on the time of the year and time of the day. Figure 1.1 shows the artful clock-face of a pendulum clock donated to the Institute of Experimental Physics of the university of Innnsbruck by empress Maria Theresia in the year 1798. It is kept in the institute's inventory catalog as item number 4.

As mankind began to travel across the seas, the need for more accurate clocks became apparent. Precise time-keeping is the starting basis for an exact calculation of a ship's longitude. John Harrison built a marine chronometer with a spring and balance wheel escapement in 1761 which would only loose a few seconds on transatlantic passage of many days on board a rolling ship.

The discovery of the piezoelectric effect by the end of the 19th century led to the a revolution in the development of clocks without gears or escapements which disturb their regular frequency. Time is measured here by observing induced electrical vibrations of a quartz crystal and displaying them through appropriate electronic circuits. A typical quartz wristwatch generates a signal which is an order of magnitude more accurate than good mechanical clocks. The best of the early crystal oscillators were already accurate to within 1 ms a day (10^{-8}/day) [1]. With this level of accuracy, variations of the earth's rotational frequency caused by melting ice caps, changes of the Earth's internal structure, or on its surface could be measured.

The dramatic improvement of quartz clocks over pendulum clocks can be explained by two fundamental principles in frequency metrology: the first being that a clock operating at a higher frequency has the advantage of higher precision because of a larger number of clock "ticks" for a given measurement time (stability), the second principle being that a clock oscillator should be chosen for a low sensitivity to external perturbations and should be well isolated from the environment (accuracy). Unfortunately, the long-term behavior of crystal oscillators is less exciting and it is impossible to reproduce two crystals with exactly the same properties. There is also a third principle which applies to any kind of standard, that is, a practical realization of a base unit should be possible anywhere, at any time, and as close as possible to the definition (reproducibility).

Atomic systems are close to an ideal realization of these three requirements. The idea of an atomic clock was first conceived in 1945 by I. I. Rabi [2] using his technique of measuring nuclear magnetic moments [3]. The pendulum for such a clock consists of the electromagnetic signal associated with a quantum transition between two energy levels of an atom. The narrow transitions typically used require fairly low excitation energies in the microwave or optical domain, thus fulfilling the criterion of stability. The immunity against a perturbing environment provides for high accuracy and since atoms of the same

Figure 1.1: The pendulum clock of the Institute for Experimental Physics in Innsbruck donated by empress Maria Theresia in 1798.

species have the same properties all across the universe - at least according to the Standard Model - it is possible to have many identical copies.

The great success of thermal cesium beam clocks employing Ramsey's method of separated fields [4] has led to the following definition of the SI base unit of one second [5]:

> *The second is the duration of 9,192,631,770 periods of radiation corresponding to the transition between the two hyperfine levels of the ground state of the cesium 133 atom.*

The advent of laser cooling techniques [6] significantly reduced errors due to Doppler shifts by reducing the thermal velocities from hundreds of m/s to the cm/s scale [7] and led to the realization of Zacharias' idea of a fountain clock [8]. Currently, the best cesium fountain clocks [9–11] have uncertainties of 5×10^{-16} or even better. The instability of a shot-noise limited clock in terms of the Allan deviation is given by [12, 13]

$$\sigma_y(\tau) \sim \frac{1}{\pi Q} \sqrt{\frac{T_c}{\tau}} \left(\frac{1}{N}\right)^{1/2}, \tag{1.1}$$

where $Q = \nu_0/\Delta\nu_{FWHM}$ is the line quality factor, T_c the cycle time, N the number of atoms (shot noise), and τ the measurement time. From this equation it is clear, that one would prefer to operate at the highest possible atomic frequency ν_0 at a given linewidth $\Delta\nu_{FWHM}$. Therefore, optical clocks are the logical extension of microwave-based atomic clocks but it requires means to count optical frequencies.

Fostered by the invention of the optical frequency comb technology [14], complicated frequency chains [15] needed to compare optical frequencies to primary Cs standards became obsolete, which only existed at a few places worldwide and would only work for a limited time due to their complexity and number of stabilization loops. An optical frequency comb generator representing the analogue of a mechanical "clockwork" allows for the direct conversion of the very fast optical oscillations at frequencies of a few 100 THz down to frequencies in the radio frequency domain on the order of 1 GHz where they can be handled by conventional electronics.

Currently, there is a lot of effort put into the development of optical frequency standards that are expected to replace the current microwave standard in cesium as the basis of the definition of the SI second in a few years from now. Recently, evaluations of systematic shifts of the best optical frequency standards, based on single trapped ions and neutral atoms held in optical lattices respectively [16, 17], have demonstrated a relative frequency uncertainty of 10^{-16} or even better, thus surpassing the systematic error budgets of the best cesium fountain clocks. But nevertheless, there is no clear indication for the optimal choice of atom or ion. For an optical ion clock, several candidates have been thoroughly investigated such as Hg^+, Al^+, Yb^+, In^+, Sr^+ [18–23]. Ca^+ has been proposed and theoretically analyzed as well [24, 25], but no serious measurement had been accomplished.

Confinement of single atoms or ions in electro-magnetic fields opens up the possibility of studying single or a few charged particles in a very well defined environment. Wolfgang Paul invented a radio frequency (RF) mass filter for mass-selecting charged particles in 1953 [26]. A modified design of his experimental setup [27] makes it possible to confine

ions in all three dimensions. Such traps have become widely used in many fields of physics, contradicting Erwin Schrödinger's famous statement from 1952 [28]:

> ...we never experiment with just one electron or atom or (small) molecule. In thought experiments we sometimes do; this invariably entails ridiculous consequences...

In 1980, the first trapping and laser cooling of a single ion was reported by Neuhauser *et al.* [29]. Since then, Paul traps have played an important role not only in mass spectrometry but also in atomic physics, because these systems allow for trapping and controlled manipulation of single or a few ions and extensive studies of their properties [30]. The possibility for laser cooling [31] in an ion trap offers the perspective of developing an optical frequency standard [32] because Doppler effects due to thermal motion are almost eliminated when operating in the Lamb-Dicke regime [33]. Together with efficient state preparation [34, 35] by optical pumping and the readout of the quantum state by the observation of quantum jumps (electron shelving technique) [36–38] with a detection efficiency close to 100%, the signal-to-noise ratio is greatly enhanced.

For precision spectroscopy and atomic clocks, an advantage of using an ion trap lies in the decoupling of the particle to a large extent from a disturbing environment leading unperturbed transition frequencies and therefore to high accuracies. Thereby, the disadvantage of a small atom number (see Eq. (1.1)) can be overcome due to practically unlimited interaction times and the observation of narrow atomic transition lines, almost free of external energy shifts caused by unwanted interactions. As the trapping potential near the trap center is close to zero, systematic frequency shifts caused by electric fields are small. On the other hand interaction with magnetic fields can be well characterized in a reproducible way, minimizing the associated systematic effects as well. Finally, ion traps are usually operated in an ultra-high vacuum environment, causing collision rates with background atoms or neighboring particles (if more than one ion is in the trap) to be very low in contrast to the case of neutral atoms. In summary, optical clocks based on single, trapped ions have the potential to reach an uncertainty limit of 10^{-18} and maybe beyond [32].

With the potential of optical clocks reaching uncertainties of 10^{-18}, the question naturally arises: What is it actually good for? The obvious reason is of course that any realization of a standard unit should be performed at its ultimate limit. The fact that frequencies are the quantities which can be measured most precisely, makes it appealing to find ways to turn measurements of other fundamental base units (volt, ampere, ohm, meter) into frequency measurements [39]. Furthermore, clocks play an important role in terrestrial navigation. Satellite navigation systems like GPS, Glonass, or the European GALILEO system, rely on the precision and accuracy of atomic clocks [40]. Therefore, these systems would greatly benefit from improved clocks. Also extra-terrestrial navigation of deep space probes would not be possible without the existence of high-performance clocks. Another important aspect of atomic clocks is the test of fundamental theories like special and general relativity or extensions of the standard model. Time dilation and gravitational redshift effects have already been observed by comparing clocks subjected

to high altitude or velocity differences [41, 42], yet the direct detection of gravitational waves is a task still to be done, where clocks could be helpful [43]. At the same time, geodesy applications and probing Earth's gravitational potential are expected to benefit greatly from clocks at the 10^{-17} level [43]. Another important task for atomic clocks is the detection of a possible time variation of fundamental constants [44–46] predicted by some theories beyond the Standard Model and suggested by astronomical observations [47–50] with partially contradicting results or investigations of fission products of the Oklo reactor [51–54]. Atomic transition frequencies depend on various parameters [55] like the Rydberg constant, the electron-to-proton mass ratio, or the fine structure constant α. Of course, the dependency is specific to the particular atom under examination. Therefore, by the measurement of many atomic transition frequencies, the different contributions can be separated. Finally, there is a less exotic application of clocks, namely the synchronization of networks reaching from data synchronization in computer networks and synchronization of different power plants for electricity, to astronomical telescopes. Here, a synthetic aperture of the size of their separation is created by linking two telescopes to increase the spatial resolution. In principle, this would also work for telescopes in space where atomic clocks could be used for maintaining their relative positions [56].

The main research focus within our group lies on quantum information processing with Ca^+ ions and one can use methods and techniques from that field in order to improve the performance of optical clocks [57] and other types of precision spectroscopy. The ability of deterministically generating entanglement is generally accepted as a key element for quantum computation [58] and quantum cryptography [59]. For the purpose of quantum metrology, the use of entangled states for an enhanced signal-to-noise ratio due to spin-squeezing [60] has been discussed [61–63] and demonstrated [64, 65] thereby beating the standard shot noise limit [66]. In addition, entangled states of two ions of different species have been used in the context of atomic clocks for efficient quantum state detection [67, 68] where electron shelving wouldn't work for technical reasons and for the measurement of scattering lengths [69].

Quantum information processing allows for the tailored design of specific states by the manipulation of individual quantum bits. Such states can be insensitive to the detrimental influences of an environment [70]. The existence of decoherence-free subspaces [71], which protect the delicate quantum information with respect to specific sources of noise, yield significantly enhanced coherence times [72] in the presence of strong technical noise which would render experiments with single or uncorrelated particles impossible on the same time scale. Therefore, entangled states with long lifetimes become very useful for high-precision spectroscopy. In this work, the use of a decoherence-free subspace with specifically designed entangled states [73] for precision spectroscopy is demonstrated. The electric quadrupole moment of Ca^+ in its metastable $D_{5/2}$ state is obtained, which is of use for frequency standard applications and for refined theoretical calculations of atomic properties. The technique makes explicit use of multi-particle entanglement and provides an approach for designed quantum metrology. Furthermore, it can be shown that entanglement is not a necessary ingredient for these measurements and classically correlated states can be used instead, although at a 50% loss of contrast.

This thesis is structured as follows. In chapter 2 the basic spectroscopic properties of $^{40}\mathrm{Ca}^+$ are presented with a theoretical description of the ion's interaction with external fields and main focus on Ramsey experiments. The experimental setup including the ion trap and the laser sources is described in chapter 3, followed by the optical frequency comb used for the absolute frequency measurement in chapter 4. Basic experimental procedures like state preparation are listed in chapter 5. Chapter 6 is dedicated to the absolute frequency measurement of the $4s\ ^2S_{1/2} - 3d\ ^2D_{5/2}$ transition. Finally, spectroscopy with correlated states are used in chapter 7 to determine the quadrupole moment of the $D_{5/2}$ level. At the end, a brief summary and an outlook of future plans are given in chapter 8.

Chapter 2

Ion trapping and interaction of an ion with external fields

In this chapter the basic theory of ion trapping and interaction of an ion with external fields is described. First, the general atomic structure of $^{40}\text{Ca}^+$ is given with a more detailed view on the $4s\ ^2S_{1/2} - 3d\ ^2D_{5/2}$ clock transition. Then, a short review on ion traps and their operation principle is presented. Basic laser-ion interaction with focus on Ramsey experiments is followed by an overview on the interaction of the ion with external fields.

2.1   Level scheme of $^{40}\text{Ca}^+$

The level structure of $^{40}\text{Ca}^+$, like for all singly ionized earth-alkali atoms, is similar to the energy level scheme of neutral alkali atoms, in particular to atomic hydrogen. The diagram in Fig. 2.1 shows the three lowest energy levels for the single valence electron. The ground state is formed by the $4S$ state, the lowest excited state by the metastable $3D$ level, which has a lifetime of $\sim$1 s [74]. This corresponds to a natural linewidth of <0.16 Hz. Spin-orbit coupling splits the D-state into two fine structure components with total angular momentum $J = 3/2$ and $J = 5/2$ and a frequency difference of 1.8 THz. The narrow $S - D$ transitions can be excited by electric quadrupole radiation at 732 nm and 729 nm, respectively. The next-higher lying excited state is the $4P$ level with a fine structure splitting of 6.7 THz. Lifetimes of $\sim$7 ns [75] for both $J = 1/2$ and $J = 3/2$ states and corresponding linewidths of 20 MHz make these levels well suited for laser cooling. In our case, we use the $S_{1/2} - P_{1/2}$ electric dipole transition at 397 nm. There is a small probability - one out of 17 - for a decay of the P into the D-levels with branching ratios given in [76, 77]. The transition wavelengths are 854 nm from $P_{3/2} - D_{5/2}$ and 866 nm for the $P_{1/2} - D_{3/2}$ transition. Additionally, there is an allowed transition from $P_{3/2}$ to the $D_{3/2}$ level with a wavelength of 850 nm which has a transition probability of about one tenth of the other two. More precise wavelengths for the transitions mentioned above, transition probabilities, oscillator strengths, and more are given in [78].
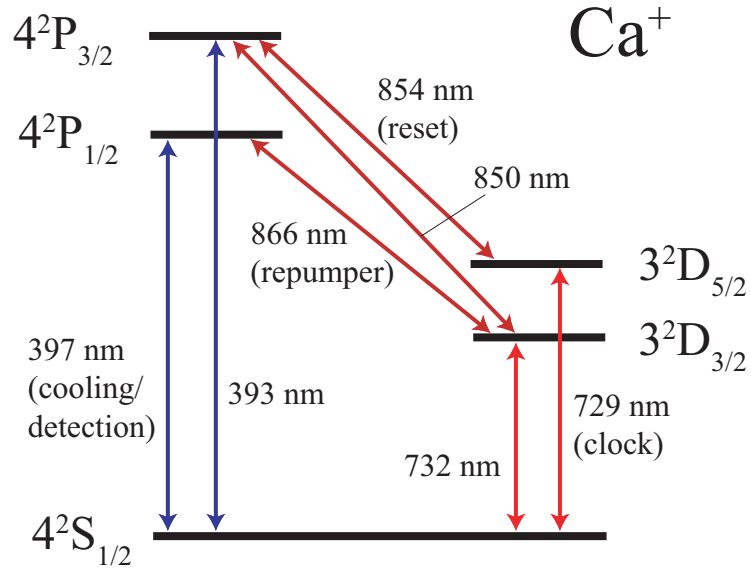
Figure 2.1: The level scheme of Ca$^+$ and the most important transitions with their respective wavelengths.

2.2 The electric quadrupole transition of ^{40}Ca$^+$

The $4s\,S - 3d\,D$ transitions are dipole-forbidden giving rise to rather long lifetimes ($\sim 1\,\mathrm{s}$) as compared to dipole allowed transitions which typically decay on a ns timescale. The long lifetimes of the $3d\,D$ states thus make these transitions ideal candidates for precision spectroscopy and optical clocks because their natural linewidth is given by the inverse of the lifetime. Furthermore, the $|S\rangle$ and $|D\rangle$ states can be used to implement a qubit where the logical information associated with logical states $|1\rangle$ and $|0\rangle$ is represented by these levels. The qubit can be manipulated by laser light as the $4s\,S$ and $3d\,D$ states radiatively couple by an electric quadrupole interaction. The field of quantum information processing is not directly part of this thesis but the tools are the same for both fields, quantum information processing and precision spectroscopy. For further information on how Ca$^+$ ions are used for quantum computing, the reader is referred to [79–81].

For a trapped ion in a magnetic field of a few Gauss, the dominant systematic shifts are caused by the Zeeman effect ($\propto 10\,\mathrm{MHz}$) induced by the static magnetic field defining the quantization axis and by the electric quadrupole shift ($\propto 10\,\mathrm{Hz}$) which is resulting from an interaction of the quadrupole moment of the $3d\,^2D_{5/2}$ level with static electric field gradients induced by the DC-trapping electrodes or spurious field gradients of patch potentials. The net nuclear spin of ^{40}Ca$^+$ is $I = 0$, therefore this isotope does not have hyperfine structure and the $4s\,^2S_{1/2} - 3d\,^2D_{5/2}$ transition splits into ten components of the Zeeman multiplet shown in Fig. 2.2. The measurement of these six transitions shown in Fig. 2.2 is sufficient to cancel these systematic effects because they are symmetric around
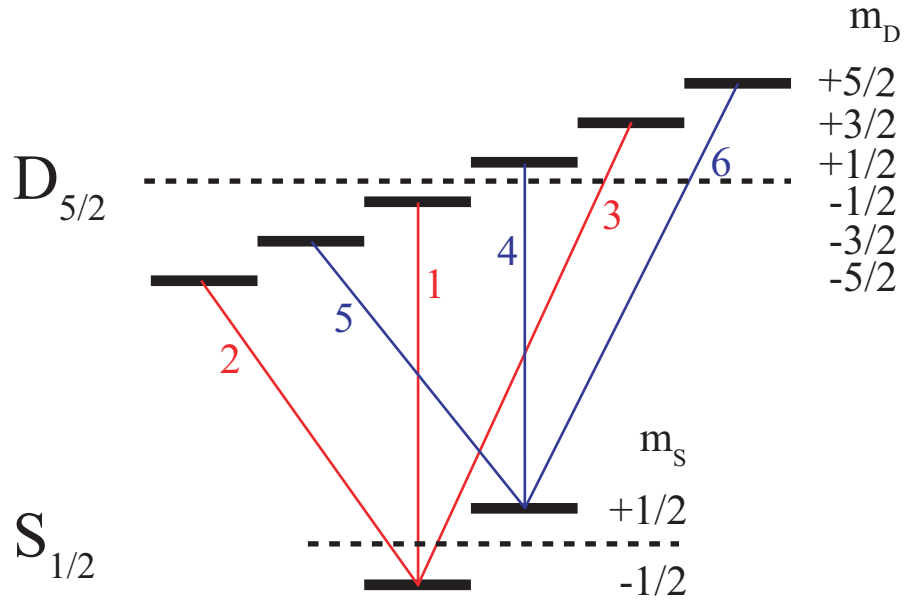
Figure 2.2: Level scheme of the $4s\,^2S_{1/2} - 3d\,^2D_{5/2}$ transition in ^{40}Ca$^+$: For the absolute frequency measurement the six possible transitions were probed in the order indicated by the number.

the line center of the transition. The corresponding transition frequencies are defined as the energy differences between the magnetic sublevels m_J of the ground and excited state:

$$
\begin{aligned}
f_1 &= \frac{1}{h}\left(E_D(|m_D = -1/2\rangle) - E_S(|m_S = -1/2\rangle)\right), \\
f_2 &= \frac{1}{h}\left(E_D(|m_D = -5/2\rangle) - E_S(|m_S = -1/2\rangle)\right), \\
f_3 &= \frac{1}{h}\left(E_D(|m_D = +3/2\rangle) - E_S(|m_S = -1/2\rangle)\right), \\
f_4 &= \frac{1}{h}\left(E_D(|m_D = +1/2\rangle) - E_S(|m_S = +1/2\rangle)\right), \\
f_5 &= \frac{1}{h}\left(E_D(|m_D = -3/2\rangle) - E_S(|m_S = +1/2\rangle)\right), \\
f_6 &= \frac{1}{h}\left(E_D(|m_D = +5/2\rangle) - E_S(|m_S = +1/2\rangle)\right).
\end{aligned}
\tag{2.1}
$$

For the absolute frequency measurement, these transitions have been measured in the order indicated by the numbers.

2.3   Operation principle of ion traps

This section will concentrate on the classical motion of a single particle to keep the discussion simple. The results, however, can be generalized to more ions in the trap if collective

motion of the ions is included in the equations of motion. More detailed information can be found in a multitude of Refs. [80, 82–85], just to name a few.
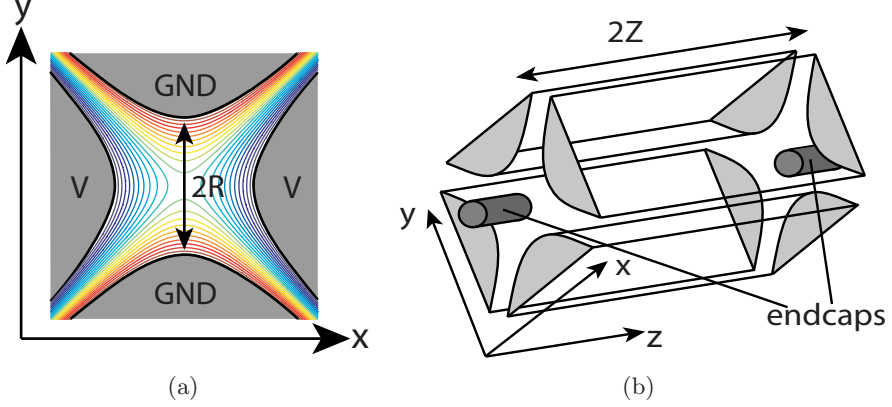
Figure 2.3: Schematic diagram of a linear Paul trap. (a) 2D view of the electrode configuration. In color: potential lines for a negative voltage V. (b) 3D view of the trap: a constant voltage applied to the endcap electrodes creates a static quadrupole potential for axial confinement.

Figure 2.3 shows a schematic diagram of a linear Paul trap. One pair of the hyperbolically shaped electrodes (Fig. 2.3(a)) is grounded while the other pair is kept at a voltage $V = V_0 \cos(\Omega_{Trap}t)$. This configuration creates a potential near the axis of the trap of the following form:

$$V(x, y, z, t) = \frac{V_0}{2} \left(1 + \frac{x^2 - y^2}{R^2} \right) \cos(\Omega_{Trap}t), \tag{2.2}$$

where R is the distance from the trap center to the electrodes. With the corresponding electric field of this (pseudo-)potential, radial confinement of the ion is achieved. To confine the ion also in axial direction, two endcap electrodes are added as depicted in Fig. 2.3(b) and kept at a fixed potential U_0. The resulting static potential can be approximated by

$$U(x, y, z) = \frac{\kappa U_0}{Z^2} \left(z^2 - \frac{1}{2} \left(x^2 + y^2 \right) \right). \tag{2.3}$$

Z is the distance from the trap center to an endcap electrode and $\kappa(<1)$ a geometrical factor. The total electric field derived from the potentials (2.2) and (2.3) is

$$\hat{\mathbf{E}}(x, y, z, t) = V_0 \left(\frac{x\hat{e}_x - y\hat{e}_y}{R^2} \right) \cos(\Omega_{Trap}t) - \frac{\kappa U_0}{Z^2} \left(2z\hat{e}_z - x\hat{e}_x - y\hat{e}_y \right), \tag{2.4}$$

$\hat{e}_i$ are the unit vectors for the directions i=x,y,z. The equations of motion for a single particle of mass M and charge Q in this field are given by Mathieu equations

$$\frac{d^2 x_i}{dt^2} + \frac{\Omega_{Trap}}{4} \left(a_i + 2q_i \cos(\Omega_{Trap}t) \right) x_i = 0, \tag{2.5}$$

12

where a_i and q_i are defined as

$$a_x = a_y = -\frac{1}{2}a_z = -\frac{4Q\kappa U_0}{MZ^2\Omega_{Trap}^2}, \tag{2.6}$$

$$q_x = -q_y = \frac{2QV_0}{MR^2\Omega_{Trap}^2}, q_z = 0. \tag{2.7}$$

For $|q_i| \ll 1$ and $|a_i| \ll 1$, stable solutions to Eqs. (2.5) exist and can be approximated by

$$x_i(t) \approx x_{1i} \cos(\omega_i t + \varphi_i)\left(1 + \frac{q_i}{2}\cos(\Omega_{Trap}t)\right), \tag{2.8}$$

where x_{1i} is the amplitude of the harmonic oscillation of frequency

$$\omega_i = \beta_i\frac{\Omega_{Trap}}{2} \quad \text{and} \quad \beta_i = \sqrt{a_i + \frac{1}{2}q_i^2}, \tag{2.9}$$

and φ_i is a phase determined by the initial position and velocity of the ion. The motion of the particle can be decomposed into two components:

- *secular motion*: harmonic oscillation with frequency ω_i about the trap center,

- *micromotion*: fast oscillation driven by the $\cos(\Omega_{Trap}t)$ term corresponding to the trapping RF field.

Additional electric fields may exist the shift the ions out of the node of the trapping field, causing excess micromotion. If an ion in the trap is illuminated by a light field, this additional micromotion creates sidebands in the excitation spectrum. The upper state population P_e in this case is proportional to:

$$P_e \sim \sum_{n=-\infty}^{\infty} \frac{J_n^2(\beta_{micro})}{(\omega_A - \omega_L + n\Omega_T)^2 + (\frac{1}{2}\gamma)^2}. \tag{2.10}$$

Here, the atomic transition frequency is given by ω_A, the frequency of the light field by ω_L and the transition linewidth by γ. The n-th sideband power is described by the Bessel function $J_n^2(\beta_{micro})$ with a modulation index β_{micro}.

2.4 Laser-ion interaction

2.4.1 Two-level atom interacting with light

For the description of a complicated atom interacting with a light field, certain approximations are necessary. Let's consider the hypothetical case of an atom having only a ground $|S\rangle$ and an excited state $|D\rangle$ separated by an energy difference of

$$\hbar\omega_A = \hbar(\omega_D - \omega_S). \tag{2.11}$$

13

This system is called two-level atom (2LA) and is an ideal test bed for quantum mechanics. In many cases, this a very good approximation to real systems and therefore widely used. The laser is described as a classical electro-magnetic field with

$$E(r,t) = E(r)e^{-i(\omega_L t + \varphi)} + c.c., \tag{2.12}$$

where $E(r)$ is the spatial dependence of the electric field, ω_L the frequency of the light, and φ the phase of the traveling light wave. The frequency difference between the laser and the atomic transition is defined as

$$\Delta = \omega_L - \omega_A. \tag{2.13}$$

The undisturbed Hamiltonian for the two-level atom without the presence of light is simply

$$H_0 = \begin{pmatrix} \hbar\omega_S & 0 \\ 0 & \hbar\omega_D \end{pmatrix}. \tag{2.14}$$

The state $|\psi\rangle = c_S |S\rangle + c_D |D\rangle$ of an atom interacting with the classical light field of Eq. (2.12) obeys the Schrödinger equation

$$i\hbar\frac{d}{dt}|\psi\rangle = \boldsymbol{H}|\psi\rangle \tag{2.15}$$

with the Hamiltonian $\boldsymbol{H} = H_0 + H_{(i)}$ where $H_{(i)}$ contains the details of the interaction. Generally, the time evolution of the state $|\psi(t)\rangle$ is given by [86]

$$|\psi(t)\rangle = U(t)|\psi(0)\rangle = e^{-\frac{i}{\hbar}\boldsymbol{H}t}|\psi(0)\rangle, \tag{2.16}$$

yielding a system of equations for the coefficients $c_i(t)$:

$$
\begin{aligned}
\dot{c}_S &= -\frac{i}{\hbar}\langle S||H_{(i)}||D\rangle\, e^{-i(\omega_A t + \varphi)}c_D, \\
\dot{c}_D &= -\frac{i}{\hbar}\langle D||H_{(i)}||S\rangle\, e^{i(\omega_A t + \varphi)}c_D.
\end{aligned}
\tag{2.17}
$$

The coupling strength is proportional to the matrix element $\langle S||H_{(i)}||D\rangle \equiv \hbar\frac{\Omega_R}{2}$ and Ω_R is usually referred to as the *Rabi frequency*.

To transform into a rotating frame, the Hamiltonian $\boldsymbol{H}$ is replaced by $U\boldsymbol{H}U^\dagger$, where U has the form

$$U = \begin{pmatrix} e^{-i\omega_L t} & 0 \\ 0 & 1 \end{pmatrix}. \tag{2.18}$$

By neglecting terms oscillating at $e^{-i2\omega_L t}$ and a redefinition of the ground state energy, the Hamiltonian in rotating wave approximation (RWA) [87] is transformed to

$$H_{RWA} = \hbar \begin{pmatrix} 0 & \frac{\Omega_R}{2} \\ \frac{\Omega_R}{2} & \Delta \end{pmatrix}. \tag{2.19}$$

14

If the excited state can decay, or in order to take decoherence effects like a finite linewidth of the laser into account, one has to use the density matrix formalism. The Schrödinger equation is then replaced by

$$\frac{d}{dt}\hat{\rho} = \frac{i}{\hbar}[H, \hat{\rho}] + \mathcal{L}(\hat{\rho}),$$

(2.20)

where $\mathcal{L}(\hat{\rho})$ contains the relaxation terms.

The dynamics of the two-level atom with a spontaneous decay rate γ is described by the *optical Bloch equations*:

$$
\begin{aligned}
\dot{\rho}_{DD} &= -\Omega_R \operatorname{Im}(\rho_{DS}) - \gamma \rho_{DD} \\
\dot{\rho}_{SD} &= -i\frac{\Omega_R}{2}(\rho_{DD} - \rho_{SS}) + (i\Delta - \frac{\gamma}{2})\rho_{SD} \\
\rho_{DD} &= 1 - \rho_{SS} \\
\rho_{DS} &= \rho_{SD}^*.
\end{aligned}
$$

(2.21)

The steady state solution for $\rho_{SS}(t=0) = 1$ for the excited state population is

$$\rho_{DD}(t \to \infty) = \frac{(\Omega_R/2)^2}{\Delta^2 + (\gamma/2)^2 + 2(\Omega_R/2)^2}.$$

(2.22)

For low saturation ($\Omega_R \ll \gamma$), the excitation probability is $\rho_{DD} \ll 1$ and yields a Lorentzian line shape

$$\rho_{DD}(\infty) = \left(\frac{\Omega_R}{\gamma}\right)^2 \frac{1}{1 + 4(\Delta/\gamma)^2}.$$

(2.23)

In the coherent regime, *i. e.* $\Omega_R \gg \gamma$, the solution exhibits damped oscillations of the population between the ground and excited state with a frequency of $\Omega = \sqrt{\Omega_R^2 + \Delta^2}$. This is known as *Rabi oscillations*. It can be interpreted as a rotation of the Bloch vector defined as

$$
\begin{pmatrix} U \\ V \\ W \end{pmatrix} = \begin{pmatrix} 2\operatorname{Re}(\rho_{SD}) \\ 2\operatorname{Im}(\rho_{SD}) \\ \rho_{DD} - \rho_{SS} \end{pmatrix}.
$$

(2.24)

The evolution of the system for a laser pulse of length θ, given the initial conditions $U(0), V(0)$, and $W(0)$, has the following matrix representation [86]:

$$
\begin{pmatrix} U(\theta) \\ V(\theta) \\ W(\theta) \end{pmatrix} = R(\Omega_R, \phi, \Delta, \theta) \begin{pmatrix} U(0) \\ V(0) \\ W(0) \end{pmatrix},
$$

(2.25)

where the transformation matrix is given by

$$R(\Omega_R, \phi, \Delta, \theta) = \begin{pmatrix} \cos(\Omega\theta) + \frac{\Omega_R^2}{\Omega^2}(1 - \cos(\Omega\theta))\cos^2\phi \\ \frac{\Delta}{\Omega}\sin(\Omega\theta) - \frac{\Omega_R^2}{\Omega^2}(1 - \cos(\Omega\theta))\cos\phi\sin\phi \\ -\frac{\Omega_R\Delta}{\Omega^2}(1 - \cos(\Omega\theta))\cos\phi - \frac{\Omega_R}{\Omega}\sin(\Omega\theta)\sin\phi \end{pmatrix}$$

$$\begin{matrix} -\frac{\Delta}{\Omega}\sin(\Omega\theta) - \frac{\Omega_R^2}{\Omega^2}(1 - \cos(\Omega\theta))\sin\phi\cos\phi \\ \cos(\Omega\theta) + \frac{\Omega_R^2}{\Omega^2}(1 - \cos(\Omega\theta))\sin^2\phi \\ -\frac{\Omega_R}{\Omega}\sin(\Omega\theta)\cos\phi + \frac{\Omega_R\Delta}{\Omega^2}(1 - \cos(\Omega\theta))\sin\phi \end{matrix} \qquad (2.26)$$

$$\begin{matrix} -\frac{\Omega_R\Delta}{\Omega^2}(1 - \cos(\Omega\theta))\cos\phi + \frac{\Omega_R}{\Omega}\sin(\Omega\theta)\sin\phi \\ \frac{\Omega_R}{\Omega}\sin(\Omega\theta)\cos\phi + \frac{\Omega_R\Delta}{\Omega^2}(1 - \cos(\Omega\theta))\sin\phi \\ 1 - \frac{\Omega_R^2}{\Omega^2}(1 - \cos(\Omega\theta)) \end{matrix}$$

with the generalized Rabi frequency $\Omega^2 = \Omega_R^2 + \Delta^2$. Equation (2.25) represents nothing else than Rabi oscillations. The time θ describes how long the atom is exposed to the interaction. An atomic oscillator is usually interrogated near the resonance, for which $\Delta \ll \Omega$. In this case, R simplifies to

$$R(\Omega_R, \phi, 0, \theta) =$$
$$\begin{pmatrix} \cos(\Omega\theta) + (1 - \cos(\Omega_R\theta))\cos^2\phi & -(1 - \cos(\Omega_R\theta))\sin\phi\cos\phi & \sin(\Omega_R\theta)\sin\phi \\ -(1 - \cos(\Omega_R\theta))\sin\phi\cos\phi & \cos(\Omega_R\theta) + (1 - \cos(\Omega_R\theta))\sin^2\phi & \sin(\Omega_R\theta)\cos\phi \\ -\sin(\Omega_R\theta)\sin\phi & -\sin(\Omega_R\theta)\cos\phi & \cos(\Omega_R\theta) \end{pmatrix}.$$
$$(2.27)$$

The rotation angle is given by $\Omega_R\theta$. An angle of $\Omega_R\theta = \pi$ corresponds to a population exchange from $|S\rangle \to |D\rangle$ and is called "π-pulse", a "$\frac{\pi}{2}$-pulse" creates an equal superposition of the ground and excited state of the form $|\psi\rangle = \frac{1}{\sqrt{2}}(|S\rangle + e^{i\phi}|D\rangle)$.

The effect of far-detuned laser light on the transition frequency can be treated by perturbation theory in second-order of the electric field. For non-degenerate states, the interaction Hamiltonian of Eq. (2.19) leads to a frequency shift often referred to as *AC Stark shift*, that is [88]

$$\Delta\nu_{Stark}(|i\rangle) = \sum_{i \neq j} \frac{|\langle j| H_{RWA} |i\rangle|^2}{\omega_i - \omega_j}. \qquad (2.28)$$

Considering real atoms again, two types of atomic transitions are considered in this thesis: electric dipole and quadrupole transitions.

Electric dipole transition

For an electric dipole-allowed transition like the $S - P$ transition, the Rabi frequency is defined via the dipole matrix element

$$\langle S| \vec{d} \cdot \vec{E} |P\rangle = \hbar\frac{\Omega_R}{2}, \qquad (2.29)$$

16

where $\vec{d} = e\vec{r}$ is the induced dipole moment and $\vec{E}$ the electric field of the light at the position of the atom. The spontaneous decay rate Γ is related to the Einstein A_{21} coefficient and the dipole matrix element by

$$\Gamma = \frac{1}{\tau} = A_{21} = \frac{\omega_A^3 |\langle S| \vec{d} \cdot \vec{E} |P\rangle|^2}{3\pi\epsilon_0 \hbar c^3} \tag{2.30}$$

with the speed of light c, and ϵ_0 the permittivity of vacuum. Therefore, the Stark shift by far detuned light can be calculated by using Eq. (2.28) and becomes

$$\Delta\nu_{Stark}(|i\rangle) = \pm\frac{|\langle S| \vec{d} \cdot \vec{E} |P\rangle|^2}{\Delta} = \pm\frac{\Omega_R^2}{4\Delta} = \pm\frac{3\pi c^2}{2\omega_A^3}\frac{\Gamma}{\Delta}I, \tag{2.31}$$

with the optical intensity $I = \frac{1}{2\mu_0 c}|E|^2$.

Electric quadrupole transition

The reason for using dipole-forbidden transitions in experiments is the long lifetime of the metastable states and the fact that decoherence due to spontaneous emission will greatly be suppressed. The transition for the absolute frequency measurement considered here is the electric quadrupole-allowed $4s\ ^2S_{1/2} - 3d\ ^2D_{5/2}$ transition. Details about the using quadrupole transitions for quantum computation are discussed in detail in [89]. The transition can be excited by a coupling of the induced quadrupole moment $\boldsymbol{Q}$[1] and the gradient of the electro-magnetic field $\nabla\boldsymbol{E}(t)$. The corresponding Hamiltonian to this type of interaction is

$$H_Q = \nabla\boldsymbol{E}(t)\boldsymbol{Q}. \tag{2.32}$$

For a more specific derivation of this interaction Hamiltonian the reader is referred to [90, 91]. The interaction strength is given by the Rabi frequency defined as

$$\Omega_R = \left|\frac{eE_0}{2\hbar}\langle S, m_S| (\boldsymbol{\epsilon} \cdot \mathbf{r})(\mathbf{k} \cdot \mathbf{r}) |D, m_D\rangle\right|, \tag{2.33}$$

where $\boldsymbol{\epsilon}$ is the polarization of the light with a propagation vector $\boldsymbol{k}$ and an electric field amplitude E_0, $\boldsymbol{r}$ is the position operator of the valence electron relative to the atomic center of mass. The coupling strength can be estimated by using $\langle S, m_S| \boldsymbol{r}^2 |D, m_D\rangle \approx a_0^2$ and one obtains [84]

$$\Omega_R \approx \frac{kE_0}{2\hbar}ea_0^2. \tag{2.34}$$

As a consequence, an electric field of $40\,\text{kV/m}$ is required for a Rabi frequency on the order of $\Omega_R/(2\pi) \sim 100\,\text{kHz}$. To achieve field strengths like this, the laser needs to be tightly focused onto the ion. In our experiment, the beam waist at the focal point is less than $2.5\,\mu\text{m}$ thus the required optical power is $40\,\mu\text{W}$ only.

---

[1]The individual components of the quadrupole tensor are $Q_k^{(2)} = r^2 C_k^{(2)}(\theta, \varphi)$ with renormalized spherical harmonics of the form $C_m^{(l)} = \sqrt{\frac{4\pi}{2l+1}}Y_{l,m}(\theta, \varphi)$.

The Einstein coefficient A_{12} describing the decay rate of the excited state is related to the reduced matrix element $\langle S_{1/2} \| r^2 C^{(2)} \| D_{5/2} \rangle$ by [89]

$$A_{12} = \frac{c\alpha k^5}{90} \left| \left\langle S_{1/2} \left\| r^2 C^{(2)} \right\| D_{5/2} \right\rangle \right|^2. \tag{2.35}$$

The reduced matrix element can be calculated using the Wigner-Eckart theorem [92] (see also Sec. A.2). Substituting the matrix element in Eq. (2.33) by the expression in Eq. (2.35), the coupling strength can be further evaluated in terms of the "specific" Clebsch-Gordan coefficients $\Lambda_{J,J'}(m, m')$ for the particular total angular momenta J, J' of the states and a part containing the geometrical dependence $g^{(\Delta m)}(\phi, \gamma)$. The Rabi frequency therefore is expressed as:

$$\Omega_R = \frac{e}{2\hbar} \sqrt{\frac{15}{c\alpha}} E_0 \sqrt{\frac{A_{12}}{k^3}} \Lambda_{J,J'}(m, m') g^{(\Delta m)}(\phi, \gamma), \tag{2.36}$$

where α denotes the fine structure constant, ϕ the angle between the laser's k-vector and the magnetic field, and γ is the angle between the laser polarization and the projection of the magnetic field onto the incident plane. Explicit expressions for these functions can be found in [79]. For the specific geometry of our trap, i. e. $\phi = 45°$ and $\gamma = 0°$, the values of the prefactors $\Lambda(m, m') g^{(\Delta m)}(\phi, \gamma)$ for $\Delta m = 0$ and $\Delta m = 2$ are given in Tab. 2.1. Transitions with $\Delta m = 1$ do not couple to the laser in the configuration above, leading to the six possible transitions mentioned in Eq. (2.1) and Fig. 2.2.

Table 2.1: The transition factors and relative coupling strengths according to the definition of the individual transitions given in Eq. (2.1).

#	Transition $|S, m\rangle \leftrightarrow |D, m'\rangle$	$\Lambda_{1/2,5/2}(m, m') g^{(\Delta m)}(\phi, \gamma)$	Rel. strength
1,4	$\pm 1/2 \leftrightarrow \pm 1/2$	$\sqrt{\frac{3}{5}} \frac{1}{2}$	1
3,5	$\pm 1/2 \leftrightarrow \mp 3/2$	$\frac{1}{\sqrt{5}} \frac{1}{\sqrt{24}}$	0.24
2,6	$\pm 1/2 \leftrightarrow \pm 5/2$	$1 \frac{1}{\sqrt{24}}$	0.53

2.4.2 Trapped two-level atom interacting with light

For a trapped atom laser-cooled to near the motional ground state, the motion of the particle has to be treated quantum mechanically. According to [93] the Hamiltonian for a two-level atom of mass m in a one-dimensional, harmonic trap of frequency ω interacting with a traveling light field of a single mode laser near the atomic resonance is given by

$$H = H_{(m)} + H_{(e)} + H_{(i)}, \tag{2.37}$$

$$H_{(m)} = \frac{p^2}{2m} + \frac{1}{2} m \omega^2 x^2, \tag{2.38}$$

$$H_{(e)} = \frac{1}{2} \hbar \omega_A \sigma_z, \tag{2.39}$$

18

where p and x are the momentum and position operators for the particle, and σ^+, σ^-, σ_z are the Pauli spin matrices. $H_{(m)}$ and $H_{(e)}$ describe the atomic motion and the electronic state of the atom. The interaction term with the classical light field of frequency ω_L and wave vector k can be expressed as

$$H_{(i)} = \frac{\hbar}{2}\Omega(\sigma^+ + \sigma^-)\left(e^{i(kx-\omega_L t)} + e^{-i(kx-\omega_L t)}\right). \tag{2.40}$$

The interaction strength is given by the Rabi frequency Ω. The model has a similar form to the Jaynes-Cummings model [94, 95] describing the interaction of a two-level system with a single cavity mode except that the role of the quantized radiation field is replaced by the quantized motion of the atom in the trap.

Because the trap is harmonic, the position and momentum operators can be replaced by the creation and annihilation operators $a^\dagger$ and a for the trap quanta. Introducing the Lamb-Dicke parameter[2]

$$\eta = k\sqrt{\frac{\hbar}{2m\omega}} \tag{2.41}$$

which relates the classical recoil energy of the photon to that of one trap quantum, the interaction Hamiltonian is given by

$$H_{(i)} = \frac{1}{2}\hbar\Omega\left(e^{i\eta(a+a^\dagger)}\sigma^+ e^{-i\omega_L t} + e^{-i\eta(a+a^\dagger)}\sigma^+ e^{i\omega_L t}\right). \tag{2.42}$$

In the interaction picture,

$$H_I = \frac{1}{2}\hbar\Omega\left(e^{i\eta(a+a^\dagger)}\sigma^+ e^{-i\Delta t} + e^{-i\eta(a+a^\dagger)}\sigma^+ e^{i\Delta t}\right). \tag{2.43}$$

Here, the rotating-wave approximation [87] was applied and terms oscillating at twice the optical frequency were neglected. Depending on the detuning Δ, this Hamiltonian will couple certain electronic $|g, e\rangle$ and motional states $|n, n'\rangle$.

In the Lamb-Dicke limit, i. e. for the condition $\eta^2(2n + 1) \ll 1$, the exponential in Eq. (2.43) can be expanded in terms of η

$$H_I = \frac{\hbar}{2}\Omega\sigma^+\left(1 + i\eta(ae^{-i\omega t} + a^\dagger e^{i\omega t})e^{-i\Delta t} + O(\eta^2)\right) + H.c. \tag{2.44}$$

As a consequence, transitions which change the vibrational quantum number by more than one are greatly suppressed. Transitions $|S\rangle|n\rangle - |D\rangle|n\rangle$, which do not change the motional state ($\Delta = 0$) are called *carrier transitions* and have a coupling strength Ω. A detuning of $\Delta = -\omega$ gives rise to *red sideband transitions* of the type $|S\rangle|n\rangle - |D\rangle|n - 1\rangle$ with a Rabi frequency of $\eta\sqrt{n}\Omega$. On the *blue sideband* for $\Delta = \omega$ the coupling strength is $\eta\sqrt{n + 1}\Omega$.

---

[2]In case of an angle ϑ between the oscillation and the laser: $\eta = k\cos\vartheta\sqrt{\hbar/2m\omega}$.

2.4.3 The Ramsey experiment

For the purpose of frequency measurements with Ramsey's method of separated fields, an atom is probed by two $\frac{\pi}{2}$-pulses separated by a waiting time τ_R. The rotation caused by these pulses are described by the transformation matrix given in Eq. (2.25). During the time where the atom is left to evolve freely and does not experience the interrogation field, a special case for the transformation matrix R applies, where $\Omega_R = 0$. Therefore, R reduces to

$$R(0,0,\Delta,\theta) = \begin{pmatrix} \cos(\Delta\theta) & -\sin(\Delta\theta) & 0 \\ \sin(\Delta\theta) & \cos(\Delta\theta) & 0 \\ 0 & 0 & 1 \end{pmatrix}. \tag{2.45}$$

In contrast to atomic fountain clocks or conventional Cs beam tubes, where the atoms pass through two interaction zones and travel through a microwave-free region, trapped atoms are interrogated by separating the laser pulses in time. In between, the light is switched off and the transition frequency ω_A is constant over the whole time.

The atom is usually prepared without any coherences ($U(0) = V(0) = 0$), but in a certain initial state characterized by the population difference $W(0) = -1$ or $W(0) = +1$ depending on wether the atoms were initialized in the ground or excited state. The modification of the atomic quantum state by the two laser pulses is given by $R_i = (\Omega_R, \phi_i, \Delta, \tau)$, with $i = 1$ the first and $i = 2$ the second pulse. The evolution during the Ramsey waiting time τ_R the is represented by $R(0,0,\Delta,\tau_R)$. The state of the atom at the end of the Ramsey experiment is simply described by a multiplication of the transformation matrices for the individual steps, so that the Bloch vector becomes

$$\begin{pmatrix} U(\tau,\tau_R,\tau) \\ V(\tau,\tau_R,\tau) \\ W(\tau,\tau_R,\tau) \end{pmatrix} = R_2(\Omega_R,\phi_2,\Delta,\tau)R(0,0,\Delta,\tau_R)R_1(\Omega_R,\phi_1,\Delta,\tau) \begin{pmatrix} 0 \\ 0 \\ W(0) \end{pmatrix}. \tag{2.46}$$

At the end of the experiment, the state of the atom can then be detected for instance by electron shelving. The detector signal is proportional to the probability $P(\tau)$ that the atom has made a transition between the $|g\rangle$ and the $|e\rangle$ state. Taking Eqs. (2.27), (2.45), and (2.46) and replacing the individual phases ϕ_i of the pulses by $\phi = \phi_2 - \phi_1$, the transition probability is

$$\begin{aligned} P(\tau) = \frac{4\Omega_R^2}{\Omega^2} \sin^2\left(\frac{1}{2}\Omega\tau\right) & \left[\cos\left(\frac{1}{2}\Omega\tau\right)\cos\left(\frac{1}{2}\Delta\tau_R + \phi\right)\right. \\ & \left. -\frac{\Delta}{\Omega}\sin\left(\frac{1}{2}\Omega\tau\right)\sin\left(\frac{1}{2}\Delta\tau_R + \phi\right)\right]^2. \end{aligned} \tag{2.47}$$

The appearance of the fringes with a periodicity of $1/\tau_R$ is characteristic for the so-called Ramsey pattern [4] and an example is shown in Fig. 2.4. The parameters for this plot are a Ramsey time $\tau_R = 1\,\text{ms}$, a pulse length of $\tau = 50\,\mu\text{s}$, and a Rabi frequency $\Omega_R/(2\pi) = 4.6\,\text{kHz}$. The dashed line marks the average value of the excitation profile and can be obtained by replacing the rapidly oscillating terms in Eq. (2.47) by their mean

values. This yields

$$P_{Rabi} = \frac{\Omega_R^2}{2\Omega^2}\left(\sin^2(\Omega\tau) + \frac{\Delta^2}{\Omega^2}(1 - \cos(\Omega\tau))^2\right),\tag{2.48}$$

independent of the pulse phase difference ϕ. It can be shown, that Eq. (2.48) is the Fourier transform of the rectangular pulse distribution. The central part of the Ramsey pattern
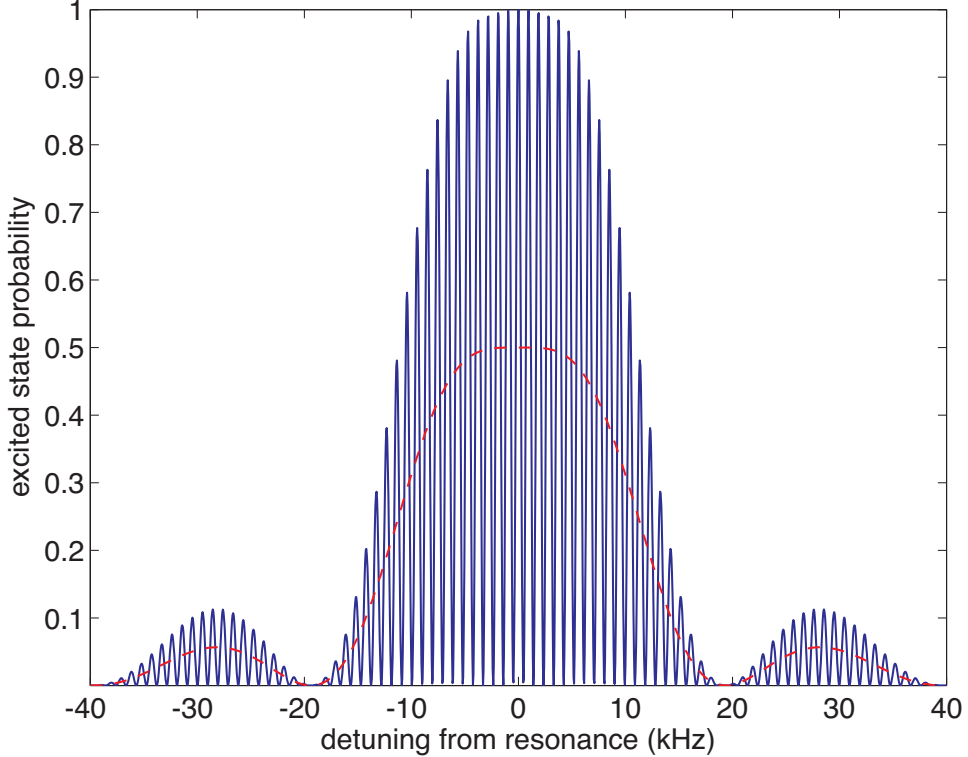
Figure 2.4: The Ramsey pattern (solid line) for a Rabi frequency of $\Omega_R/(2\pi) = 4.6\,\text{kHz}$ and a pulse separation of $1\,\text{ms}$. The Rabi pedestal is indicated by the dashed line.

is of special interest as it provides the practical information about detuning of the laser from the transition line center. For $\Delta \ll \Omega_R$, Eq. (2.47) can be simplified to

$$P(\tau) = \frac{1}{2}\left[1 + \cos\left(\Delta(\tau_R + \frac{4\tau}{\pi}) + \phi\right)\right]\sin^2(\Omega_R\tau),\tag{2.49}$$

where $(\tau_R + \frac{4\tau}{\pi})$ can be interpreted as an effective Ramsey time, taking into account the precession of the Bloch vector around the z-axis during the Ramsey pulses. This is in agreement with a slightly different approach discussed in [81]. Equation (2.49) is further reduced to

$$P(\tau) = \frac{1}{2}\left[1 + \cos(\Delta\tau_R + \phi)\right]\sin^2(\Omega_R\tau)\tag{2.50}$$

21

under the condition $\tau \ll \tau_R$, which is typically used in the context of text book examples of Ramsey experiments. The error for an insufficient near-resonance condition is given by a first order expansion of

$$\Delta P(\tau) = -\frac{2\Delta}{\Omega_R} \tan(\frac{1}{2}\Omega_R \tau) \sin(\Delta \tau_R + \phi) \sin^2(\Omega_R \tau). \qquad (2.51)$$

For $\phi = 0$ there is a maximum of Eq. (2.47) at $\Delta = 0$, when the frequency of the laser equals the atomic transition frequency. The value for the maximum also depends on the Rabi frequency and reaches the upper limit of unity at $\Omega_R \tau = \frac{\pi}{2}$. If we have $\phi = \pm\frac{\pi}{2}$ the pattern is shifted by half a fringe and the excitation probability reaches 50%. At this point, the pattern has the steepest slope with respect to the detuning, the ideal case for a frequency discriminator. The two excitation probabilities P_i obtained for the two different phase settings $\phi = \frac{\pi}{2}$ for $i = 1$ and $\phi = -\frac{\pi}{2}$ for $i = 2$ can be combined to calculate the detuning to the laser with respect to the atomic resonance in the following way:

$$\Delta/(2\pi) = \arcsin\left(\frac{P_2 - P_1}{(P_1 + P_2)C}\right) / \left(2\pi(\tau_R + \frac{4\tau}{\pi})\right), \qquad (2.52)$$

where C is introduced to describe a loss of the fringe contrast caused by decoherence effects or insufficient state preparation.

Please note, that the crossing point for the two cases $\phi = \pm\frac{\pi}{2}$ lies at a detuning of $\Delta = 0$ and - for a fixed pulse time τ - does not depend on the actual Rabi frequency Ω_R. Errors due to a change of the excitation strength caused by a drift in the laser intensity, are relevant only if the transition is probed at a non-zero detuning. As an example, for a pulse length of $\tau = 54\,\mu s$ necessary to realize a $\frac{\pi}{2}$-pulse at $\Omega_R/(2\pi) = 4.63\,kHz$ and a Ramsey time of $\tau_R = 1\,ms$, an offset in Rabi frequency of 6% leads to a frequency error that can be approximated by

$$\Delta\nu_{intensity} \approx 2.2 \times 10^{-3}\Delta/(2\pi). \qquad (2.53)$$

The result above can be interpreted in terms of a rotating spin. A time-dependent change of any two-level quantum system may be described as an effective spin-$\frac{1}{2}$ particle placed in a static magnetic field [96]. For simplicity, $\phi = 0$ and $\Omega_R \tau = \frac{\pi}{2}$ is assumed and the atom is prepared in the ground state. The evolution of the Bloch vector is illustrated in Fig. 2.5. The Bloch vector for an atom in the ground state is pointing along the z-direction. During the first interaction pulse the spin rotates along an axis x into the x-y plane. In between the Ramsey pulses the Rabi frequency $\Omega_R = 0$ and the spin precesses around the y axis. The rotation angle is given by

$$\varphi_0 = \Delta \cdot \tau_R \qquad (2.54)$$

if the detuning of the laser $\Delta = \omega_L - \omega_A$ is constant during the period of free precession. The second pulse rotates the spin again along the x-axis ($\phi = 0$!). The population change can now be measured by a projection of the Bloch vector onto the z-axis.

22
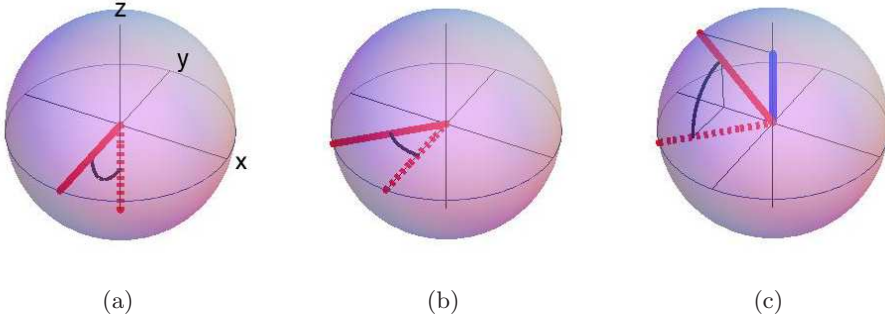
Figure 2.5: Bloch sphere pictures for a Ramsey experiment. First, the spin is rotated into the equatorial plane by the $\frac{\pi}{2}$ pulse (a), then the system can evolve freely for a time τ_R where the precession angle determined by the frequency detuning (b), and the second $\frac{\pi}{2}$ pulse rotates out of the xy-plane again (c). The precession angle can now be measured by a projection onto the z direction.

2.4.4 Ramsey contrast

The Ramsey experiment was treated so far without taking decoherence effects into account which occur for real experiments. In Eq. (2.52) the contrast C was introduced without giving a more detailed explanation. In $^{40}Ca^+$, two effects can lead to a loss of contrast due to decoherence, when probing the $4s\ ^2S_{1/2} - 3d\ ^2D_{5/2}$ transition. One effect is of course related to frequency fluctuations of the interrogation laser, the other one is caused by magnetic field fluctuations which affect the different transitions according to their magnetic quantum numbers. Mathematically, these effects can be treated identically as they both lead to a fluctuating detuning Δ of the transition. In order to calculate the contrast as a function of the waiting time τ_R, we have to assume a certain noise model.

First a Gaussian "shot-to-shot" noise is considered with the following distribution of frequency fluctuations

$$P(\Delta) = \frac{1}{\sigma\sqrt{\pi}} \exp\left(-\frac{\Delta^2}{\sigma^2}\right), \tag{2.55}$$

where σ is the half width at the $1/e$-point. Therefore, each individual Ramsey experiment will accumulate a different phase factor $\exp(i\Delta\tau_R)$. The contrast can be calculated by the average of the phase fluctuations, that is

$$C(\tau_R) = |\langle\exp(i\Delta\tau_R)\rangle| = \left|\int_{-\infty}^{+\infty} d\Delta P(\Delta)\exp(i\Delta\tau_R)\right| = \exp\left(-\frac{\sigma^2\tau_R^2}{4}\right). \tag{2.56}$$

The FWHM of the frequency fluctuations for the above definition of σ is

$$2\pi\Delta\nu_{FWHM} = 2\sqrt{\ln 2}\ \sigma. \tag{2.57}$$

Taking this into account, $C(\tau_R)$ can be expressed as

$$C(\tau_R) = \exp\left(-\frac{\pi^2\Delta\nu_{FWHM}^2\tau_R^2}{4\ln 2}\right). \tag{2.58}$$

23

Let $\tau_{1/2}$ be the time for which the contrast reaches 50% of the initial value, the corresponding FWHM of the laser frequency is given by

$$\Delta\nu_{FWHM} = \frac{2\ln 2}{\pi}\frac{1}{\tau_{1/2}}. \tag{2.59}$$

Analogous to Gaussian frequency fluctuations, the contrast can be calculated in case of a Lorentzian distribution

$$P(\Delta) = \frac{1}{\pi}\frac{\gamma}{\gamma^2 + \Delta^2} \tag{2.60}$$

with a half width at half maximum of γ. The contrast then decays exponentially with the waiting time given by

$$C(\tau_R) = \exp\left(-\gamma\tau_R\right). \tag{2.61}$$

The laser linewidth is related to the time $\tau_{1/2}$ where the contrast has decayed to 50% by

$$\Delta\nu_{FWHM} = \frac{\gamma}{\pi} = \frac{\ln 2}{\pi}\frac{1}{\tau_{1/2}}. \tag{2.62}$$

Measurements of the Ramsey decay are therefore a valuable means for an investigation of the laser linewidth of an ultra-stable laser, particularly interesting for experiments where no second ultra-stable laser system for an optical beat measurement is available.

2.5 Interaction with magnetic and electric fields

2.5.1 Zeeman shift

The total angular momentum J of the valence electron is given by

$$J = L + S. \tag{2.63}$$

Each of the fine structure levels J consists of $(2J+1)$ sublevels which are related to the angular distribution of the electron wave function. They are labeled by the magnetic quantum number $m_J = -|L+S| \leq J \leq L+S$. The degeneracy of the magnetic sublevels is lifted in the presence of a non-zero magnetic field $\boldsymbol{B}$. The Hamiltonian describing the interaction of the magnetic moment $\boldsymbol{\mu}$ of the atom with the magnetic field in first order perturbation theory is

$$H_{Zeeman} = -\boldsymbol{\mu}\boldsymbol{B}. \tag{2.64}$$

If the energy shift of the magnetic field is small compared with the fine structure splitting, the magnetic moment can be written in terms of the total angular momentum of Eq. (2.63) and the interaction Hamiltonian becomes

$$H_{Zeeman} = -\mu_B g_J \boldsymbol{J}\boldsymbol{B}, \tag{2.65}$$

where μ_B is the Bohr magneton and g_J the Landé g-factor, which is given by [97]

$$g_J = g_L \frac{J(J+1) - S(S+1) + L(L+1)}{2J(J+1)} + g_S \frac{J(J+1) + S(S+1) - L(L+1)}{2J(J+1)}$$
$$\simeq 1 + \frac{J(J+1) + S(S+1) - L(L+1)}{2J(J+1)}. \tag{2.66}$$

Here, g_L and g_S are the g-factors for the orbital and spin magnetic moments and the second expression is an approximation for $g_L \simeq 1$ and $g_S \simeq 2$. Equation (2.66) does not contain QED effects and corrections for the complicated multi-electron structure of ^{40}Ca$^+$. The g-factor in the ground state of ^{40}Ca$^+$ has been precisely measured by Tommaseo *et al.* [98] to be $g_J(4s\ ^2S_{1/2}) = 2.002\ 256\ 64(9)$ while $g_J(3d\ ^2D_{5/2}) \simeq 1.2$.

For $\boldsymbol{B} = B\boldsymbol{e}_z$ and $\boldsymbol{J} = m_J\boldsymbol{e}_z$, where $\boldsymbol{e}_z$ is the unit vector in the quantization direction, the frequency shift of a magnetic sublevel can be calculated as

$$\Delta\nu_{linZ} = m_J g_J \frac{\mu_B B}{\hbar} \tag{2.67}$$

to lowest order in B. This is called the *anomalous Zeeman effect*. The higher order contribution to the Zeeman effect has a quadratic component which shifts the levels which couple to the sublevels of the $3d\ ^2$D$_{3/2}$ state. By using second order perturbation theory [99], the quadratic Zeeman shift is

$$\Delta\nu_{quadZ} = K \frac{(\mu_B B)^2}{h^2 \nu_{FS}}, \tag{2.68}$$

where ν_{FS} is the fine structure splitting and h the Planck constant and K a constant depending on the magnetic sublevel given by

$$K = \frac{6}{25} \quad \text{for } m_D = \pm\tfrac{1}{2},$$
$$K = \frac{4}{25} \quad \text{for } m_D = \pm\tfrac{3}{2},$$
$$K = 0 \quad \text{for } m_D = \pm\tfrac{5}{2}. \tag{2.69}$$

In most cases this correction of a few Hz is negligible compared to the linear contribution which is on the order of MHz but for the clock measurement it represents the largest shift in the error budget after the cancellation of the linear Zeeman effect and the quadrupole shift.

There is also a non-zero mean-square magnitude of the magnetic field caused by black-body radiation. According to [100], it can be expressed as

$$\langle B^2(t) \rangle = (28 \text{ mG})^2 \left(\frac{T}{300 \text{ K}}\right)^4. \tag{2.70}$$

At room temperature, the estimated shifts for the individual transitions would be well below $1\,$mHz and therefore completely masked by other magnetic fields.

2.5.2 Electric quadrupole shift

The non-spherical charge distribution of the upper D level gives rise to an electric quadrupole moment that can interact with any electric field gradient present in the trap, for example those gradients generated by the DC electrodes of a linear Paul trap or by patch potentials on the trap electrode structure. According to [91], the electric quadrupole moment $\boldsymbol{\Theta}(\gamma, J)$ of an atom in the electronic state $|\gamma, J\rangle$ having a the total angular momentum J in the magnetic sublevel with maximum magnetic quantum number m_J is defined as

$$\boldsymbol{\Theta}(\gamma, J) = -e \left\langle \gamma, J, m_J = J \left\| \sum_{i=1}^{N} r_i^2 C_0^2(\theta_i, \phi_i) \right\| \gamma, J, m_J = J \right\rangle, \quad (2.71)$$

where the sum is taken over all electrons i with the radial coordinate r_i and angular coordinates θ_i, ϕ_i and the renormalized spherical harmonic $C_0^{(2)}(\theta_i, \phi_i) = \sqrt{\frac{4\pi}{5}} Y_{2,0}(\theta_i, \phi_i)$.

The interaction Hamiltonian for the atomic quadrupole moment coupled to an electric field gradient is given by Eq. (2.32). Here, the components of the tensor describing the gradient of the external field $\nabla \boldsymbol{E}$ for a electric trapping potential given in Eq. (2.3) is

$$\begin{aligned}
\nabla E_0^{(2)} &= -A, \\
\nabla E_{\pm 1}^{(2)} &= 0, \\
\nabla E_{\pm 2}^{(2)} &= \sqrt{\frac{1}{6}} \epsilon A,
\end{aligned} \quad (2.72)$$

where the term proportional to ϵ takes into account a possible field gradient which is not oriented along the trap axis, e. g. created by a patch potential. The trapping potential therefore is modified by an extra component $U'(x, y, z) = \epsilon A(x^2 - y^2)$. The Hamiltonian then takes the form

$$H_Q = -A Q_0^{(2)} + \sqrt{\frac{1}{6}} \epsilon A (Q_2^{(2)} + Q_{-2}^{(2)}). \quad (2.73)$$

The magnitude of the electric field gradient in z-direction can be calibrated by the trap frequency ω_z and is given by

$$A = \nabla E = \frac{M \omega_z^2}{e} \quad (2.74)$$

using the gradient of the electric field from Eq. (2.4) and inserting Eqs. (2.6) and (2.9).

Comparing the results obtained by [101] for the quadrupole shift in Sr$^+$, the shift for the $3d\,^2D_{5/2}$ levels in ^{40}Ca$^+$ can be calculated as

$$\Delta\nu_{Quad} = \frac{eA}{h} \langle 3d| r^2 |3d\rangle \left(\frac{1}{4} - \frac{3}{35} m^2 \right) [(3\cos^2\beta - 1) - \epsilon\sin^2\beta(\cos^2\alpha - \sin^2\alpha)], \quad (2.75)$$

where the orientation of the quantization axis and the electric field gradient has been parameterized by a set of Euler angles $\{\alpha, \beta, \gamma\}$.

Theoretical calculations for the $3d\,^2D_{5/2}$ levels in ^{40}Ca$^+$ predicted a quadrupole moment of $1.89\,ea_0^2$ and $1.92(1)\,ea_0^2$ [24, 102, 103], recent calculations with $1.85(2)\,ea_0^2$ [104] and

$1.82\,ea_0^2$ [105] lie closer to the experimentally obtained result described in Chp. 7. For typical field gradients in our linear Paul trap of $25\,\mathrm{V/mm^2}$ at a tip voltage of $1000\,\mathrm{V}$ and assuming that the gradient direction is along the trap axis, but at an angle of $30°$ with respect to the quantization axis, the expected shifts are on the order of $\Delta\nu_{Quad}{=}10\,\mathrm{Hz}$. Taking the sum over the factor $\left(\frac{1}{4} - \frac{3}{35}m^2\right)$ for all possible values of m, the shift adds to zero. This means, that for an absolute frequency measurement of the $4s\ ^2S_{1/2} - 3d\ ^2D_{5/2}$ transition, averaging of transitions involving all sublevels of the $3d\ ^2D_{5/2}$ state completely cancels the quadrupole shift [23]. The same can be achieved by averaging over three mutually orthogonal directions of the quantization axis which was proposed in [91].

Chapter 3

Experimental setup

In this chapter a description of the experimental setup is given. After a complete overview a part is dedicated to the ion trap setup followed by a brief review of the laser systems used for cooling and repumping which have recently been remodeled. The setup for the laser at 729 nm and the fiber noise cancellation are explained in more detail. And finally, the detection of optical beat notes for the analysis of the laser's spectral properties is presented.

3.1   Overview

For most of the measurements in this thesis except for the optical frequency comparisons and measurement of the $4s\ ^2S_{1/2} - 3d\ ^2D_{5/2}$ transition in $^{43}\text{Ca}^+$, the linear ion trap dedicated to quantum information processing at the labs of the University of Innsbruck was used. The mentioned frequency comparison and the measurement with $^{43}\text{Ca}^+$ was done with the help of an additional ion trap experiment located at the Institut für Quantenoptik und Quanteninformation (IQOQI). An aerial image of the campus with the location of the labs and the optical fiber link can be seen in Fig. 1. In Fig. 3.1 a sketch of the experimental setup with focus on the measurement of the optical frequency of the two spectroscopy lasers at 729 nm is shown. The setup at the University consisted of five major building blocks: the ion trap, a frequency comb with the transportable Cs atomic fountain clock from LNE-SYTRTE in Paris (Fig. 3.2), the laser systems, and the computer controls (not shown). The lasers were set up on two optical tables, one carrying two solid-state laser pumped[1] Titanium:sapphire lasers[2] and a frequency doubler[3] (SHG) to generate light at 397 nm for cooling and at 729 nm for spectroscopy, the other one carrying the lasers for repumping at 854 and 866 nm as well as the reference cavities for the Pound-Drever-Hall stabilization of the cooling and the repumping lasers. The spectroscopy laser was locked to an ultra-stable, high finesse cavity mounted on a vibration isolation platform[4]

---

[1]Coherent 10 W Verdi lasers
[2]Coherent 899 Ti:sa ring lasers
[3]LAS Wavetrain
[4]Minus-K BM-4
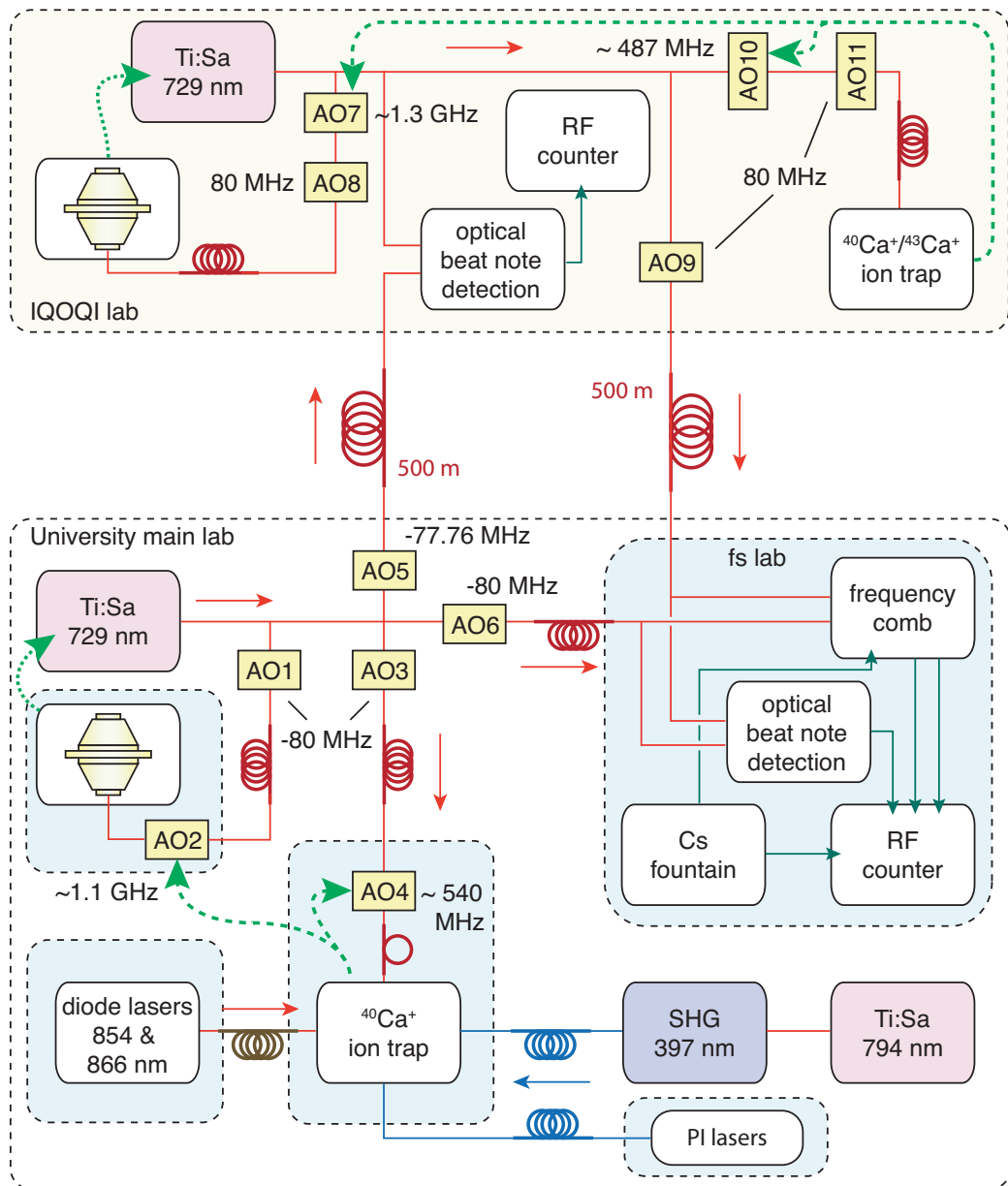
Figure 3.1: Overview of the frequency measurement setup: Two similar ion experiments can be compared via 500 m long polarization maintaining fibers. A single experiment setup consists of a linear Ca$^+$ ion trap and Ti:Sa lasers stabilized to an ultrastable high finesse cavity. The numbers show the AOM (yellow blocks) frequencies in MHz.
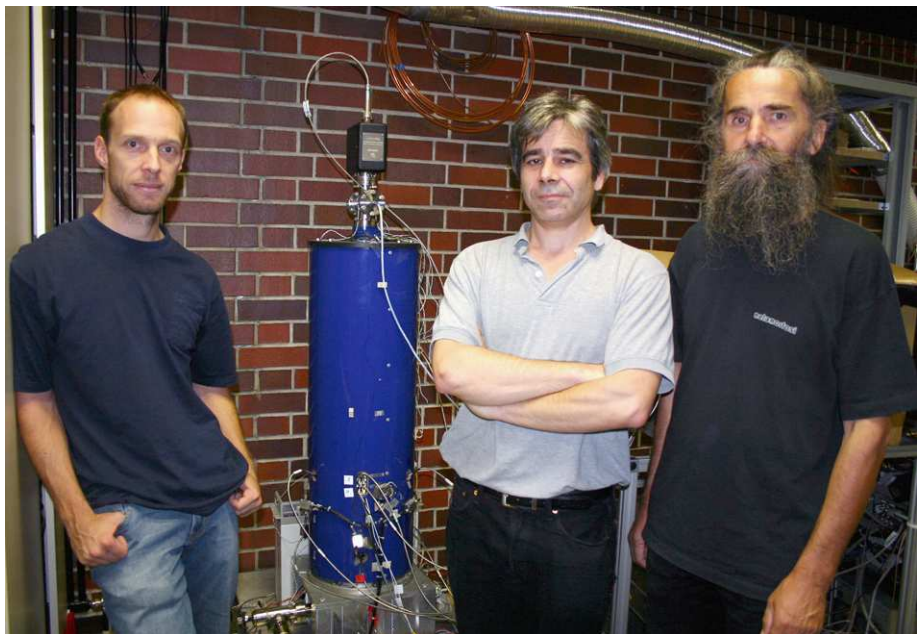
Figure 3.2: The transportable Cs atomic fountain clock (FOM) of LNE-SYRTE in the lab at Innsbruck in 2007. Photo: IQOQI.

by the Pound-Drever-Hall method. The lasers needed for photo-ionization (PI lasers) were located on a small breadboard next to the optical table with the ion trap system and the ion detection was composed of a photo multiplier tube (PMT) and a sensitive CCD camera[5]. All laser beams are transported via polarization maintaining fibers except for the photo ionization light which only requires a single mode fiber. The fibers for transportation of 729 nm light are stabilized to compensate for optical path length changes due to stress induced by acoustic vibrations or temperature changes. One of these fibers leads into a different room (fs lab) where a frequency comb is residing and also the transportable Cs atomic fountain clock that was used to reference the frequency comb and all RF sources to the SI standard of the second. An additional ion trap located at IQOQI served as a reference system for frequency comparisons of Ca^+ ions as well as for an absolute frequency measurement of $^{43}Ca^+$. A detailed description of that experiment can be found in Jan Benhelm's PhD thesis [81]. The two buildings are connected through two 500 m long, length stabilized polarization maintaining fibers for 729 nm light and optical beat notes can be detected independently at each site. Both lasers can be referenced to calcium ions at their experiment by feeding back onto the frequency of acousto-optic modulators (AOM) for cancellation of slow drifts of the reference cavities (AO2 and AO7) and to compensate for changes of the magnetic field and addressing of individual Zeeman transitions (AO4 and AO10).

---

[5]Andor iXon DU860AC-BV

3.2 Linear ion trap

The linear ion trap at the University lab consists of four blade-shaped electrodes for radial and two endcaps for axial confinement. A picture and a sketch with the exact dimensions are given in Fig. 3.3. This trap has been designed by Stephan Gulde and a more thorough description can be found in his PhD thesis [79]. The details about the ion trap at IQOQI are discussed in [81]. For typical operation conditions of the University trap, a radio frequency $\Omega_{Trap}/2\pi$ =23.5 MHz from a (up to) 50 W power amplifier is coupled into a helical resonator with a quality factor $Q = 250$ to boost the voltage $V=V_0\cos(\Omega_{Trap}t)$ at one of the blade pairs to $V_0 \sim 1$ kV while the other pair is connected to ground. The static potential applied to the end caps is provided by a stable high voltage supply[6] with 10^{-6} stability. For a radio frequency power of 9 W and a tip voltage of 1000 V we typically get

(a) Picture of the trap. (b) Dimensions of the trap.
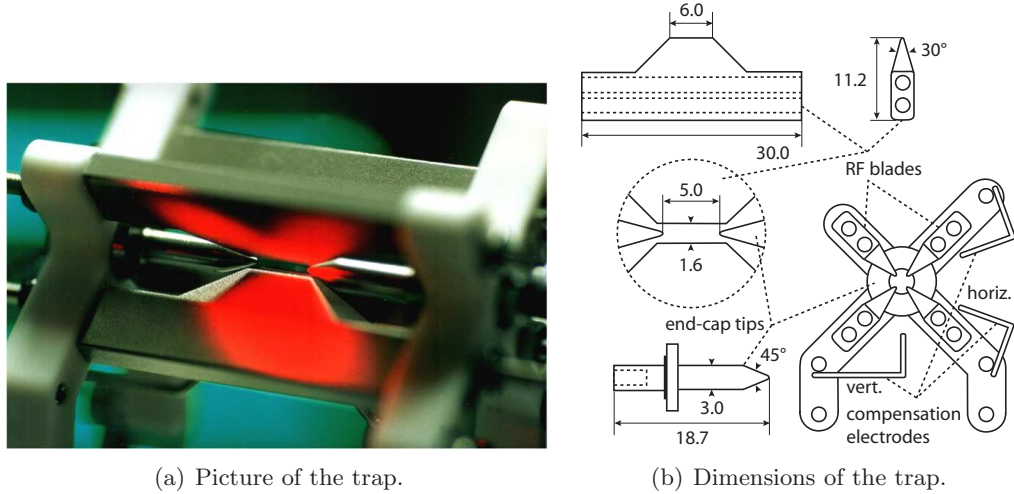
Figure 3.3: The ion trap of the University of Innsbruck. The dimensions are given in mm.

secular trap frequencies of $\omega_a/2\pi = 1.2$ MHz in the axial and $\omega_a/2\pi = 3.4$ MHz in the radial directions.

3.2.1 Vacuum vessel and optical access

The ion trap is mounted in a vacuum vessel shown in Fig. 3.4. The trap axis is tilted with an angle of β_0=28° with respect to the magnetic field defining the quantization axis produced by the main coil pair $C\sigma$. The tilt of the field is necessary since the optical access along the trap axis is blocked by the end-cap tips. This is also the direction of a beam of σ-polarized light at 397 nm for optical pumping into the desired $|S, m_s\rangle$ state. To control the field in horizontal direction there is another pair of coils CD along the direction of the Doppler cooling beam which also contains the repumping lasers at 854 and 866 nm. The magnetic field gradient can be changed by a single coil at the viewport

---

[6]ISEG EHQ F020p

(a) Top view.　　　　　　　　　(b) Side view.
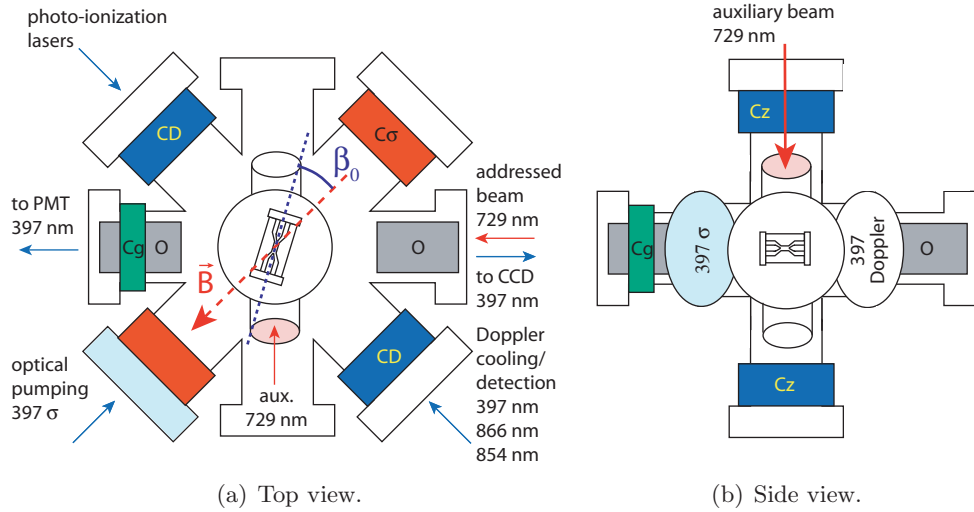
Figure 3.4: The optical access and magnetic field coils. The dashed lines indicate the quantization magnetic field and the trap axis.

between the Doppler and σ ports. Also shown are the two objectives (O) for imaging of the ion's fluorescence at 397 nm onto a photo-multiplier (PMT) or onto the CCD camera. The latter objective's main purpose though is to focus the 729 nm spectroscopy light tightly onto the ions with a spot-size of less than $3\,\mu$m [80]. The beam can be steered along the ion string for individual addressing with the help of an electro-optic deflector. Along the vertical direction the magnetic field can be controlled by a third pair of coils Cz. Additionally, there is an auxiliary port for light at 729 nm at an angle of 45° to the vertical axis and the horizontal plane. It is used for micromotion compensation and simultaneous coherent operations on all ions of the ion string. The whole apparatus is covered by a μ-metal box for shielding of surrounding magnetic stray fields, for example produced in the lab by power supplies or a BEC experiment next door. The damping factor at the line frequency of 50 Hz which is the dominant contribution to the magnetic field noise is ~ 200. A magnetic field sensor sensitive in all three spatial directions placed inside this shielding box shows an RMS magnetic field of $37\,\mu$G. An estimation using Eq. (2.58) and the obtained Ramsey contrasts in Sec. 6.1 confirms a residual magnetic field amplitude at the position of the ion of $25\,\mu$G.

3.2.2 Measurement of the trap temperature

For the error budget of the $4s\ ^2S_{1/2} - 3d\ ^2D_{5/2}$ transition frequency measurement it is necessary to measure the trap temperature because of the AC Stark shift induced by black body radiation. Unfortunately, with the current setup it is not possible to have direct access to the temperature since there are no sensors built in and the viewports are opaque for light with a wavelength larger than $2\,\mu$m so a thermal camera could not be used. Therefore, a test trap with unused leftover-parts had to be built including two PT100
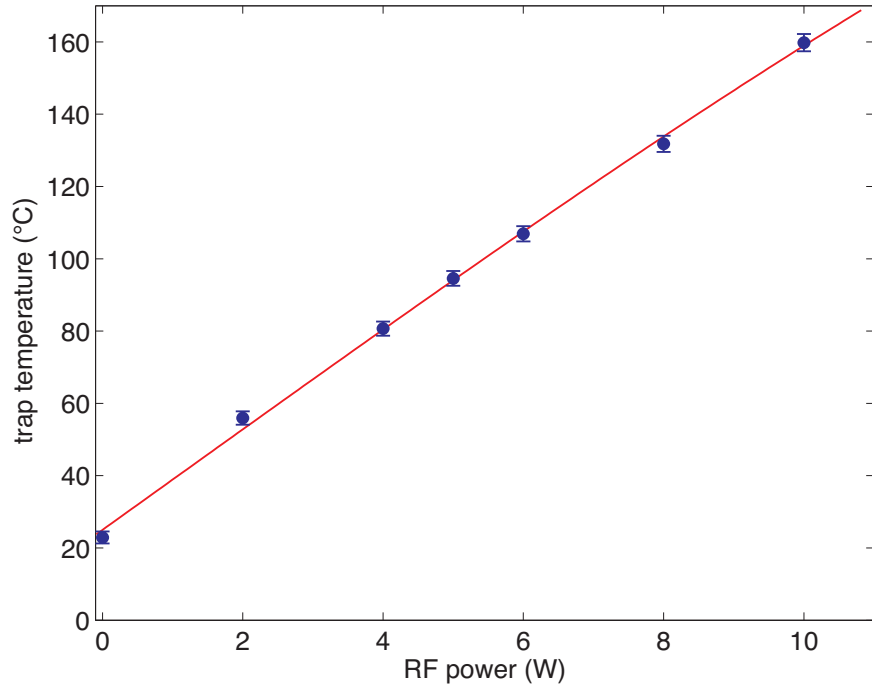
Figure 3.5: The temperature of a test trap vs. the radio frequency drive power.

temperature sensors glued directly onto one of the RF blades and to the Macor® holder next to one of the ground blades. The trap was mounted with similar thermal conductivity as the real experiment trap and connected to a helical resonator with $Q = 280$. The setup was driven by an RF synthesizer[7] and a power amplifier[8]. The frequency was adjusted by minimizing the reflection with a standing wave ratio meter[9] which was also used to measure the power in forward direction. The resistance of the PT100 temperature sensors was measured with a precision multimeter[10] and the temperature could be calculated by using standard parameters for PT100. Fig. 3.5 shows the trap temperature as a function of trap power. The fitted line is a simple model combining heat conduction through the feed-throughs and thermal radiation. The temperature T as a function of RF power P can be approximated by $T(P) = 25 + 14\,P - 0.003\,P^2 - 0.002\,P^3 - 0.0004\,P^4$. At the typical operating power of $9\,\mathrm{W}$ a trap temperature of $150\,^\circ\mathrm{C}$ can be inferred according to this model. The uncertainty of the measurement on the test trap is a few $^\circ$C but for the real experiment trap an error of 50°C is assumed for the following reasons: The resistance measurement could only be performed with the RF switched off. The time delay

---

[7]HP Network Analyser 3577B
[8]Minicircuits ZHL-10W
[9]Daiwa CN-801HP
[10]Keithley DMM 2000

between the switch off and the measurement is responsible for a few °C lower temperature. Furthermore, the cable diameters and materials necessary for the estimation of the heat conductivity for the real trap could only be guessed from pictures since this information has not been documented. This is one of the reasons why the comparison of the two traps and the temperature at the real trap is somewhat difficult. Another reason is that the helical resonator for the test trap had a quality factor of 280 instead of 250 as for the experiment trap. This might lead to slightly different trap temperatures due to a different amount of resistive heating.

Overall, it is quite safe to assume such a large error because there is already a hint for the real temperature of the trap. When the trap power is changed from $<2\,\mathrm{W}$ to $15\,\mathrm{W}$ a displacement of the ions in vertical direction on a CCD camera of $\Delta l = 80\,\mu\mathrm{m}$ can be observed [79]. Together with the thermal expansion coefficient of $16\times10^{-6}\,\mathrm{K}^{-1}$ for the $10\,\mathrm{cm}$ long stainless steel rods suspending the trap the change of the mean temperature is $\Delta T{=}50°\mathrm{C}$. The end of the rods is assumed to heat up to about $100°\mathrm{C}$ assuming that the trap setup at $2\,\mathrm{W}$ power is already $50°\mathrm{C}$. This is reasonably close to the temperature obtained with the test trap given the fact that the exact dimensions and materials of the mounting structure are not well known and that there might be a temperature difference between the Macor® holder and the trap itself due to the different thermal conductivity.

3.3   Laser sources for the dipole transitions

Ion trap experiments with Ca^+ ions have a great technological advantage. All the laser sources needed for photo-ionization, laser cooling, optical pumping, and detection, re-pumping of the D-levels and spectroscopy are nowadays commercially available as diode lasers. At the time when the experiment at University was built, this was not the case yet, so the lasers for cooling/detection at $397\,\mathrm{nm}$ and for spectroscopy of the $4s\,^2S_{1/2}{-}3d\,^2D_{5/2}$ transition at $729\,\mathrm{nm}$ are still generated from Titanium:Sapphire lasers (Ti:Sa) pumped by diode pumped solid-state laser systems (DPSS). For laser cooling, the output of the second Ti:Sa at $794\,\mathrm{nm}$ is frequency doubled. The wavelengths of the laser systems can be measured by a commercial wavemeter[11] with $60\,\mathrm{MHz}$ accuracy. Also, the optics like lenses, mirrors, polarizers, optical fibers, etc. are mostly standard, off-the-shelf components.

3.3.1   Laser system at 397 nm

The Ti:Sa at $794\,\mathrm{nm}$ is locked to a reference cavity by the Pound-Drever-Hall method and can be adjusted in frequency by changing the voltage of piezoelectric transducers (PZT) holding one of the mirrors of the cavity. The mirror is mounted on two PZT rings similar to the method described in [81]. This way, thermal drifts caused by the thermal expansion of the piezo material, which is two orders of magnitude higher than for the Zerodur® spacer, are highly suppressed.

The light is frequency doubled by a Lithium triborate crystal (LBO) in a resonator stabilized by the Hänsch-Couillaud method. It generates about $100\,\mathrm{mW}$ of light at $397\,\mathrm{nm}$ which

---

[11]HighFinesse WS-7

is distributed to three independent $^{40}\mathrm{Ca}^+$ experiments by polarizing beam splitters (PBS) and half-waveplates. Each experiment has its own AOM[12] in double pass configuration with separate amplitude and frequency control (center frequency 80 MHz). In front of the cat's eye prism for retro-reflection of the beam a mechanical shutter is placed to block the zeroth order from the AOM. If needed like in the event the ion crystal has melted or for easier loading of the trap, the far red-detuned (160 MHz) light from the zeroth order helps in (re-)crystallizing. The light is then focused into a polarization maintaining optical fiber[13] and transported to the vacuum vessel housing with the ion trap. The light can be switched off by a factor of $<10^{-5}$ with two RF switches[14] and a mechanical shutter for the zeroth order.

At the experiment table the light gets split into two parts: one part for optical pumping and one for cooling and detection of the ion. Each branch includes an AOM in single pass configuration (center frequency 80 MHz) for individual amplitude and frequency control. The light can be switched off with more than 60 dB in each branch. The light is finally made overlapping with the repumping light at 854 and 866 nm and transmitted to the viewports via photonic crystal fibers[15] and focused onto the ion string.

3.3.2 Laser systems at 854 and 866 nm

The light at 854 nm for resetting the $\mathrm{D}_{5/2}$ level and 866 nm for repumping the $\mathrm{D}_{3/2}$ level is generated by two commercially available, grating stabilized diode lasers[16]. Both lasers are stabilized to separate reference cavities by the Pound-Drever-Hall method. The resonators share the same Zerodur$^{\textregistered}$ spacer together with the cavity for the stabilization of the 794 nm laser and the same temperature stabilized vacuum vessel. The frequency of the lasers can be tuned by changing the cavity length with mirrors mounted on PZTs the same way as mentioned above. Again, these laser sources are shared by all $^{40}\mathrm{Ca}^+$ experiments at the University and each beam line has it's own double-pass AOM[17] for individual amplitude and frequency control. When the lasers are switched off, the light levels of both lasers after the polarization maintaining fibers[18] on the experiment table are less than 0.1 nW each.

3.3.3 Lasers for photo-ionization

In order to load ions into our trap a beam of neutral calcium atoms is ionized near the trap center. In the past, this was achieved by electron bombardment causing a bunch of problems like creating stray charges on the trap electrodes and the supporting structure, the necessity of a high calcium flux, or the ionization of impurities like background atoms. This can be avoided by photo-ionizing the calcium atoms using two laser sources at 423 nm

---

[12]Brimrose QZF80-20-397

[13]Schäfter & Kirchhoff OXF-SM-400-125-P

[14]Minicircuits ZYSW-2-50DR

[15]Crystal Fibre PM-9

[16]Toptica DL-100

[17]Crystal Technologies 3200-121

[18]Schäfter & Kirchhoff PMC-850-5,5-NA011-3-APC

for driving the $4s\ {}^1\mathrm{S}^1 - 4p\ {}^1\mathrm{P}^1-$ transition and 390 nm for transferring the electron into the continuum as described in [106]. Both are grating stabilized diode lasers[19] without any further stabilization. The frequency of the 423 nm laser can be tuned by a PZT changing the grating position or the diode temperature.

3.4 The spectroscopy laser at 729 nm

At the heart of the experiment is the ultra-stable laser at 729 nm used for spectroscopy of the $4s\ {}^2S_{1/2} - 3d\ {}^2D_{5/2}$ transition. In addition, the laser is used for:

- frequency resolved optical pumping,

- sideband cooling to the motional ground state,

- coherent manipulation of qubits for quantum information processing,

- precision spectroscopy on the $4s\ {}^2S_{1/2} - 3d\ {}^2D_{5/2}$ transition.

Since the natural linewidth of the transition is $\Delta\nu_0 =$ 140 mHz, it requires a narrow-band laser for optimal state manipulation. The laser system is based on a Ti:Sa ring laser pumped by a DPSS laser at 532 nm. The standard Coherent 899 ring laser provides high output power (600 mW at 7 W pump power) with a linewidth of roughly 500 kHz. In order to improve the performance the system had to be upgraded by an intra-cavity electro-optic modulator (EOM) [107] and stabilized to an external reference. More details about the stabilization of a Ti:Sa at 729 nm and the setup at IQOQI can be found in [108].

3.4.1 The Titanium:Sapphire ring laser

In the following, the system used for the absolute frequency measurement of the $4s\ {}^2S_{1/2} - 3d\ {}^2D_{5/2}$ transition is explained in more detail. Figure 3.6 shows a sketch of the Coherent 899 ring laser with the intra-cavity elements. The three elements used for the external frequency stabilization are highlighted with dashed circles. To increase the servo bandwidth an EOM[20] was inserted into the upper beam which led to a boost of the bandwidth from a few kHz to more than one MHz.

Though the Ti:Sa crystal has a very broad gain profile (650 to 1100 nm), the geometry of the laser cavity ensures single transverse mode operation. To ensure single-mode operation also in longitudinal direction and to provide for frequency tuning, several frequency-selective intra-cavity elements are required. The birefringent filter (BF) consists of three birefringent plates with a thickness ratio of 1:4:16. Only those modes survive for which the optical path length for the ordinary as well for the extraordinary direction match integer multiples of the wavelength. By tuning the angle of the BF this optical path length can be adjusted but the transmission peak is very broad and the resulting frequency selectivity is still insufficient. In order to fully achieve longitudinal single mode operation two prisms

---

[19]Toptica DL-100
[20]Linos PM25
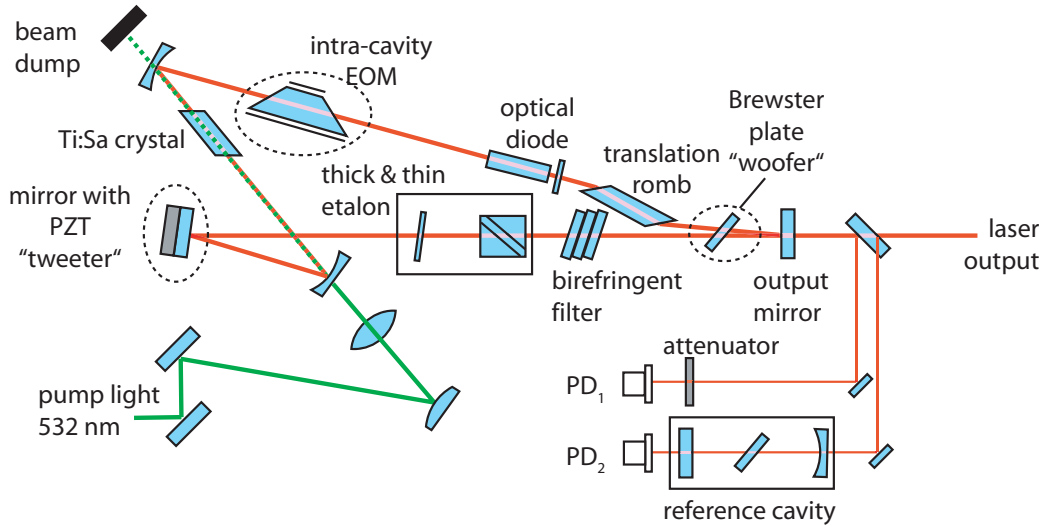
Figure 3.6: Optical setup of the Ti:Sa laser at 729 nm. Feedback can be applied to a mirror mounted on a piezo ("tweeter"), to an angle tunable glass plate around the Brewster angle ("woofer"), and an intra-cavity EOM for fast corrections.

and a glass plate called thick and thin etalon are used for further frequency selection. Depending on the optical path length l in these elements, only laser modes are transmitted with wavelengths $\lambda = N\,l$ which are integer multiples N of the optical path length. Single mode operation occurs when all transmission functions have overlapping maxima at one particular frequency. Therefore, the thick etalon is internally locked to a transmission maximum by lock-in detection of a 2 kHz signal to a piezo transducer to ensure long term stability. The angle of the thin etalon can be galvo-controlled manually for coarse tuning of the laser frequency (FSR~8 GHz). Since the Ti:Sa crystal can emit both in forward and backward direction an optical diode is inserted into the beam to select a particular direction and to ensure stable operation without mode-competion.

For fine tuning of the laser frequency with the Coherent electronic control box, the laser can be locked to the side of a fringe of a low finesse reference cavity using the difference of the signals from the photo detectors PD$_1$ and PD$_2$. The reference cavity can be scanned over 30 GHz by a galvo plate and the signal is fed forward to most of the other elements to maintain single mode operation. The feedback is applied to the piezo of one of the mirrors ("tweeter") and the Brewster plate ("woofer"). The "woofer" can be angle tuned with a frequency response of 400 Hz and a range of 15 GHz. The tuning range of the "tweeter" is 1 GHz with an eigenfrequency of 5 kHz. The effective bandwidth is increased to about 18 kHz by a passive two-fold notch filter ("tweeter trap") that suppresses the two largest mechanical resonances. The laser as delivered from the manufacturer has a linewidth on the order of 500 kHz.
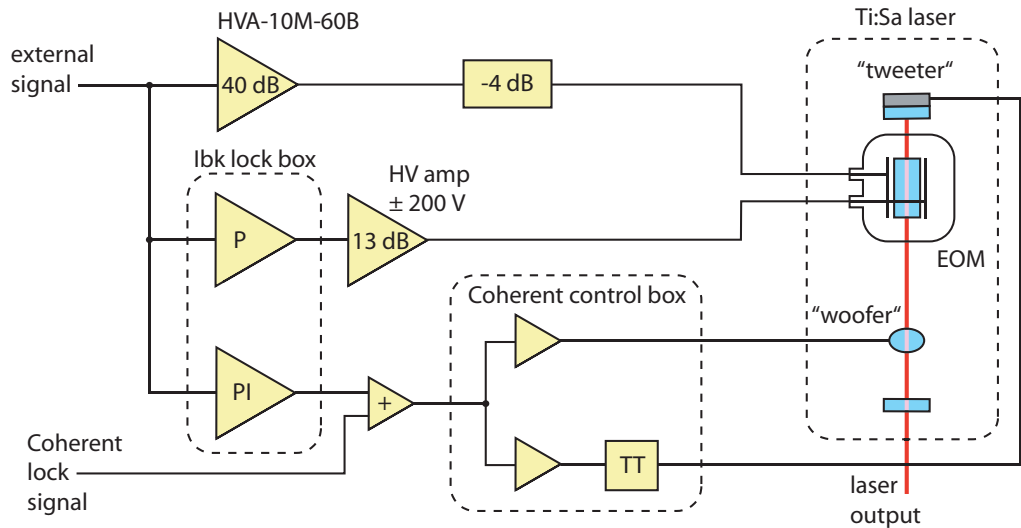
Figure 3.7: Schematic of the laser lock. The external error signal is split into three parts: a slow part with an integrating amplifier for frequencies lower than 20 kHz, a mid-frequency part with a high voltage amplifier for frequencies up to 150 kHz and a fast part for larger frequencies (>150 kHz). The latter two branches feed back onto the two electrodes of the intra-cavity EOM, the integrating part is combined with the internal error signal of the Coherent lock and fed to the "woofer" and "tweeter". The circuit marked "TT" is the "tweeter trap", a two-fold notch filter to suppress the largest mechanical resonances of the "tweeter".

3.4.2 Locking of the spectroscopy laser to an external reference

For applications requiring a linewidth of less than 500 kHz, the laser has to be locked to an external reference with higher stability. A diagram showing a simplified sketch of the electronic feedback signals is given in Fig. 3.7. The external error signal can be added to the internal feedback loop by a modification of the original electronic circuit which incorporates a single extra operational amplifier adding the two signals. Furthermore, the loop bandwidth has to be increased by the insertion of the intra-cavity EOM as mentioned above (see Fig. 3.6). It can provide an extra frequency tuning range of 200 kHz/V with a 3 dB bandwidth of 100 MHz. Since it is difficult to build fast high voltage amplifiers with a bandwidth exceeding a few 100 kHz the signal is split into two parts: a high voltage branch[21] (± 200 V max., bandwidth 300 kHz) and a low voltage fast branch (± 15 V max.) with a commercial amplifier[22] having a nominal bandwidth of 10 MHz. The signals are separately fed onto an electrode of the EOM each sharing a common ground. The overall loop bandwidth of the fast branch is 1.2 MHz because the signal has to travel back and forth to the external reference cavity which is set up at a quiet corner of the lab and connected through a 15 m long optical fiber and a BNC cable. Therefore, the phase change

---

[21]The circuit design is described in [107].
[22]Femto HVA-10M-60-B

due to the time delay reaches π already for a frequency of 3.3 MHz. The high voltage part has a loop bandwidth of 140 kHz. With this setup it is possible to substantially narrow the linewidth of the laser to much less than 100 Hz. The necessary parts to achieve this goal are explained in the following.

3.4.3 The external high finesse resonator

The construction of an ultra-stable laser necessitates an ultra-stable frequency reference. For laser stabilization an optical reference cavity formed by two mirrors attached to a rigid spacer is a good choice because of the exceptionally good short term stability that is on the order of 10^{-15} and even better over time intervals ranging from 1 to 100 s for some of these systems. The most stable lasers have been achieved with stabilization schemes to high finesse cavities [109–114].

The vertical cavity design and setup

The crucial point for a stable reference is its sensitivity to external perturbations. For an optical cavity the frequency stability is determined by the stability of the mirror distance. Vibrations caused by acoustics in the vicinity of the cavity or seismic vibrations caused by a shaking building can change the mirror distance. The goal therefore is to build a reference cavity with low sensitivity to external accelerations and to shield the system as much as possible from the environment. The cavity design developed by Notcutt et al. [110] at JILA realizes this principle by mounting the cavity vertically exactly at the mid plane between the mirrors. This way, length changes due to vertical acceleration which are most likely in a typical lab environment cancel to first order. Fig. 3.8 shows a picture of the cavity used for the laser stabilization of the laser at the University incorporating this design. If the cavity is accelerated upwards the upper part gets compressed and the lower part sags so that the net length change is zero and vice versa. The cavity spacer as well as the mirror substrates are made out of ultra-low expansion glass (ULE®) with a thermal expansion coefficient of below $10^{-8} \, \mathrm{K}^{-1}$. The mirrors are optically contacted to the spacer of 7.75 cm length. The upper mirror has a curvature of $r = 50$ cm while the lower is planar. To avoid standing waves within the mirror substrates or etalon effects with any parallel optical surface, the back sides of the mirrors were antireflection coated to less than 0.1%. The cavity is mounted at the mid-plane by three PTFE rods which are themselves resting in a Zerodur® base plate. Since the cavity stability is determined by the mirror distance, also length changes due to thermal fluctuations or changes of the index of refraction have to be avoided. The cavity needs to be placed into a temperature-stabilized vacuum system as sketched in Fig. 3.9. The vacuum vessel is mounted in a box of 5 mm thick aluminum which is covered by heating mats[23] and thermal insulation material. Six temperature sensors are placed at each side of the box and the temperature can be stabilized at temperatures between 25°C to 30°C where the ULE® was specified to have a minimum of the thermal expansion coefficient. Unfortunately, some part of the ion

---

[23]available at RS components
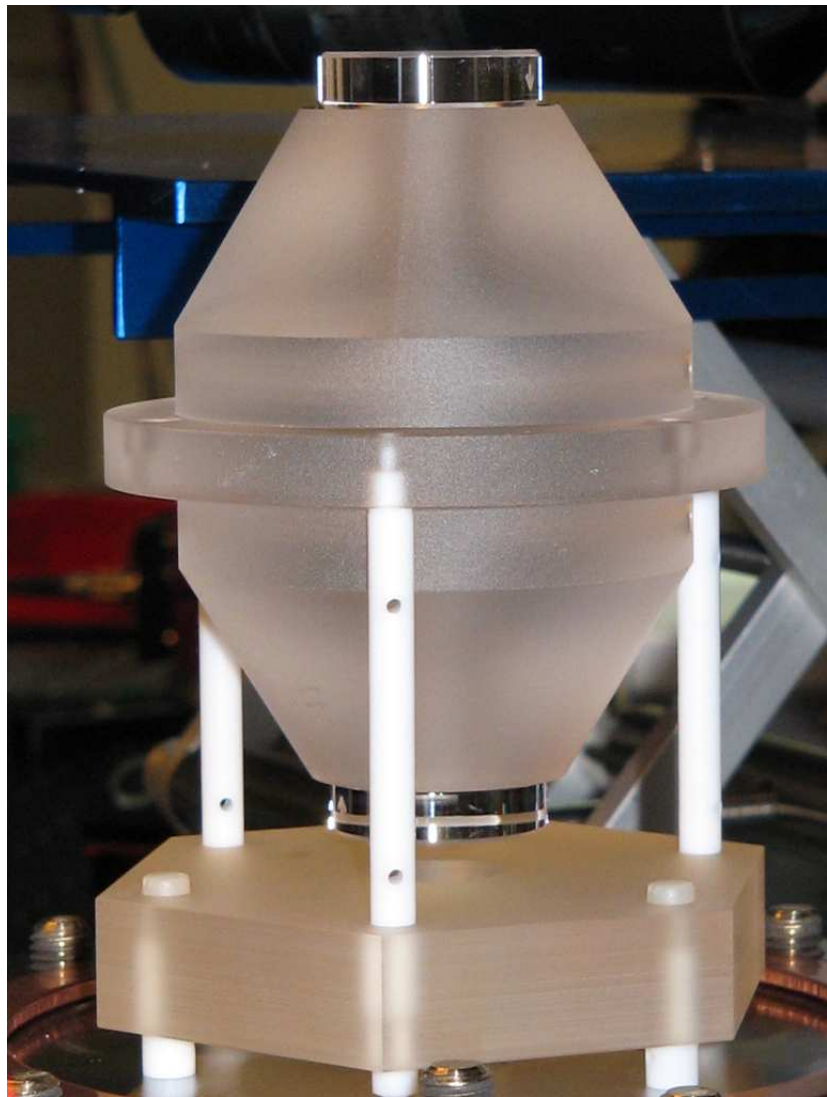
Figure 3.8: Picture of the external reference cavity. The cavity is mounted at the symmetry plane between the two mirrors to compensate for length changes due to vertical acceleration.
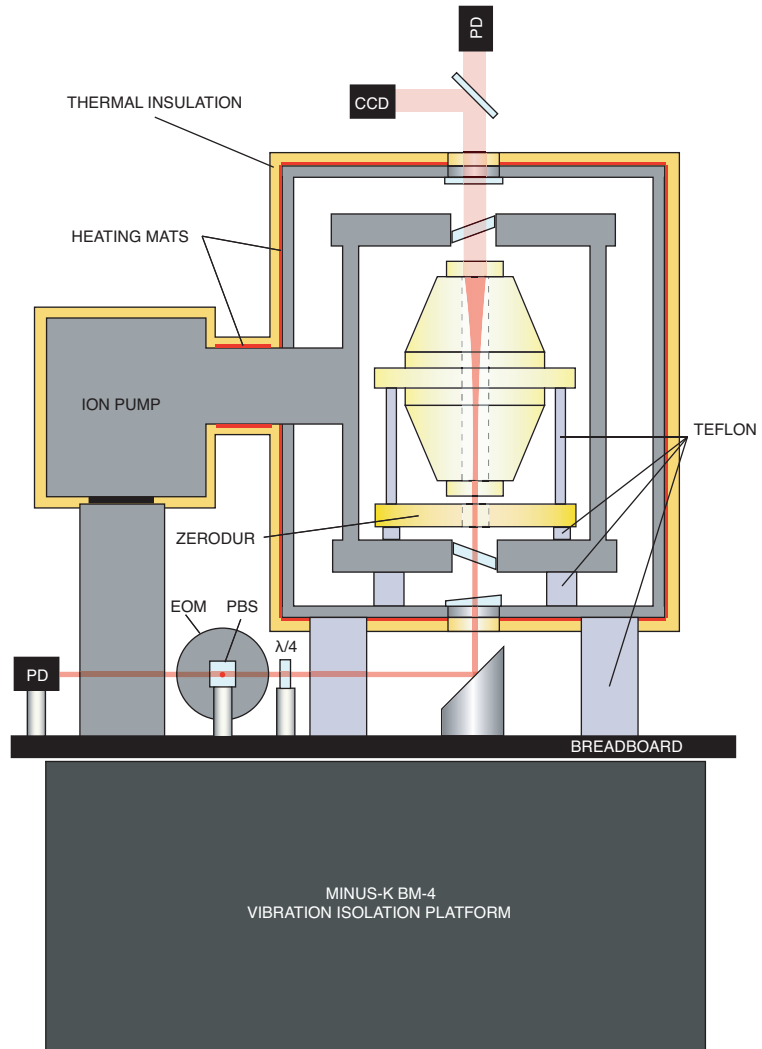
Figure 3.9: Details of the cavity setup

pump is not covered by the aluminum box and an extra temperature stabilization of the flange is necessary. In fact it turns out, that this is the limiting factor of the temperature stability which is about 1 mK or less per hour measured at the vacuum vessel. Glass plates glued to the openings of the outer box prevent air convection caused by the temperature difference to the outside. These plates have wedges and are mounted at various angles including the vacuum windows such that no unwanted etalons can be formed by parallel optical surfaces. On top of the setup, a CCD camera and a photo diode are placed to monitor the cavity transmission. The cavity and the necessary optics are mounted on a breadboard which is screwed onto the top of a vibration isolation platform[24]. It has a very low natural frequency of 600 mHz. The platform is resting on a 250 kg block of granite with 16 semi-spheres of Sorbothane® for vibration isolation. The whole setup is covered by a wooden box with the walls enhanced by lead mats and acoustic foam. Additionally, the box is temperature stabilized by cooling water.
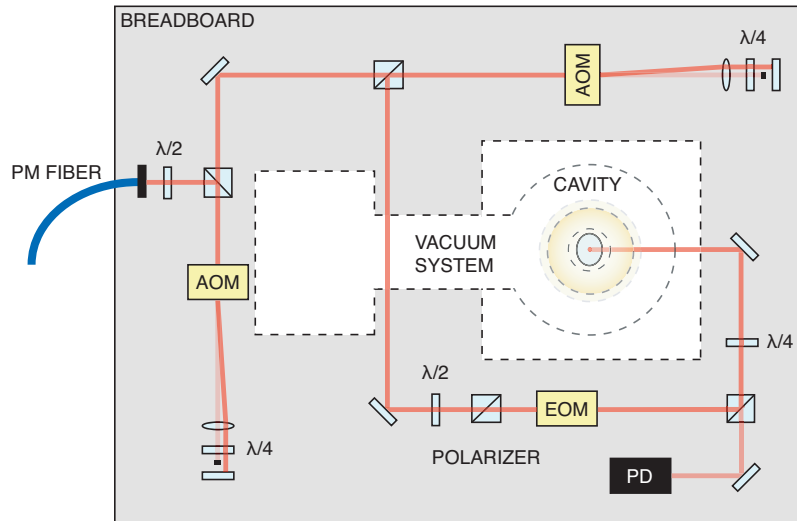

Figure 3.10: The breadboard with the cavity setup and the optics for locking and frequency tuning of the laser.

The optical setup is shown in Fig. 3.10. The light is transported via a polarization maintaining fiber and fed through two consecutive AOMs[25] in double pass configuration for frequency tuning before it is sent to an EOM[26] for the modulation of sidebands at 11.5 MHz. The light polarization is filtered beforehand at a Glan-Thompson polarizer[27] and is aligned with the principal axis of the EOM. If the polarization of the light does not match the axis of the EOM the light becomes polarization modulated at the modulation frequency Ω. This polarization modulation is converted to an unwanted amplitude modulation at the subsequent polarizing beamsplitter and has to be avoided. The particular

---

[24]Minus-K BM-4
[25]Brimrose TEF-270-100-800
[26]Linos PM 25
[27]manufactured by B. Halle Nachfl. GmbH, exctinction ratio 10^{-8}

EOM used has the advantage that it consists of two matched crystals which compensate for a modulation of the beam pointing caused by the electro-optic properties of the crystal material which would also lead to amplitude modulation by a change in coupling efficiency. The only disadvantage of the model is that it requires a rather large voltage of 1000 V for a phase change of $\lambda/2$. The modulation signal at a power of 7 dBm from a synthesizer[28] is therefore amplified by 29 dB with a power amplifier[29] and further amplified by a resonant, home-built LC circuit ($Q \sim 60$) to reach a modulation depth of a $\sim 20\%$. The light is then sent through a quarter waveplate and coupled to the cavity. We typically lock to a TEM$_{00}$ mode and all other modes are suppressed by more than 90%. The back-reflected light passes the waveplate again and is detected by a fast photodiode with a bandwidth of 125 MHz at the output of the polarizing beam splitter.

Cavity parameters

An optical cavity consisting of two highly reflecting mirrors at a distance L can be characterized by two parameters: the free spectral range FSR depending on the mirror distance and the finesse $\mathcal{F}$ depending on the reflectivity R, transmission T and the mirror losses A. A detailed theoretical description can be found in [115]. The most important parameters are shortly discussed in the following.

The FSR is the frequency distance of two neighboring longitudinal modes of the same kind. The FSR is given by the inverse of the roundtrip time

$$FSR = \frac{c}{2L}, \tag{3.1}$$

where c is the speed of light and L the resonator length. In the case of a 7.75 cm long cavity this corresponds to a $FSR = 1.934(2)$ GHz as was verified by [108] at IQOQI with an identical cavity. The linewidth of the cavity is related to the finesse $\mathcal{F}$

$$\mathcal{F} = \frac{\pi \tau c}{L} = \frac{FSR}{\Delta \nu} = \frac{\pi \sqrt{R}}{1 - R}, \tag{3.2}$$

which therefore is a measure for the photon storage time τ of the cavity. Equation (3.2) can be modified to include also losses A by the relation $R = 1 - A - T$

$$\mathcal{F} = \frac{\pi \sqrt{1 - A - T}}{A + T}. \tag{3.3}$$

The cavity linewidth is important for the slope of the error signal as will be shown later. It is difficult to be measured directly since this requires a laser with a bandwidth smaller than the cavity linewidth from the beginning. Instead, it is easier to measure the photon storage time by a ring-down measurement. Fig. 3.11 shows the result of such a measurement for the University cavity. The laser was locked to the old cavity setup [107] and tuned into resonance with the help of the two double-pass AOMs mentioned

---

[28]SRS DS345
[29]Minicircuits ZHL-1-2W
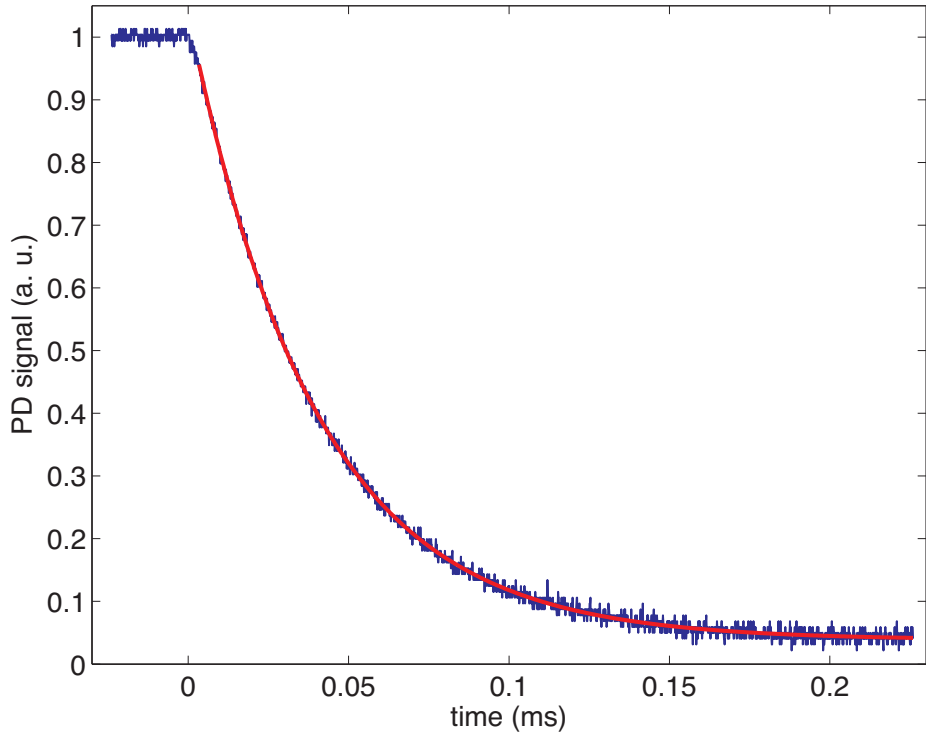
Figure 3.11: Measurement of the cavity ring-down with a fast photo diode (125 MHz). After the light has been switched off at $t = 0$, the decay time $\tau = 39.5(1)\,\mu$s is obtained by an exponential fit. The finesse therefore is 479500(1600).

above. At time $t = 0$ the driving RF was switched off and the transmission of the cavity measured with a fast photo diode (bandwidth 125 MHz). The experimental data is fitted by an exponential decay with a lifetime of $\tau = 39.5(1)\,\mu$s. This corresponds to a finesse $\mathcal{F} = 479500(1600)$ and a cavity linewidth of $\Delta\nu = 4034(19)$ Hz. The combined losses for the measured finesse are $6.55(3)\ 10^{-6}$ and the reflectivity of the cavity mirrors is $R = 0.999\ 993\ 45(3)$.

Temperature dependence of the TEM$_{00}$ mode frequency

The vertical cavity has a FSR of approximately 2 GHz meaning that the $4s\,^2S_{1/2} - 3d\,^2D_{5/2}$ transition could have a maximum offset from the nearest TEM$_{00}$ mode of 1 GHz. Since the thermal expansion coefficient is $10^{-8}\,\mathrm{K}^{-1}$ the frequency tuning by changing the temperature would have required an unrealistic temperature variation over 240°C. For this reason, the frequency of the laser can instead be tuned by two AOMs in double pass configuration centered at 270 MHz. With the AOM bandwidth of 100 MHz each one can cover almost the whole required frequency range of 1 GHz.
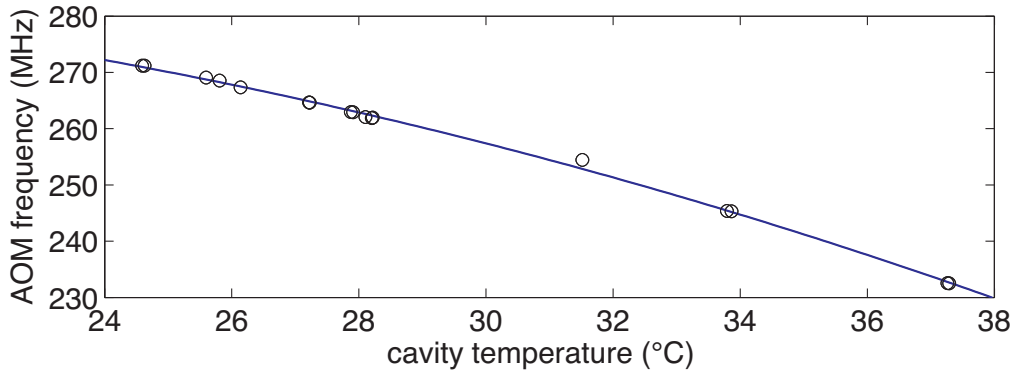
Figure 3.12: AOM frequency versus temperature of the vertical cavity.

Figure 3.12 shows the measurement of the AOM driving frequency versus temperature of the vertical cavity. The laser was locked to a horizontal high-finesse cavity which was previously used in the experiment [79]. The AOMs for the vertical cavity were driven by a frequency synthesizer[30] and adjusted that also this cavity was resonant with the laser. A quadratic fit represented by the line yields a minimum of the frequency change at a temperature of $T_0 = 9(12)°$C. Despite the large fitting error due to lack of data for temperatures lower than 24°C, this is within 4°C of the result later obtained with similar cavities [114]. They were produced from the same batch of material and both results for the minimum in the thermal expansion coefficient are contrary to what was specified by the manufacturer. To operate at the optimum temperature would require a complete redesign of the setup including thermo-electric cooling of the cavity. We decided that this was not necessary because the achieved temperature stability of better than 1 mK/h allowed for laser drift rates of less than 1 Hz/s which we regard as sufficient for our purpose. Additionally, the SML-01 frequency synthesizer can be phase-coherently switched with a minimum step size of 0.1 Hz. It is used to successfully compensate the cavity drift as will be explained later.

3.4.4 Pound-Drever-Hall stabilization method

The laser stabilization method developed by Hall et. al. is a simple, but efficient way to stabilize a laser to a Fabry-Perot type optical resonator. It combines the advantage of a large locking range with a very steep slope at the zero-crossing of the error signal as compared to other methods [116] and both parameters can be chosen independently. The error signal is generated by detection of a reflected signal of a phase-modulated laser beam as shown in Fig. 3.13. The laser beam is phase modulated at a frequency Ω with the help of an EOM and for a modulation index $m \ll 1$ the electric field of the light $E(t)$ becomes

$$E(t) = E_0 \ e^{i(\omega t + m \sin(\Omega t))} \approx E_0 \left(J_0(m) e^{i\omega t} + J_1(m) e^{i(\omega + \Omega)t} + J_{-1}(m) e^{i((\omega - \Omega))} \right) \quad (3.4)$$

---

[30]Rohde & Schwarz SML-01

46
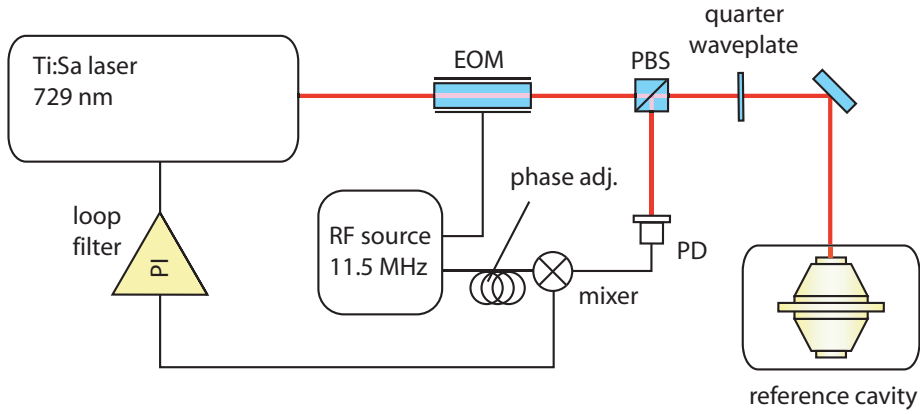
Figure 3.13: Pound-Drever-Hall locking scheme. The laser beam is phase-modulated by an EOM driven from a RF source at 11.5 MHz. The light reflected by the reference cavity passes the quarter wave plate twice and is therefore deflected by the PBS. The beat signal of the sidebands with the carrier is detected by a fast photodiode and mixed with the RF source to obtain a phase sensitive error signal which is subsequently processed by the loop filter and fed back to the laser.

with the Bessel functions of the first kind $J_i(m)$ and ω the carrier frequency. The carrier and the sidebands are reflected from the cavity depending on the relative frequency difference with respect to a particular longitudinal mode of the cavity. Their respective amplitudes and phases are given by

$$F(\omega) = r \frac{e^{i\frac{\omega}{FSR}} - 1}{1 - r^2 e^{i\frac{\omega}{FSR}}}, \tag{3.5}$$

where r is the amplitude reflection coefficient of the mirrors and FSR the cavity mode spacing in frequency. The quarter-wave plate acts as an effective half-wave plate on the way back and forth and the reflected light is deflected by a polarizing beam splitter (PBS) onto a fast photodiode where the sidebands and the carrier can interfere and produce an electronic signal proportional to the light intensity

$$I(t) \propto J_0(m)J_1(m) \left(\text{Re}\big\{ F(\omega)F^*(\omega+\Omega) - F^*(\omega)F(\omega-\Omega) \big\} \cos(\Omega t) \right.$$
$$\left. + \text{Im}\big\{ F(\omega)F^*(\omega+\Omega) - F^*(\omega)F(\omega-\Omega) \big\} \sin(\Omega t) \right). \tag{3.6}$$

The phase of the signal can be measured by mixing it with a local oscillator of frequency Ω and phase θ to produce the error signal $\epsilon(\Delta)$ which depends on the detuning from the cavity mode Δ and the cavity linewidth Γ:

$$\epsilon(\Delta) \propto \frac{\Delta\Omega\Gamma^2(\Gamma^2 + \Delta^2 + \Omega^2)}{(\Gamma^2 + \Delta^2)(\Gamma^2 + (\Delta+\Omega)^2)(\Gamma^2 + (\Delta-\Omega)^2)} \cos(\theta)$$
$$- \frac{\Delta\Omega\Gamma^2(\Gamma^2 - \Delta^2 + \Omega^2)}{(\Gamma^2 + \Delta^2)(\Gamma^2 + (\Delta+\Omega)^2)(\Gamma^2 + (\Delta-\Omega)^2)} \sin(\theta). \tag{3.7}$$
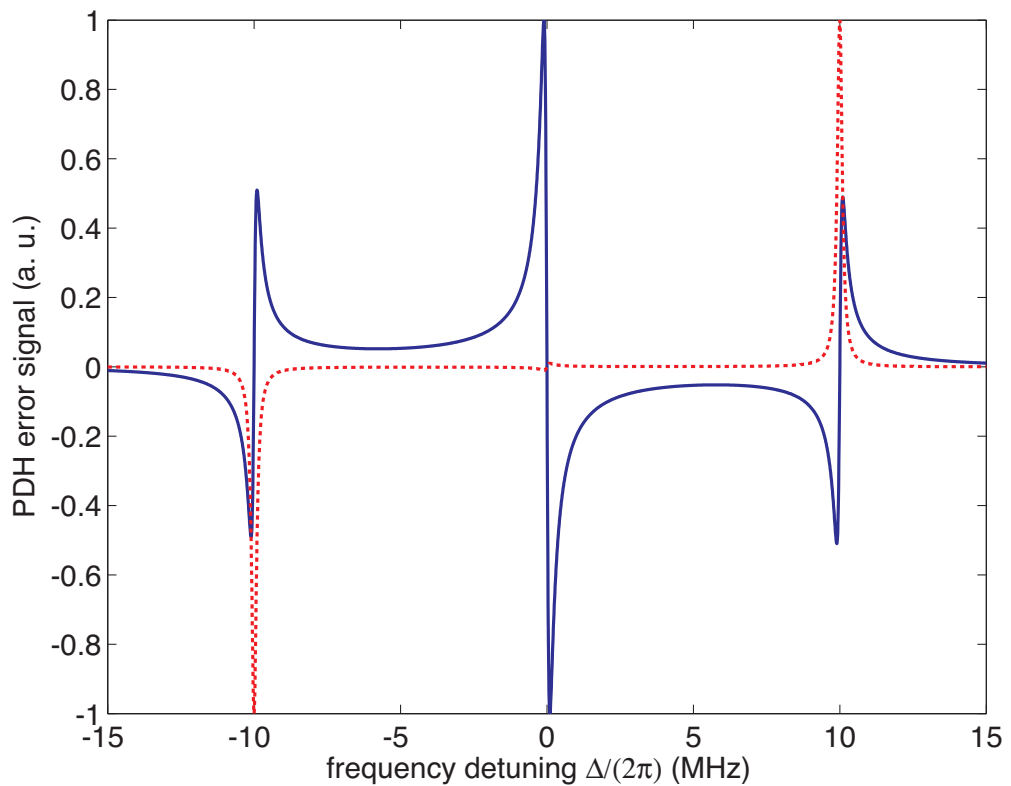
Figure 3.14: Pound-Drever-Hall error signal calculated for two different phases of the local oscillator with a cavity linewidth of $100\,\mathrm{kHz}$ and a modulation frequency of $10\,\mathrm{MHz}$. The solid line corresponds to a phase $\theta = 0°$, the dashed line to $\theta = 90°$.

The phase of the local oscillator can be adjusted by building an electronic phase shifter or simply by changing the cables to the right length and therefore the appropriate time delay. The resulting shape of the error signal is displayed in Fig. 3.14 for a cavity linewidth of $\Gamma/(2\pi) = 100\,\text{kHz}$ and a modulation frequency $\Omega/(2\pi) = 10\,\text{MHz}$ at a phase of $\theta = 0°$(solid line) and $\theta = 90°$ phase (dashed line). The interesting case for laser stabilization is $\theta = 0°$ where the slope of the error signal at the center is inversely proportional to the linewidth. Therefore, in order to increase the slope one has to decrease the cavity linewidth and the need for a high finesse cavity becomes apparent. Furthermore, the capture range of the signal, i. e. the range of frequency excursions that produce an error signal with correct sign only depends on the modulation frequency and can be chosen independently. Finally, the feedback loop is closed by passing the error signal through an appropriate loop filter with integrating characteristics (PI controller) to keep track of long term drifts. Thereby, feedback is provided onto the frequency sensitive elements described above.

3.4.5 Laser stabilization

In this section the stabilization of the spectroscopy laser to the high finesse cavity by the method of Pound-Drever-Hall (see Sec. 3.4.4) is discussed and the performance of the system is analyzed. Additionally, minor improvements concerning the laser lock are mentioned. Since a huge number of sidebands were created at multiples of the thick etalon modulation frequency in the Coherent setup, they had to be eliminated by building an external lock. Finally, fluctuations of the laser intensity were be reduced by intensity stabilization.

Frequency stabilization

The optical setup for the frequency stabilization has already been discussed in Sec. 3.4.3. The signal modulated at $\Omega/(2\pi) = 11.5\,\text{MHz}$ is detected by a fast photodiode, amplified with a gain of $20\,\text{dB}$[31] and mixed[32] with part of the radio frequency signal as mentioned above to generate the error signal. It is split up into three different branches as described in Sec. 3.4.2 with an individual loop filter each to increase the total servo bandwidth to about 1 MHz. The relative performance of the lock can be investigated by analyzing the residual error signal. Figure 3.15 shows a combination of spectrum analyzer traces of different span normalized by the square-root of the filter bandwidth so that they can be combined independent of the spectrum analyzer settings. It clearly shows that the noise between 200 Hz and 5 kHz is dominating the spectrum where the lock is not able to completely eliminate the perturbations.

The maximum peak to peak amplitude of the error signal is $490(10)\,\text{mV}$ when scanning over the resonance. Using the calibration of the Minicircuits ZAD-1 mixer in [108], this corresponds to a true amplitude of $1000(260)\,\text{mV}$ due to non-linearities of the mixer. The slope of the error signal at the line center therefore is $D = 2.0(5)\,\text{mV/Hz}$. The residual

---

[31]Minicircuits ZFL-1000LN
[32]Minicircuits ZAD-1
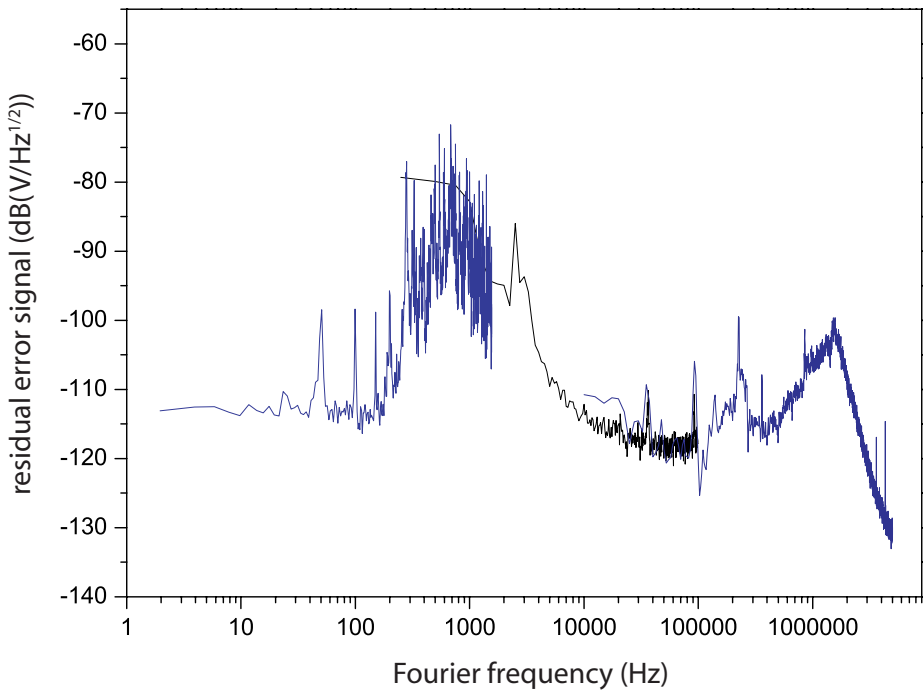
Figure 3.15: Fast Fourier transform of the residual in-loop error signal. Four different servo bumps can be identified: the "woofer" at 700-800 Hz, the "tweeter" at 3 kHz, the high voltage part of the EOM at 300 kHz, and the low voltage part of the EOM at 1.2 MHz.

error signal can be measured with an oscilloscope and is $U_{RMS} =9(1)$ mV indicating a relative linewidth of $\Delta\nu_{Laser} = \frac{\pi D^2 U_{RMS}^2}{B} =0.5(4)$ Hz.

New stabilization of the thick etalon

An analysis of the residual error signal revealed a series of distinct frequencies with a spacing of exactly the drive frequency of the thick etalon lock ranging from a few kHz to more than 200 kHz and amplitudes considerably larger than the background noise. This "frequency comb" is generated internally by the Coherent control electronics. It uses an amplifier driven into saturation in order to produce a rectangular signal for the internal lock-in detector starting from a sinusoidal signal. It is responsible for feeding back high harmonics of the modulation signal onto the supply voltage where it affects all other control electronics especially around resonances of the system. Fig. 3.16 shows a Fourier-transform of the error signal up to 100 kHz. The dashed line represents the error signal obtained with the internal (Coherent) lock, the solid line shows considerable improvement as a result of the external servo loop. Note that around 93 kHz the signal hits a resonance and exceeds neighboring peaks by orders of magnitude.

The thick etalon error signal is created by a lock-in detection of an amplitude-modulated intensity signal using the photodiodes of the Coherent reference cavity (see Fig. 3.6). As a
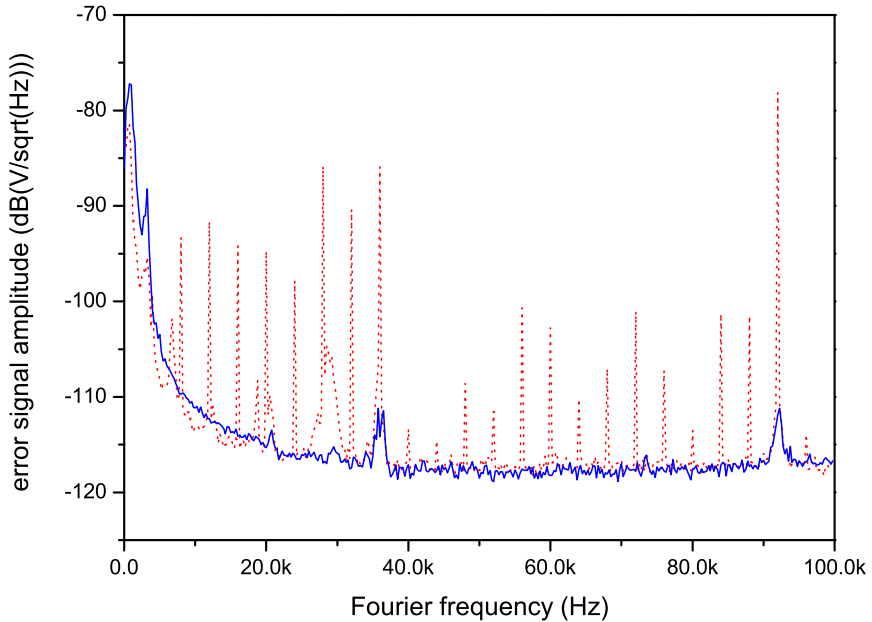
Figure 3.16: Spectral components of the error signal. The solid line is a Fourier transform of the signal when the thick etalon is stabilized with the external lock-in detector, the dashed line is the signal when locked to the Coherent internal circuitry. One can clearly see that the high harmonics of the drive frequency disappear for the external lock.

replacement we use an external photodiode[33] PD_1 as shown in Fig. 3.17 and a commercially available lock-in amplifier[34] for the generation of the error signal. As the loop filter we use a standard lock box built by our electronic workshop and set the integration constant to 3 ms. The final stage is a home-built HV amplifier similar to the one used for the PDH stabilization. The amplified signal was inserted into the circuit replacing resistor R85 of the Coherent electronic board 1-A1. By careful adjustment of the proportional gain we achieve a mode-hop free scanning range of the laser of more than 10 GHz which is more than enough for our purpose.

Intensity stabilization

The output power of the Ti:Sa laser exhibits power fluctuations of up to 10% on the time-scale of a few ms to seconds. Furthermore, even polarization maintaining fibers can have slow variations of the output polarization and thereby create additional amplitude

---

[33]Thorlabs DET110

[34]Femto LIA-MV-150

modulation when polarization sensitive optics is used. Amplitude modulation can cause two main problems: First, it causes a variation of the Rabi frequency at the position of the ion and second, amplitude noise is converted into frequency noise at the PDH stabilization by a fluctuating error signal amplitude.

The solution to this problem is rather simple. For the intensity and polarization stabilization of the fiber guiding light from the laser to the experiment table (see Fig. 3.1) we take a reflex of a wedge used for the fiber noise cancellation (see section below) placed after a polarizing beam splitter. The light intensity is monitored with a fast photodiode (bandwidth 120 MHz). The error signal is created by subtracting a constant offset voltage from the PD signal with a PID controller[35] and fed to a variable attenuator[36] controlling the radio frequency power of the fiber noise cancellation AOM. The attainable servo bandwidth is 92(1) kHz. The intensity stabilization for the reference cavity light is set up in a slightly different way. Here, the transmission of the cavity is used for stabilization with the same kind of equipment but the servo bandwidth is of course limited by the cavity bandwidth. Both systems are capable of reducing the amplitude noise to below 1%.

3.4.6 Fiber noise cancellation

The optical setup for the distribution of the 729 nm light is outlined in Fig. 3.17. The main part of the light (300 mW) is sent to the experiment table by a polarization maintaining fiber after passing a 2:1 telescope for adjusting the beam size to the fiber collimator[37] and AO1 for stabilizing the optical path length described below. A few mW are sent to the high finesse cavity and the frequency comb, the rest of the light is guided through the 500 m long fiber to IQOQI (see Fig. 1) for the beat note detection. All these beams pass AOMs and the -1st diffraction order is sent to the fiber couplers. The AOM frequencies are indicated in the figure by the numbers in MHz.

The light transported by optical fibers is affected by acoustic vibrations, thermally or air pressure induced stress. These effects cause changes in the index of refraction and therefore the optical path length. The resulting broadening of the laser spectrum can be quite severe and leads to an increased linewidth of about 1 kHz in case of the 500 m long polarization maintaining fibers. This is not tolerable for precision spectroscopy and especially bad if the light is sent to the stabilization cavity because the fiber-induced noise would be transferred onto the laser. It is therefore necessary to interferometrically stabilize the optical path length. We used the approach developed by Ma and coworkers [117].

The setup consists of a beamsplitter, an AOM and a fast photodiode (PD) as shown for each beam in Fig. 3.17. The (minus-)first diffraction order of the AOM is sent through the fiber and is affected by fiber noise. Part of the light (typical 4% glass reflection) is back-reflected at the 0° angle-polished fiber end and sent back through the fiber thereby picking up the noise twice. In case of the at both ends angle-polished fiber guiding light to the experiment, we use a glass wedge after a polarizing beam splitter to retro-reflect the light. The beamsplitter is used for polarization cleaning. After passing the AOM the

---

[35]SRS SIM960
[36]Minicircuits TFAS-2SM
[37]Schäfter & Kirchhoff 60FC
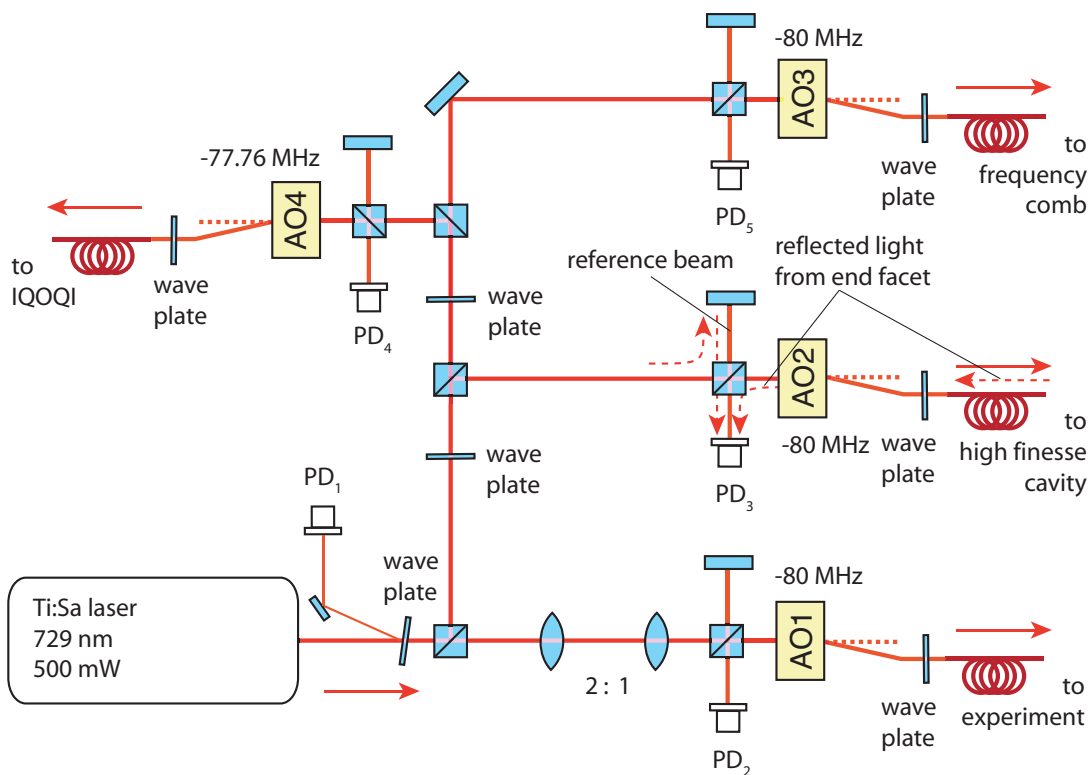
Figure 3.17: The distribution of the 729 nm light with the elements for fiber noise cancellation. The light paths for the fiber stabilization of the reference cavity fiber are indicated by the dashed arrows.

second time the light is combined with part of the unmodulated light at the beamsplitter in front of the AOM. A beat note at twice the AOM frequency can be detected with a fast photodiode. The electronic beat signal is mixed down with a reference signal from a stable RF synthesizer[38] to produce an error signal at DC. The phase difference between the beat signal and the reference is fed to a voltage-controlled oscillator (VCO) driving the AOM after passing an integrating loop filter. This closes the loop and the fiber noise is compensated by a phase-locked loop (PLL). The servo bandwidth depends on the VCO bandwidth (typically 300 kHz) and on the signal delay by the optical path length. Even for the 500 m long fiber a loop bandwidth of 35 kHz was achieved.

The effect of fiber noise broadening the light used for the laser stabilization is shown in Fig. 3.18. The fiber[39] to the high finesse cavity is 15 m long. At typical noise conditions in our lab the spectrum broadens to a full width at half maximum (FWHM) $\Delta\nu_{FWHM}$=557(7) Hz indicated by the Gaussian fit in Fig. 3.18(a). When the stabilization is active the noise gets significantly reduced to below 1 Hz as it has been demonstrated in [108]. A comparison of the unstabilized to the stabilized case is shown in Fig. 3.18(b). The central peak has a linewidth of 0.9 Hz and is limited by the resolution bandwidth of the spectrum analyzer[40]. The loop bandwidth of the stabilization is 170 kHz.

3.4.7 Optical beat note detection

In the previous sections the frequency stability of the laser was only analyzed with respect to the reference cavity. The analysis of the residual error signal provides a means to evaluate the quality of the laser lock relative to the resonator. The true spectral properties of a laser cannot be investigated this way. Instead, comparison to an independent system is necessary, like for instance by detecting a beat note with a second laser system. An alternative could also be to compare the laser frequency with the transition frequency of a narrow atomic transition as described in Sec. 7.2, or at the side of a fringe from an optical resonator.

For a beat note detection, the spectroscopy laser of the ^{40}Ca$^+$ experiment at the university was compared against the laser system of the $^{40/43}$Ca$^+$ experiment at IQOQI. The light of the two lasers can be transported to both sites by two 500 m long, polarization maintaining fibers equipped with fiber noise cancellation. The two lasers are overlapping on a non-polarizing beam splitter (BS) and sent to a photodetector, that measures the interference of the two light fields. The resulting photo-current is proportional to the optical intensity:

$$I(t) \sim |E_1(t) + E_2(t)|^2 = |E_1(t)|^2 + |E_2(t)|^2 + 2\mathrm{Re}\{E_1^*(t)E_2(t)\}. \tag{3.8}$$
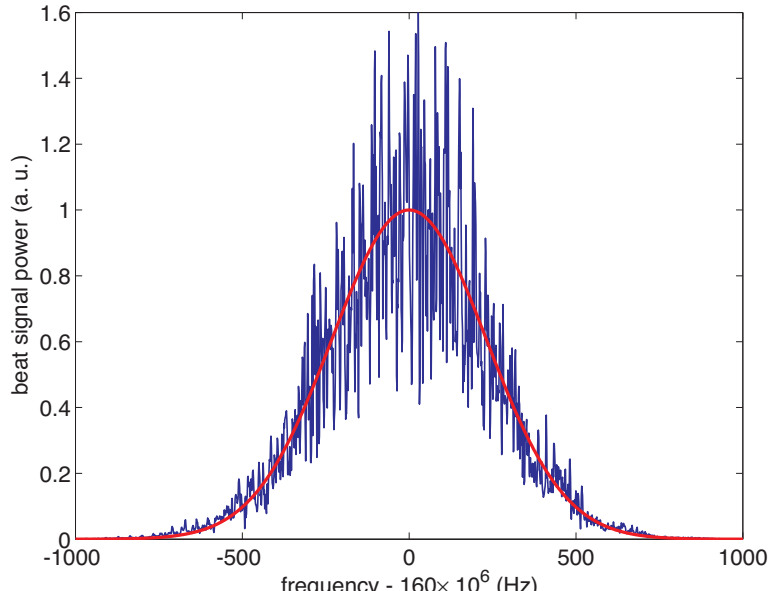
The power spectrum of the beat signal is a convolution of the power spectra of the two lasers, that is

$$S_{E_1^*E_2}(f) = S_{E_1}(f) \otimes S_{E_2}(f). \tag{3.9}$$

---
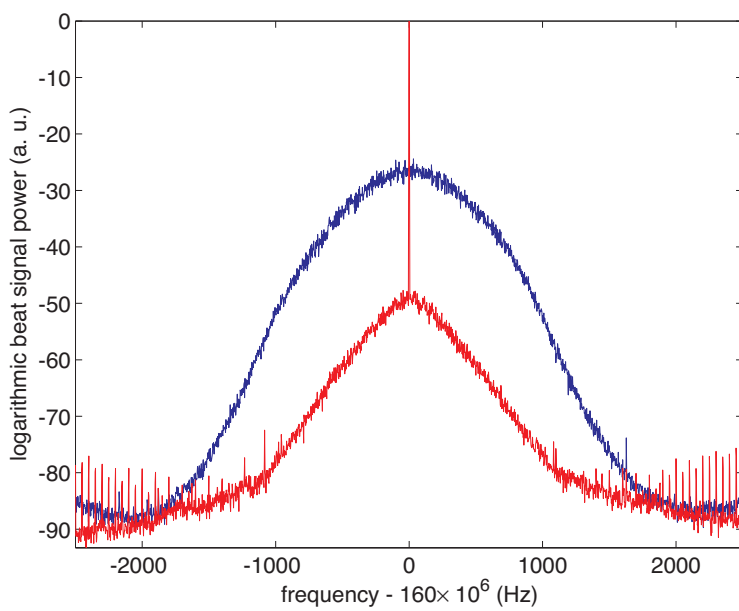
[38]Marconi 2023A
[39]Oz Optics PMJ-3A3-633-4/125-3-10-1
[40]Rohde & Schwarz FSP-13

(a)

(b)

Figure 3.18: The effect of the noise of the cavity fiber on the laser frequency. The unstabilized signal shown on a linear scale in the upper graph has a linewidth of $\Delta\nu_{FWHM}{=}557(7)$ Hz. The lower graph demonstrates the effect of the stabilization compared to the unstabilized case on a logarithmic scale.

The spectral properties of the convoluted signal can be investigated with a spectrum analyzer. For Gaussian laser frequency noise, the resulting spectrum is Gaussian with $\Delta\nu_{FWHM} = \sqrt{\Delta\nu_1^2 + \Delta\nu_2^2}$. If the lasers are dominated by white noise, the spectrum is Lorentzian where the FWHM of the convoluted signal is the sum of the two individual widths $\Delta\nu_{FWHM} = \Delta\nu_1 + \Delta\nu_2$.
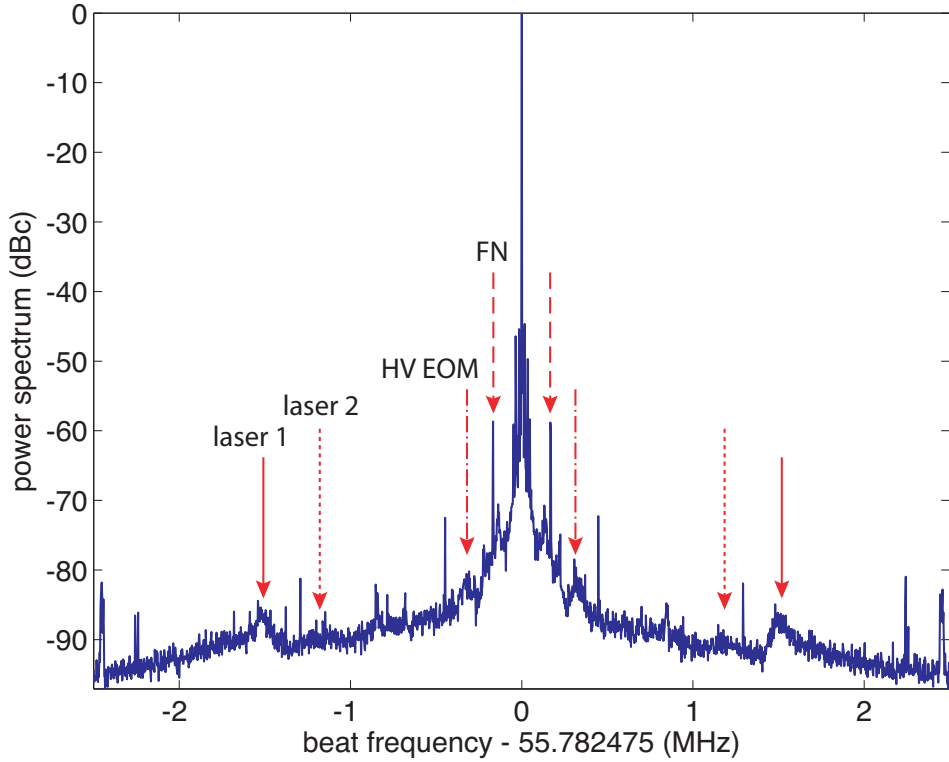

Figure 3.19: The beat signal spectrum for 5 MHz span. The arrows mark the servo bumps of the fast EOM part for laser 1 (solid), laser 2 (dotted), of the high voltage EOM part of one of the lasers (dashed-dotted), and one of the fiber noise cancellations for the reference cavity (dashed).

In the experiment, the light power in each beam was on the order of a few mW. A GaAs photodiode[41] with a bandwidth of 16 GHz serves as a fast optical detector followed by a 6 GHz bias tee[42] and a broadband amplifier[43]. Such a high bandwidth is required if the $4s\,^2S_{1/2} - 3d\,^2D_{5/2}$ transition between the isotopes ^{40}Ca$^+$ and ^{43}Ca$^+$ is compared due to the isotope shift of 5.5 GHz [118]. The beat note signal is mixed down with various stages[44]

---

[41]Hamamatsu G4176

[42]Minicircuits ZBFT-6GW

[43]Miteq AFS42-00101000-20-10P-42, bandwidth 10 GHz

[44]synthesizer: Rohde&Schwarz SML-03, mixer: Minicircuits ZMX-10G and ZLW-1, optional frequency doubler: Miteq MAX2J010060, appropriate low-pass filters

to a frequency of $\sim 10\,\text{MHz}$ in order to match a narrow-band bandpass filter[45]. The filter is used to improve the signal-to-noise ratio for the counting electronics. The measured signal is either analyzed by a spectrum analyzer[46] or sent to the frequency counter[47]. Fig. 3.19 shows such a spectrum with $\pm 2.5\,\text{MHz}$ span around the line center at $55.782475\,\text{MHz}$. The characteristics of the servo electronics is clearly visible and marked by the arrows. The solid and the dotted arrows mark the location of the "servo bumps" for the individual lasers at 1.2 and $1.6\,\text{MHz}$. Closer to the center, at $310\,\text{kHz}$, one can find the fingerprint of the high voltage servo part of one of the lasers feeding back to the intra-cavity EOM. Another servo bump stems from the fiber noise cancellation of the fiber to the university's
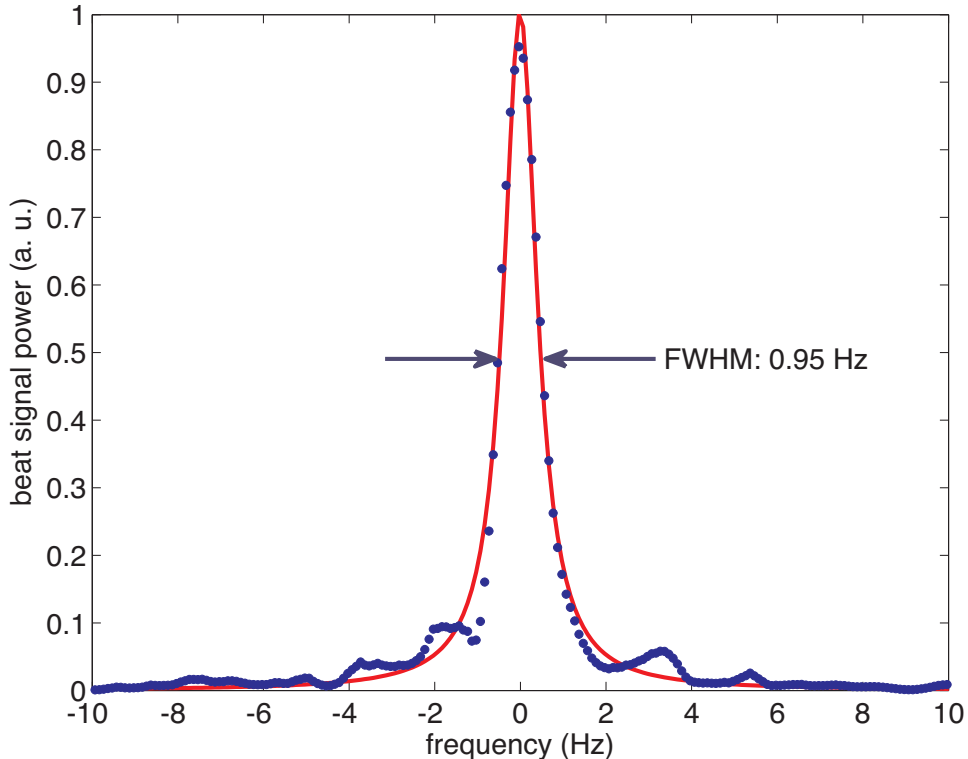
Figure 3.20: The beat signal spectrum for a span of $20\,\text{Hz}$ at $51.806800\,\text{MHz}$. The averaged data set consisting of 5 individual scans (aquisition time $1\,\text{s}$ each) with overlapped centers is fit by a Lorentzian with a FWHM of $0.95(2)\,\text{Hz}$.

reference cavity which has a bandwidth of $170\,\text{kHz}$ and is in fact oscillating in this case. Nevertheless, more than 99.97% of the power is concentrated inside an interval of $\pm 2.5\,\text{kHz}$ obtained by integrating the power spectral density.

---

[45] Minicircuits BBP-10.7
[46] Rohde&Schwarz FSP-13
[47] Kramer+Klische FXM

In order to measure the linewidth of the lasers, both of them were referenced to a $^{40}Ca^+$ ion to cancel slow drifts. The beat signal was analyzed on the spectrum analyzer with an integration time of 4 s to achieve a resolution bandwidth of 1 Hz. For Fig. 3.20 five scans were combined by overlapping the individual centers and taking the average. The data (dots) is fitted by a Lorentzian with a FWHM of $\Delta\nu_{FWHM} = 0.95(2)$ Hz. Neglecting the contribution of the spectrum analyzer, an individual linewidth of $\Delta\nu_{FWHM}/2$ can be attributed to each laser, if both contribute equally to the signal. Please note, that this measurement represents a collection of the best shots.
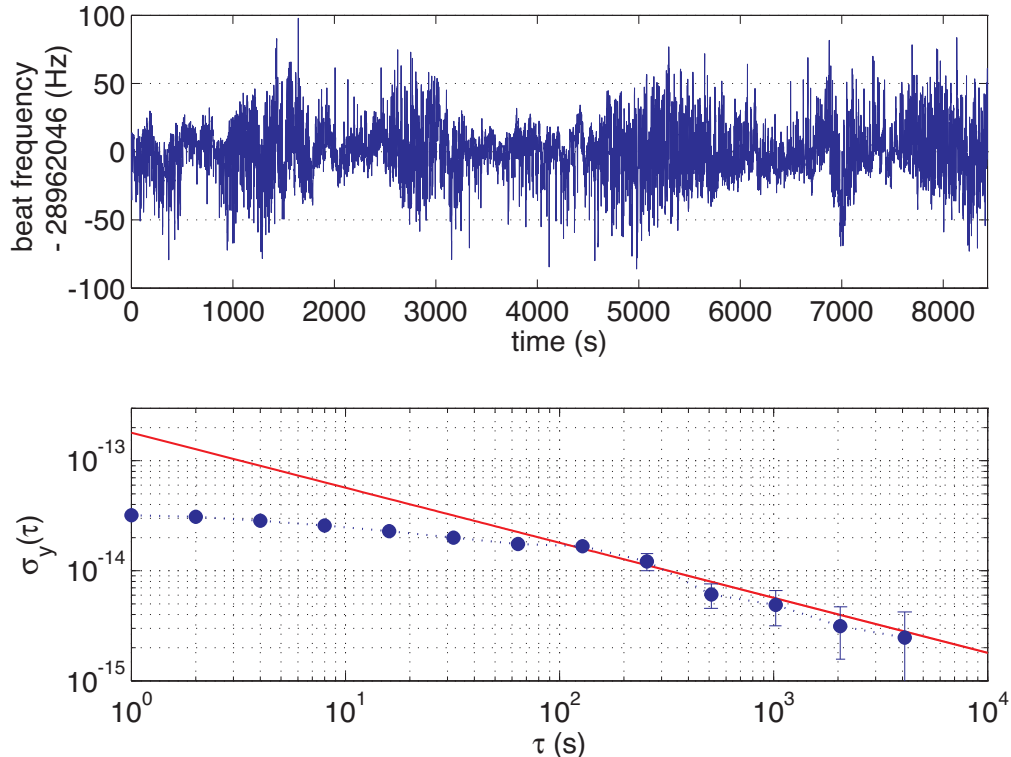
Figure 3.21: Beat signal analysis. The upper graph shows the frequency of the optical beat signal measured with an RF counter for more than two hours. The lower graph represents the Allan standard deviation for this data set.

On the time scale of less than a second, the linewidth is typically limited by the spectrum analyzer's bandwidth. For durations of a few seconds, the linewidth is most of the time close to 10-20 Hz and on the order of 50 Hz FWHM when observed over the course of more than two hours. The frequency counter results for a measurement with a similar setup as described above at IQOQI [81] are shown in Fig. 3.21 in the upper graph. The Allan deviation [119] in the lower graph has a pedestal at a few 10^{-14} before decreasing with $\tau^{-1/2}$. This indicates that after 120 s, the lock of the lasers to the atomic transition comes into effect and is able to dominate frequency jitter most likely caused by seismic noise of the reference cavities. The solid line is a fit with $\sigma_y(\tau) = 1.8(2) \times 10^{-13}\tau^{-1/2}$.

This is expected to improve dramatically for reference cavities with less sensitivity to seismic vibrations and lower drift rates. At the moment, the time required for frequency comparisons at the $0.1\,\text{Hz}$ level (2.4×10^{-16}) as required for a more precise investigation of systematic effects of the $4s\ ^2S_{1/2} - 3d\ ^2D_{5/2}$ transition, is longer than six days. A histogram of the data set yields a FWHM of $\Delta\nu_{FWHM} = 41(1)\,\text{Hz}$ for a Gaussian fit and is shown in Fig. 3.22.
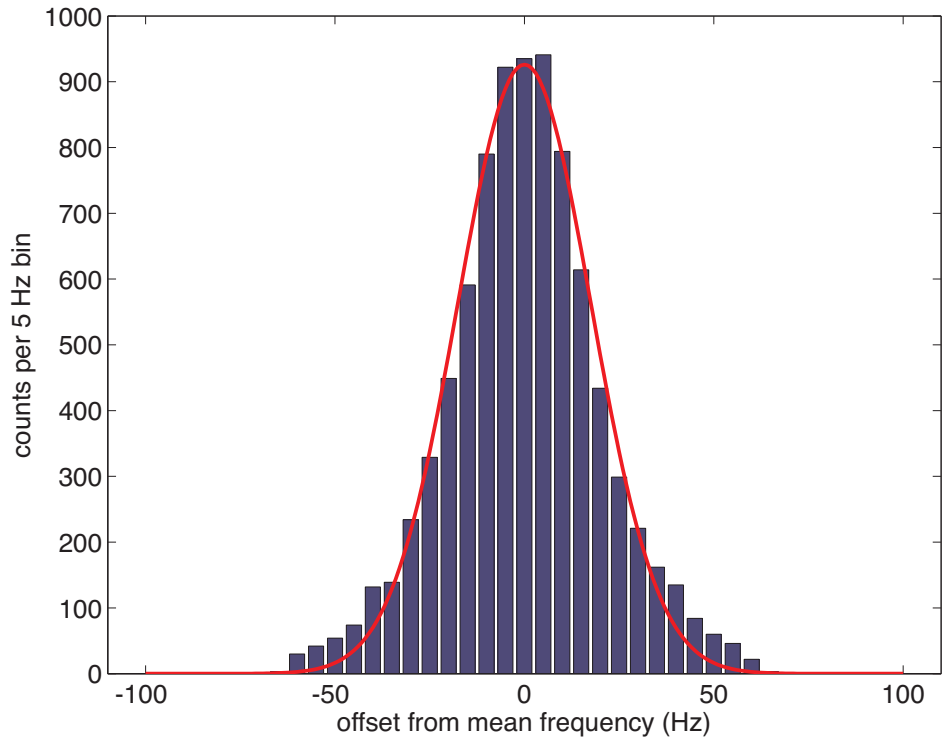

Figure 3.22: Histogram of the beat signal recorded with an RF counter for more than two hours. A Gaussian fit with $\Delta\nu_{FWHM} = 41(1)\,\text{Hz}$ is indicated by the solid line.

Chapter 4

The frequency comb
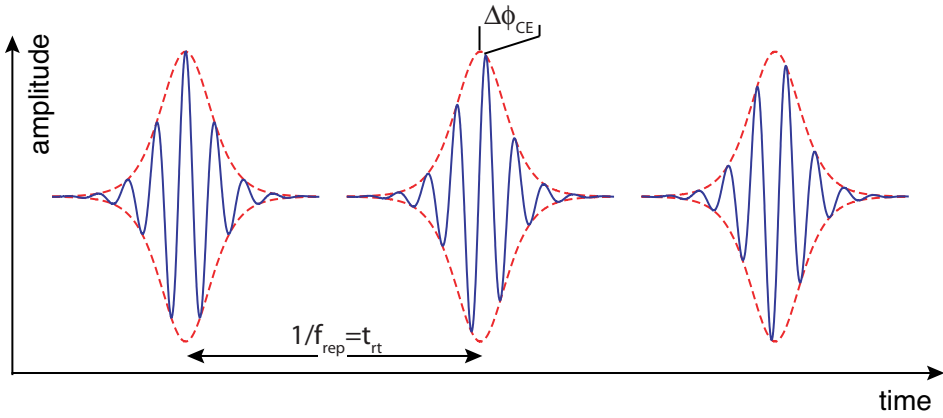
The development of self-referenced frequency combs in 1999 [120, 121] opened a new era in optical metrology and ultra-fast physics. It allows for a direct link of optical frequency and microwave standards [14, 22, 122, 123] as well as for the production of ultra-short, phase stable light pulses of a few cycles [124–127] of the electric field. This opens up a new field in the direction of optical waveform synthesis [128] and investigation of ultra-fast processes like in semiconductor physics [129]. Frequency combs can be also used for wavelength calibration of astronomical spectrographs [130]. On the frequency metrology side, the most striking feature is the simplicity of the system as compared to the complicated and unreliable frequency chains [131] previously used for absolute frequency measurements. Instead of trying to keep many different oscillators and phase-locked loops (PLL) under control, it suffices to stabilize the fs oscillator with two PLL's which stands for a major simplification of optical frequency metrology.

This chapter contains a short review of the operation principle of frequency combs, a detailed description of the setup and the stabilization scheme, and the tools for a measurement of an optical frequency.
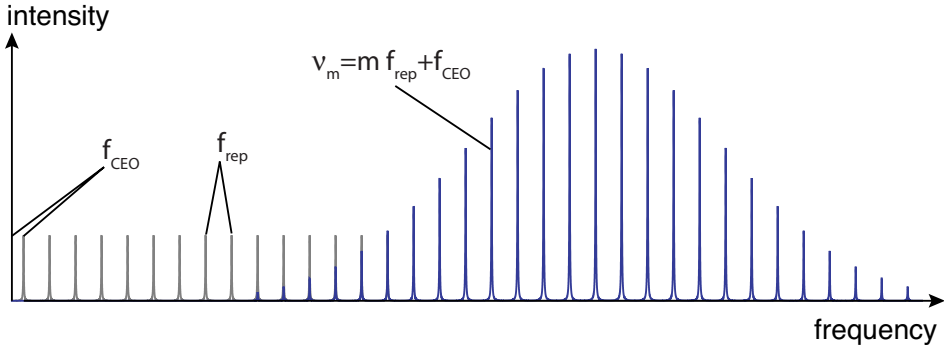
4.1 Principle of operation

The workhorse for the optical frequency metrology are mode-locked laser which emit a train of ultra-short pulses. Upon first glance, it seems rather counter-intuitive that a pulsed laser can be used to measure the frequency of a continuous wave laser. But a closer look at the spectrum reveals that a pulse is formed as a coherent superposition of numerous, equally spaced optical frequencies. The pulses emitted by a mode-locked laser, which are separated in time by one cavity round-trip time t_{rt}, are illustrated in Fig. 4.1. As a consequence, the Fourier spectrum consists of a series of delta functions in frequency with each spectral component separated by $f_{rep} \equiv = 1/t_{rt} = \frac{c}{L}$, with the speed of light c and the length of the cavity L.

Modelocking of the laser spectrum, which is required for the formation of an ultra-short light pulse, is forcing each longitudinal mode $f_n = n \ f_{rep}$ of the laser cavity to have a common phase relationship. This carrier-envelope phase ϕ_{CE} defines the phase of the

(a) Time domain.

(b) Frequency domain.

Figure 4.1: (a) The pulse train of a mode-locked laser in the time domain. (b) The pulse train in the frequency domain.

electric field with respect to the pulse envelope and results in a spectral shift f_{CEO} of the entire frequency comb by the relation

$$f_{CEO} = \frac{1}{2\pi} \frac{d\phi_{CE}}{dt} \approx \frac{\Delta\phi_{CE}}{2\pi t_{rt}}. \tag{4.1}$$

The phase change is related to the difference of the group $(v_g = c/n_g)$ and phase $(v_p = c/n)$ velocities of the laser cavity, which according to [132] is given by

$$\Delta\phi_{CE} = l_c \omega_c \left(\frac{1}{v_g} - \frac{1}{v_p} \right), \tag{4.2}$$

where l_c is the cavity length and ω_c the carrier frequency. The average group index of refraction can be expressed as $n_g = n + \omega \frac{dn}{d\omega}$, therefore connecting the carrier offset frequency f_{CEO} to the cavity dispersion properties.

As a result of the strong mode-locking condition, in particular for the Kerr-lens mode-locked Titanium:Sapphire laser used, each comb element in the spectrum may be charac-

terized by only two frequencies, the carrier offset frequency f_{CEO} and the laser repetition rate f_{rep} [14], that is

$$\nu_m = mf_{rep} + f_{CEO}, \qquad (4.3)$$

where m is an integer number on the order of $\sim 10^6$. For further details, the reader is referred to [133]. Both frequencies, f_{rep} and f_{CEO}, lie in the radio frequency domain. Therefore, the frequency comb provides a direct link between optical and microwave frequencies. Application of single frequency laser stabilization techniques allow for simple, but very efficient stabilization methods, thus making the frequency comb the ideal tool for high precision measurements of optical atomic transitions. This explains the major impact the advent of the optical frequency comb had on optical frequency metrology.

4.2   The fs oscillator: a Kerr lens mode-locked (KLM) laser

The frequency comb used for the absolute frequency measurement of the $4s\,^2S_{1/2}-3d\,^2D_{5/2}$ transition in ^{40}Ca$^+$ is a commercial system sold by MenloSystems[1]. It consists of three major building blocks: a $5\,\mathrm{W}$ DPSS pump laser system, the KLM laser[2] producing a train of ultra-short pulses, and the stabilization and frequency detection unit. A detailed sketch of the experimental setup is shown in Fig. 4.2. The intensity of the pump light at $532\,\mathrm{nm}$ can be controlled by diffracting a small amount of light into the first order of an AOM and varying the RF power driving the AOM operated at $40\,\mathrm{MHz}$. The green light is focused tightly into the Ti:Sa crystal where it generates light centered around $810\,\mathrm{nm}$ as shown in Fig. 4.3. The laser cavity is formed by six mirrors. Five of them are so-called "double-chirped" mirrors for dispersion compensation [134]. Pulsed operation is achieved by passive mode-locking of the laser spectrum. This requires that the longitudinal modes of the laser cavity are equally spaced. However, the bandwidth of the cavity is limited by dispersion of the intra-cavity elements so that dispersion compensation is needed. Negative dispersion in the "chirped" mirrors is obtained by a stack of dielectric coatings where the penetration depth of the light depends on the wavelength. As a result, pulse broadening by the Ti:Sa crystal can be compensated over a broad range. The process of the pulse formation in a KLM laser is a complicated matter, but the basic idea can be summarized by invoking the concepts of self-focusing and self-phase modulation. The transverse intensity profile of the light pulse results in the formation of a intensity-dependent lens (Kerr lens) inside the Ti:Sa crystal due to a nonlinear index of refraction (self-focusing). This nonlinear effect is used as a passive saturable absorber meaning that the mode-locked operation has a better spatial overlap with the pump beam as compared to the CW mode [135, 136]. The temporal effect of a high-intensity laser pulse is a time change in the refractive index leading to a phase modulation at the pulse edges [137]. This coherently generates new frequency components in the pulse (self-phase modulation) and together with the dispersion compensation yields a shorter pulse. Knocking on one of the mirrors starts mode-locking by the formation of a weak pulse which is then amplified by the nonlinear effects. The mirror without

---

[1]MenloSystems FC8003
[2]Gigaoptics Gigajet

63
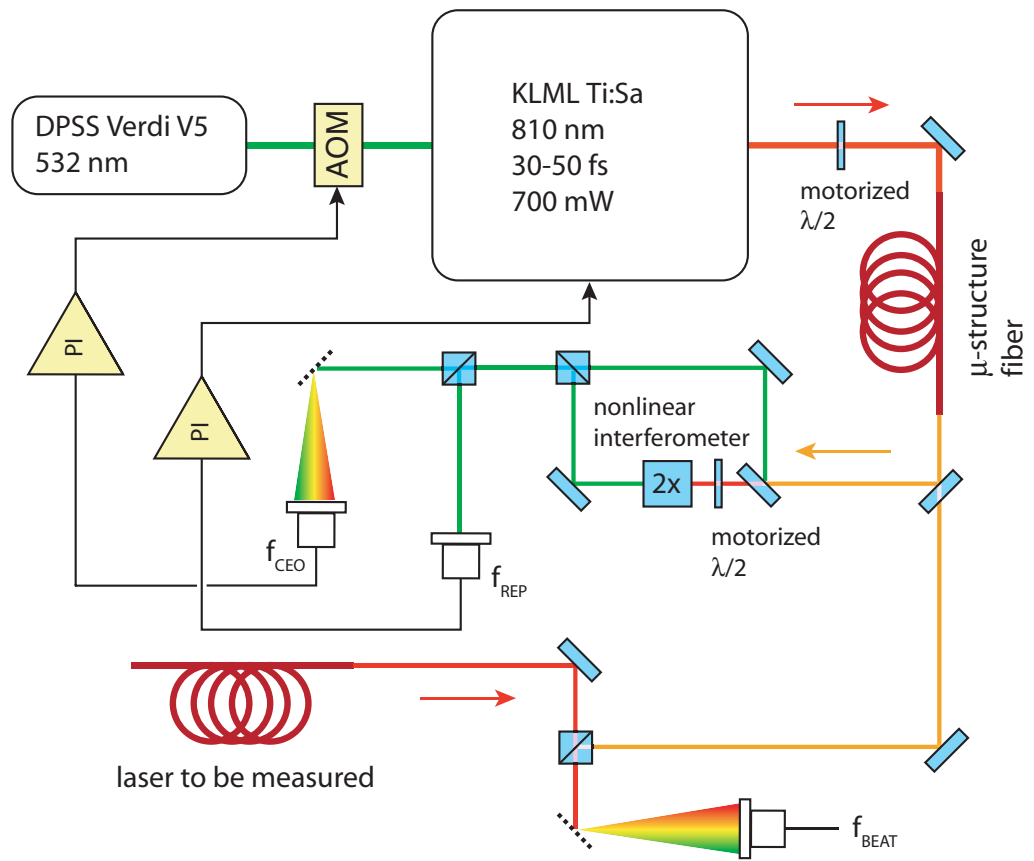
Figure 4.2: The frequency comb setup.

the dispersion compensation coating acts as the output coupler (OC). The output of the Ti:Sa oscillator is a train of light pulses with pulse lengths on the order of 30-50 fs and a repetition rate of 825 MHz.

The output of the laser is tightly focused into a microstructured fiber for spectral broadening by a microscope objective mounted on a motorized XYZ translation stage[3] which can be computer-controlled[4]. The broadening technique makes use of the high intensity maintained in the core of a photonic crystal fiber with a small mode field diameter[5]. The fiber is composed of a honeycomb structure of air holes surrounding the core, creating a periodic potential which is preventing the light from penetrating into the cladding for a bandwidth of more than one octave (photonic crystal) [138]. Spectral broadening is obtained once again by self-phase modulation and other highly nonlinear effects [139]. The zero dispersion point of this fiber was optimized for the central wavelength of the fs laser output resulting in a spectral broadening ranging from 500 to 1100 nm. This octave

---

[3]XYZ translation stage with Thorlabs PE4

[4]Thorlabs MDT693

[5]core diameter $\approx 2\,\mu$m
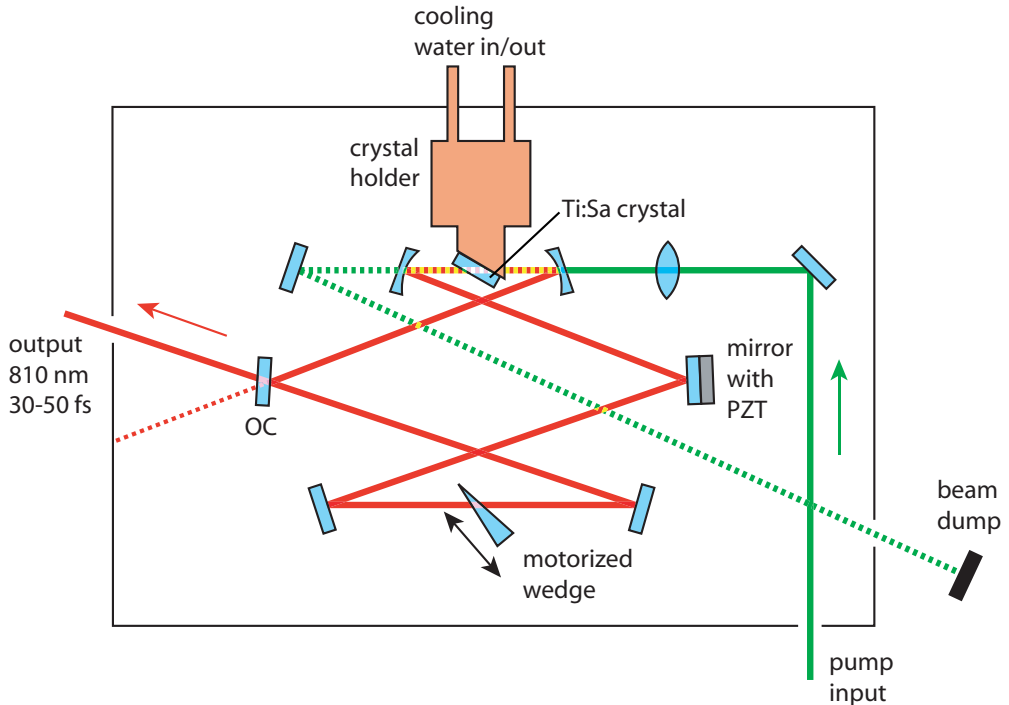
Figure 4.3: The femto-second laser.

spanning frequency comb allows for self-referencing of the offset frequency f_{CEO} as will be explained in the next section. Geometrical imperfections of the fiber during its production process lead to a preferred polarization direction for optimal broadening. The 20 cm fiber piece is glued into a holder, which makes it susceptible to changes of its birefringence induced by thermal stress. The slow degradation of the efficiency due to polarization drifts can be compensated by a motorized half-wave plate at the fiber input.

At the output of the microstructure fiber the light is split into two parts by a dichroic mirror. The "red" part ranging from 650 to 850 nm is used for the absolute frequency detection with external lasers, while the infrared and green light enters the nonlinear interferometer for the f_{CEO} and f_{rep} detection and stabilization. The beat note signals for f_{CEO} and with the external lasers are detected by avalanche photodetectors[6], the repetition rate detection uses a fast Ga:As photodiode[7] on a bias tee[8] followed by an 20 dB amplifier[9]. For better signal-to-noise of the weak beat signals the corresponding beams are spectrally separated by diffraction gratings with 1200 gr/mm. Details of the stabilization schemes and the optical beat note detection are presented in the following sections.

---

[6]MenloSystems APD210
[7]Hamamatsu G4176
[8]Minicircuits SFBT-4R2GW-FT
[9]Minicircuits ZEL-0812LN
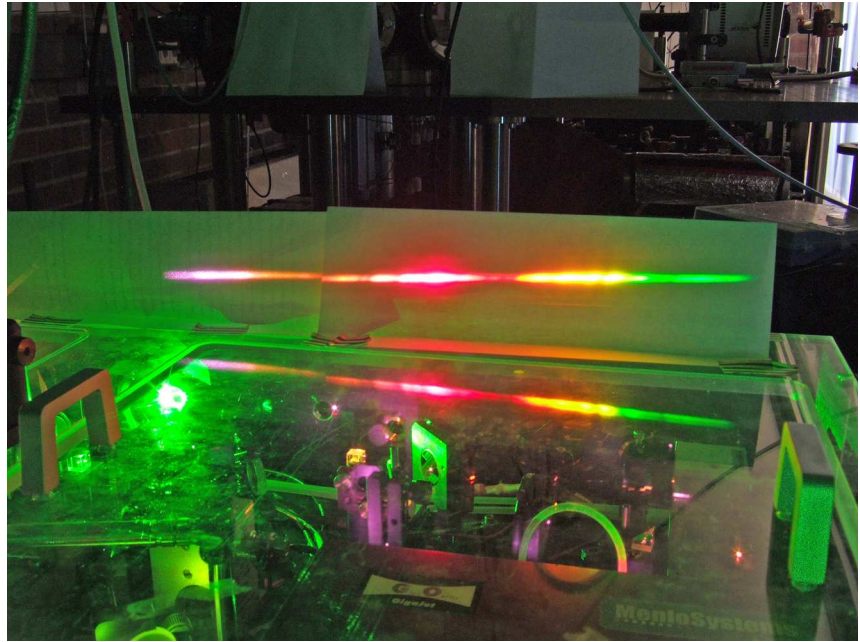
Figure 4.4: The output spectrum of the photonic crystal fiber ranging from 500 to 1100 nm.

4.2.1 The stabilization of the carrier offset frequency

The breakthrough of optical frequency combs was marked by the advent of the self-referencing technique and the use of microstructured fibers for octave-broadening [140–142]. Up to now, there exist no electronic detectors which are capable of directly detecting the electric field of a fs pulse which would be necessary for a direct measurement of ϕ_{CE}. By nonlinear self-comparison of spectral harmonics of comb components [143], it is possible to observe an optical beating signal which is proportional to f_{CEO}, that is

$$|N(nf_{rep} + f_{CEO}) - M(mf_{rep} + f_{CEO})| \stackrel{Nn=Mm}{=} |N - M|f_{CEO}. \qquad (4.4)$$

In the simplest case, $N = 2$ and $M = 1$, the spectrum of the frequency comb is required to span at least one octave. Then, the low-frequency part of the spectrum can be frequency-doubled ($\nu_1 = 2 \times (mf_{rep} + f_{CEO})$) and compared to the high frequency part $\nu_2 = 2mf_{rep} + f_{CEO}$, yielding a frequency difference of

$$\nu_1 - \nu_2 = f_{CEO}. \qquad (4.5)$$

The optical setup of the nonlinear interferometer in Mach-Zehnder geometry is shown in Fig. 4.2. A fast photodetector detects the beat note at f_{CEO}. A prism pair (not shown in the figure) in the green arm of the interferometer serves to compensate possible path length differences. The motorized half-wave plate in the red arm is used to adjust the polarization of the infrared light to the polarization axis of the frequency doubling crystal. The radio frequency signal is amplified and band-pass filtered at 20 MHz. The offset frequency can

be tuned with the help of a motorized quartz wedge in the fs oscillator. The error signal is generated by mixing the beat signal with 20 MHz obtained from frequency doubling[10] of the 10 MHz reference. The feedback is established by a PI controller modulating the amplitude of the RF source for the AOM placed into the pump beam. Part of the f_{CEO} signal is split off by a directional coupler and used to monitor the signal-to-noise ratio which is usually better than 40 dBc in a 100 kHz bandwidth. It is also used to optimize the position of the motorized wave plates and the coupling into the microstructure fiber.

The mechanism behind the stabilization is the highly nonlinear index of refraction $n(x,t)$ inside the laser crystal which is dependent on the spatial and temporal intensity $I(x,t)$ and is given by

$$n(x,t) = n_0 + I(x,t)n_2, \tag{4.6}$$
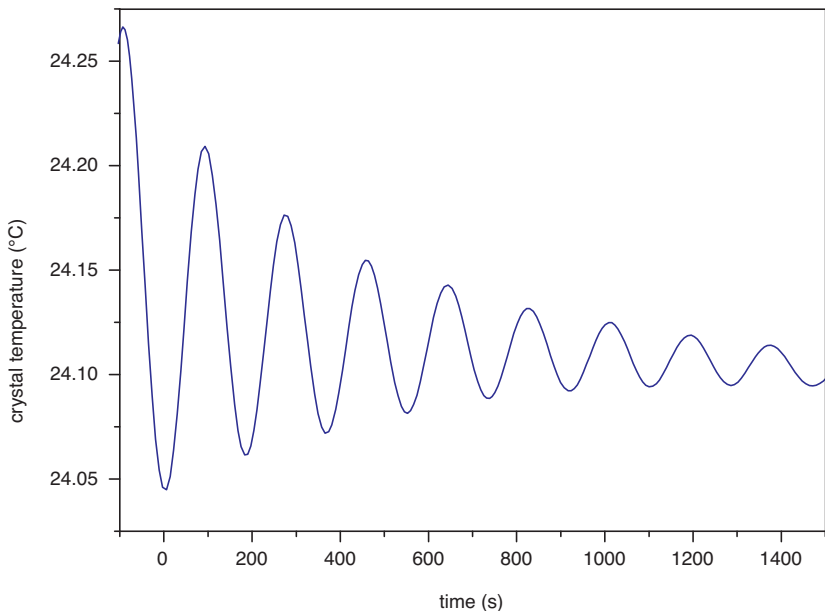
where n_0 is the linear and n_2 the nonlinear index of refraction. Taking Eq. (4.2) and the intensity sensitive index of refraction from Eq. (4.6), it can be shown that f_{CEO} becomes related to the optical intensity [144]. Amplitude modulation of the pump power changes the index of refraction and thus the group velocity which in turn induces a change of ϕ_{CE}.

With the setup as it was delivered, stable locking of the offset frequency and even mode-locking at all is only achieved for a couple of minutes. Large part of the problem stems from the fact that the housing of the laser and the baseplate are thermally not stable. For instance the pumping beam hit the back wall of the housing after passing the two curved mirrors and the crystal holder was temperature stabilized with the same water which is used for cooling the pump laser's base plate. The water chiller used for this purpose is by no means designed to provide a stable temperature. For better thermal stability two improvements made a huge difference. First, the pump light was guided into a beam dump outside the frequency comb housing. A modification a bit more complicated was the temperature stabilization of the Ti:Sa crystal. Here, a temperature sensor was glued onto the crystal holder and used to stabilize water temperature from a home-built chiller. A PI controller with a integration time constant of 800 s controls the current through a thermo-electric element heating or cooling the water. After settling, the achieved temperature stability was below 0.01 °C/h. Fig. 4.5 shows the correlation between the temperature and f_{CEO} during the ringing after switching on the temperature stabilization. From this, the temperature sensitivity for this laser system can be estimated to be 4(1) MHz/°C. Together with the external beam dump, these improvements were able to extend the typical duty cycle of operation from a few ten minutes to more than three hours maximum.
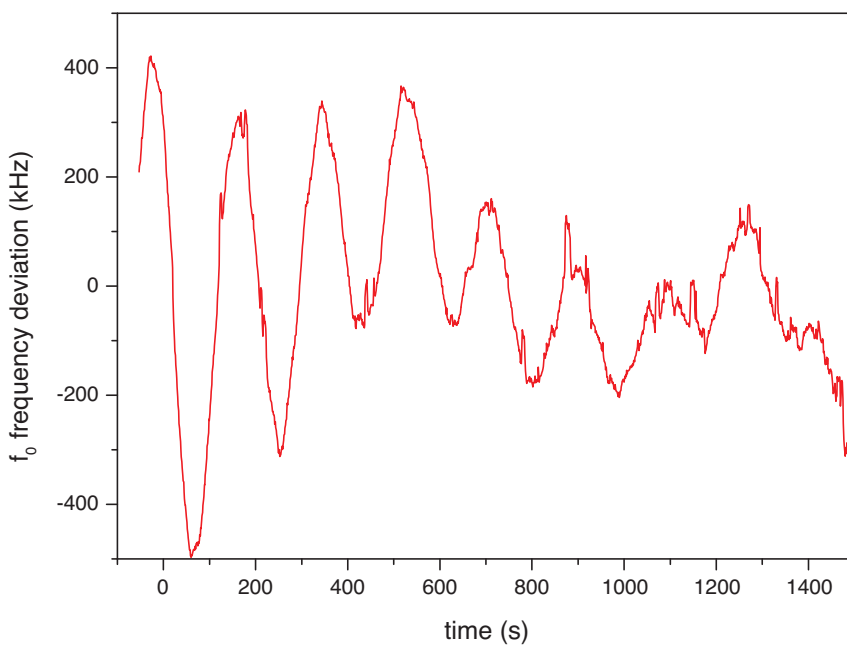
4.2.2   Stabilization of the repetition rate

The heart of the frequency comb stabilization is the frequency lock of the repetition rate. For an optical frequency measurement, the necessary measurement time for a given level of precision depends also on the stability of the frequency comb, provided the (in-)stability of the laser to be measured is negligible. Since the errors in f_{rep} are multiplied by 10^6 in the optical domain, this is the critical parameter. The measurement of the repetition frequency is quite simple, because for typical cavity lengths of 30 cm it is directly measurable by a

---

[10]Minicircuits FD-2 followed by a bandpass filter BBP-21.4

(a)

(b)

Figure 4.5: f$_{CEO}$ and crystal temperature.
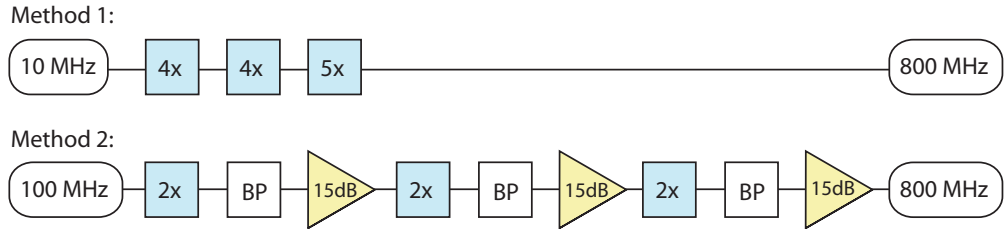
Figure 4.6: The frequency reference for the repetition rate stabilization.

fast photodiode. Neighboring modes produce a strong heterodyne signal when shining part of the comb light onto a detector with excellent signal-to-noise as many modes contribute to the signal. The stabilization scheme is similar to the one used for f_{CEO}. The RF signal is amplified and compared with a synthesized frequency reference. The error signal is shaped by a loop filter and corrections of f_{rep} are applied to one of the laser cavity mirrors mounted on a PZT to stabilize the cavity length. Thereby, the repetition rate is phase-locked to the reference.

During the absolute frequency measurement of $^{40}Ca^+$ the frequency comb was locked to a transportable Cs atomic fountain clock. The clock had two outputs with 10 and 100 MHz derived from an ultra-stable quartz crystal with an amazing short term stability of 8×10^{-14} in 1 s. This offered two possibilities to generate a frequency reference at 800 MHz for the stabilization of f_{rep}. A schematic diagram of the two methods is displayed in Fig. 4.6. The first method uses the 10 MHz signal isolated from other ports by a distribution amplifier[11]. The multiplication chain consists of two low noise frequency quadruplers[12] and a low noise odd-order multiplier[13] with internal amplifiers. For the second method, simple frequency doublers[14], bandpass filters made of lowpass and highpass filters[15] and amplifiers[16] were combined to generate the 800 MHz from the 100 MHz reference. The photodiode signal at 825 MHz was mixed[17] with the reference to produce an intermediate signal at 25 MHz which was compared to the signal from a tunable synthesizer[18] with a second mixer[19] to finally generate the error signal. In case of method 2, the intermediate frequency was first mixed with the 10 MHz reference before mixing it with the synthesizer signal.

Fig. 4.7 presents a comparison of the two different methods to generate a frequency reference for the f_{rep} stabilization. The signals are optical beat notes at 35 MHz of the frequency comb with a laser stabilized to a $^{40}Ca^+$ ion. Details of how these signals are obtained are discussed in the next section. For the moment, the important thing to notice is that the two methods have significantly different widths, for method 1(dark blue) the

---

[11]TimeTech 10274
[12]Wenzel Assoc. LNHQ
[13]Wenzel Assoc. LNOM-5
[14]Minicircuits FD-2
[15]Minicircuits BLP and BHP
[16]Minicircuits ZFL-500HLN and ZFL-1000LN
[17]Minicircuits ZEM-2B
[18]SRS DS345
[19]Minicircuits ZAD-1

FWHM is $\Delta\nu_1 =$790(10) Hz, for method 2 (light blue) it is $\Delta\nu_2 =$420(10) Hz. This is no surprise, as more phase noise is expected for method 1 due to a higher multiplication factor. Please note, that a factor of two in the noise means a factor of four in measurement time for a given level of precision. Still, the achieved level of stability of 4.3×10^{-13} is a factor
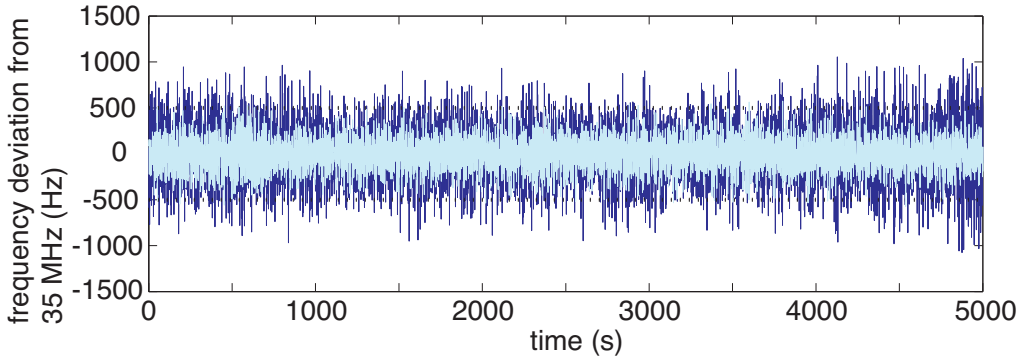

Figure 4.7: The beat signal of the frequency comb with an external laser for two different references for locking the repetition rate.

of five higher than it would be expected from the stability of the Cs clock reference. Here, more dedicated RF parts could lead to a significant improvement or for the best possible result, stabilization of the repetition rate to the optical beat note would be required.

4.3 Optical beat note detection for the absolute frequency measurement

The self-referenced frequency comb stabilized as described in the section before can be used to measure the frequency of an external laser by detection of a beat note signal with the nearest comb line. For this purpose, the laser and part of the frequency comb are aligned on a beam splitter for maximum overlap as shown in Fig. 4.2 and spectrally separated by a diffraction grating for a better signal-to-noise ratio. Both light fields interfere on a fast photodetector and generate a beat note signal proportional to the difference and the sum of the frequencies. The latter is an optical frequency and can therefore not be detected. The difference frequency $\Delta\nu_L$ lies in the radio-frequency domain and is limited to $\Delta\nu_L \leqslant f_{rep}/2$. In fact, the frequency comb is split into two branches by a 50:50 beamsplitter, so that two external lasers can be measured at the same time with two similar setups. To enhance the signal-to-noise ratio, the beat signals are amplified and band-pass filtered because the frequency counters used did not count reliably if the signal-to-noise ratio was below 30 dB in a 100 kHz bandwidth. The counters are designed for frequencies below 40 MHz, therefore it was required that one of the beat signals was mixed to a detectable frequency with the help of an RF synthesizer[20]. The other beat signal was tuned to a range between

---

[20]Marconi 2023A

35 to 40 MHz by changing the frequency of the tunable synthesizer of the repetition rate lock. Thereby, the cavity length of the fs laser gets adjusted.

In order to detect cycle slips, i. e. events when the counters lost track of the signal, an
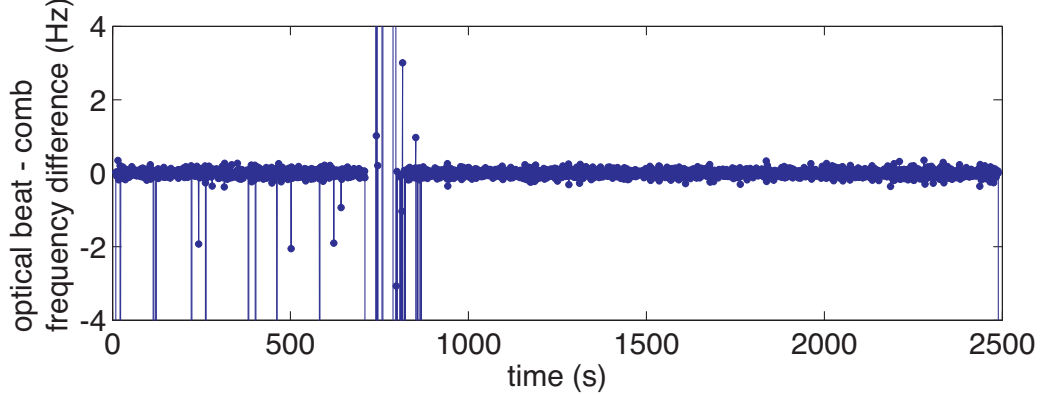
Figure 4.8: Counter difference: comparison of the two optical frequencies measured by the frequency comb against the signal obtained from an optical beat measurement.

optical beat note of the two lasers was measured directly on a fast photodiode[21]. The difference of the optical frequencies measured by the frequency comb was compared to the frequency of the direct beat signal. Any counting error would show up as a difference of >1 Hz, given the counting interval of 1 s. An example of such a trace is shown in Fig. 4.8. This simple technique is also applicable for systems, where only a single laser is measured by a frequency comb. Comparing for instance, the external laser against itself but detuned in frequency by an AOM, could yield a reliable tool to detect cycle slips.

---

[21]Hamamatsu G4176 on a Minicircuits bias tee ZBFT-6GW followed by a Miteq AFS42-00101000-20-10P-42 amplifier

Chapter 5

Experimental prerequisites and techniques

In this chapter a few experimental techniques and requirements are described which are necessary for the absolute frequency measurement of the $4s\,^2S_{1/2} - 3d\,^2D_{5/2}$ transition in $^{40}\mathrm{Ca}^+$ and for the measurement of the electric quadrupole moment of the 3d $^2\mathrm{D}_{5/2}$ level. It contains information about micromotion compensation, calibration of the magnetic field, an alternative method for optical pumping, and the prerequisites for Ramsey spectroscopy like frequency and phase control of the laser exciting the quadrupole transition, Ramsey experiments with switched phase, and the stabilization of the laser to the ion.

5.1   Compensation of excess micromotion

Electric stray fields may exist which shift the ion from the zero-point of the RF field to a region where the ion motion is driven by the trapping field in contrast to unavoidable micromotion caused by secular motion (see Eq. (2.8)). These fields can be generated by localized surface charges (patch potentials) on the trap structure or by geometrical imperfections of the trap like misalignment of the DC end caps. As a result, enhanced micromotion modulates the coupling strength of the ion to laser fields. The resulting first-order Doppler shift can significantly broaden the line of an atomic transition leading to an increased cooling limit. The final temperature T_D for Doppler cooling is determined by the effective linewidth γ_{eff} of a transition ($T_D \approx \frac{\hbar\gamma_{eff}}{2k_B}$). It is even possible that heating occurs for a laser which is detuned near, but above a micromotion sideband [82]. Therefore, compensation of excess micromotion is an essential ingredient for efficient laser cooling and important for experiments with cold ions, for example experiments in quantum information processing. From a high-accuracy spectroscopy point of view, excessive micromotion is responsible for large AC Stark as well as for second-order Doppler shifts [82]. In our case, the compensation is achieved by applying voltages to additional electrodes placed in the vicinity of the trap as shown in Fig. 3.3 (b). Please note that a voltage applied to the vertical electrode shifts the ion vertically but affects the horizontal micromotion and vice

versa as the electric field lines near the trap center are aligned perpendicular to the axes of the trap (see inset of Fig. 5.1).

There exist three important methods commonly used for coarse compensation. One is to minimize the position change of an ion observed by a camera when the RF power is changed, another one is to optimize the scattering rate on resonance for a cooling transition. A bit more precise than the two methods before is the correlation method. Here, the correlations of photon arrival times from light scattered at the cooling transition with the phase of the driving RF field are minimized. The correlations are caused by the Doppler effect due to micromotion which is modulating the scattering rate. Further details of these
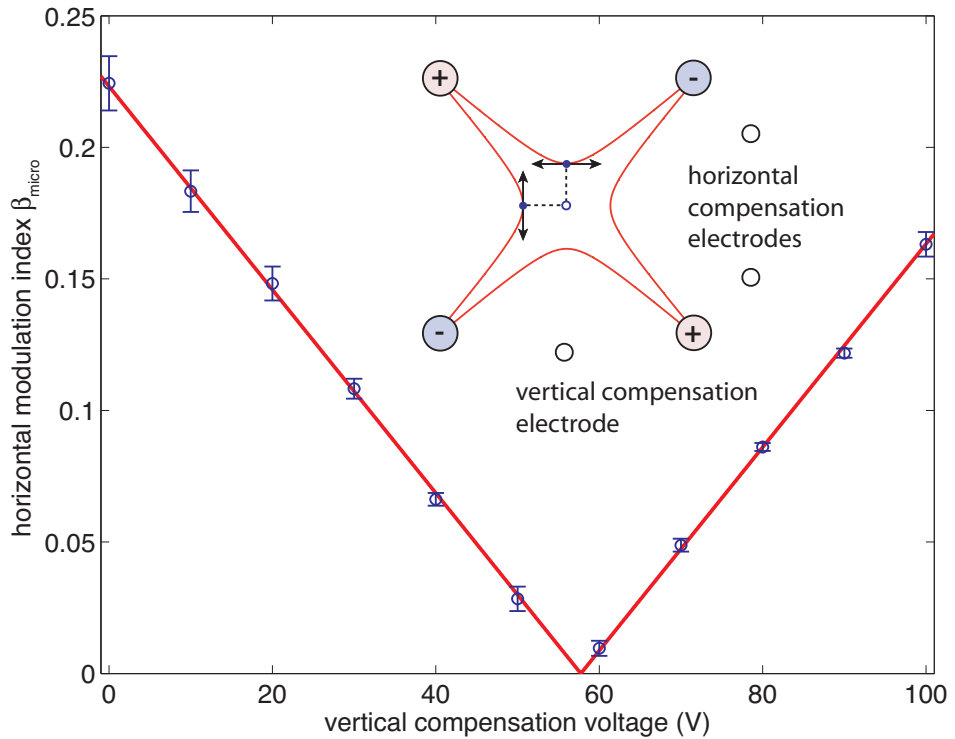
Figure 5.1: The modulation index β_{micro} of the first micromotion sideband in horizontal direction depending on the vertical compensation voltage. The inset shows a cross section of the trap and the micromotion directions associated with electric field lines of the quadrupole field.

methods are discussed in [79, 84]. However, the best results can be achieved by directly observing the micromotion sideband on a narrow transition. With the correlation method the necessary compensation voltages can be reliably determined to achieve a modulation index within $\beta_{micro} \approx 1\%$ [79]. Starting from that point, the compensation is further improved by detecting the micromotion sideband on the $4s\ ^2S_{1/2} - 3d\ ^2D_{5/2}$ transition with the help of two beams from two different directions so both components of the micromotion can be minimized. The dependence of the horizontal micromotion compensation on

the applied voltage with respect to the vertical electrode is shown in Fig. 5.1. For this measurement the Rabi frequency on the micromotion sideband was measured at different compensation voltages and compared to the value on the carrier. In the case of optimal compensation we can achieve a modulation index as low as $\beta_{micro} = 0.004(1)$, but the determination of the Rabi frequency becomes more and more difficult. The decoherence due to fluctuations of the magnetic field and the laser frequency limits the contrast of the Rabi flops after a few milliseconds. Experience shows that with the photoionization technique to create ions in the trap we do have to check the micromotion compensation every few months only and the applied voltage corrections are usually a few volts. Therefore, the uncertainty of the micromotion modulation index for the absolute frequency measurement of the $4s\ ^2S_{1/2} - 3d\ ^2D_{5/2}$ transition can conservatively be assumed to be well below $\Delta\beta_{micro} < 0.1$.

5.2 Frequency resolved optical pumping using the laser at 729 nm

For most of the experiments in quantum information processing or for spectroscopy with our setup it is necessary to initialize the ion(s) in a well defined electronic state. Sometimes there is even need for a defined state of the motional degrees of freedom for which normal Doppler cooling is not sufficient (e. g. Bell state creation). Optical pumping with σ^- polarized light at 397 nm along the quantization axis is used to initialize the electronic state of the ion into $\left|S_{1/2}, m_S = -1/2\right\rangle$. Given the geometry and the optical access of our trap, this is a simple and efficient solution as the state population ends up in the right state with an efficiency of better than 99% after $60\,\mu$s of pumping with σ^- light. Unfortunately, the particular method of optical pumping leads to restrictions related to the freedom of choosing the orientation for the quantization axis. It would be very inconvenient and sometimes even impossible to realign the σ beam path each time the angle of the magnetic field is changed which was necessary for the measurement of the electric quadrupole moment described in chapter 7.

Therefore, we investigated whether initialization of the ion in a particular Zeeman ground state can be achieved using the laser at 729 nm. Instead of relying on selection rules related to the polarization of the laser exciting the broad $S_{1/2}-P_{1/2}$ transition, we can make use of the frequency-selective pumping on the narrow quadrupole transition. The main advantages are:

- The pumping should be insensitive against imperfect polarization.

- The optical pumping beam does not need to be aligned with the B-field defining the quantization axis.

For testing the optical pumping, we first prepared the ion in the m_S=-1/2 state by standard optical pumping using a beam of σ^- polarized light at 397 nm (dashed lines in Fig. 5.2). Then, we switched on the laser at 729 nm with a Rabi frequency of $\Omega/(2\pi) = 18(1)\,$kHz resonant with the m_S=-1/2 to m_D=+1/2 transition as well as the resetting laser at 854 nm
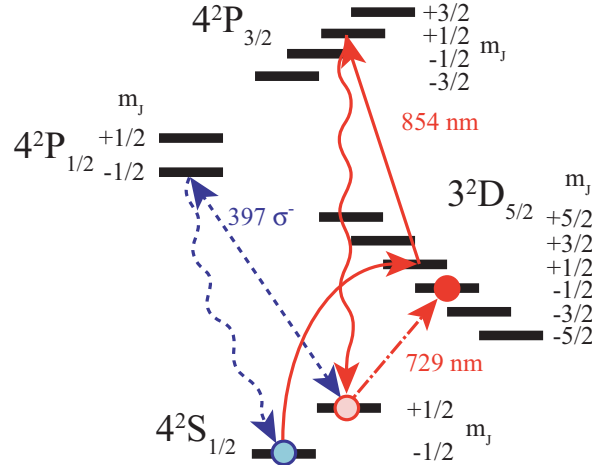
Figure 5.2: Involved levels in frequency resolved optical pumping. For testing, the ion was initialized in $|S, m_S = -1/2\rangle$ by pumping with σ^--light at 397 nm. Light resonant with the $|S, m_S = -1/2\rangle - |D, m_D = +1/2\rangle$ transition together with light at 854 nm pumps into the $|S, m_S = +1/2\rangle$ level. The remaining S-state population is probed after transferring the population from $|S, m_S = +1/2\rangle$ into the D-manifold by means of a π-pulse.

with its power set to "quench" the level i. e. shorten the effective lifetime of the $D_{5/2}$ state (solid lines). The laser pulses should pump the ion to the m_S=+1/2 state. Finally, we applied a π-pulse on the m_S=-1/2 to transfer the remaining m_S=-1/2 population to the $^2D_{5/2}$ level (dashed-dotted line). The following detection reveals how much of the population is in one of the $S_{1/2}$ levels. Fig. 5.3 shows the remaining $D_{5/2}$ state population as a function of the pumping time. The exponential fit yields a pumping constant of τ =86(3) μs. After an excitation time of 600 μs at least 99% of the population should have been pumped into the m_S =+1/2 state.

When the pumping time constant is plotted against the Rabi frequency as shown in Fig. 5.4, the pumping time is inversely proportional to Ω_R^2. This is expected since for low saturation the scattering rate of an atomic transition is proportional to $\frac{\Omega_R^2}{\Delta^2}$ [88]. It can be seen that optical pumping can be achieved within 100 μs but for higher laser power non-resonant excitations spoil the efficiency. That is most likely the reason for the rather large deviation from the fit for the two data points with the highest Rabi frequency. In order to avoid this effect we set the Rabi frequency to moderate $\Omega_R/(2\pi) \approx$ 20 kHz and with a pumping time of 1 ms we made sure that we were not limited by insufficient optical pumping.

5.3 Calibration of magnetic field coils

The magnetic field at the center of the trap can be adjusted by changing the current of mutually orthogonal coil pairs in Helmholtz configuration as shown in the inset of Fig. 5.5
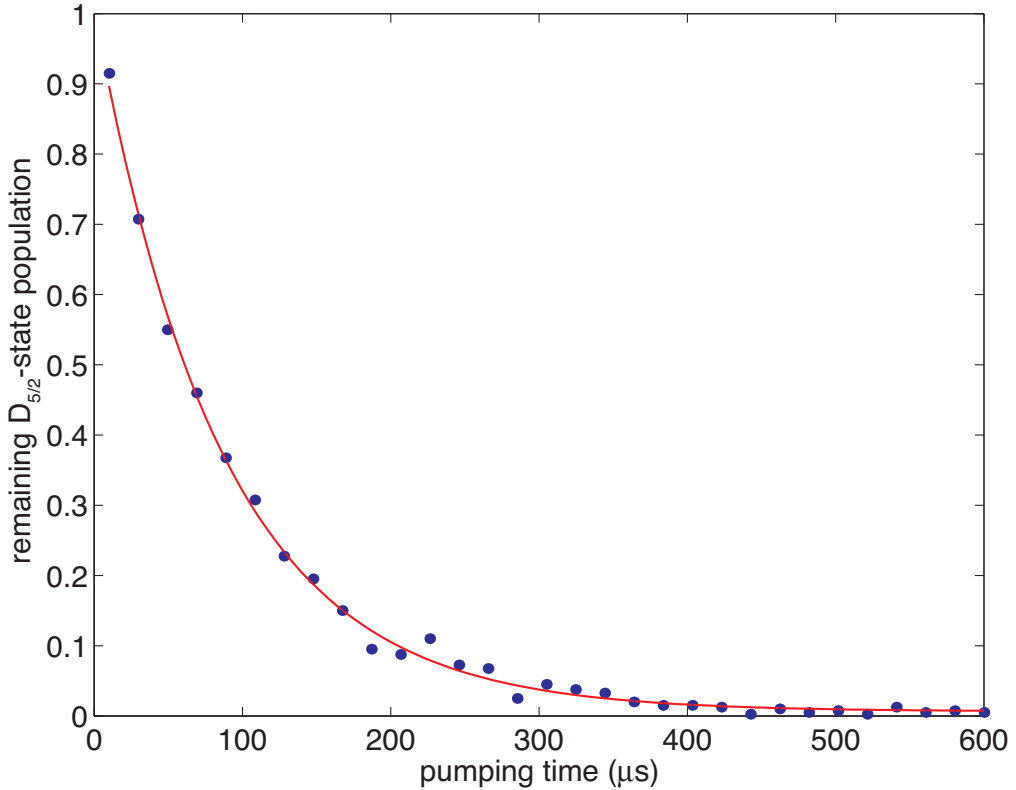
Figure 5.3: Frequency resolved optical pumping as a function of pumping time.

(see also Fig. 3.4) for the horizontal plane. The quantization field is mainly produced by the σ-coils ($C\sigma$) while the other two pairs (CD and Cz) are typically used to compensate the earth's and laboratory's bias fields. To achieve good optical pumping, sideband cooling on the quadrupole transition, and small AC Stark shifts due to neighboring Zeeman transitions, a magnetic field of 3 G is applied. The currently chosen geometry of the laser k-vector, laser polarization, and magnetic field favors transitions with $|\Delta m| = |m_D - m_S| = 0$ or 2. For this reason only six of the ten possible transitions have good coupling strength. During the measurement of the quadrupole moment of the $^2D_{5/2}$ level, however, measurements had to be carried out for various angles of the magnetic field. In order to maintain a certain field magnitude the magnetic field produced by the coils had to be calibrated.

The magnetic field $\vec{B} = \vec{B}_D + \vec{B}_\sigma$ is the sum of the individual fields produced by the Doppler ($\vec{B}_D$) and σ ($\vec{B}_\sigma$) coil pairs. By setting the current for one of the pairs to a particular value first and readjusting the other, one is able to find two alternative settings of the second current (positive and negative) where the total magnitude of the magnetic field $B = |\vec{B}|$ is the same. If a laser is resonant with a transition sensitive to the linear Zeeman effect for the given B, this can easily be probed.

77
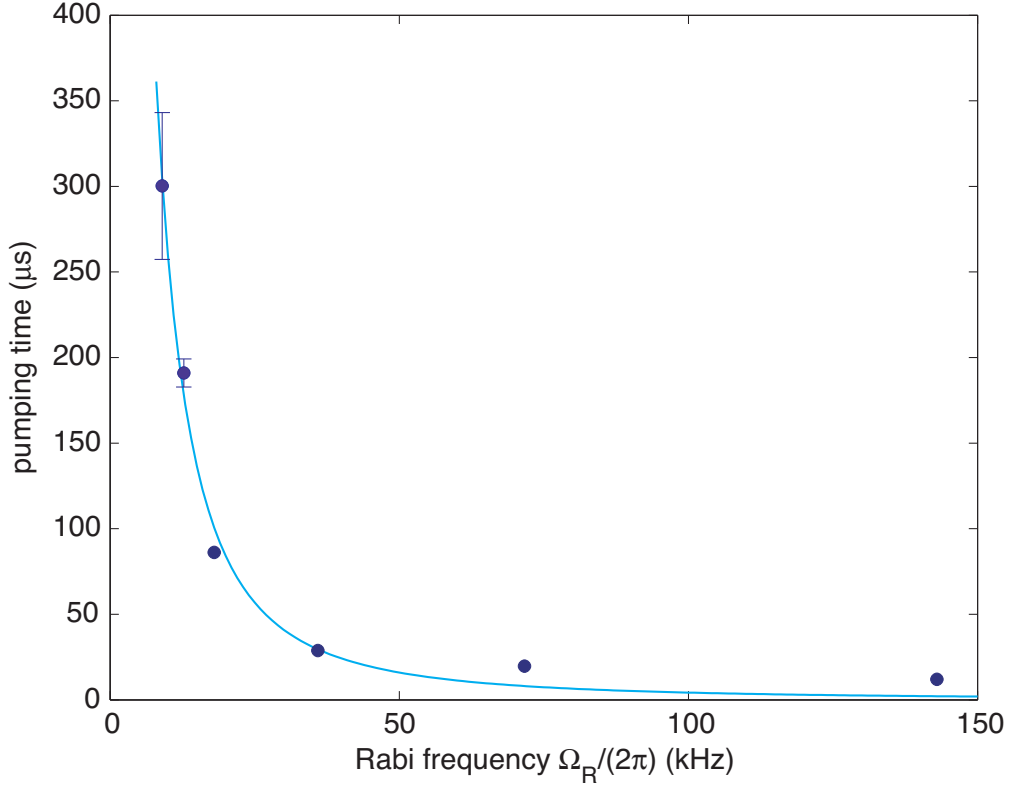
Figure 5.4: Optical pumping as a function of Rabi frequency Ω_R. The solid line is a fit that shows the pumping time is inversely proportional to Ω_R^2 as expected. The error bars are shown for data points where they are actually larger than the point size.

The calibration measurements were carried out on the $|m_S = -1/2\rangle - |m_D = -1/2\rangle$ transition at a fixed magnetic field magnitude of 2.957(1) G. The laser frequency was kept constant as described in Sec. 5.4.1. The excitation pulse lengths were ranging from $400\,\mu$s to $2\,$ms, depending on the excitation strength for the actual laser-magnetic field geometry. Apart from a constant laser frequency one has to make sure that the chosen value of the first coil current does not produce a magnetic field which is already larger than the desired magnitude. Figure 5.5 shows those values of the coil currents (I_σ, I_D) that brought the transition into resonance for the given magnetic field of 2.957(1) G. The magnetic field produced by these currents can be described by following equation:

$$B^2 = (I_D - I_{D,0})^2 \eta_D^2 \sin^2 \alpha + [(I_\sigma - I_{\sigma,0})\eta_\sigma + (I_D - I_{D,0})\eta_D \cos \alpha]^2 \,, \qquad (5.1)$$

where the conversion coefficients of current into magnetic field are given by $\eta_{D,\sigma}$ and bias fields (Earth's field and lab environment) are cancelled by offset currents $I_{D/\sigma,0}$. Here, α denotes the angle between the coil pairs which would be $90°$ in the ideal case. A fit using the data shown in Fig. 5.5 yielded bias currents of $I_{\sigma,0} = +58(1)\,$mA in σ and
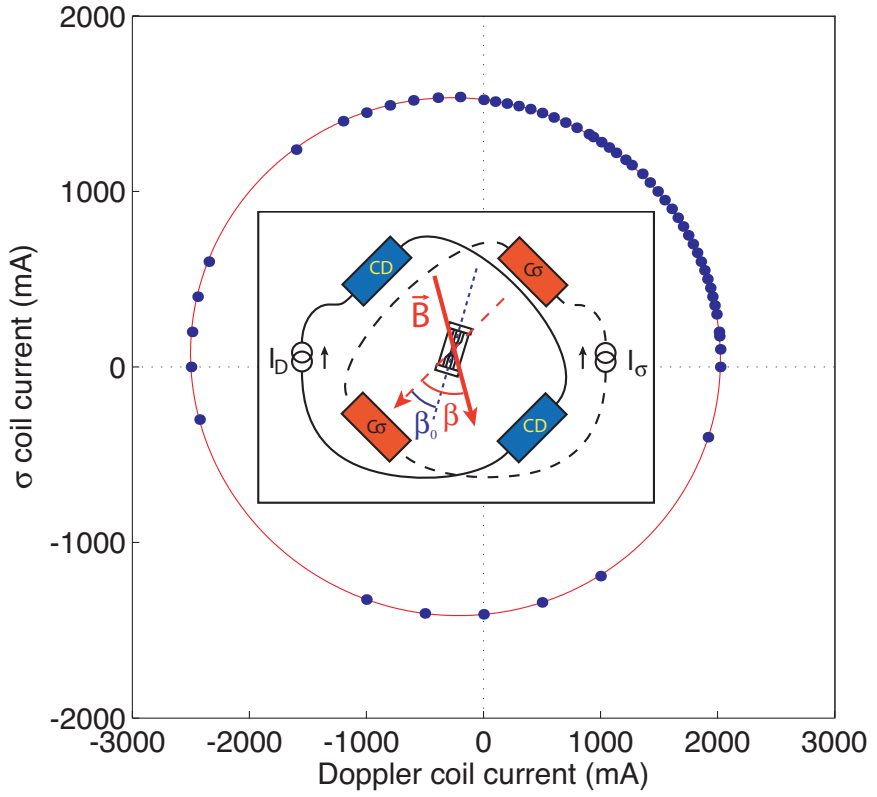
Figure 5.5: Calibration of the magnetic field. The measurement points show combinations of coil currents where a modulus of the magnetic field of 2.957(1) G is achieved. The inset indicates the configuration of magnetic field coils and the trap in the horizontal plane.

$I_{D,0}$ =-237(2) mA in Doppler direction. The conversion coefficients were determined to be $\eta_\sigma = 2.006(1)$ G/A and $\eta_D = 1.305(2)$ G/A, respectively. The angle between the coil pairs was fitted to be α =89.3(1)°.

The calibration of the coil currents finally allows for turning the magnetic field in the horizontal plane of the trap into any necessary direction according to

$$\begin{pmatrix} I_D \\ I_\sigma \end{pmatrix} = \begin{pmatrix} I_{D,0} \\ I_{\sigma,0} \end{pmatrix} + \begin{pmatrix} B\sin\beta/(\eta_D\sin\alpha) \\ (B\cos\beta - (I_D - I_{D,0})\eta_D\cos\alpha)/\eta_\sigma \end{pmatrix} \overset{\alpha\approx90°}{\approx} \begin{pmatrix} I_{D,0} + B\sin\beta/\eta_D \\ I_{\sigma,0} + B\cos\beta/\eta_\sigma \end{pmatrix},$$
(5.2)

where β denotes the angle between the axis of the σ-coil and the magnetic field as shown in the inset of Fig. 5.5. For the vertical direction the same method can be applied but since it is only necessary to keep the magnetic field in the horizontal plane only the bias field of the laboratory environment was compensated.

79

5.4 Ramsey experiments

At the heart of the absolute frequency measurement of the $4s\,^2S_{1/2}-3d\,^2D_{5/2}$ transition are Ramsey experiments to infer the detuning of the laser relative to the atomic transition. The method is named after Norman Ramsey who developed the technique for the interrogation of a beam of thermal atoms in a microwave oscillator to serve as an atomic clock [4]. The Ramsey method consists of two laser pulses $R_{1,2}(\theta = \frac{\pi}{2}, \phi)$ separated by a time τ_R. The first laser pulse of length τ with $\Omega\tau = \pi/2$ creates an equal superposition of ground and excited state. Then, the system is let alone for a free evolution during the Ramsey waiting time τ_R. In a rotational frame with respect to the transition frequency of the atom, the Bloch vector picks up a phase according to the frequency difference of the laser with respect to the transition. The second laser pulse projects the system back onto the measurement basis and the phase can be detected as a variation of the state population. Fig. 5.6
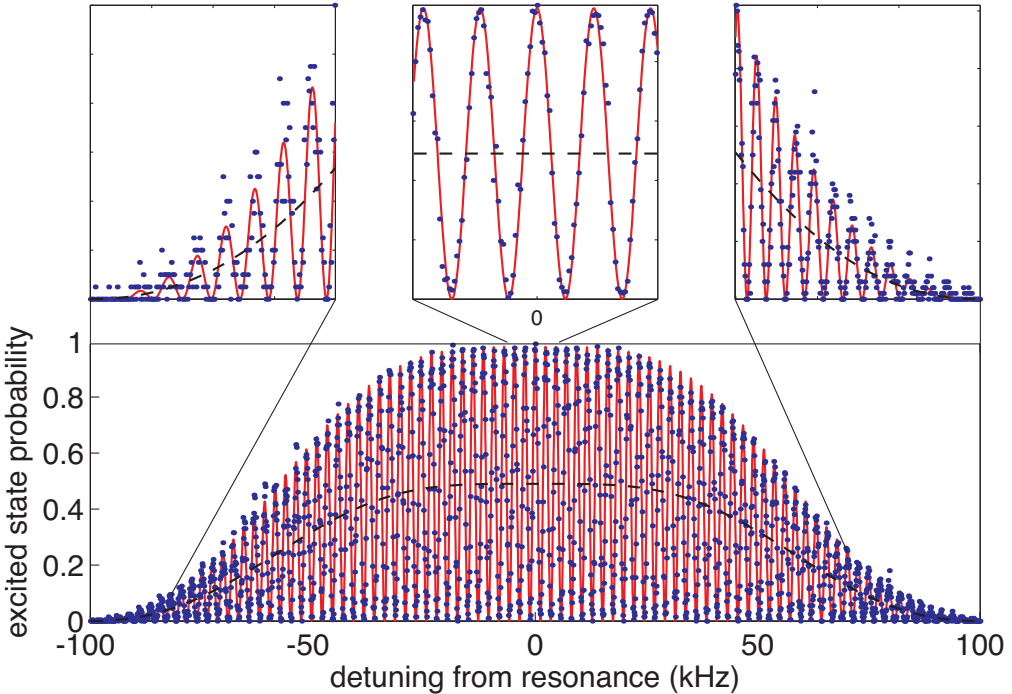
Figure 5.6: Ramsey pattern with an excitation pulse length of $9.7\,\mu s$ and a Ramsey waiting time of $\tau_R = 417\,\mu s$.

shows an experimental Ramsey pattern obtained on the $|S, m_S = -1/2\rangle - |D, m_D = -1/2\rangle$ transition with the laser frequency swept across the resonance over a range of $100\,kHz$. The actual data is indicated by the dots, the solid line is obtained directly from Eq. 2.47. The parameters for this scan were a pulse length of $9.7\,\mu s$, a relative phase $\phi = 0$ of the Ramsey pulses, and a Ramsey time of $\tau_R = 416.9\,\mu s$ which was the only fit parameter. Also shown in this plot as a dashed line is the underlying Rabi pedestal (Eq. 2.48). The insets

demonstrate the remarkable agreement between theory and experiment. The line center of such a Ramsey pattern in an atomic clock is usually measured by probing the transition at a detuning of ±half a fringe width around the central fringe. The goal is to get 50% excitation in both cases. At these points the sensitivity of the method to frequency errors is maximal. A difference in excitation probability yields information about the magnitude and sign of the frequency difference. In order to avoid lightshifts due to the interrogation laser at such a detuning, we use a slightly different method. Instead of red and blue detuning of the excitation pulses the relative phase ϕ of the two $\frac{\pi}{2}$ pulses gets switched by 90°. Two alternating phase settings $R_1(\frac{\pi}{2},0)\xleftrightarrow{\tau_R}R_2(\frac{\pi}{2},\frac{\pi}{2})$ and $R_1(\frac{\pi}{2},\frac{\pi}{2})\xleftrightarrow{\tau_R}R_2(\frac{\pi}{2},0)$ allow for a measurement at the line center and at the maximum of the sensitivity again. By this technique an error by an incorrectly set phase is cancelled. Ideally, the experiment should end up at an excitation probability of 50% for each setting if the laser is perfectly on resonance. An excitation difference provides information not only about the magnitude but also about the sign of the required frequency correction.
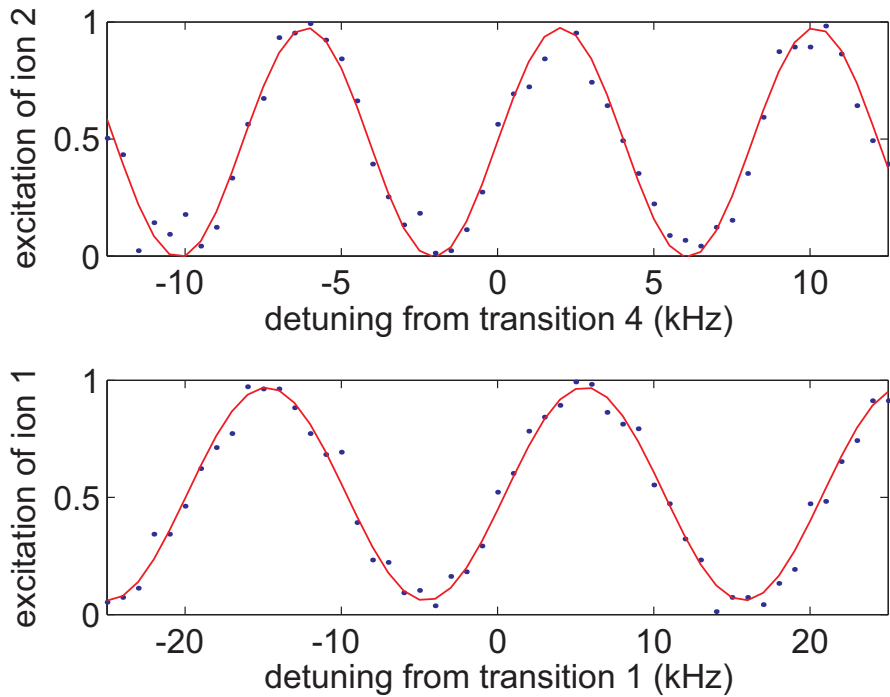
Figure 5.7: Ramsey patterns around the line centers of two interleaved, simultaneous Ramsey phase experiments on two different transitions of two ions detected with a CCD camera. (a) excitation time $\tau = 2.6\,\mu s$ and Ramsey waiting time $\tau_R = 123\,\mu s$, (b) excitation time $\tau = 2.6\,\mu s$ and Ramsey waiting time $\tau_R = 50\,\mu s$.

Fig. 5.7 shows detailed scans of the laser frequency for this technique around the line center of two different transitions. In this case the experiment was done on two ions

simultaneously. A Ramsey phase experiment on a transition from $|S, m_S = -1/2\rangle - |D, m_D = -1/2\rangle$ on ion 1 was sandwiched into another Ramsey phase experiment on $|S, m_S = +1/2\rangle - |D, m_D = +1/2\rangle$ on ion 2. Detection with a CCD camera provided information about the excitation of the individual ions. Such a scan can be used to infer the contrast of a particular transition which is necessary for the precise calculation of the frequency deviation from the center. For these scans the contrasts were 95(3)%.

5.4.1 Locking the laser to the $4s\ ^2S_{1/2} - 3d\ ^2D_{5/2}$ transition

The result of a Ramsey experiment yields information about the frequency difference of the interrogation laser with respect to a particular transition of ^{40}Ca$^+$ as was mentioned before. The individual transition frequencies of the $4s\ ^2S_{1/2} - 3d\ ^2D_{5/2}$ clock transition mainly depend on two parameters: the undisturbed center frequency of the transition ($\approx 4\times10^{14}$ Hz) and the (linear) Zeeman shift depending on the magnetic sub-levels involved ($\approx$1-12 MHz for a magnetic field of 3 G). The frequency of the laser is stabilized to the reference cavity which is subject to long-term drifts of the cavity length and therefore the laser frequency. A measurement of two transitions can be used to determine the current frequency difference of the reference cavity relative to the atomic line center, as well as the current strength of the magnetic field. By changing the frequencies that drive AOMs in the beam path of the laser, i. e. AO2 and AO4 in Fig. 3.1, the necessary frequency corrections can be applied. For our purpose, this model is a little bit too simple as it neglects the electric quadrupole shift, which is an interaction of the D$_{5/2}$-level with electric field gradients on the order of 10 Hz. The quadrupole shift cannot directly be determined by the measurement of two different transitions but enters the model as a fixed parameter and has to be determined beforehand. How this can be done is described in section 7.2. This simple model though neglects the quadratic Zeeman shift. Since both the electric quadrupole and the quadratic Zeeman shift are parabolic in the magnetic quantum number m_D of the excited state such a model can still lead to quite accurate predictions, provided the Landé g-factors are known well enough. In total, the quadratic Zeeman effect produces a systematic offset of the mean laser frequency from the transition's center. For a magnetic field of 3 G the offset is 2.5 Hz but since also the quadrupole shift is underestimated due to the quadratic Zeeman shift for the particular preparation measurement (-1.2 Hz deviation), the net shift is 1.3 Hz. On the other hand, the offset is completely irrelevant for the absolute frequency measurement because the laser frequency is continuously measured by the frequency comb and the applied RF frequencies and the measured frequency differences are recorded simultaneously and do not depend on the applied model.

The actual measurement procedure is explained in the following. From time to time, typically every couple of minutes, service measurements of a particular pair of Zeeman transitions are taken. A pair of Zeeman sublevels symmetric around the line center like transitions 1 and 4 ($|m_S = -1/2\rangle \leftrightarrow |m_D = -1/2\rangle$ and $|m_S = +1/2\rangle \leftrightarrow |m_D = +1/2\rangle$) is a good choice since their linear Zeeman effect cancels and quadrupole shift is the same. Together with precise knowledge of the g-factors, and the prediction for the quadrupole shift obtained in independent measurements, one can extract an effective current magnetic field
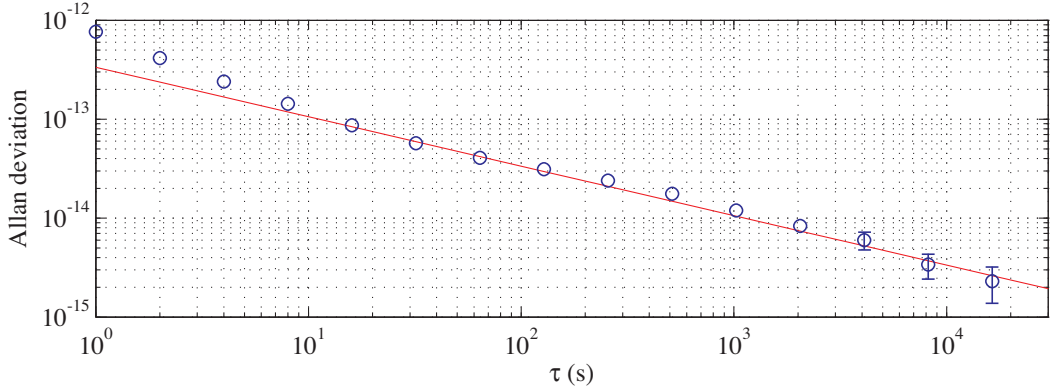
Figure 5.8: Allan standard deviation of the total frequency comb measurements.

and the current frequency difference between the reference cavity and the clock transition. Additionally, a quadratic fit to the history of these service measurements is used to predict the laser and magnetic field drift until the next service measurement. The laser frequency correction is applied to the radiofrequency synthesizer (Rohde & Schwarz SML01) driving the two double pass AOMs going to the reference cavity, while the magnetic field corrections are applied by adjusting the various transition frequencies for the AOM in the beam path to the ion trap. Additionally, the frequency synthesizer for the reference cavity can be phase continuously stepped in 0.1 Hz steps to compensate the cavity drift according to the fitted drift rate. Typical parameters for the absolute frequency measurement were a time interval of 23 s between the measurements and a history length of 10 minutes. This locking method is good enough to get rid of long term drifts as shown in Fig. 5.8 by the overlapping Allan deviation [119] of the laser frequency measured by the frequency comb over the whole measurement time. The red line is a fit with $3.1(1) \times 10^{-13} \tau^{-1/2}$. It is clear that the method is not optimized in any way to achieve the best lock of the laser to the ion as it would be necessary for an optical clock, but we regard the residual laser drift with $-2 \pm 600 \times 10^{-8}$ Hz/s still remarkable.

This simple model together with the measured contrasts, the quadrupole shift, and the Landé g-factors was good enough to probe the transitions near the line centers within their respective statistical errors. Histograms of the deviations from the predicted line centers for 455600 individual measurements are shown in fig. 5.9. The mean deviations from the predicted line centers were 0.1(3) Hz and 0.2(3) Hz for transitions 1 & 2, 0.3(3) Hz and -0.4(3) Hz for transitions 2 & 6, and -0.4(3) Hz and 0.4(4) Hz for transitions 3 & 5, where a large part of the error can be attributed to quantum projection noise (0.2 Hz). The rest is assumed to be due to fluctuations of the magnetic field and laser frequency noise.
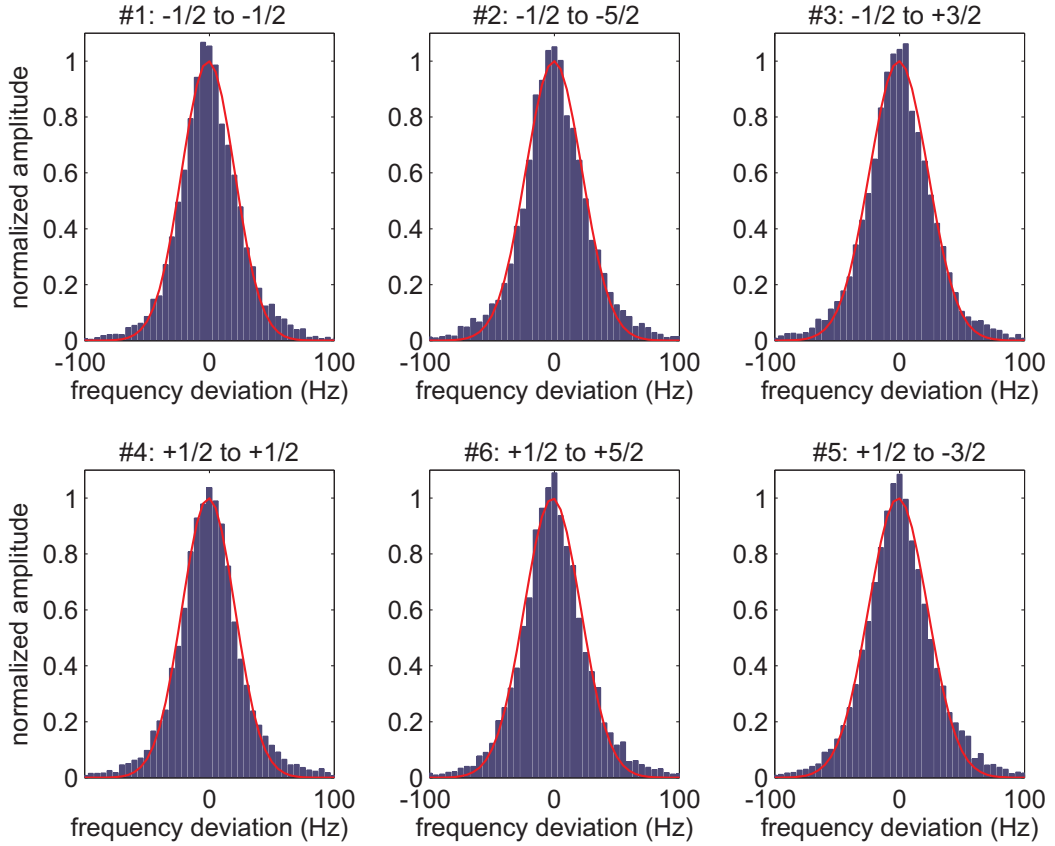
Figure 5.9: Histograms of the frequency deviations from the expected line centers. The maximum offset was 0.4(4) Hz.

5.5 Frequency and phase control of the 729 nm light

The radio frequency feeding the double-pass AOM for coherent manipulation of the $^{40}Ca^+$ ions with laser light at 729 nm is generated by a programmable pulse generator (PPG) developed as an open source project in collaboration with various groups. Documentation can be found in the thesis of Philipp Schindler [145]. For our experimental setup it consists of two direct digital synthesizers (DDS) for the frequency synthesis, a variable gain amplifier (VGA) for pulse shaping and amplitude control, and a digital-to-analog converter (DAC) for the conversion of the amplitudes into an analog voltage. The device has a frequency resolution of 0.18 Hz and digital phase control. It is capable of phase coherent and phase continuous switching.

The phase accuracy of the Ramsey pulses is extremely critical for Ramsey experiments where the phase of the pulses is switched. In the measurement scheme used for the absolute frequency measurement, the phase θ of the Ramsey pulses is switched by 90°. A phase error of only 1° would lead to a systematic shift of the Ramsey pattern by 2.8 Hz
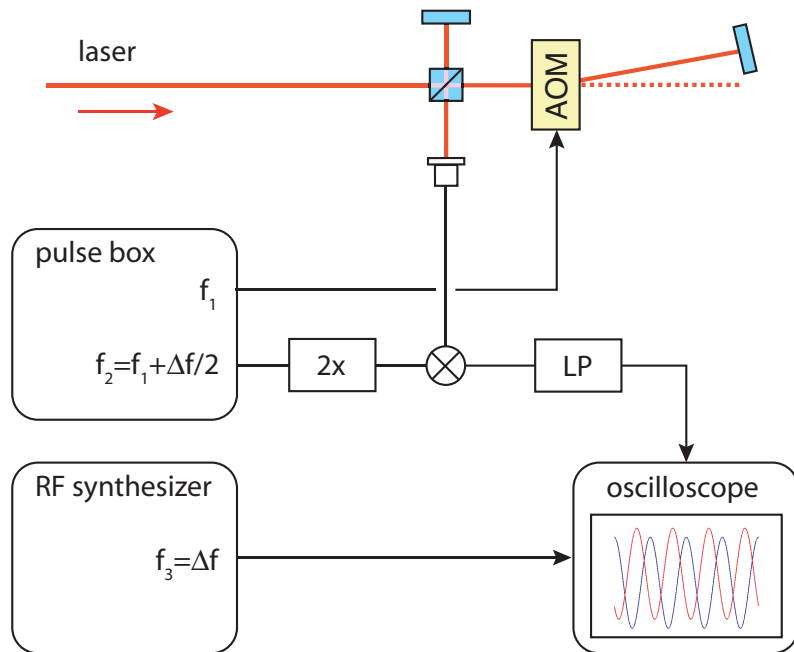
Figure 5.10: The setup for the investigation of a possible phase shift of the AOM due to the RF pulses.

for a pulse separation time of 1 ms. By repeating the Ramsey experiment with reversed pulse order, an error by a systematically incorrect setting is cancelled though. What's still important is the phase reproducibility because timing jitter of the PPG can lead to phase errors in spite of the fact that the phase register has 12 bit resolution. To fully profit from such a high resolution, this jitter would have to be smaller than 1 ps at typical operation frequencies around 270 MHz. In order to investigate this effect, a train of RF pulses with relative phase 0° and 90° was created, centered at 270 MHz and varied about the frequency range which was necessary to probe the individual Zeeman transitions for the absolute frequency measurement. The RF was mixed down[1] to 5 kHz with the second, phase stable output of the PPG. The output of the mixer was recorded with a fast oscilloscope[2] and sinusoidal functions were fitted to each pulse with variable amplitude, frequency, and phase. The phase reproducibility for 13,668 sets of pulses as it was used for the absolute frequency measurement of the $4s\,^2S_{1/2} - 3d\,^2D_{5/2}$ transition in this case was 0.003° which corresponds to a frequency uncertainty of 8 mHz at a Ramsey time $\tau_R = 1$ ms or 2×10^{-17} relative uncertainty for the absolute frequency measurement. The corresponding timing jitter is <3 ps.

There is another effect that could cause a systematic frequency shift if the AOM used for frequency and phase shifting of the laser beam would introduce phase shifts that are unequal for the first and the second laser pulse. Errors of this kind might arise because

---

[1] Minicircuits ZAD-1
[2] LeCroy WP7300A
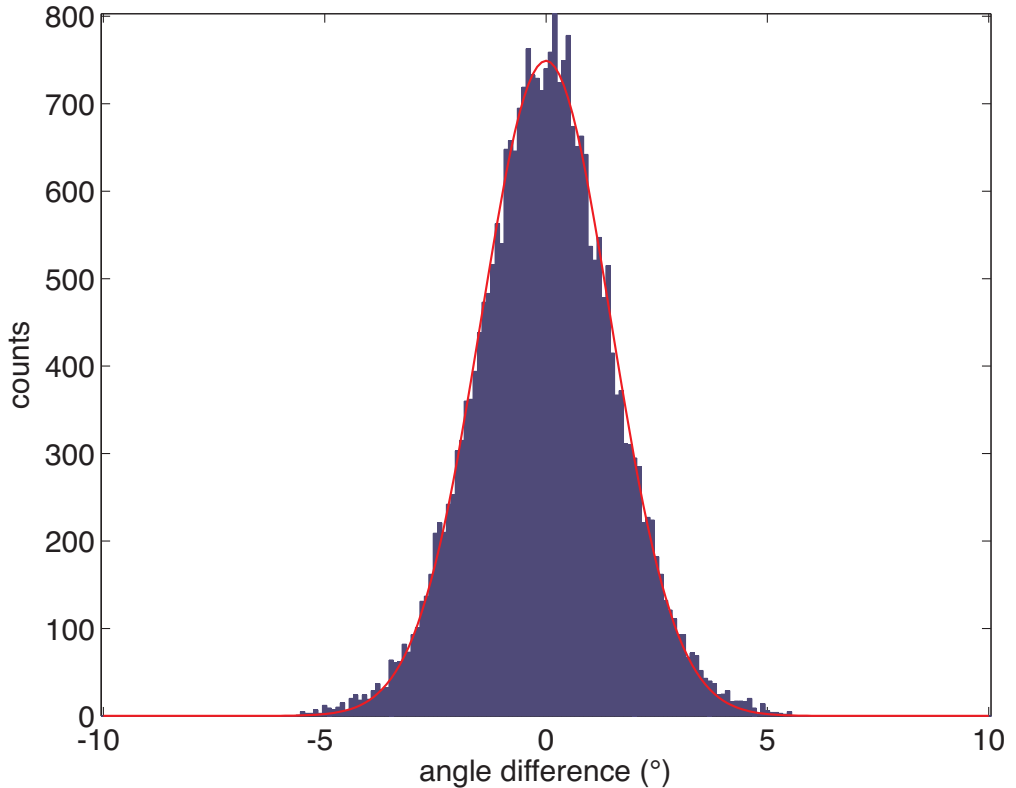
Figure 5.11: Investigation of a possible heating effect of the AOM. The histogram of 28,000 measurements is fitted by a Gaussian centered a 0° and a standard deviation (1-σ) of 1.6°. The relative phase change of two 50 μs long pulses separated by 100 μs therefore is 0.0001±0.009°.

of thermal effects in the device. For an investigation of this effect an interferometer comparing the light entering and coming out of the double pass AOM was built as shown in Fig. 5.10. The AOM was driven by pulses with similar length (49 μs) and power as it was used for the absolute frequency measurement and the beat note was detected with a fast photodiode[3]. Again, the signal was mixed down[4] to a lower frequency (5 MHz) by the second frequency output of the PPG with a fixed phase relation, low-pass filtered with 200 MHz 3dB-frequency[5] and finally compared to a third source at 5 MHz from a frequency synthesizer[6]. Both signals, the pulsed beat signal and the continuous reference at this

---

[3]MenloSystems APD210
[4]Minicircuits ZAD-1
[5]Minicircuits BLP-200
[6]Marconi 2023A

frequency were recorded with a fast oscilloscope[7] and multiplied on a computer. The mean values for the obtained beat signal frequencies and the fitted amplitudes of the original signals were used to calculate the corresponding phase. For 28000 experiments with a pulse length of $50\,\mu$s and a pulse separation of $100\,\mu$s the relative phase change was only $\Delta\theta =0.0001°\pm0.009°$. The phase change was also measured for pulse separations of $50\,\mu$s, $250\,\mu$s, $500\,\mu$s, and $1000\,\mu$s but for a smaller number of repetitions. The average phase change and the corresponding standard deviations were -0.05(7), 0.002(66), -0.14(12), and 0.14(8). This measurement was done to make sure that a possible phase change does not depend on the Ramsey time, at least not starting from a pulse separation of $50\,\mu$s. Especially for the longer Ramsey times the amount of collected data for the fixed resolution of $1\,$GS/s started to become large, and also interferometric stability was beginning to play a role, noticable in an increased standard deviation. For this reason the measurement statistics is worse than for the $100\,\mu$s data. Nevertheless, the thorough investigation of the relative phase shift at $100\,\mu$s allows for a reliable interpolation of the phase error to $1\,$ms and was reassured by the additional measurements at different waiting times. Moreover, the effect of differential heating - which is the most likely cause for a change in the optical path length - of the Ramsey pulses should be much worse at shorter pulse separation than is actually used in the experiment.

---

[7]LeCroy WP7300A

Chapter 6

Absolute frequency measurement of the $4s\ ^2S_{1/2} - 3d\ ^2D_{5/2}$ clock transition

Building an ion clock based on Ca^+ has the technological advantage that all necessary wavelengths for laser cooling and state manipulation including lasers for photo-ionization can nowadays be generated by commercially available diode lasers. In order to show that clocks based on Ca^+ ions are a suitable candidate for an optical ion clock, Ca^+ has to be compared against the Cs frequency standard on which the current definition of the SI second is based. In the first part of this chapter the absolute frequency measurement on $^{40}Ca^+$ ions will be presented which was performed when a transportable Cs fountain clock with an accuracy of $< 10^{-15}$ was present in our lab. The interrogation lasers probing $^{40}Ca^+$ and $^{43}Ca^+$ ions were compared against Cs through a frequency comb. The next part contains an analysis of the expected frequency shifts and presents the final result for $^{40}Ca^+$ with a detailed error budget. It represents the first absolute frequency measurement on Ca^+ at the level of 10^{-15}. Finally, a comparison of the $^{40}Ca^+$ results for different trap powers and a preliminary measurement of the isotope shift of $^{43}Ca^+$ are quickly discussed.

6.1 Spectroscopy on the $4s\ ^2S_{1/2} - 3d\ ^2D_{5/2}$ transition

There are two commonly used techniques of measuring the line center of an atomic transition:

- simple Rabi excitations, or

- Ramsey's method of separated fields.

In terms of frequency determination both schemes - Ramsey and Rabi excitation - are almost equivalent. Peik *et al.* [146] have investigated both schemes in consideration of building an optical clock with a single ion as reference and concluded that the Ramsey scheme can be slightly better (30% for optimal parameters) regarding the highest possible

stability. We have chosen the latter method for the following reason. Our initial goal was to perform spectroscopy with entangled states where Ramsey spectroscopy is the only choice. The Bell state preparation required individual addressing of the ions for which we used an electro-optical deflector (EOD). Unfortunately, the deflector induced significant phase errors on the order of 50 Hz when switching back and forth between the ions. Therefore we had to do the frequency measurement with a single ion and simply kept the measurement strategy in order to demonstrate that it actually is suitable for measurements in the 10^{-15} regime.
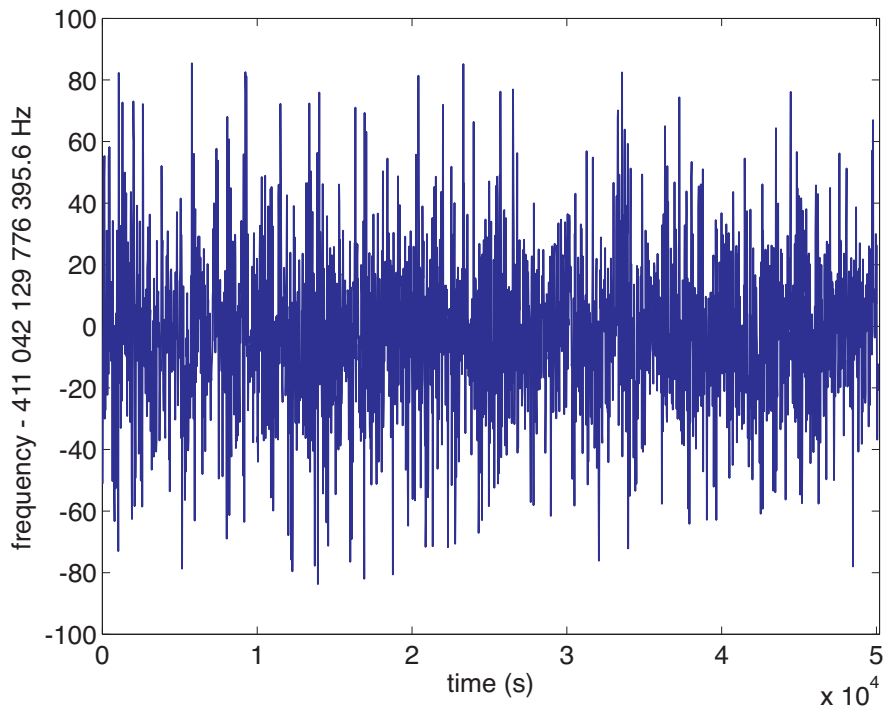
Figure 6.1: Total frequency measurement data at a trap power of 9 W: frequency comb readings combined with the ion trap data and the mean frequency of 411 042 129 776 395.6 Hz substracted.

The frequency measurement of the $4s\ ^2S_{1/2} - 3d\ ^2D_{5/2}$ transition consisted of probing the six transitions shown in Fig. 2.2 by Ramsey phase experiments and the simultaneous measurement of the probe laser's frequency by the frequency comb. The Ramsey phase experiments were done for a waiting time of $\tau_{Ramsey} = 1000\,\mu$s at the assumed center of the transition of interest calculated by the model discussed in the Sec. 5.4.1. The experiments with a cycle time for a single Ramsey phase experiment of 18 ms were repeated for 100 times to minimize the error by quantum projection noise. As a result these experiments yielded a stream of data containing the mean measurement time, the mean frequency for each transition, and a mean excitation difference of the two phase settings to calculate the
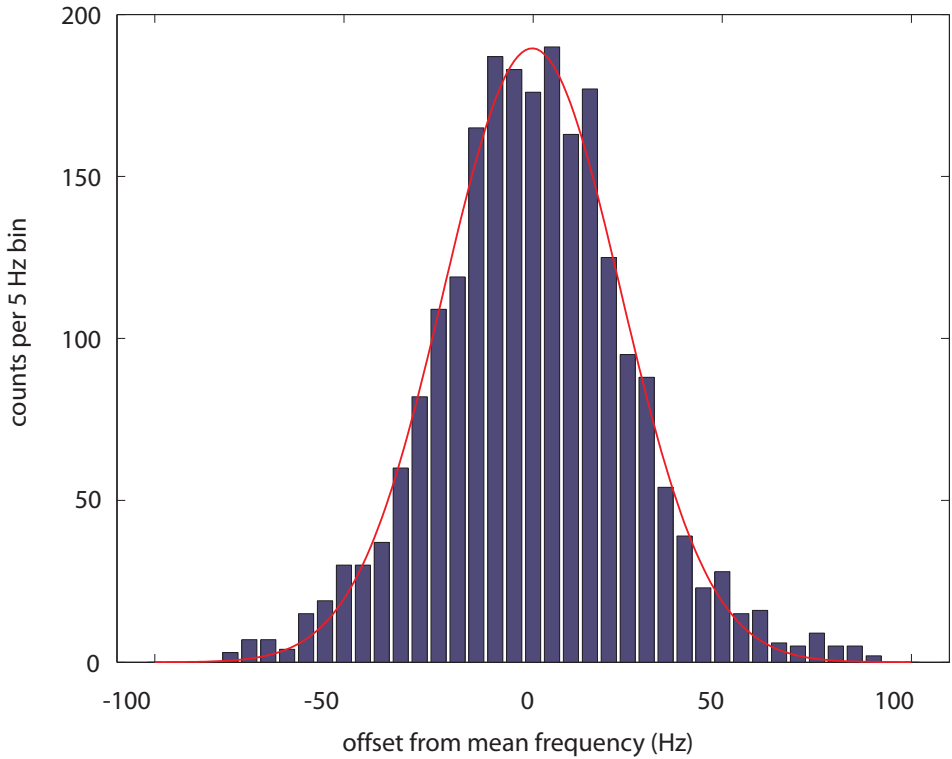
Figure 6.2: Histogram of the total frequency measurement data. It fits a Gaussian distribution with 23(1) Hz standard deviation shown as the solid line.

line center. In order to calculate the correct frequency deviations the contrast for each transition had to be calibrated. The calibration was frequently checked during periods where the frequency comb wasn't operating by scanning the phase of one of the Ramsey pulses and fitting a sinusoidal to the data. The mean values of the contrasts during the whole measurement time were $\{95(1)\%, 90(1)\%, 88(1)\%, 92(1)\%, 87(1)\%, 90(1)\%\}$ for the transitions $\{1, \ldots, 6\}$. The laser powers for the individual transitions were adjusted to get similar excitation times of $\tau \approx 54(5)\,\mu$s. These values were also checked every couple of hours and turned out to be constant to better than 6%. According to Eq. (2.53), that source of error is only important if the transition is probed detuned from the line center. The error for a 6% change of the Rabi frequency as was observed during the course of the absolute frequency measurement at 0.4 Hz maximum offset from the line center (see Sec. 5.4.1) leads to a frequency error of $\Delta\nu_{intensity} = 0.9\,$mHz only and is therefore negligible.

For the determination of the absolute transition frequency, the data of the ion trap experiment were combined with the frequency comb data for which the computers for data taking had to be synchronized. This was achieved by a program called Automachron[1]

---

[1] http://oneguycoding.com/automachron/
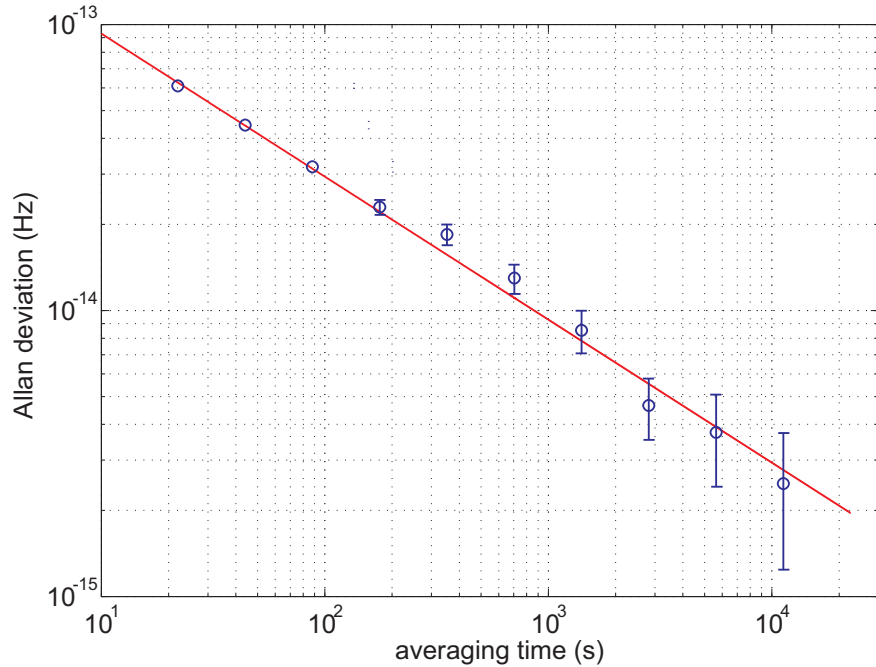
Figure 6.3: Allan standard deviation of the total frequency measurement data with statistical error bars. The solid line is a fit with $\sigma_y(\tau) = 2.9(1) \times 10^{-13} \ \tau^{-1/2}$.

which synchronized the internal clock of each computer with the signal of a time server provided by the University of Innsbruck[2] over internet. The synchronization could be checked by comparison of the individual log files so we can safely assume computers were synchronized to better than 0.1 s. Since the laser drift was compensated by our measurement and feedback scheme a timing error on this order of magnitude was not limiting us at this point. Valid data points for the optical frequency measurement where combined in the following way: The optical frequency measured by the comb was preprocessed. At first, obvious frequency errors due to events where the laser or the comb were out of lock were removed by setting a maximum allowed deviation from the median of a few kHz. Then, points with deviations of more than $3 \ \sigma$ different from the resulting mean value were rejected. The second ion trap experiment at IQOQI could be used to check the validity of the counter results as well by the method described in Sec. 4.3. The optical beat note of the two lasers at 729 nm was compared to a beat note obtained by the difference of the two optical frequencies measured by the comb. It provided an additional means of detecting cycle slips of the counters if the deviation of the two beat signals was larger than 0.5 Hz. The frequencies and frequency deviations calculated from the excitation differences using Eq. (2.52) of six consecutive Ramsey phase experiments for the transitions 1-6 were averaged together with the mean optical frequency obtained by the comb. If the

---

[2]time2.uibk.ac.at

frequency comb was producing valid data during 50% within that time window the data point was accepted and the frequency corrections for the Cs reference were applied. At the end remaining outliers were removed by rejecting points which were more than 3 σ different from the mean value.

Measurement result at a trap power of 9 W

A plot of the total frequency measurement data for a trap power of 9 W finally used to determine the ^{40}Ca$^+$ $4s\ ^2S_{1/2} - 3d\ ^2D_{5/2}$ transition frequency is shown in Fig. 6.1. It consists of 2278 combined measurements which had an acquisition time of 22 s each. A histogram of the deviations is shown in Fig. 6.2. The solid line is a Gaussian fit with a standard deviation of 23(1) Hz. The stability of the frequency measurement, however, is shown by the fractional overlapping Allan deviation [119] in Fig. 6.3. Here, the solid line is representing a fit with $\sigma_y(\tau) = 2.9(1) \times 10^{-13}\ \tau^{-1/2}$, suggesting white frequency noise as the dominant noise source. The expected Allan deviation from quantum projection noise was $\sigma_{QPN}(\tau) = 5.2 \times 10^{-14}\ \tau^{-1/2}$. The difference can be attributed to the lock of the frequency comb's repetition rate to the Cs clock. The final mean frequency of the $4s\ ^2S_{1/2} - 3d\ ^2D_{5/2}$ transition of ^{40}Ca$^+$ without correction for systematic shifts was determined to be 411 042 129 776 395.6(5) Hz.

Comparison of measurements at different trap powers

The frequency measurements were done at a trap power of 9 W. At this power the trap heats up to about 150°C. In order to check for systematic effects related to the trap temperature or the RF field we repeated the frequency measurements for a lower trap power of 3 W. Figure 6.4 shows the result of that comparison. The circles indicate the average frequency of the $4s\ ^2S_{1/2} - 3d\ ^2D_{5/2}$ transition accumulated over one day with their respective statistical uncertainties, the squares are the results for the reduced trap power on the last two measurement days representing a total of 456 individual measurements. The solid line is the mean value of all the 9 W-measurements which represents 2278 individual measurements with a precision shown by the dashed line.

The mean value of the $4s\ ^2S_{1/2} - 3d\ ^2D_{5/2}$ transition for the reduced trap power is 411 042 129 776 393.6(1.0) Hz. The mean values for the two power settings differ by 2 Hz with an error of 1.5 Hz. At this level, no significant difference is apparent as the expected frequency difference due to the change in black body radiation is on the order of -0.4(4) Hz. Taking this into account, the measured frequency difference at 3 W and 9 W is 1.6(1.6) Hz. The two frequency results are therefore still in agreement. Unfortunately, the limited operation time of the frequency comb did not allow for a systematic investigation of the transition frequency depending on the trap power for a long enough time in order to reduce the statistical error to make meaningful statements.
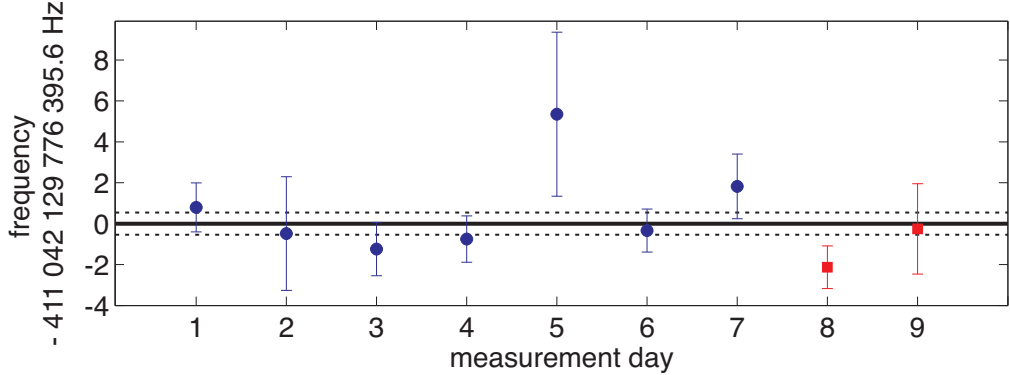
Figure 6.4: Mean values of the transition frequency on different days. The total average is marked by the solid line with the statistical uncertainty as dashed lines. The daily results at normal trap power are indicated by the circles, the average frequency at low trap power by the squares.

6.2 Systematic shifts

The great attraction of optical frequency standards lies in the superior resonance line quality factors allowing for higher stability and shorter averaging times. Another advantage is the low sensitivity to external perturbations and therefore higher accuracy. In the following section a summary of the most important systematic shifts for $^{40}Ca^+$ is given as well as an analysis of their repective uncertainties.

6.2.1 The Zeeman effect

The dominant shift of the $4s\ ^2S_{1/2} - 3d\ ^2D_{5/2}$ transition is caused by the Zeeman effect. The total nuclear magnetic moment of $^{40}Ca^+$ ions is zero, so there is no hyperfine structure. The two $4s\ ^2S_{1/2}$ ground, as well as the six $3d\ ^2D_{5/2}$ excited states, are shifted by the Zeeman effect in the presence of an external magnetic field. The linear frequency shift can be calculated by Eq. (2.67). The level shift of adjacent Zeeman levels is 2.8 MHz/G for the ground and 1.7 MHz/G for the excited state. There is also a small quadratic contribution from coupling of the $D_{5/2}$ sublevels with $|m_D| \leq 3/2$ to the $D_{3/2}$ level but it is rather small due to the fine structure splitting of 1.819 THz. The average shift over all six levels is $0.19\ Hz/G^2$, see Eq. (2.68).

Cancellation of the linear Zeeman shift

For a transition frequency measurement at the 10^{-15} level, it is necessary to have control over the Zeeman effect. By averaging the transitions 1-6 the linear dependence on the magnetic field completely cancels because they are symmetric with respect to the line

center. The error is limited by the number of measurements only. In order to calculate the statistical error for the data the individual AOM frequencies and the respective frequency deviations were used. The laser was locked to the ion by the method described above and its frequency can be regarded as constant over time. This is a valid assumption as demonstrated by the Allan standard deviation in Fig. 6.3. For the actual data we obtained a statistical error of $\pm 0.2\,\mathrm{Hz}$ for the averaged line center. The shot noise limit for an atomic clock using Ramsey's method the frequency error is given by [66]

$$\Delta\nu_{QPN} = \sqrt{p(1-p)}\frac{1}{\sqrt{N}}\frac{f_R}{\pi}, \tag{6.1}$$

where p is the excitation probability, f_R the Ramsey fringe spacing, and N the number of measurements. The total amount of data finally used for the absolute frequency determination was 2278 sets of measurements of all six transitions. For each set we repeated a single Ramsey phase experiment for 100 times and probed the transition twice with reversed phase to get rid of phase errors as mentioned before. This corresponds to a total number of measurements $N_{tot} = 2278 \times 100 \times 2 \times 6 =$ 2,733,600 at an excitation probability $p = 0.5$. The expected error from quantum projection noise therefore is $\Delta\nu_{QPN} \approx 0.1\,\mathrm{Hz}$. The experimental excess noise can be explained by line frequency noise of the magnetic field and laser frequency fluctuations.

Unfortunately, the magnetic field was not always constant. Probably due to temperature changes in the lab, the current for the magnetic field coils was slowly changing, resulting in an average magnetic field drift of $2(1)\ 10^{-8}\,\mathrm{G/s}$. This led to a measurement offset of $28(14)$ mHz because this effect is not completely canceled by averaging of the six transitions without changing their order.

Measurement of the $\mathrm{g}_{5/2}$-factor

The measured transition frequencies 1-6 and the frequency deviations can be used to calculate the Landé $\mathrm{g}_{5/2}$-factor of the $\mathrm{D}_{5/2}$ level, provided the g-factor of the $\mathrm{S}_{1/2}$ level is precisely known. For a prediction of the transition frequencies with sub-Hertz precision in the presence of a magnetic field of a few Gauss, the g-factors have to be known to better than 10^{-7}. Also, here it was sufficient to use the spectroscopic data only because the laser frequency was constant as the laser was locked to the ion. Three transitions starting from one Zeeman ground state and one from the other ground state form a system of equations with three free parameters that can be determined unambiguously: the magnitude of the magnetic field B, the quadrupole shift q, and the g-factor $g_{5/2}$. The necessary g-factor of the $\mathrm{S}_{1/2}$ ground state has been measured by Tommaseo et. al. [98] with 10^{-8} accuracy. Using two different combinations of transitions increases the measurement statistics. Transition frequency differences are defined as

$$f_{ij} = f_i - f_j. \tag{6.2}$$
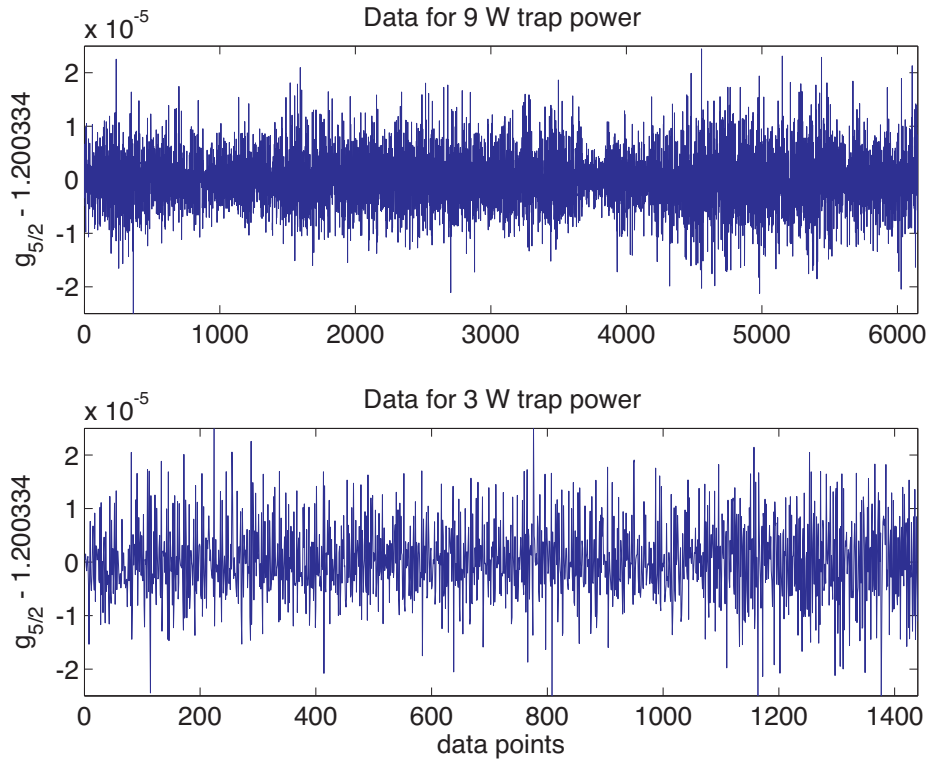
Figure 6.5: The measured g$_{5/2}$ value for two sets of transitions (see text).

Transition set 1 consists of $\{f_{12}, f_{31}, f_{41}\}$, set 2 of $\{f_{45}, f_{64}, f_{41}\}$. The equation system for the first set then is:

$$f_{12} = \frac{6}{25}\frac{(\mu_B B)^2}{h^2 \delta_{FS}} + 2g_{5/2}\frac{\mu_B B}{h} + \delta_q(1,2),$$

$$f_{31} = -\frac{2}{25}\frac{(\mu_B B)^2}{h^2 \delta_{FS}} + 2g_{5/2}\frac{\mu_B B}{h} + \delta_q(3,1),$$

$$f_{41} = (g_{1/2} + g_{5/2})\frac{\mu_B B}{h},$$ (6.3)

and for set 2 it is

$$f_{64} = -\frac{6}{25}\frac{(\mu_B B)^2}{h^2 \delta_{FS}} + 2g_{5/2}\frac{\mu_B B}{h} + \delta_q(6,4),$$

$$f_{45} = \frac{2}{25}\frac{(\mu_B B)^2}{h^2 \delta_{FS}} + 2g_{5/2}\frac{\mu_B B}{h} + \delta_q(4,5),$$

$$f_{41} = (g_{1/2} + g_{5/2})\frac{\mu_B B}{h},$$ (6.4)

where $\delta_q(i,j)$ denotes the difference of the quadrupole shifts of individual transitions i, j. Using the data for an RF trap power of 9 W and both sets of transitions, the Landé g-

factor of the $D_{5/2}$ level is then $g_{5/2} = 1.2003340 \pm 2.5 \times 10^{-7}$, where the error comes from an assumed frequency error on the transitions of $1\,\text{Hz}$ while the statistical error is on the order of 10^{-8}. The result for the data taken at a RF trap power of $3\,\text{W}$ yields a consistent result of $g_{5/2} = 1.2003342 \pm 2.8 \times 10^{-7}$. A plot of the deviations from 1.200334 of the measured g-factors for the $9\,\text{W}$ and $3\,\text{W}$ data is shown in Fig. 6.5.

2nd-order Zeeman shift

Coupling of the inner Zeeman levels of $D_{5/2}$ to the $D_{3/2}$ levels is responsible for a small quadratic frequency correction on the order of a few Hz. It can be calculated by using second-order perturbation theory. The average magnetic field during the frequency measurement was $3.087(2)\,\text{G}$. The $|m_D = 3/2|$ levels were shifted by $1.642(2)\,\text{Hz}$, the $|m_D = 1/2|$ levels by $2.462(3)\,\text{Hz}$ while the outer levels were unaffected. These shifts are not symmetric around the baseline at zero magnetic field and therefore are not cancelled by our measurement technique. The total shift averaged over transitions 1-6 is $1.368(2)\,\text{Hz}$ which is actually the largest shift in the whole error budget. But for the given uncertainty of the magnetic field and the large fine structure splitting ($1.8196\,\text{THz}$) the error is only $2\,\text{mHz}$ or 5×10^{-18} in relative uncertainty.

There is also a contribution from the non-zero mean-square magnitude of the magnetic field from black body radiation (see Eq. (2.70)) but this effect is small compared to the shift by the quantization field. The magnetic black body shift, which is maximum for the $m_D = \pm 1/2$ levels, is $1\,\text{mHz}$ only at a temperature of $150°\text{C}$. Taking into account that most of the surrounding environment ($\sim 2/3$) of the ion is at room temperature, the relative shift and the relative uncertainty are on the order of 10^{-18} and below.

6.2.2 Electric quadupole shift

The electric quadrupole moment of the $D_{5/2}$ levels couples to static electric field gradients caused by either the DC-trapping fields and possible spurious field gradients of patch potentials. For axial confinement we applied a voltage of $1000\,\text{V}$ to the tips of our trap creating a static electric field gradient of $25\,\text{V/mm}^2$. This led to shifts of $\Delta\nu_Q = Q\,(3\,m_J^2 - J(J+1))$ where $Q \approx 1.15(3)\,\text{Hz}$ was the shift at this particular field gradient and orientation of the quantization axis. But the effect completely cancels when averaging over all transitions [23] because the shift for $m_D = \pm 5/2$ is equal to the combined shifts of $m_D = \pm 3/2$ and $m_D = \pm 1/2$ which have opposite sign. Similar to the linear Zeeman effect the error is determined by the statistical error of the sum of the measurements. Therefore, the electric quadrupole shift cancels with $\pm 0.2\,\text{Hz}$ and a relative uncertainty of 5×10^{-16}. The individual measured shifts were $10.1(3)\,\text{Hz}$ for the $|m_D = \pm 5/2\rangle$ states, $-2.0(3)\,\text{Hz}$ for the $|m_D = \pm 3/2\rangle$ states, and $-8.2(2)\,\text{Hz}$ for the $|m_D = \pm 1/2\rangle$ states.

In order to take the effect into account when predicting the individual transition frequencies, the quadrupole shift parameter Q had to be measured beforehand. The method designed to extract the quadrupole shift will be described in the next chapter. As a result it led to $Q = 0.98(1)\,\text{Hz}$. The result does not take the quadratic Zeeman effect into

account. At a mean magnetic field of 3.100(1) G, the corrected value was $Q = 1.05(1)$ Hz. Alternatively, the transition frequency data can be used to calculate the quadrupole shift. It is one of the three parameters determined by the set of Eqs. (6.3). The result was $Q = 1.15(3)$ Hz and is in reasonable agreement with the shift obtained from the previous measurement.

6.2.3 AC Stark shifts

All laser beams have to be switched off during the waiting times of a Ramsey experiment in order to avoid AC Stark shifts caused by laser light. In our experiment, this can be done by switching off the RF sources of AOMs used for detuning the individual lasers. Since this cannot be done perfectly, the residual light fields coming from stray light and incompletely switched off RF are expected to cause AC Stark shifts. Additionally, micromotion and black body radiation from the environment can also be responsible for frequency shifts.

Light at 729 nm

The AC Stark shift caused by the probe laser has been thoroughly studied in our experiment [147]. The result of this investigation is summarized by the following equation:

$$\Delta\nu_{729}^{AC} = \frac{\Omega_R^2}{8\pi}\left(2b - \frac{a_{\pm 5/2}}{\Delta_{\pm 5/2}} - \frac{a_{\pm 1/2}}{\Delta_{\pm 1/2}} - \frac{a_{\mp 3/2}}{\Delta_{\mp 3/2}}\right), \tag{6.5}$$

where Δ_i denotes the detuning from the transition $|m_S\rangle = \pm 1/2 - |m_D = i\rangle$ and b the coupling to far detuned dipole transitions. Please note, that Eq. (6.5) is only valid for the chosen geometry of magnetic field, laser polarization, and k-vector and also other transitions of the Zeeman mulitplet have to be taken into account. The coefficients a_i are the squared relative coupling strengths from Tab. 2.1 and the dipole contribution has been measured to be $b = 0.112(5)/(2\pi)$ MHz^{-1}.

There are two contributions of probe light to the Stark shift during the probe time of a Ramsey experiment. The first is simply the leakage of 729 nm light when the double pass AOM is switched off. This light has a detuning of $\Delta/(2\pi) = 540$ MHz with respect to the $S-D$ transition. In the case of the absolute frequency measurement, a residual background light of 0.7(1) nW was measured. Compared to the light level of 7.4 µW necessary for a Rabi frequency of $\Omega_R/(2\pi) = 8.3$ kHz on the $|m_S\rangle - |m_D = -1/2\rangle$ transition, a shift of 34(1) mHz can be expected. The second part of the Stark shift stems from the fact, that the condition $\tau \ll \tau_R$ is not fulfilled well for our parameters. This means, the phase picked up during the Ramsey experiment (see Eq. (2.54)) is modified by an additional component equal to the product of the effective pulse time $\tau\frac{4}{\pi}$ from Eq. (2.49) and the corresponding Stark shift calculated from Eq. (6.5). Taking Eq. (2.54) and using a pulse time of 54(5) µ, the shift amounts to 80(4) mHz. The total shift by light at 729 nm then is $\Delta\nu_{729}^{AC} = 0.11(4)$ Hz which corresponds to 2.7×10^{-16} relative uncertainty for the absolute frequency measurement.

Light at 854 nm

The laser at 854nm is used to quench/reset the $^2D_{5/2}$ level. It it is sent through a double pass AOM which can be attenuated by 70 dB to compensate for reference cavity drifts. Unfortunately, there might still be some light leaking through. At normal experimental conditions, the residual light level is below the sensitivity of our power meter. Since this light acts on the $D_{5/2} - P_{3/2}$ dipole transition, it may cause considerable light shifts. There are two possibilities, either:

- the light is coming from the AOM's zeroth order by not completely blocking the light, or

- the light is near resonant due to insufficient switch-off of the RF.

In order to distinguish between these effects we performed two measurements. The first experiment was to investigate the effect of zero-order light. Therefore, we had to deliber-
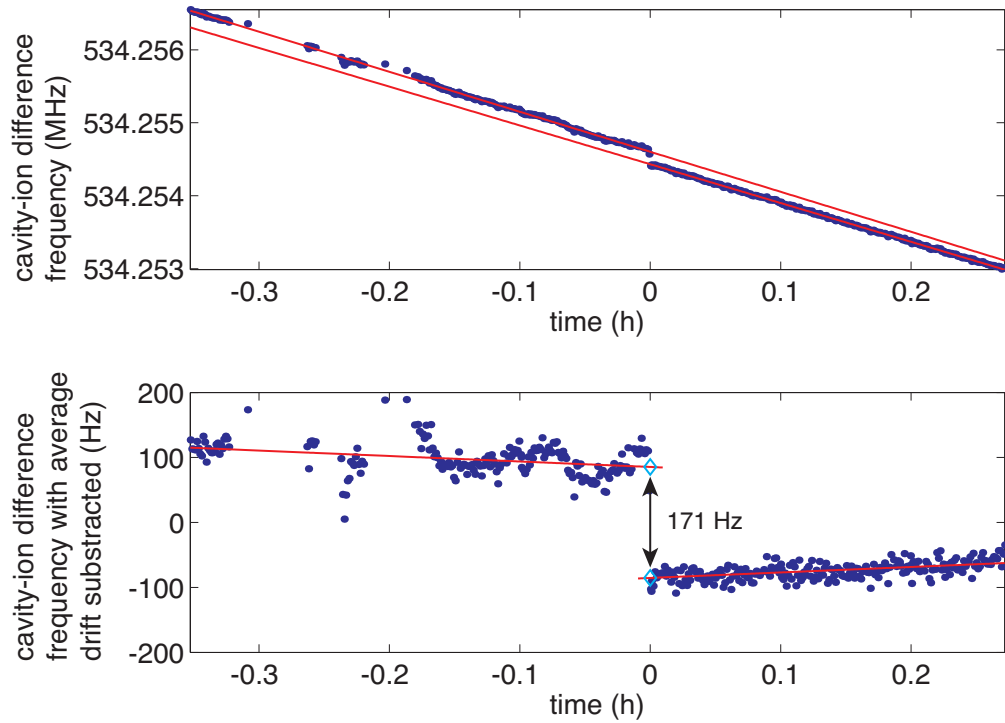
Figure 6.6: Effect of off-resonant light at 854 nm with a detuning of 200 MHz on locking the probe laser to the atomic transition. A jump in the frequency difference of the reference cavity and the ion is visible when the light is blocked at a certain time. The average drift has been substracted for the lower graph.

ately send a given amount of the zeroth order light to the ion to detect a measurable shift and extrapolate to the level at normal operating conditions. We locked the laser to the ion with $3.4(1)\,\mu W$ of zero-order light arriving at the experiment table and let the lock

settle down for about 20 minutes to get a reliable signal of the cavity drift due to slowly changing Stark shifts. We then blocked the light and observed a jump of the cavity-ion difference frequency. Again, we then continued measuring for 15 minutes to measure the frequency drift. We used linear fits for each data set to measure a shift of -170(40) Hz when the light was blocked as shown in Fig. 6.6. The power meter reading at normal operation was 0.1 nW, which was limited by background light. Therefore, the expected shift for zero-order light is -5(2) mHz.

The second experiment was a measurement of the lifetime of the $^2D_{5/2}$ state. The presence of near-resonant light would result in a reduction of the lifetime due to scattering events. The ion was initialized in the $|S, m_S = -1/2\rangle$ state and transferred into the
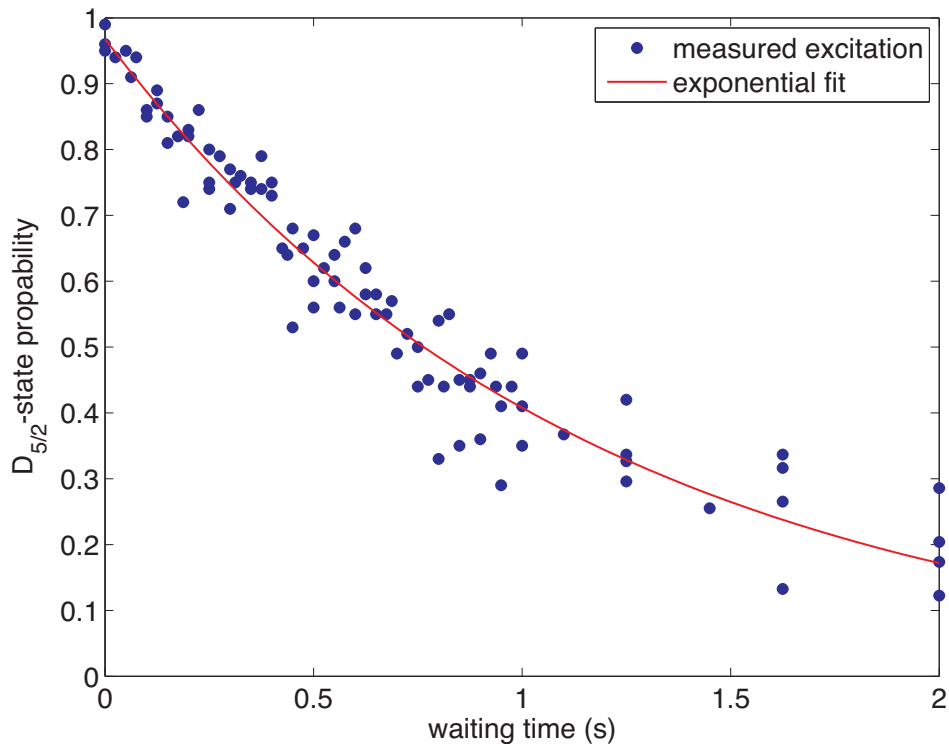
Figure 6.7: A lifetime measurement of the metastable $D_{5/2}$-state yields a decay constant of 1.16(4) s.

$|D, m_D = -1/2\rangle$ level by a π-pulse resonant with this transition. After a variable waiting time the remaining D-state population was detected as shown in Fig. 6.7 (points). An exponential fit (solid line) yielded a lifetime of 1.16(4) s which is within the errorbars identical to the lifetime measured by [148, 149]. In other words, there is no observable reduction of the D-state lifetime. The error of the lifetime can be used to set a limit on the possible scattering rate of 0.03(1) /s caused by the unwanted light. The corresponding

shift according to Eq. (2.31) would be $2\,\text{mHz}$ so that the total shift for light at $854\,\text{nm}$ is $\Delta\nu_{854} = 5(4)\,\text{mHz}$ with 1×10^{-17} relative uncertainty.

Light at 866 nm

The shift by the repumping laser at $866\,\text{nm}$ is estimated by making the following assumptions: the residual amount of light which could be detected by the power meter $(0.1(1)\,\text{nW})$ is tightly focused onto the ion. We assume a beam waist of $15\,\mu\text{m}$ which is probably much tighter than in reality. The corresponding shift on the $D_{5/2} - P_{3/2}$ transition using Eq. (2.31) and the decay rate from [75] is below $10\,\text{mHz}$. For light intensities similar to the light level at $854\,\text{nm}$ we expect a shift of much less than $20\,\mu\text{Hz}$. The shift can safely be estimated to be $\Delta\nu_{866} = 0(10)\,\text{mHz}$ with 2.4×10^{-17} fractional uncertainty.

Light at 397 nm

The shift by the laser at $397\,\text{nm}$ on the cooling transition can be estimated by a worst-case scenario: the residual amount of light is assumed to be focused onto the ion with a detuning of half a linewidth where the shift would be maximum. The light from the laser can be switched off in two ways. First, there is a double-pass AOM on the laser table and single-pass AOMs on the experiment table for each branch (optical pumping and cooling). The maximum amount of light detected in front of the vacuum window was $0.3\,\text{nW}$ and the attenuation factor of the double-pass AOM could be measured to be better than 10^5. At a beam waist of $15\,\mu\text{m}$ the worst case shift would be $0.1\,\text{Hz}$. Since the residual light is probably scattered light from all kinds of surfaces like AOM crystals, lenses, beam cubes, etc. while the RF sources are switched off pretty well ($>80\,\text{dB}$) it is likely to be detuned by $3\times80\,\text{MHz}$. This would cause a shift of only $4\,\text{mHz}$. The total shift for light at $397\,\text{nm}$ is then $\Delta\nu_{397} = 0.004(0.1)\,\text{Hz}$ and a relative uncertainty of 2.4×10^{-16}. Furthermore, extremely long coherence times exceeding $30\,\text{s}$ of a Bell-state consisting of the two ground states $\left|S_{1/2}, m_S = -1/2\right\rangle$ and $\left|S_{1/2}, m_S = -1/2\right\rangle$ could be demonstrated with this apparatus [150]. From that measurement an average photon scattering rate of one in 8 minutes could be estimated, indicating that the error mentioned above can be considered as a conservative estimate.

Black body radiation

The largest uncertainty in the error budget however, stems from the AC Stark shift induced by black body radiation. The ion is exposed to thermal fields emanating from the surrounding vacuum vessel at room temperature and the ion trap which gets heated up by the applied RF power. The mean-square of the frequency-dependent electric field emitted by a black body at temperature T is given by [151]

$$\langle E^2(t)\rangle = (831.9 \text{ V/m})^2 \left(\frac{T}{300 \text{ K}}\right)^4. \tag{6.6}$$

The total black body radiation shift can be calculated as the difference between the shifts of the individual levels involved. The static scalar polarizabilities of the $S_{1/2}$ and $D_{5/2}$

states are taken from [152], that is $\alpha_0(4S_{1/2}) = 76.1(1.1)4\pi\epsilon_0 a_0^3/h$ and $\alpha_0(3D_{5/2}) = 32.0(1.1)4\pi\epsilon_0 a_0^3/h$, respectively. There is also a tensorial part [24, 91] for the D level, but this contribution is averaged out if the thermal radiation field is isotropic, or as in our case, if all sublevels with the tensorial contribution are measured similar to the cancellation of the electric quadrupole shift. Therefore, the blackbody radiation shift can be written as

$$\Delta\nu_{BBR} = -\frac{1}{2h}\langle E^2(t)\rangle(\alpha_0(3D_{5/2}) - \alpha_0(4S_{1/2})). \tag{6.7}$$

The actual trap temperature as a function of the applied RF power can only be roughly estimated with the help of the test setup mentioned in Sec. 3.2.2. At the input power of 9 W that was applied for the frequency measurement, the trap heats up to about 150±50 °C. The trap only covers about one third of the total solid angle while the rest is covered by the surrounding vacuum vessel at a temperature of 25±2 °C. Using Eqs. (6.6) and (6.7) and taking into account both contributions and their respective solid angles, we estimate the black body shift to be $\Delta\nu_{BBR} =$0.9(7) Hz with a fractional uncertainty of 1.7×10^{-15}. The uncertainty has two main contributions, the first being the 50% uncertainty in the solid angle and the already discussed estimation of the temperature.

Micromotion and thermal motion

Thermal secular motion and excess micromotion cause the ion to be exposed to non-zero mean-square electric fields from the trap. The resulting Stark shift for excess micromotion can be calculated by [82]

$$(\Delta\nu_S)_{micro} \simeq 2\alpha_0 \left(\frac{2M\Omega_T}{ek\cos\phi_k}\right)^2 \frac{R_1}{R_0}, \tag{6.8}$$

with the ratio of the micromotion sideband powers $\frac{R_1}{R_0} = \frac{J_1^2(\beta_{micro})}{J_0^2(\beta_{micro})}$, the angle between the micromotion and the incident light ϕ_k, the mass of the ion M, and the Stark shift rate α_0 [152] from the section above. Typically, we achieve micromotion compensation with modulation indices $\beta_{micro} < 0.004$ in both directions. In the limit $\beta_{micro} \ll 1$, the power in the micromotion sidebands can be expanded in terms of the modulation index

$$\frac{R_1}{R_0} \approx \left(\frac{1}{2}\beta_{micro}\right)^2. \tag{6.9}$$

Using Eqs. (6.8) and (6.9) and assuming $\beta_{micro} = 0.004(\pm0.1)$, the expected Stark shift due to micromotion therefore becomes $(\Delta\nu_S)_{micro} =$0.2 mHz. Again, the tensorial contribution is averaged to zero by the measurement of all $3D_{5/2}$ levels.

We hardly have to correct the compensation voltages on a time scale of months. Therefore it is safe to assume an error of well below 0.1 for the modulation index. An estimate of the expected uncertainty is then <125 mHz, given that the direction is not well known ($73°\pm10°$). The relative uncertainty of this contribution to the error budget is 3×10^{-16}.

The Stark shift contribution of the thermal motion can be calculated by [101]. For a Doppler cooled $^{40}\mathrm{Ca}^+$ ion ($T \approx 0.5\,\mathrm{mK}$), the expected shift

$$(\Delta\nu_S)_{thermal} = \alpha_0 \frac{3M\Omega_T^2 k_B T}{e^2}, \tag{6.10}$$

is on the order of $1\,\mathrm{mHz}$ so that the total Stark shift due to motion is clearly dominated by the micromotion contribution.

6.2.4 Gravitational shift

A gravitational potential difference between two clocks gives rise to a frequency difference due to general relativity. For earth-based clocks, the relative frequency shift is approximately given by the height difference Δh and the gravitational acceleration g provided the clocks are almost at the same height [40]

$$\left(\frac{\Delta\nu}{\nu}\right)_g = \frac{g\Delta h}{c^2}, \tag{6.11}$$

leading to a sensitivity of $1.1 \times 10^{-16}\,\mathrm{m}^{-1}$. The vertical distance between the Cs fountain and the $^{40}Ca^+$ trap could be estimated to be less than $0.5(1)\,\mathrm{m}$. The gravitational frequency shift is therefore estimated by $\Delta\nu_g = 0.023(5)\,\mathrm{Hz}$.

The difference between the lab levels at the university and IQOQI has been measured by the university's civil engineering department to $4.41\,\mathrm{m}$ with a precision of $1\,\mathrm{cm}$ [153]. The ion trap difference is $4.5(5)\,\mathrm{m}$. Therefore, the expected shift between the two experiments should be $0.20(2)\,\mathrm{Hz}$. This can be important for future experiments at the 10^{-17} level dedicated to a more detailed analysis of systematic shifts, e. g. a comparison of the two experiments at different trap powers to investigate the blackbody radiation shift.

6.2.5 2nd-order Doppler shift

Another relativistic effect is caused by excess micromotion or the thermal motion. It can shift the transition line center by the relativistic Doppler effect. This shift is produced due to the ion motion relative to the laboratory frame. For a Doppler cooled $^{40}\mathrm{Ca}^+$ ion ($T \approx 0.5\,\mathrm{mK}$), the shift can be estimated by

$$\left(\frac{\Delta\nu}{\nu}\right)_{therm} = -\frac{3k_B T}{2Mc^2} \tag{6.12}$$

and is $-0.7(7)\,\mathrm{mHz}$. The contribution to the relativistic Doppler shift of the micromotion given by [82] is

$$\left(\frac{\Delta\nu}{\nu}\right)_{micro} = -\left(\frac{\Omega_T}{ck\cos\phi_k}\right)^2 \left(\frac{1}{2}\beta\right)^2 \tag{6.13}$$

and depends on the micromotion modulation index. In our case, the expected shift is much smaller than $-1(3)\,\mathrm{mHz}$ so the total effect of the 2nd-order Doppler shift is $-1(4)\,\mathrm{mHz}$ with 1×10^{-17} relative uncertainty.

6.2.6 Errors related to the Ramsey phase experiments

As already mentioned in Sec. 5.5, the total phase error for the Ramsey experiments is $<0.01°$, corresponding to a frequency uncertainty of 28 mHz. Another source of error could be an incorrectly determined Ramsey contrast if the transition is probed off-center. Taking the maximum offset from a transition center from Sec. 5.4.1 and a 5% error in the contrast, the frequency error becomes 21 mHz on the transitions with the lowest contrast. The total error therefore is 35 mHz or 8.5×10^{-17} relative uncertainty.

6.2.7 Uncertainty of the Cs fountain clock

The relative accuracy of the mobile Cs fountain clock (FOM) is stated as 7.7×10^{-16} [10]. Nevertheless, the frequency of the clock was influenced by various effects and has been evaluated carefully by Rovera *et al.* [154]. The systematic frequency correction for a change in temperature, atom number (collisions), and magnetic field was $-9.1(1) \times 10^{-15}$ on average and was applied to the frequency measurement data. The fountain clock was characterized by comparisons with the ensemble of fountains (FO1 and FO2) in Paris
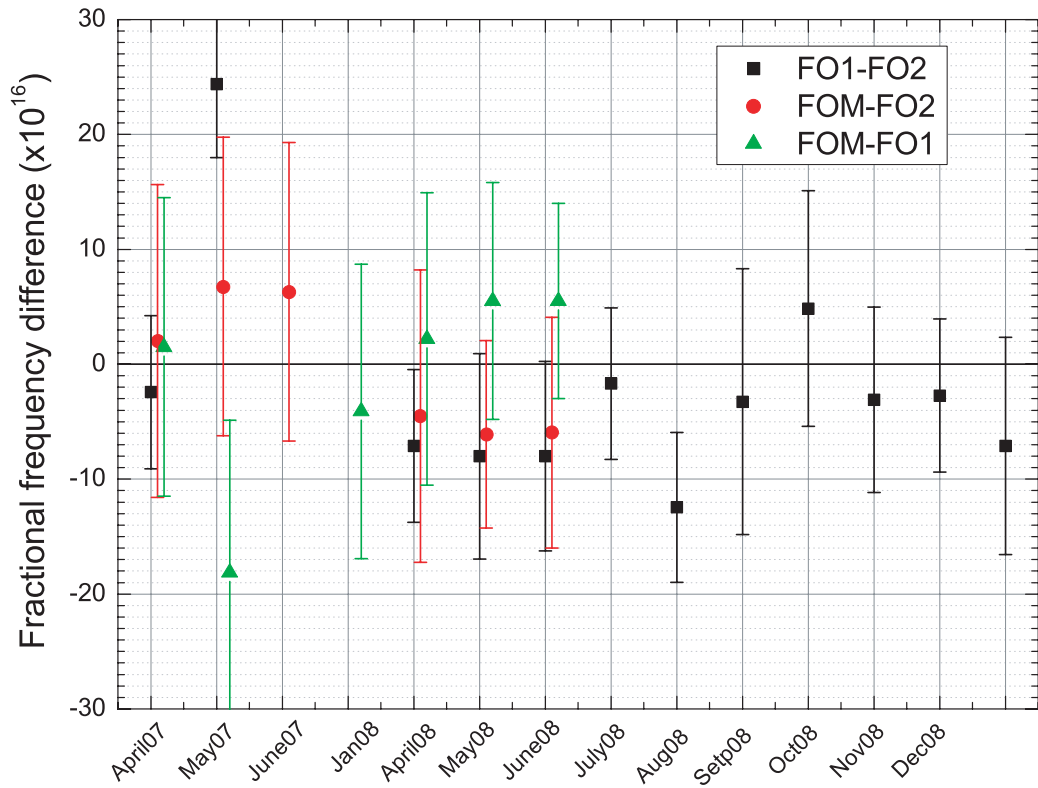

Figure 6.8: Comparison of the mobile Cs atomic fountain clock (FOM) of LNE-SYRTE vs. the stationary Cs clocks of LNE-SYRTE FO1 (triangles) and FO2 (disks). The squares show FO1 vs. FO2. Image by courtesy of Michel Abgrall, LNE-SYRTE.

before and after the experiment. As shown in Fig. 6.8 the deviations of FOM vs. FO2 lie within 10^{-15} so that the accuracy for the ^{40}Ca$^+$ frequency measurement can be taken as better than 1×10^{-15}.

6.2.8   Total error budget and result

The errors sources described in detail in the sections above lead to the overall error budget shown in table 6.1. The total shift is 2.4 Hz with an error of 1.0 Hz which is the square root of the sum of the individual errors squared. The corrected value of the $4s\ ^2S_{1/2} - 3d\ ^2D_{5/2}$ transition taking into account these systematic shifts is $\nu_{Ca^+} = 411\,042\,129\,776\,393.2(1.0)$ Hz which corresponds to $2.4 \cdot 10^{-15}$ relative uncertainty. To our knowledge this is the most accurate of any Ca$^+$ transition frequency measurement so far. There is a preliminary measurement which claims 10^{-14} precision by Matsubara *et al.* [155]. Their measurement differs from our measurement by -8 Hz with an uncertainty of 18 Hz. In contrast to our measurement, the transition was investigated by the Rabi method on two transitions for a set of 48 measurements only, namely $|m_S = -1/2\rangle - |m_D = -1/2\rangle$ and $|m_S = 1/2\rangle - |m_D = 1/2\rangle$. Thereby the linear Zeeman effect is canceled but not the quadrupole shift. Since the quadrupole shift has never been measured in their trap, there is need for further investigation.

6.3   The measurement of the ^{43}Ca$^+$ $4s\ ^2S_{1/2} - 3d\ ^2D_{5/2}$ transition

For the absolute frequency measurement of the ^{43}Ca$^+$ $4s\ ^2S_{1/2} - 3d\ ^2D_{5/2}$ transition the light of the laser exciting this transition was sent to the frequency comb through a length-stabilized optical fiber. An overview of the setup is shown in Fig. 3.1. The laser was referenced to the $\left|S_{1/2}, F = 4\right\rangle - \left|D_{5/2}, F = 6\right\rangle$ transition by probing the $|S, m_F = 4\rangle - |D, m_F = 6\rangle$ sublevels and feedback was applied in a similar way as in the experiment at the university by changing the frequency of AO7. The transition frequencies were interrogated employing the Ramsey method just as for the ^{40}Ca$^+$ measurement. The setup and the measurement technique is described in more detail in [81]. From the model mentioned there, the center frequency of the transition was calculated and extrapolated to zero magnetic field according to

$$E_{|F,m_F\rangle} = \mu_B g_F m_F B \tag{6.14}$$

together with the hyperfine energy shift

$$\Delta E_{hfs} = \frac{1}{2} A_{hfs} K + B_{hfs} \frac{\frac{3}{2}K(K+1) - 2I(I+1)2J(J+1)}{2I(2I-1)J(2J-1)}, \tag{6.15}$$

where g_F is the hyperfine g-factor, A_{hfs} and B_{hfs} the hyperfine constants with their values given in [118], I, J the nuclear and electron angular momenta, $F = J + I$ the total angular momentum, and $K = F(F+1) - I(I+1) - J(J+1)$. The remaining frequency difference to the ^{40}Ca$^+$ transition frequency is attributed to the isotope shift.

Effect	Shift (Hz)	Error (Hz)	Fractional error ($\times 10^{-15}$)
Statistical error	-	0.5	1.2
1st-order Zeeman	0	0.2	0.5
Magnetic field drift	0.03	0.01	0.024
2st-order Zeeman: quantization field	1.368	0.002	0.005
2st-order Zeeman: black body	<0.001	<0.001	<0.002
Electric quadrupole	0	0.2	0.5
AC Stark: probe laser	0.11	0.02	0.05
AC Stark: quenching laser	-0.005	0.004	0.01
AC Stark: repumping laser	0	0.01	0.02
AC Stark: cooling laser	0	0.1	0.2
AC Stark: black body radiation	0.9	0.7	1.7
AC Stark: motion	0	0.1	0.2
2nd order Doppler	-0.0007	0.0007	0.002
Graviational shift	0.023	0.005	0.01
Ramsey phase error	0	0.03	0.07
Cs uncertainty	0	<0.4	<1
Total shift	**2.4**	**1.0**	2.4×10^{-15}

Table 6.1: ^{40}Ca$^+$ error budget. A list of the most important effects with their size and error in Hz and the fractional uncertainty in units of 10^{-15}. The total offset of the frequency measurement is 2.4 Hz with an error of 1.0 Hz which is the square root of the sum of the squared individual errors. This corresponds to 2.4×10^{-15} relative uncertainty.

The frequency of the $4s\ ^2S_{1/2} - 3d\ ^2D_{5/2}$ transition of ^{43}Ca$^+$ compared to ^{40}Ca$^+$ was measured at four different magnitudes of the magnetic field and the results of the obtained isotope shifts with the average value subtracted are listed in Tab. 6.2. At each setting of the magnetic field the statistical errors for their mean values are on the order of a few Hertz but the center frequencies differ by 1.6 kHz minimum-maximum. Therefore, an average isotope shift of 4,134,711,040(700) Hz is obtained as the mean value of the complete data set. This result is in reasonable agreement with the value obtained by [118] in a previous measurement which yielded 4134.713(5) MHz. On the other hand, the measurement reported here does not contain any analysis of systematic effects and therefore has to be treated with care. The close agreement is a little bit surprising, given the fact that the transition frequencies differ quite a lot for the various magnetic fields, indicating an unknown systematic effect related to this. The most likely explanation for the differences are AC Stark shifts induced by the trapping field as some of the hyperfine states lie close to the 25 MHz drive field of the trap. At this stage, the precision of the ^{43}Ca$^+$ $4s\ ^2S_{1/2} - 3d\ ^2D_{5/2}$ transition frequency measurement is 1.2×10^{-11} due to the precision in the isotope shift. All other sources of systematic shifts and related errors are expected to be much smaller and similar to the case of the ^{40}Ca$^+$ measurement.

Table 6.2: The isotope shift of the ^{43}Ca$^+$ $4s\ ^2S_{1/2} - 3d\ ^2D_{5/2}$ transition with the average value of 4,134,711,040(700) Hz subtracted for different magnetic fields.

Magnetic field (G)	Frequency difference (Hz)	Stat. Error Δf (Hz)
0.55	+421	4
1.13	+652	3
1.69	-931	6
3.04	-143	3

Nevertheless, the ^{43}Ca$^+$ isotope represents another good candidate for an optical clock transition and a rich field for further investigation. Especially, considering that an atomic transition linewidth of 16 Hz at the transition $S(F = 4, m_F = -4) \leftrightarrow D(F = 3, m_F = 3)$ with vanishing differential Zeeman shift around $B =$ 4 G has been observed [81].

Chapter 7

Precision spectroscopy with correlated atoms

The creation of entangled atoms is recognized as a key resource for quantum cryptography and quantum computation. In this field, ion trap experiments have enabled spectacular results in processing quantum information [156–158] or the creation of entanglement of up to 8 ions [159, 160]. But entanglement is also of interest in the context of metrology and laser spectroscopy. Maximally entangled states can be used for efficient quantum state detection by entangling an atom which is difficult to detect with another atom that is easier to detect [67] and it has been demonstrated that entangled states provide a means of improving the signal-to-noise ratio in precision spectroscopy experiments [60, 65, 66, 161, 162]. In addition, it is sometimes possible to identify specific states in the state space of many-particle quantum systems that are immune to decoherence [71] with respect to noise sources otherwise dominating single-atom systems [70]. Such decoherence-free subspaces protect quantum information and yield enhanced coherence times. Therefore these subspaces offer the prospect of high resolution spectroscopy even in the presence of strong technical noise. The question arises whether entanglement is a mandatory ingredient for this kind of measurement. As will be shown later it turns out that measurements with classically correlated atoms can be used in a similar way even if the atoms are not entangled.

In this chapter, experiments with two entangled $^{40}\mathrm{Ca}^+$ ions will be presented, which were used to determine the electric quadrupole moment and the magnetic field gradient at the position of the ions. It will be shown how entangled states can be used to measure the linewidth of a narrow-band laser. The second part of this chapter is dedicated to measurements with a pair of correlated, but not maximally entangled $^{40}\mathrm{Ca}^+$ ions used to verify the measurement results with entangled ions.

7.1 Spectroscopy with entangled states

In a Ramsey experiment, information about an atomic transition frequency is obtained from a measurement of the relative phase $\varphi = \varphi_L + \Delta\tau$ (determined by the phase φ_L of the exciting laser and the detuning Δ from the transition) of a superposition of the ground

and excited state $\frac{1}{\sqrt{2}}(|g\rangle + e^{i\varphi}|e\rangle)$ by mapping the states $\frac{1}{\sqrt{2}}(|g\rangle \pm |e\rangle)$ to the measurement basis $\{|g\rangle, |e\rangle\}$. This is done by the application of the second $\pi/2$-pulse.

Spectroscopy with entangled states can be realized by a generalized Ramsey experiment where the relative phase of a Bell state $\Psi_\varphi = \frac{1}{\sqrt{2}}(|g\rangle_1 |e\rangle_2 + e^{i\varphi}|e\rangle_1 |g\rangle_2)$ is measured in analogy to a single-ion Ramsey experiment. Here, the phase $\varphi = \varphi_1 - \varphi_2$ is measured by applying the $\pi/2$-pulses to both atoms followed by state detection. For $\pi/2$-pulses with the same phase the singlet state $\frac{1}{\sqrt{2}}(|g\rangle|e\rangle - |e\rangle|g\rangle)$ is mapped onto itself, whereas the triplet state $\frac{1}{\sqrt{2}}(|g\rangle|e\rangle + |e\rangle|g\rangle)$ is mapped onto a state $\frac{1}{\sqrt{2}}(|g\rangle|g\rangle + e^{i\varphi}|e\rangle|e\rangle)$.

A measurement of the parity operator $\sigma_z^{(1)}\sigma_z^{(2)}$ yields information about the relative phase φ of the Bell state's constituents by

$$\langle \sigma_z^{(1)}\sigma_z^{(2)}\rangle = \cos\varphi. \tag{7.1}$$

If the atomic transition frequencies for both ions are not exactly the same, the phase will evolve according to $\varphi(\tau) = \varphi_0 + \Delta\tau$, where $\Delta = \Delta_1 \pm \Delta_2$ and Δ_i are the frequency differences of the laser from the individual transitions. The $+$ sign applies if the Bell state is a superposition of both atoms in the excited and both atoms in the ground state, the $-$ sign is for the state where an atom in the ground state is associated with the other atom being in an excited state and vice versa. Thus, a measurement of the phase evolution rate directly yields information about the difference frequency Δ of the constituents of the Bell state. If the atomic transition frequency is the same for both ions, the phase evolution will be twice as sensitive to the phase $\varphi(\tau) = 2\varphi_0 + 2\Delta\tau$ as compared to a single ion measurement.

7.1.1 Measurement of the quadrupole moment

Ramsey experiments with a two-ion Bell-state $\Psi = \frac{1}{\sqrt{2}}(|m_1\rangle|m_2\rangle + |m_3\rangle|m_4\rangle)$, where the magnetic quantum numbers m_i of the state $|m_i\rangle \equiv |D_{5/2}, m_i\rangle$ fulfill $m_1 + m_2 = m_3 + m_4$ are to first order insensitive to fluctuations of the magnetic field. Both parts of the Bell-state are shifted by the same amount due to the linear Zeeman effect. This means, that a state like Ψ is suitable for spectroscopy in a decoherence free subspace with respect to the magnetic field if the inter-ion distance d is much smaller than the scale on which the magnetic field varies, i. e. the magnetic field is the same for both ions. The measurement strategy is especially useful where magnetic field noise would otherwise render a measurement scheme with single ions difficult. Also, frequency noise of the probe laser is only relevant during the relatively short preparation of the Bell-state and the read-out analysis but not during the long Ramsey interrogation period making sub-Hertz spectroscopy feasible even with a laser that has a linewidth on the order of a few ten Hz. Since the states $|m_i\rangle$ are sensitive to the electric quadrupole shifts these Bell-states can be designed to measure the electric quadrupole moment of the $3d\ ^2D_{5/2}$ level.

The Bell state $\Psi_Q = \frac{1}{\sqrt{2}}(|-5/2\rangle|+3/2\rangle + |-1/2\rangle|-1/2\rangle)$ is used for the measurement of the quadrupole shift. The level diagram with respect to the two most important energy shifts for this state (linear Zeeman and electric quadrupole effect) is
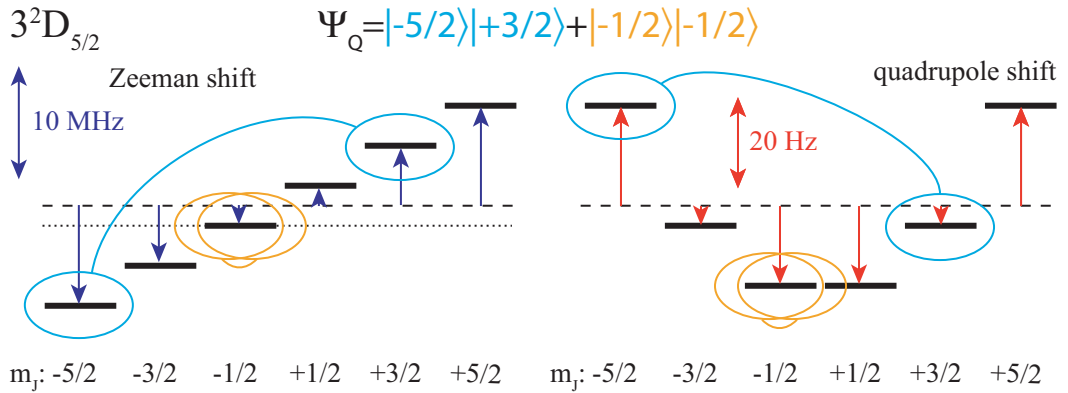
Figure 7.1: Level diagram for the state Ψ_Q. The left part shows the linear Zeeman shift of the $D_{5/2}$ level for a magnetic field of $\sim 3\,\text{G}$ and the right part the quadrupole shift at $\sim 25\,\text{V/mm}^2$ for the involved levels. The state Ψ_Q is sensitive to the electric quadrupole shift but completely symmetrical with respect to the linear Zeeman shift.

shown in Fig. 7.1. The state Ψ_Q is created by applying additional carrier π-pulses to $\Psi_{SD}^{\pm} = \frac{1}{\sqrt{2}}\left(|S,-1/2\rangle\,|D,-1/2\rangle \pm |D,-1/2\rangle\,|S,-1/2\rangle\right)$ which can be generated with three laser pulses and a fidelity of 90% [72]. The sensitivity of the state Ψ_Q to a static electric field gradient is $\hbar\Delta_Q = 24/5\,\hbar\delta$ where $\hbar\delta$ is the shift that a single ion in states $|\pm 5/2\rangle$ would experience. The two-ion shift is bigger because the presence of a second ion increases the electric field gradient at the location of the first ion by a factor of two. For the shift measurement, we applied a method using generalized Ramsey experiments. The state Ψ_Q is prepared and let to evolve into $\Psi_Q(\tau) = \frac{1}{\sqrt{2}}\left(|-5/2\rangle\,|+3/2\rangle + \exp\left(i\Delta_Q\tau\right)|-1/2\rangle\,|-1/2\rangle\right)$ for waiting times τ ranging from 0 to $300\,\text{ms}$. After that, $\Psi_Q(\tau)$ is transferred back to $\Psi_{SD}^{\pm}(\tau)$ and the phase of the parity is measured according to (7.1). The resulting parity oscillations with a frequency of $\Delta_Q = (2\pi)33.35(3)\,\text{Hz}$ are shown in Fig. 7.2(a). The decoherence due to spontaneous decay is responsible for the damping of the oscillations with a damping time constant of $\tau_d = 590(70)\,\text{ms}$. This is in agreement with the expected value of $\frac{1}{2}\tau_{D_{5/2}} = 584(4)\,\text{ms}$ [148, 149].

Any difference of the magnetic field at the position of the ions leads to an additional contribution to the oscillation frequency of the parity. In order to distinguish the effect of the electric quadrupole shift and the magnetic field gradient in the direction of the ion crystal another state $\Psi_{Q'} = \frac{1}{\sqrt{2}}\left(|+3/2\rangle\,|-5/2\rangle + |-1/2\rangle\,|-1/2\rangle\right)$ has to be investigated where the states of the ions have been interchanged. Fig. 7.2(b) shows the parity oscillations of the state $\Psi_{Q'}(\tau)$ with a frequency of $\Delta_{Q'} = (2\pi)36.52(4)\,\text{Hz}$ and a decay constant of $\tau_d = 530(60)\,\text{ms}$. Both contributions to the phase oscillations can be determined separately by taking the average $\Delta = (\Delta_Q + \Delta_{Q'})/2$ and the difference $\Delta_{B'} = |\Delta_Q - \Delta_{Q'}|/2$ of the two signals. The parity oscillations were taken at a tip voltage of $750\,\text{V}$ and five different data sets were combined for each plot. Data for waiting times up to $20\,\text{ms}$ were repeatedly taken to exclude slow drifts of the initial parity. The magnetic field gradient
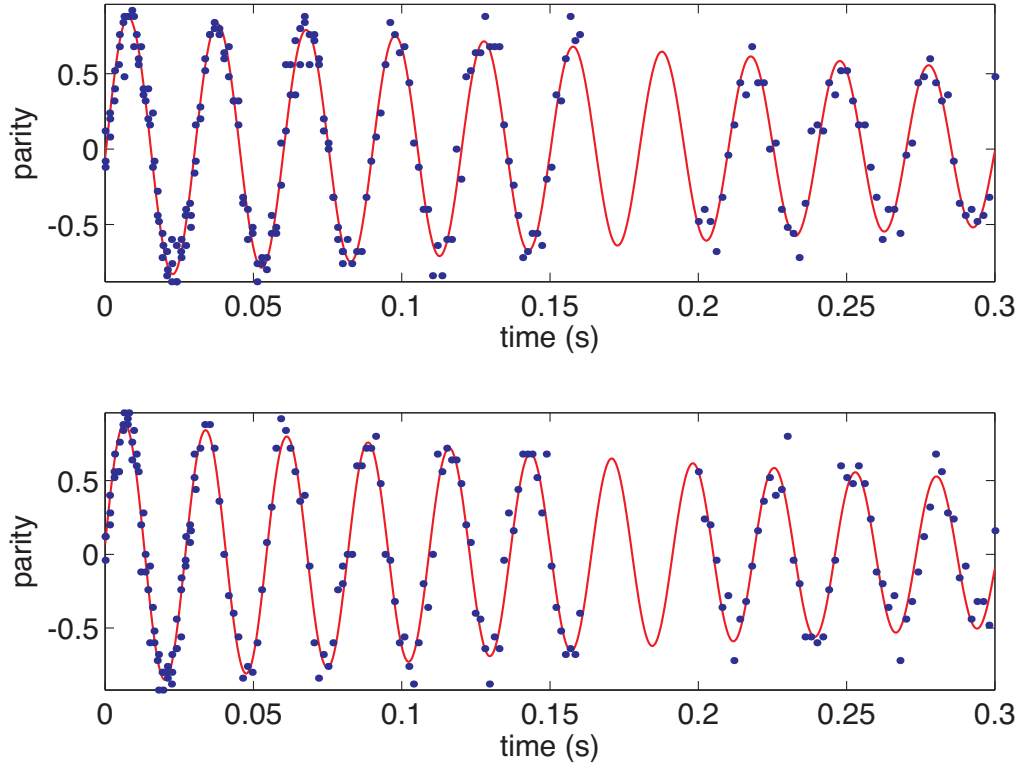
Figure 7.2: Ramsey experiments with two entangled ions for a measurement of the electric quadrupole shift with states Ψ_Q and $\Psi_{Q'}$ at a tip voltage of $750\,\mathrm{V}$. A sinusoidal function with exponential damping is fitted to the data.

was $\Delta_{B'} = (2\pi)1.41(7)\,\mathrm{Hz}$ and the electric quadrupole shift $\Delta = (2\pi)34.94(7)\,\mathrm{Hz}$.

Near the trap center, the DC voltage applied to the tip electrodes creates a rotationally symmetric static elelectric quadrupole potential. Generally, it cannot be guaranteed that this potential has perfect rotational symmetry. In this case, the geometry factor $3\cos(\beta)^2 - 1$ has to be expanded into $\big(3\cos(\beta)^2 - 1\big) - \epsilon\sin^2(\beta)\cos(2\alpha)$, where the asymmetry is characterized by a parameter ϵ and its direction α. The second term of the geometry factor, however, vanishes for $\beta = 0°$. For a precise measurement of the quadrupole moment, the magnetic field direction has to be well aligned with the principal trap axis. This can be done by changing the driving currents of two sets of horizontal, orthogonal coils as described in section 5.3 and requires the different method of optical pumping demonstrated in Sec. 5.2 because the usual method with a σ-polarized laser at $397\,\mathrm{nm}$ is not possible for the current setup due to limited optical access. Fig. 7.3 shows the angular dependence of the measured quadrupole shift $\Delta/(2\pi)$ at a tip voltage of $1000\,\mathrm{V}$. For an angle $\beta_0 = 28(3)°$ the shift has a maximum. To make sure the overlap of the magnetic field with the trap axis is optimum, another measurement was performed in perpendicular direction by changing the current in a third pair of coils orthogonal to the horizontal plane and again maximizing the shift. With these measurements performed the calibration of the system was finished
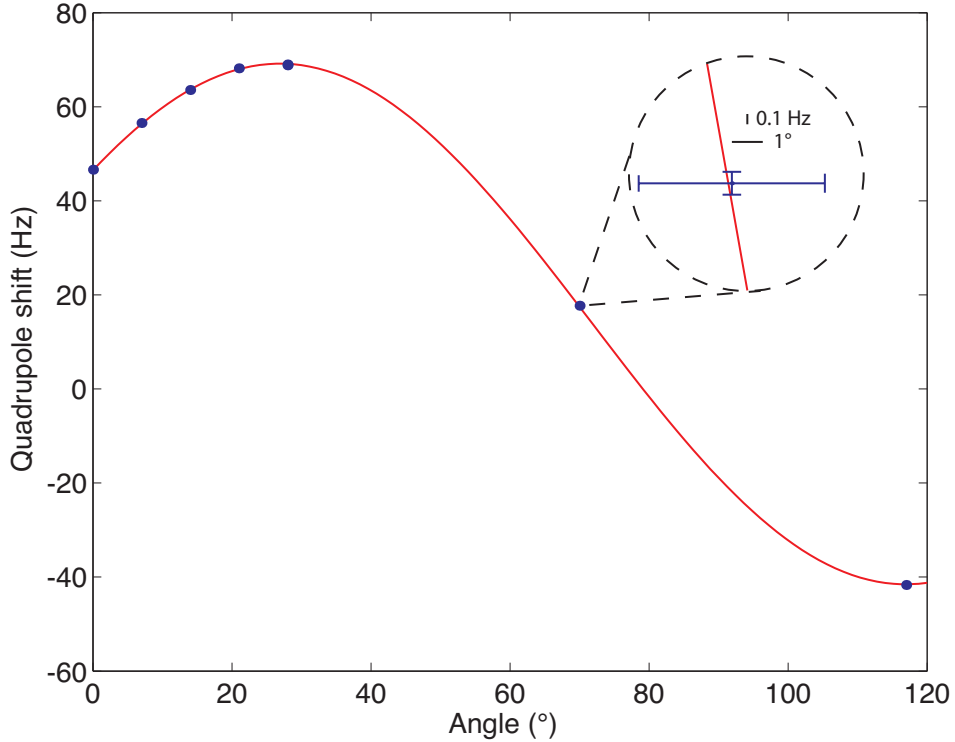
Figure 7.3: Quadrupole shift as a function of the magnetic field orientation at a tip voltage of 1000 V. The fitting function $\phi = \phi_0 + \phi_1 \cos^2(\beta - \beta_0)$ yields the angle β_0 where the quadrupole shift is maximum.

and the measurement of the quadrupole moment was ready.

At the angle of the maximum shift β_0, the quadrupole shift was measured as a function of the electric field gradient dE_z/dz. By applying tip voltages ranging from 500 to 2000 V, the axial center-of-mass (COM) mode frequency $\omega_z/(2\pi)$ could be varied from 850 to 1700 kHz. Using Eq. (2.74) the electric field gradient can be calibrated by measurements of the COM mode frequency. The quadrupole shift as a function of the electric field gradient is shown in Fig. 7.4. Fitting a linear function $\Delta/(2\pi) = \Delta_0/(2\pi) + a\frac{dE_z}{dz}$ to the data, the slope a=2.975(2) Hz mm^2/V and the offset $\Delta_0/(2\pi)$ =-2.6(1) Hz can be determined. The offset is well explained by the second-order Zeeman effect which is -2.9 Hz at a bias field of 2.9 G. The remaining difference can be attributed to electric field gradients created by stray charges. The slope a is proportional to the quadrupole moment $\Theta(3d, 5/2) = \frac{5}{12}ha$ and could be measured with an uncertainty of less than 10^{-3}. Together with the uncertainty of the angle $\Delta\beta$ =3°, the quadrupole moment is determined to be

$$\Theta(3d, 5/2) = 1.83(1)\, ea_0^2.$$

The best theoretical prediction before our measurement was $1.92\, ea_0^2$ [102, 103], recent
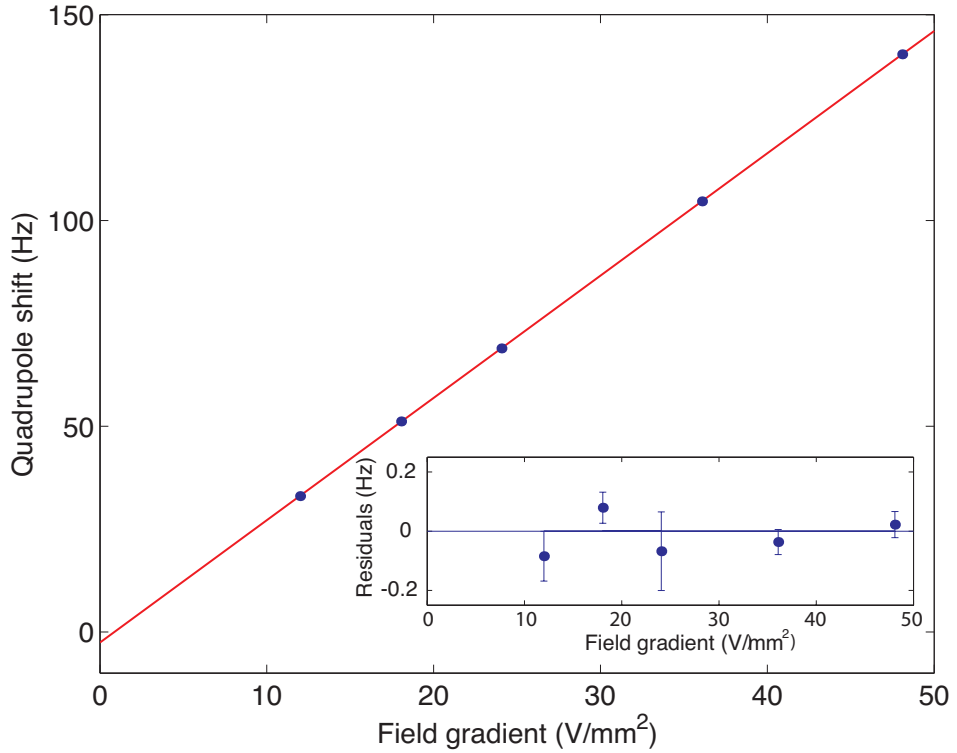
Figure 7.4: Quadrupole shift as a function of the applied field gradient.

improved calculations seem to confirm our measurement results as their results $1.85(2)\,ea_0^2$ [104] and $1.82\,ea_0^2$ [105] are closer to the experimentally obtained values.

7.1.2 Measurement of the magnetic field gradient

In experiments dedicated to quantum information processing using optical qubits a gradient of the magnetic field along the trap is undesirable because it leads to different Zeeman shifts for all ions in the string. Performing identical operations on different ions would require different laser frequencies. Therefore, the gradient caused by stray fields of the ion getter pump or asymmetrically installed magnetic field coils has to be minimized. A Ramsey experiment with the Bell state $\Psi^+ = \frac{1}{\sqrt{2}}(|S\rangle_1 |D\rangle_2 + |D\rangle_1 |S\rangle_2)$ can be used to detect a gradient of the magnetic field at the position of the ion string. This state is insensitive to fluctuations of both the magnetic field and to deviations of the laser frequency from the atomic transition as both constituents of the Bell state have the same energy. In case of a magnetic field gradient this degeneracy is lifted and the sensitivity for the chosen levels $|S\rangle \equiv |S, m_S = -1/2\rangle$ and $|D\rangle \equiv |D, m_S = -1/2\rangle$ is $d\nu/dB = 560\,\text{kHz/G}$. For a measurement of the magnetic field gradient, the parity oscillations were recorded for waiting times ranging from 0 to 300 ms. They are shown in Fig. 7.5 and fitted by

114
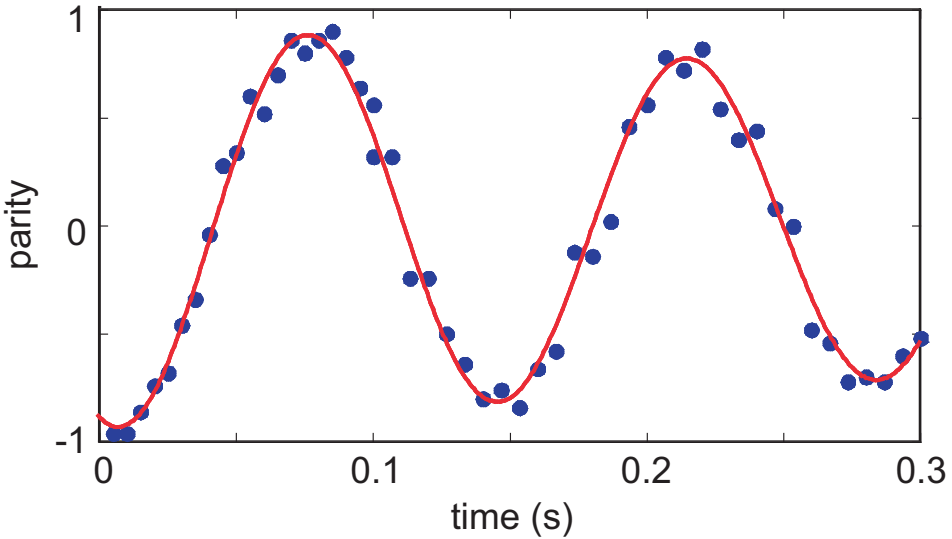
Figure 7.5: Ramsey experiment of an entangled state $|SD\rangle - |SD\rangle$ for a measurement of the magnetic field gradient. The phase evolution rate is $7.2(1)$ Hz and the decay time $550(50)$ ms.

an exponentially damped sinusoidal with a frequency of $7.2(1)$ Hz and a damping time of $550(50)$ ms. This indicates that the coherence of the state Ψ^+ is mainly limited by the lifetime of the excited state $\tau_{D_{5/2}} = 1.168(7)$ s [148, 149]. With the help of an additional coil on one of the main magnetic field coils the parity oscillation frequency could be reduced to below 1 Hz. This corresponds to a magnetic field difference of $1.8\,\mu$G at the position of the ions and to a residual gradient of below 0.4 G/m. The precision of this method can be increased by using a transition more sensitive to the linear Zeeman effect and operating the trap at lower axial confinement in order to increase the distance between the ions.

As already mentioned, the difference frequency of the frequencies Δ_Q and $\Delta_{Q'}$ used for the quadrupole shift measurement is proportional to the magnetic field gradient. It represents another possibility to gather information about the magnetic field gradient but slightly complicates the measurement procedure as it takes two measurements of the parity oscillation frequency. The frequency difference caused by a magnetic field gradient $\Delta_{B'}$ is displayed in Fig. 7.6. Since the inter-ion distance d decreases from 6.2 to $3.9\,\mu$m for higher tip voltages applied ranging from 500 to 2000 V, the magnetic field gradient B' decreases as well, because $B' \propto d \propto (dE_z/dz)^{-1/3}$.

7.1.3 Measurement of the linewidth of the laser exciting the quadrupole transition

For frequency standard applications, measurements with entangled states can provide a means which is insensitive to otherwise dominant sources of noise like fluctuations of the magnetic field for atomic transitions with even isotopes. By using a state like $\Psi_{metro} =$
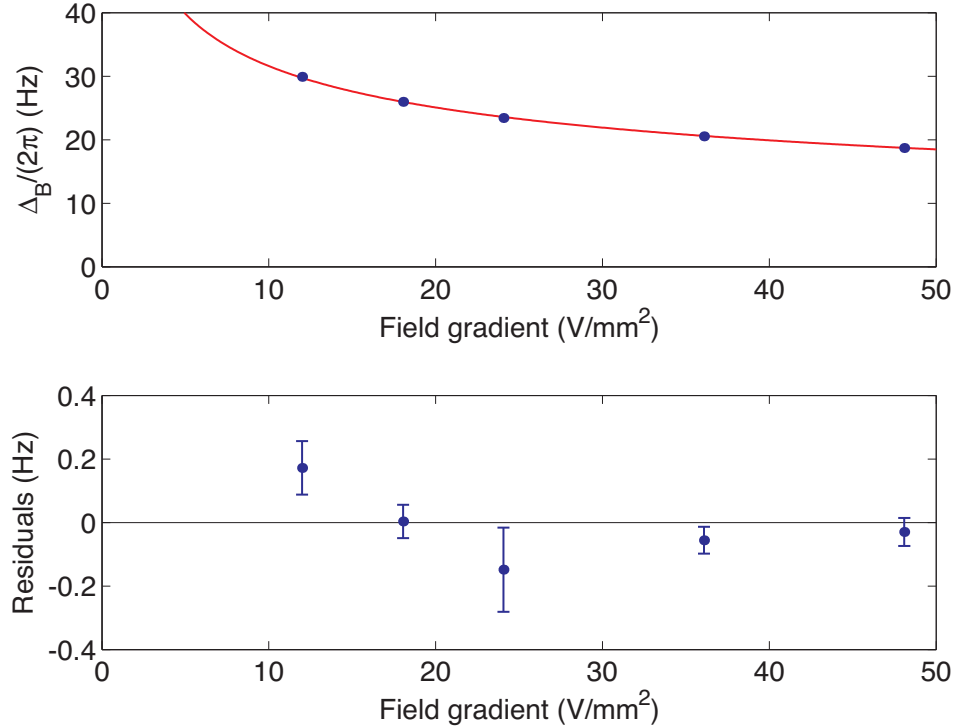
Figure 7.6: The shift caused by the magnetic field gradient as a function of the applied electric field gradient and the residuals of the fitted function. The fitted line is inversely proportional to the cube root of the applied electric field gradient.

$\frac{1}{\sqrt{2}}(|S, m = -1/2\rangle |S, m = +1/2\rangle + |D, -m'\rangle |D, m'\rangle)$ with $m' = \{\frac{1}{2}, \frac{3}{2}, \frac{5}{2}\}$ the $4s\,^2S_{1/2} - 3d\,^2D_{5/2}$ transition in $^{40}\mathrm{Ca}^+$ can be probed in the absence of decoherence due to magnetic field noise and by averaging over all three combinations of m' the electric quadrupole shift can be cancelled as well. As a preliminary measurement, a state Ψ_{metro} with $m' = 1/2$ was used to investigate the linewidth of the probe laser at 729 nm. The phase of the analyzing pulses for different waiting times was scanned from 0 to 2π and the parity signal recorded. To each scan sinusoidals of fixed period were fitted to infer the contrast of the parity oscillations. The contrast as a function of waiting time is shown in Fig. 7.7. The contrast is fitted by a Gaussian with a half-life of $\tau_{1/2} = 1.8(2)$ ms and an initial contrast of 80%. According to Eq. (2.59), this corresponds to a laser linewidth of $\Delta\nu_L = 123(14)$ Hz. At Ramsey times larger than 4 ms, where the contrast should have already decayed to zero there is still some coherence left. A closer investigation revealed that the loss of contrast cannot be explained by decoherence only. For some data sets with initially low contrast the sinusoidal pattern showed a different oscillation period which is the reason for the fitting routine being unable to correctly fit the data set.

116
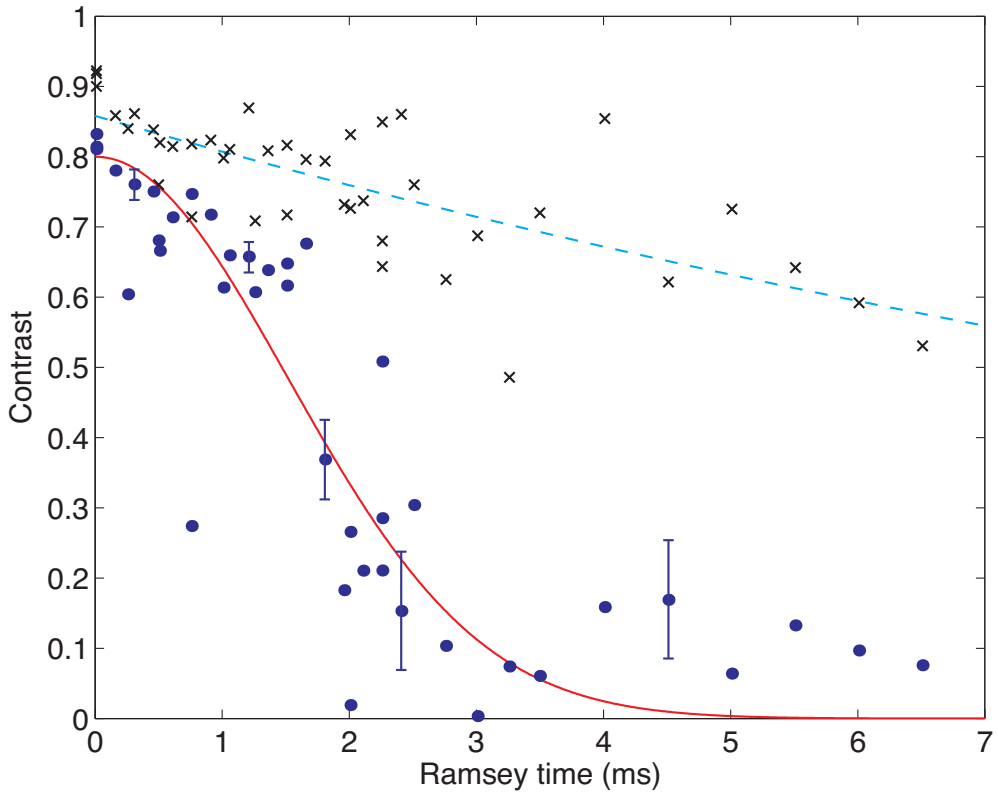
Figure 7.7: The fitted Ramsey contrast as a function of the waiting time is indicated by the circles while the crosses mark the peak-to-peak amplitude of the parity oscillations. Error bars of the fitted contrasts are given for a few representative points while the error bars for the peak-to-peak values are on the order of 1%. A Gaussian fit to the contrast yields a lifetime of $\tau_{1/2} = 1.8(2)$ ms corresponding to a laser linewidth around 123(14) Hz. The peak-to-peak values are fitted best by an exponential decay with a time constant of 16(5) ms and an estimated linewidth of 9.8(3.2) Hz.

Especially for longer Ramsey times, the phase pattern gets distorted by slow frequency fluctuations of the interrogation laser which happen on the same time scale it takes to record a phase scan. Since it is difficult to adjust the fitting routine by a frequency chirp, the peak-to-peak amplitude $\sim (\max - \min)/(\max + \min)$ of the parity signal is also shown in Fig. 7.7. This way, sometimes even for Ramsey times as large as 10-15 ms, a clear sinusoidal variation of the parity signals is recognizable with contrasts larger than 50%.

The peak-to-peak amplitude is best fit by an exponential decay with a time constant of 16(5) ms. Using Eq. (2.62), this would indicate a laser linewidth of $\Delta\nu_{FWHM} =$ 9.8(3.2) Hz. It should be pointed out that this result is rather preliminary. The peak-to-peak amplitude is probably not the best measure for the contrast because it does not distinguish between periodic and non-periodic behaviour. But still, it produces a reasonable result when compared to the beat measurement or the measurement with unentangled states (see Sec. 7.2.2). Particularly the Allan variance of the beat measurement (see Fig. 3.21) shows that the laser frequency is fluctuating by $\Delta\nu_{FWHM} =$ 40 Hz on time scales of a few seconds to hours which agrees with the change of the oscillation period during the phase scans.

7.2 Spectroscopy with correlated but unentangled states

The question is, whether entanglement is really necessary for the measurement technique described in the section above. In fact, it can be even applied to completely unentangled ions because the product state

$$\Psi_p = \frac{1}{2}(|S\rangle + |D\rangle)_1 \otimes (|S\rangle + |D\rangle)_2 = \frac{1}{\sqrt{2}}|\Psi_+\rangle + \frac{1}{2}|S_1\rangle|S_2\rangle + \frac{1}{2}|D_1\rangle|D_2\rangle \qquad (7.2)$$

contains the Bell state Ψ_+. This state will quickly decay into the mixed state described by the density operator

$$\rho_p = \frac{1}{2}|\Psi_+\rangle\langle\Psi_+| + \frac{1}{4}|SS\rangle\langle SS| + \frac{1}{4}|DD\rangle\langle DD| \qquad (7.3)$$

under the influence of collective phase noise like fluctuating magnetic fields. A measurement of the parity operator will produce the same result as for a maximally entangled state given in Eq. (7.1) apart from a reduced contrast of 50%. This is a very promising result because the creation of entangled states in the presence of strong decoherence might be difficult, but the question still remains if both methods yield the same result.

7.2.1 Measurement of the quadrupole moment

In order to check the validity of the quadrupole moment measurement and to prove that the measurement can be done with classically correlated, but unentangled ions, we prepared the state

$$\Psi_p = \frac{1}{2}(|D, -5/2\rangle + |D, -1/2\rangle)_1 \otimes (|D, +3/2\rangle + |D, -1/2\rangle)_2 \qquad (7.4)$$

which contains the Bell state Ψ_Q as it was used for the measurement of the quadrupole moment with entangled ions. This state quickly turned into a mixed state by fluctuations

118
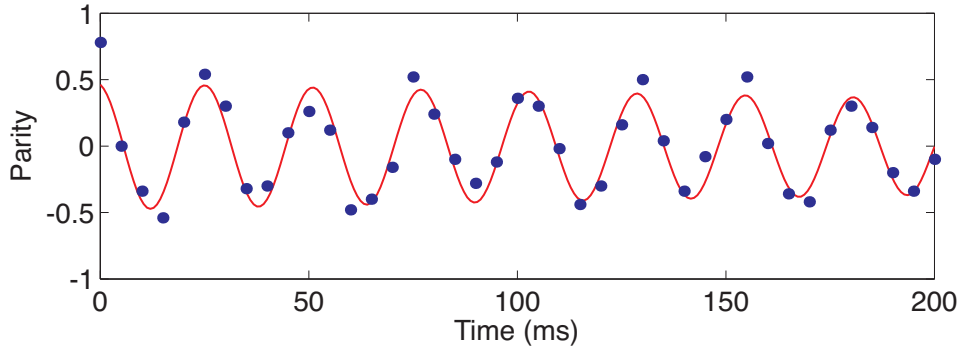
Figure 7.8: Parity oscillations for a product state Ψ_p sensitive to a static electric field gradient. The quadrupole shift is inferred from the oscillation frequency.

of the magnetic stray fields. After Ramsey waiting times of up to 200 ms the $\pi/2$ pulses were applied and the parity was measured just as for the Bell state measurements. An example for the resulting parity oscillations is shown in Fig. 7.8 for a tip voltage of 1000 V. A sinusoidal fit where the first data point was neglected as the initial state may not yet have completely decayed into a mixed state yields an oscillation frequency of 38.6(2) Hz. The parity signal decays with a time constant $\tau_d =$ 730(540) ms consistent with the damping time constant of 584(4) ms expected from the lifetime of the $D_{5/2}$ state [148, 149].

The measurement of the quadrupole moment was done in a similar way as for the entangled state measurement. The quadrupole shift was again measured for different tip voltages and the electric field gradient was calibrated by measurements of the axial COM oscillation frequency. Also for this measurement, the direction of the magnetic field coincided with the trap axis. Fig. 7.9 shows the quadrupole shift as a function of the electric field gradient. Fitting a straight line to the data allows for a calculation of the quadrupole moment provided the angle between the quantization axis and the electric field gradient is known. The configuration was the same as for the measurement with entangled states. Shown in the inset of Fig. 7.9 is the maximization of the quadrupole shift as a function of the angle of the vertical magnetic field by varying the current driving the vertical coil pair. The slope of the linear fit $\alpha \propto dE/dz =$ 2.977(11) Hz/(V/mm^2) is in close agreement with the result obtained with entangled states ($\alpha =$ 2.975(2) Hz/(V/mm^2)) and confirms that both measurements with entangled states as with product states give the same result. Deviations of the data from the fit obtained with entangled states are shown in Fig. 7.10. The dots indicate the residuals of the measurements with entangled states and the squares show the deviations obtained with the classically correlated states. As expected, the error bars are much larger for the product state measurements because of the reduced Ramsey contrast and the higher quantum projection noise. Nevertheless, this method is attractive because it is much easier to realize as it does not require ground state cooling on the quadrupole transition and a narrow-band laser for the quadrupole transition. The measurement of the quadrupole moment is not limited by measurement statistics but rather by systematic errors, the alignment of the magnetic field with the
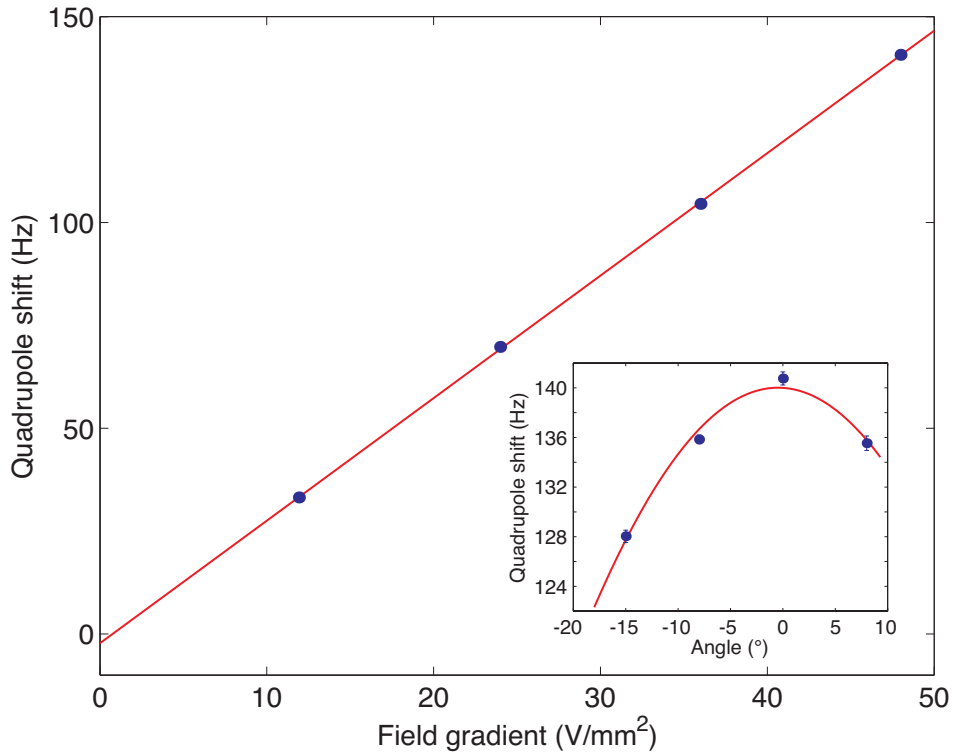
Figure 7.9: Measurement of the electric quadrupole shift with a pair of ions in a product state. The shift varies linearly with a change of the electric field gradient. The inset shows the maximization of the shift by changing the vertical magnetic field.

trap axis being the most important effect.

7.2.2 Measurement of the laser linewidth

Often, the linewidth of a narrow-band laser is investigated by setting up an identical system and analyzing the beat note of the two. In the case where no second laser is available, Ramsey experiments can be used as a tool to infer the laser linewidth. However, this requires an atomic transition which is not broadened by phase noise to an extent comparable to that of the laser to be investigated. In $^{40}Ca^+$ this is difficult to achieve because the transitions depend on the magnetic field in first order. Again, a pair of ions in a correlated product state can be a solution to this problem.

In order to investigate the linewidth of the Ti:Sa laser exciting the $^{40}Ca^+$ $4s\,^2S_{1/2} - 3d\,^2D_{5/2}$ transition we prepared the state defined by

$$\Psi_L = \frac{1}{2}(|S,-1/2\rangle + |D,-1/2\rangle)_1 \otimes (|S,+1/2\rangle + |D,+1/2\rangle)_2. \qquad (7.5)$$
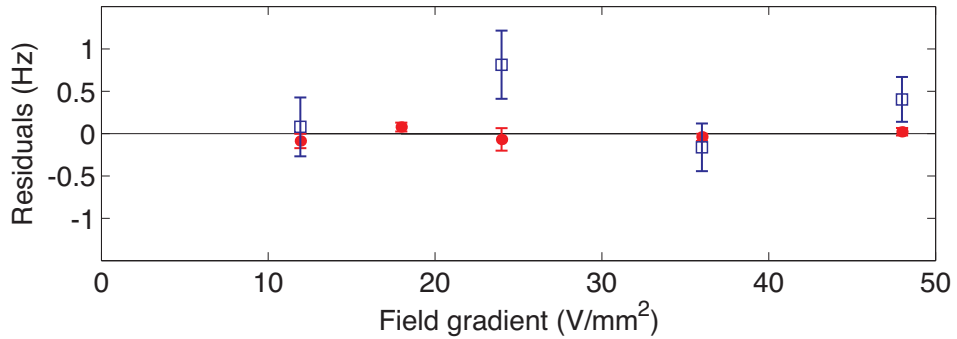
Figure 7.10: Residuals of the electric quadrupole measurements: The deviations of the measurements with correlated, but unentangled ions (squares) from the fitting result with entangled ions (circles) are shown. The deviations from the fit achieved with entangled states are indicated by the dots.
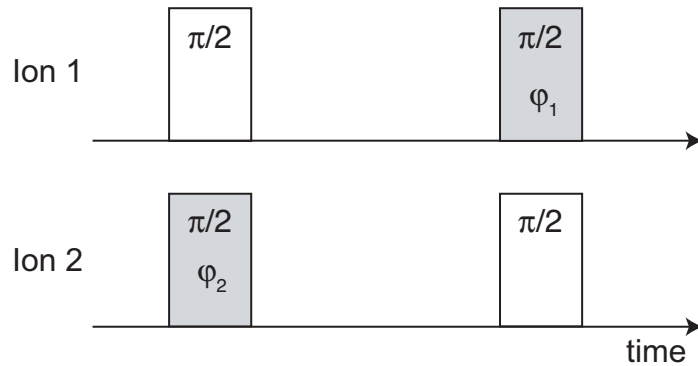

Figure 7.11: Pulse scheme for a randomization of the phase: By using two independent sources indicated by the shading for the Ramsey pulses a Ramsey experiments with two unentangled ions for a measurement of the laser linewidth can be realized.

The phase of a single-ion Ramsey signal is composed of three contributions: (a) the phase accumulated due to a detuning of the laser from the atomic resonance $\varphi_L = \Delta \tau_R$, (b) the phase shift φ_B arising from fluctuations of the magnetic field around its mean value, and (c) the relative phase of the Ramsey pulses φ_i, i denotes the number of the ion. A projective measurement of $\langle \sigma_z^{(i)} \rangle = \langle \cos(\varphi_L + (-1)^i \varphi_B + \varphi_i) \rangle$ results in the well known Ramsey fringe pattern. Please note that the magnetic field phase contributions φ_B have opposite sign for the chosen magnetic substates. The two-ion parity signal is therefore given by

$$\langle \sigma_z^{(1)} \sigma_z^{(2)} \rangle = \langle \cos(\varphi_L - \varphi_B + \varphi_1) \cos(\varphi_L + \varphi_B + \varphi_2) \rangle$$
$$= \frac{1}{2} \left(\langle \cos(2\varphi_L + \varphi_2 + \varphi_1) \rangle + \langle \cos(2\varphi_B + \varphi_2 - \varphi_1) \rangle \right). \tag{7.6}$$

By choosing the phases $\varphi_{1,2}$ to be random variables but with a fixed relation it is possible

121

to make either the first or second term vanish and detect either fluctuations of the laser frequency or the magnetic field. If the phases are chosen to be $\varphi_1 = \varphi_0 + \varphi_X$ and $\varphi_2 = -\varphi_X$, where φ_X is a random variable uniformly distributed over $[0, 2\pi[$, the magnetic field dependent term averages to zero and the parity signal becomes $\langle \sigma_z^{(1)} \sigma_z^{(2)} \rangle = \langle \cos(2\varphi_L + \varphi_0) \rangle$, since the sum $\varphi_1 + \varphi_2 = \varphi_0$ is not a random number. By setting $\varphi_1 = \varphi_0 + \varphi_X, \varphi_2 = \varphi_X$ the signal becomes insensitive to laser fluctuations and is detecting decoherence caused by magnetic field fluctuations only. Two independent RF sources were used to drive an AOM in double pass configuration to create the laser pulses for the two-ion Ramsey experiments. Therefore, the relative phase between the two sources φ_X is randomly distributed over $[0, 2\pi[$ for each experiment. For a Ramsey experiment sensitive to magnetic field fluctuations the first and the second pulses on the ions have to be from the same source while for the laser-sensitive method the second pulse on the first ion and the first pulse of the second ion need to be produced by the same source. The pulse configuration shown in Fig. 7.11 realizes the situation needed for a laser-sensitive Ramsey experiment. The shading indicates by which source the pulses are produced. By varying the phase φ_0 ranging
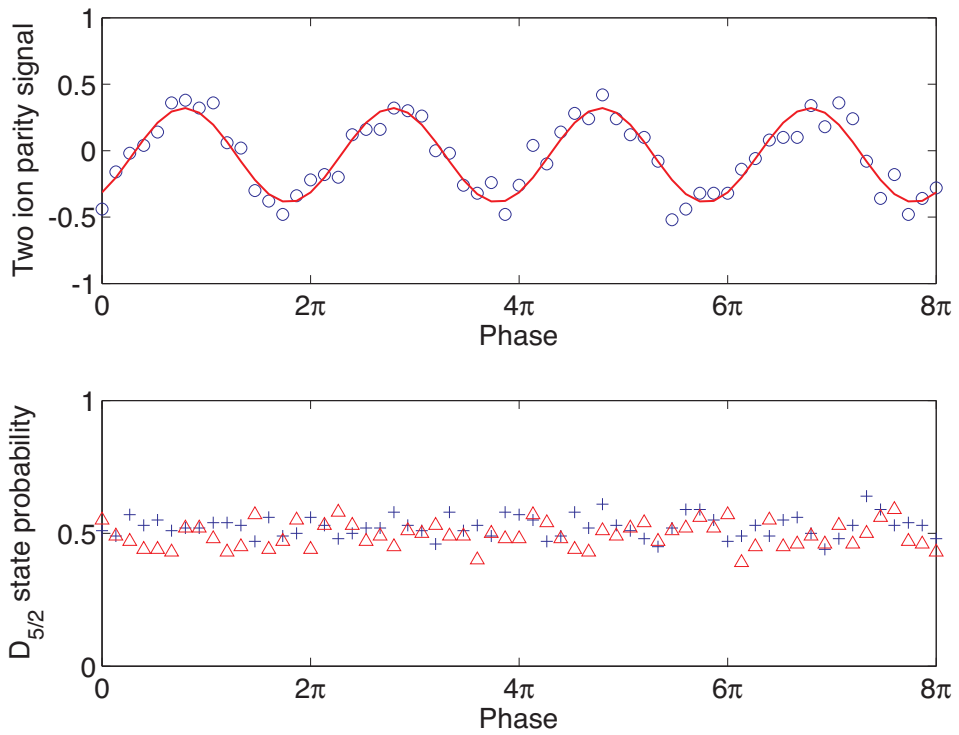
Figure 7.12: Ramsey experiment with two unentangled ions for a measurement of the laser linewidth: The phase of the second Ramsey pulse on ion 1 is scanned ranging from 0 to 8π. In the upper graph oscillations of the two-ion parity signal are shown while the single-ion coherences show no correlation as they are completely random.

from 0 to 8π parity oscillations can be recorded as shown in Fig. 7.12 in the upper graph. The single ion coherences displayed in the lower graph are completely flat as result of the randomization of the phase. The Ramsey waiting time was $\tau_R = 1.5$ ms.
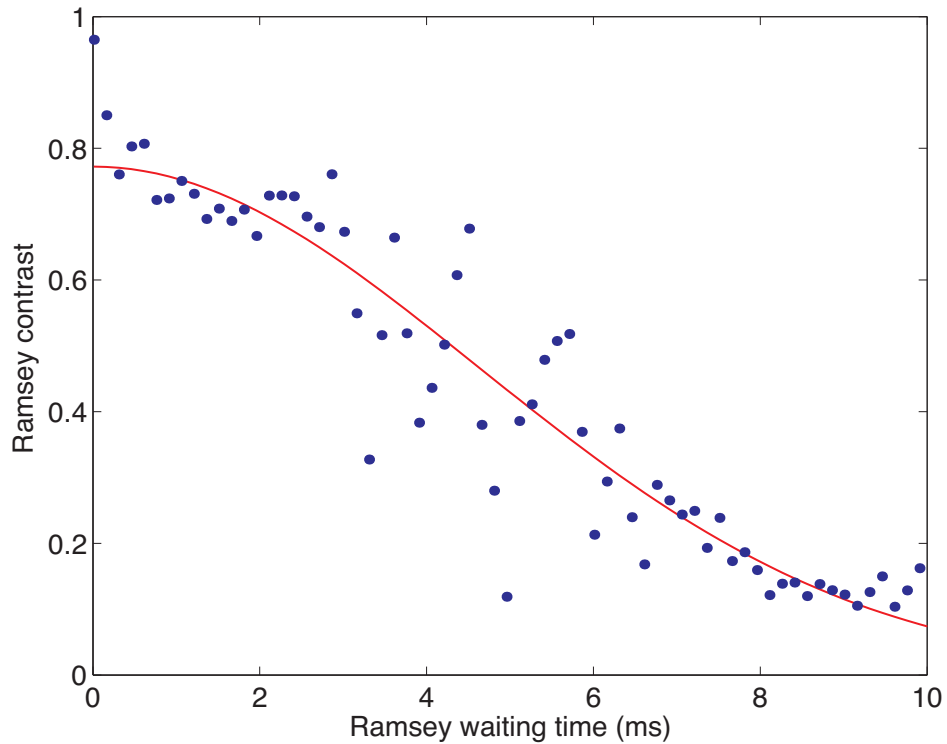
Figure 7.13: Measurement of the laser linewidth by a two-ion Ramsey experiment with unentangled ions. The Ramsey contrast is plotted against the waiting time and fits a Gaussian function with half-width $\tau_{1/2} = 4.6(2)$ ms. This corresponds to a laser linewidth of 48(2) Hz.

A series of Ramsey experiments was performed with waiting times from 0 to 10 ms. In Fig. 7.13 the contrast is plotted against the waiting time. As the broadening of the laser line is dominated by low-frequency noise the data can be fitted by a Gaussian function with a half-width of $\tau_{1/2} = 4.6(2)$ ms. The decay is twice as fast as compared to standard Ramsey experiments with a single ion because of the factor $2\varphi_L$ in Eqn. 7.6. From this decay constant, we infer a laser linewidth of 48(2) Hz on the time scale of several minutes. This is in agreement with observations of the beat note with another laser system located at IQOQI labs.

123

Chapter 8

Summary and outlook

In this thesis, precision spectroscopy with trapped ^{40}Ca$^+$ ions could be demonstrated. The absolute frequency of the $4s\ ^2S_{1/2} - 3d\ ^2D_{5/2}$ transition was measured to 1 Hz total uncertainty with the help of a frequency comb referenced to a transportable cesium fountain clock. It was clearly shown that correlated states, maximally entangled or even classically correlated, are suitable for high-resolution spectroscopy in the presence of a noisy environment if these states are designed such that they are immune against these perturbations.

First, before starting spectroscopy experiments, an ultra-stable laser system had to be constructed in order to be able to perform Hz-level measurements. The Ti:Sa laser used for this purpose was locked to a vertical reference cavity and short-term linewidths of well below 10 Hz and a $\Delta\nu_{FWHM}$=40 Hz over more than one hour could be observed. The frequency drift of the reference cavity can be compensated by phase-contiuously switching the frequency applied to two double pass AOMs between the laser and the resonator.

The optical frequency was measured by a commercial frequency comb which was enhanced for better operating stability. The repetition frequency and the carrier-envelope-offset frequency were stabilized to a radio frequency signal obtained from the mobile Cs fountain clock FOM of LNE-SYRTE from Paris with an accuracy of better than 10^{-15}. By simultaneous detection of the optical beat note from two independent lasers and comparison to the frequency comb readings of the two, cycle slips can be efficiently be detected.

The absolute frequency of the ^{40}Ca$^+$ $4s\ ^2S_{1/2} - 3d\ ^2D_{5/2}$ transition was measured to ν_{Ca^+} =411 042 129 776 393.2 (1.0) Hz including a statistical uncertainty of the measurement of 0.5 Hz and the five largest systematic uncertainties of the Stark shift by black body radiation (0.7 Hz), the Cs uncertainty (<0.4 Hz), the cancellation of the linear Zeeman effect and the quadrupole shift (0.2 Hz each), and the Stark shift by the cooling laser (0.1 Hz). A total systematic shift of 2.4 Hz was taken into account. This represents the first absolute frequency measurement of an optical transition applying Ramsey's method of separated fields at the 10^{-15} level. In addition, the spectroscopy data could be used for a precise determination of the Landé g-factor of the $D_{5/2}$ level $g_{5/2} = 1.2003340 \pm 2.5 \times 10^{-7}$.

Processing quantum information is a field of research closely related to metrology: By high-resolution spectroscopy with two ^{40}Ca$^+$ ions we have shown how Bell states can

be used for difference frequency measurements with sub-Hertz precision. Thereby, the quadrupole moment of the $D_{5/2}$ level was determined to be $\Theta(3d, 5/2) = 1.83(1)\, ea_0^2$ by designing a state insensitive to magnetic field noise. These experiments show that measurements with correlated ions prepared in decoherence-free subspaces allow for substantially longer coherence times than experiments limited by single-ion coherences. While the use of entangled states achieves the optimum signal-to-noise ratio, substantial improvements can already be obtained by experimenting with classically correlated but not entangled ions. Additional measurements of magnetic field gradients and the linewidth of the narrow-band spectroscopy laser demonstrated the versatility of this method.

Possible improvements and further experiments

One of the goals of this thesis was the application of quantum information processing techniques to precision metrology other than increasing signal-to-noise [60] or quantum state readout [67]. For the development of an optical clock it appears realistic that an experiment with Ca^+ especially designed for metrology could lead to an accuracy of 10^{-17} or even better. Ca^+ represents a technological alternative for an optical frequency standard because all required lasers including those for photo ionization can be generated by diode lasers and no deep-UV light with all its technical complications of the optical setup is necessary.

Nevertheless, there are some improvements necessary to reach this level. As a first step improved light attenuation with fast mechanical shutters would completely eliminate AC Stark shifts caused by the cooling and repumping lasers. Only the AC Stark shift of the probe laser during the Ramsey pulses would still exist but could be avoided by lower excitation power. Another minor improvement which could be immediately implemented concerns the magnetic field drift. In order to eliminate a systematic frequency offset caused by a linear drift in the magnetic field, the transition frequencies would have to be measured in a different order.

Part of the largest errors of the error budget are statistical errors due to limited averaging time. This has two reasons: one is the stability of the frequency comb and the other the stability of the clock laser itself. Improvement on both systems could substantially shorten the required measurement time. For the current stability of the frequency comb it would take 84 (!) days to get down to $< 10^{-16}$. The lock of the comb's repetition rate to the external reference needs improvement. This could be realized by choosing a higher harmonic of the repetition rate to increase the sensitivity and a more careful way of generating the reference. On the probe laser side an improved cavity setup could make investigating systematic effects a lot more efficient by comparison of the two ion trap experiments. At the moment it would take 5 days of averaging to reach the 0.1 Hz level. A laser with 1 Hz stability can get to 0.01 Hz in 10 000 s. Additionally, better laser stability would allow for longer Ramsey waiting times and reduced averaging times due to quantum projection noise. At the same time, lower power of the excitation pulses affordable due to longer waiting time could improve on the Stark shift by the probe laser.

The most difficult improvement is related to the Stark shift by black body radiation. A direct measurement of the trap temperature with the current setup is not possible. The

126

only possibility for a reduced error would require a frequency comparison of the two ion trap experiments at different trap RF powers but needs a laser with improved stability in order to keep the measurement time at a reasonable scale. An alternative would be a completely new trap design with the possibility to measure the trap temperature exactly. Additionally, operating the trap in a cryogenic environment [45, 91] would dramatically reduce the frequency uncertainty due to the black body shift.

Employing entangled states for frequency measurements has been considered yet as a means to improve the signal-to-noise ratio [61] and for read-out of the clock ion's quantum state [67]. States like $\Psi = \left|S_{1/2}, m_S\right\rangle \left|S_{1/2}, -m_S\right\rangle + \left|D_{5/2}, m_D\right\rangle \left|D_{5/2}, -m_D\right\rangle$ are to first order immune against magnetic field fluctuations and represent a kind of "super-atom" especially designed for cancellation of the largest systematic effect in this system. They could be used for generalized Ramsey experiments with probe times limited only by the probe laser stability and spontaneous decay of the metastable state and by averaging over all combinations of possible transitions, the electric quadrupole shift is cancelled as well. First tests with these states, however, revealed significant phase errors caused by changes in the optical path length when our electro-optical deflector is used to steer the beam for addressing of individual ions. To overcome this problem, beam steering of a strongly focused laser could be avoided by generating high-fidelity entanglement [158] with a laser beam collectively interacting with the ions, and combining this wide beam with a second strongly focused laser beam inducing phase shifts to make the ions distinguishable for carrying out coherent operations on a single ion.

The same measurement principle could be applied for a measurement of the isotope shift in an ion crystal consisting of different isotopes. Another possible application would be a measurement of the tensor polarizability of the D levels by exposing the ions to a transverse static field and a measurement of the quadratic Stark effect as presented in [163, 164]. It has been shown that Bell pairs of ions can be separated in a segmented trap without loss of coherence [165]. Then, one ion could be transported close to a surface/object and experience a frequency shift induced by local electromagnetic fields acting as a microscopic sensor. Finally, a Bell state consisting of two ions with similar transition frequencies but different dependence on fundamental constants might be interesting in the search for a possible time variation of fundamental constants.

Appendix A

A.1 Fundamental constants

Table A.1: Fundamental physical constants used in this thesis according to the 2006 CODATA recomended values [166].

speed of light	c	$299{,}792{,}458 \, \mathrm{m/s}$
magnetic constant	μ_0	$4\pi \times 10^{-7} \, \mathrm{N/A^2}$
Planck constant	$h = 2\pi\hbar$	$6.626\ 068\ 96(33) \times 10^{-34} \, \mathrm{Js}$
permittivity of vacuum	ϵ_0	$8.854\ 187\ 817 \times 10^{-12} \, \mathrm{F/m}$
elementary charge	e	$1.602\ 176\ 487(40) \times 10^{-19} \, \mathrm{C}$
Bohr magneton	μ_B	$9.274\ 009\ 15(23) \times 10^{-24} \, \mathrm{J/T}$
Bohr radius	a_0	$0.529\ 177\ 208\ 59(36) \times 10^{-10} \, \mathrm{m}$
atomic mass unit	u	$1.660\ 538\ 782(83) \times 10^{-27} \, \mathrm{kg}$
electron mass	m_e	$9.109\ 382\ 15(45) \times 10^{-31} \, \mathrm{kg}$
Boltzmann constant	k_B	$1.380\ 650\ 4(24) \times 10^{-23} \, \mathrm{J/K}$

A.2 Reduced matrix elements

The matrix elements of an irreducible tensor operator $T_{q,k}$ can be calculated using the Wigner-Eckart theorem [167, 168], such that

$$
\left\langle J, m_J \left\| T_{q,k} \right\| J', m'_J \right\rangle = (-1)^{J-m_J} \sqrt{2J+1} \begin{pmatrix} J & q & J' \\ -m_J & k & m'_J \end{pmatrix} \left\langle J \left\| T^{(q)} \right\| J' \right\rangle, \qquad \text{(A.1)}
$$

with $\begin{pmatrix} J & q & J' \\ -m_J & k & m'_J \end{pmatrix}$ denoting Wigner 3-j symbols involving purely geometrical properties and $\left\langle J \left\| T^{(q)} \right\| J' \right\rangle$ the reduced matrix element containing the physical nature of the tensor operator. The reduced matrix element can be found by evaluating Eq. (A.1) for special values of $T_{q,k}$.

In the case of the quadrupole operator $Q_{2,k} = r^2 C_k^{(2)}(\theta, \varphi)$ with renormalized spherical harmonics of the form $C_m^{(l)} = \sqrt{\frac{4\pi}{2l+1}} Y_{l,m}(\theta, \varphi)$, the reduced matrix element can be found as

$$
\begin{aligned}
\left\langle J, m_J \left\| r^2 C_0^{(2)} \right\| J', m'_J \right\rangle &= \left\langle J, m_J \left\| r^2 \frac{3\cos^2\theta - 1}{2} \right\| J', m'_J \right\rangle \\
&= (-1)^{J-m_J} \sqrt{2J+1} \begin{pmatrix} J & 2 & J' \\ -m_J & 0 & m'_J \end{pmatrix} \left\langle J \left\| r^2 C^{(2)} \right\| J' \right\rangle.
\end{aligned}
\tag{A.2}
$$

A.3 Effective Ramsey time

For $\Delta \ll \Omega_R$ and $\phi = 0$ Eq. 2.47 can be expanded yielding

$$
\begin{aligned}
P(\tau) &= \sin^2(\Omega_R \tau) + \frac{\Delta^2}{4\Omega_R^2} \sin(\Omega_R \tau) \left[4(\tau + \tau_R)\Omega_R \cos(\Omega_R \tau) \right. \\
&\quad \left. -4\tau_R \Omega_R - (4 + \tau_R^2 \Omega_R^2 \sin(\Omega_R \tau)) \right] + O(\Delta^3) \\
&= \frac{1}{\sin^2(\Omega_R \tau)} \left\{ 1 + \frac{\Delta^2}{4\Omega_R^2} \csc(\Omega_R \tau) \left[4(\tau + \tau_R)\Omega_R \cos(\Omega_R \tau) \right. \right. \\
&\quad \left. \left. -4\tau_R \Omega_R - (4 + \tau_R^2 \Omega_R^2 \sin(\Omega_R \tau)) \right] + O(\Delta^3) \right\}.
\end{aligned}
\tag{A.3}
$$

Under the condition $\Omega_R \tau \approx \frac{\pi}{2}$, this is reduced to

$$
P(\tau) = 1 + \frac{\Delta^2}{4\Omega_R^2}(\tau_R^2 + 4\tau_R \Omega_R + 4) = 1 + \frac{1}{4}\left(\frac{2\Delta}{\Omega_R} + \Delta\tau_R\right)^2.
\tag{A.4}
$$

Because $\Delta \to 0$, this can be further simplified to

$$
P(\tau) = \frac{1}{2}\left[1 + \cos(\Delta(\tau_R + \frac{2}{\Omega_R}))\right] = \frac{1}{2}\left[1 + \cos(\Delta(\tau_R + \frac{4\tau}{\pi}))\right],
\tag{A.5}
$$

since $\Omega_R \tau = \frac{\pi}{2}$.

Appendix B

Journal publications

The work of this thesis resulted in a number of publications:

1. "Absolute frequency measurement of the ^{40}Ca$^+$ $4s\,^2S_{1/2}-3d\,^2D_{5/2}$ clock transition", **M. Chwalla**, J. Benhelm, K. Kim, G. Kirchmair, T. Monz, M. Riebe, P. Schindler, A. S. Villar, W. Hänsel, C. F. Roos, R. Blatt, M. Abgrall, G. Santarelli, G. D. Rovera, Ph. Laurent, Phys. Rev. Lett. **102**, 023002 (2009).

2. "Precision spectroscopy with two correlated atoms", **M. Chwalla**, K. Kim, T. Monz, P. Schindler, M. Riebe, C. F. Roos, R. Blatt, Appl. Phys. B **89**, 483 (2007).

3. "'Designer atoms' for quantum metrology", C. F. Roos, **M. Chwalla**, K. Kim, M. Riebe, and R. Blatt, Nature **443**, 316 (2006).

Additional articles have been published related to the general context of this thesis:

4. "Realization of the quantum Toffoli gate with trapped ions", T. Monz, K. Kim, W. Hänsel, M. Riebe, A. S. Villar, P. Schindler, **M. Chwalla**, M. Hennrich, R. Blatt, Phys. Rev. Lett. **102**, 040501 (2009).

5. "Deterministic entanglement swapping with an ion trap quantum computer", M. Riebe, T. Monz, A. S. Villar, P. Schindler, **M. Chwalla**, M. Hennrich, R. Blatt, Nature Physics **4**, 839 (2008).

6. "Teleportation with atoms: quantum process tomography", M. Riebe, **M. Chwalla**, J. Benhelm, H. Häffner, W. Hänsel, C. F. Roos and R. Blatt, New J. Phys. **9**, 211 (2007).

7. "Scalable multiparticle entanglement of trapped ions", H. Häffner, W. Hänsel, C. F. Roos, J. Benhelm, D. Chek-al-kar, **M. Chwalla**, T. Körber, U. D. Rapol, M. Riebe, P. O. Schmidt, C. Becher, O. Gühne, W. Dür and R. Blatt, Nature **438**, 643 (2005).

8. "Robust Entanglement", H. Häffner, F. Schmidt-Kaler, W. Hänsel, C.F. Roos, T. Körber, **M. Chwalla**, M. Riebe, J. Benhelm, U. D. Rapol, C. Becher, R. Blatt, Appl. Phys. B **81**, 151 (2005).

131

Bibliography

[1] W. A. Marrison, *The crystal clock*, Proceedings of the National Academy of Sciences of the United States of America **16**, 496 (1930).

[2] N. F. Ramsey, *History of atomic clocks*, J. Res. Natl. Inst. Stand. Technol. **88**, 301 (1983).

[3] I. I. Rabi, J. R. Zacharias, S. Millman, and P. Kusch, *A new method of measuring nuclear magnetic moments*, Phys. Rev. **53**, 318 (1938).

[4] N. F. Ramsey, *A molecular beam resonance method with separated oscillating fields*, Phys. Rev. **78**, 695 (1950).

[5] J. Levine, *Introduction to time and frequency metrology*, Rev. Sci. Inst. **70**, 2567 (1999).

[6] H. J. Metcalf and P. van der Straten, *Laser cooling and trapping*, Springer, New York, 1999.

[7] W. D. Phillips, *Nobel lecture: Laser cooling and trapping of neutral atoms*, Rev. Mod. Phys. **70**, 721 (1998).

[8] A. Clairon, C. Salomon, S. Guellati, and W. D. Phillips, *Ramsey resonance in a Zacharias fountain*, Europhys. Lett. **16**, 165 (1991).

[9] S. R. Jefferts, J. Shirley, T. E. Parker, T. P. Heavner, D. M. Meekhof, C. Nelson, F. Levi, G. Costanzo, A. D. Marchi, R. Drullinger, L. Hollberg, W. D. Lee, and F. L. Walls, *Accuracy evaluation of NIST-F1*, Metrologia **39**, 321 (2002).

[10] S. Bize, P. Laurent, M. Abgrall, H. Marion, I. Maksimovic, L. Cacciapuoti, J. Grunert, C. Vian, F. dos Santos, P. Rosenbusch, P. Lemonde, G. Santarelli, P. Wolf, A. Clairon, A. Luiten, M. Tobar, and C. Salomon, *Cold atom clocks and applications*, J. Phys. B **38**, 449 (2005).

[11] R. Wynands and S. Weyers, *Atomic fountain clocks*, Metrologia **42**, 64 (2005).

[12] A. Bauch, *Caesium atomic clocks: function, performance and applications*, Measurement Science and Technology **14**, 1159 (2003).

[13] G. Santarelli, P. Laurent, P. Lemonde, A. Clairon, A. G. Mann, S. Chang, A. N. Luiten, and C. Salomon, *Quantum projection noise in an atomic fountain: A high stability cesium frequency standard*, Phys. Rev. Lett. **82**, 4619 (1999).

[14] T. Udem, R. Holzwarth, and T. W. Hänsch, *Optical frequency metrology*, Nature **416**, 233 (2002).

[15] J. L. Hall, *Optical frequency measurement: 40 years of technology revolutions*, IEEE J. of Quant. Electron. **6**, 1136 (2000).

[16] T. Rosenband, D. B. Hume, P. O. Schmidt, C. W. Chou, A. Brusch, L. Lorini, W. H. Oskay, R. E. Drullinger, T. M. Fortier, J. E. Stalnaker, S. A. Diddams, W. C. Swann, N. R. Newbury, W. M. Itano, D. J. Wineland, and J. C. Bergquist, *Frequency ratio of Al^+ and Hg^+ single-ion optical clocks; Metrology at the 17th decimal place*, Science **319**, 1808 (2008).

[17] A. D. Ludlow, T. Zelevinsky, G. K. Campbell, S. Blatt, M. M. Boyd, M. H. G. de Miranda, M. J. Martin, J. W. Thomsen, S. M. Foreman, J. Ye, T. M. Fortier, J. E. Stalnaker, S. A. Diddams, Y. Le Coq, Z. W. Barber, N. Poli, N. D. Lemke, K. M. Beck, and C. W. Oates, *Sr lattice clock at 1×10^{-16} fractional uncertainty by remote optical evaluation with a Ca clock*, Science **319**, 1805 (2008).

[18] W. H. Oskay, S. A. Diddams, E. A. Donley, T. M. Fortier, T. P. Heavner, L. Hollberg, W. M. Itano, S. R. Jefferts, M. J. Delaney, K. Kim, F. Levi, T. E. Parker, and J. C. Bergquist, *Single-atom optical clock with high accuracy*, Phys. Rev. Lett. **97**, 020801 (2006).

[19] T. Rosenband, P. Schmidt, D. Hume, W. Itano, T. Fortier, J. Stalnaker, K. Kim, S. Diddams, J. Koelemeij, J. Bergquist, and D. Wineland, *Observation of the ${}^1S_0 \longrightarrow {}^3P_0$ clock transition in ${}^{27}Al^+$*, Phys. Rev. Lett. **98**, 220801 (2007).

[20] J. Stenger, C. Tamm, N. Haverkamp, S. Weyers, and H. R. Telle, *Absolute frequency measurement of the 435.5-nm ${}^{171}Yb^+$ -clock transition with a Kerr-lens mode-locked femtosecond laser*, Opt. Lett. **26**, 1589 (2001).

[21] P. J. Blythe, S. A. Webster, H. S. Margolis, S. N. Lea, G. Huang, S.-K. Choi, W. R. C. Rowley, P. Gill, and R. S. Windeler, *Sub-kilohertz absolute-frequency measurement of the 467-nm electric octupole transition in ${}^{171}Yb^+$*, Phys. Rev. A **67**, 020501 (2003).

[22] J. von Zanthier, T. Becker, M. Eichenseer, A. Y. Nevsky, C. Schwedes, E. Peik, H. Walther, R. Holzwarth, J. Reichert, T. Udem, T. W. Hänsch, P. V. Pokasov, M. N. Skvortsov, and S. N. Bagayev, *Absolute frequency measurement of the In^+ clock transition with a mode-locked laser*, Opt. Lett. **25**, 1729 (2000).

[23] H. S. Margolis, G. P. Barwood, G. Huang, H. A. Klein, S. N. Lea, K. Szymaniec, and P. Gill, *Hertz-Level Measurement of the Optical Clock Frequency in a Single ${}^{88}Sr^+$ Ion*, Science **306**, 1355 (2004).

[24] C. Champenois, M. Houssin, C. Lisowski, A. Knoop, G. Hagel, A. Vedel, and F. Vedel, *Evaluation of the ultimate performances of a Ca^+ single-ion frequency standard*, Phys. Lett. A **331**, 298 (2004).

[25] M. Kajita, Y. Li, K. Matsubara, K. Hayasaka, and M. Hosokawa, *Prospect of optical frequency standard based on a $^{43}Ca^+$ ion*, Phys. Rev. A **72**, 3404 (2005).

[26] W. Paul and H. Steinwedel, *Ein neues Massenspektrometer ohne Magnetfeld*, Zeitschrift f. Naturforschung A **8**, 448 (1953).

[27] R. F. Wuerker, H. Shelton, and R. V. Langmuir, *Electrodynamic containment of charged particles*, Journal of Applied Physics **30**, 342 (1959).

[28] E. Schrödinger, *Are there quantum jumps?: PART I**, Br J Philos Sci **III**, 109 (1952).

[29] W. Neuhauser, M. Hohenstatt, P. E. Toschek, and H. Dehmelt, *Localized visible Ba^+ mono-ion oscillator*, Phys. Rev. A **22**, 1137 (1980).

[30] A. A. Madej and J. E. Bernard, *Frequency measurement and control*, chapter "Single-ion optical frequency standards and measurement of their absolute optical frequency", pages 153–195, Springer, Berlin, 2001.

[31] D. J. Wineland and W. M. Itano, *Laser cooling of atoms*, Phys. Rev. A **21**, 1521 (1979).

[32] H. G. Dehmelt, *Mono-ion oscillator as potential ultimate laser frequency standard*, IEEE Trans. Instr. Meas. **31**, 83 (1982).

[33] R. H. Dicke, *The effect of collisions upon the doppler width of spectral lines*, Phys. Rev. **89**, 472 (1953).

[34] J. A. Abate, *Preparation of atomic sodium as a two-level atom*, Opt. Comm. **10**, 269 (1974).

[35] D. J. Wineland, J. C. Bergquist, W. M. Itano, and R. E. Drullinger, *Double-resonance and optical-pumping experiments on electromagnetically confined, laser-cooled ions*, Opt. Lett. **5**, 254 (1980).

[36] W. Nagourney, J. Sandberg, and H. Dehmelt, *Shelved optical electron amplifier: Observation of quantum jumps.*, Phys. Rev. Lett. **56**, 2797 (1986).

[37] T. Sauter, W. Neuhauser, R. Blatt, and P. E. Toschek, *Observation of quantum jumps*, Phys. Rev. Lett. **57**, 1696 (1986).

[38] J. C. Bergquist, R. G. Hulet, W. M. Itano, and D. J. Wineland, *Observation of quantum jumps in a single atom*, Phys. Rev. Lett. **57**, 1699 (1986).

[39] S. A. Diddams, J. C. Bergquist, S. R. Jefferts, and C. W. Oates, *Standards of Time and Frequency at the Outset of the 21st Century*, Science **306**, 1318 (2004).

[40] D. W. Allan, N. Ashby, and C. Hodge, *The science of timekeeping*, Hewlett-Packard Application Note 1289 (1997).

[41] R. F. C. Vessot, M. W. Levine, E. M. Mattison, E. L. Blomberg, T. E. Hoffman, G. U. Nystrom, B. F. Farrel, R. Decher, P. B. Eby, C. R. Baugher, J. W. Watts, D. L. Teuber, and F. D. Wills, *Test of relativistic gravitation with a space-borne hydrogen maser*, Phys. Rev. Lett. **45**, 2081 (1980).

[42] J. P. Turneaure, C. M. Will, B. F. Farrell, E. M. Mattison, and R. F. C. Vessot, *Test of the principle of equivalence by a null gravitational red-shift experiment*, Phys. Rev. D **27**, 1705 (1983).

[43] S. Schiller, A. Görlitz, A. Nevsky, J. C. J. Koelemeij, A. Wicht, P. Gill, H. A. Klein, H. S. Margolis, G. Mileti, U. Sterr, F. Riehle, E. Peik, C. Tamm, W. Ertmer, E. Rasel, V. Klein, C. Salomon, G. M. Tino, P. Lemonde, R. Holzwarth, and T. Hänsch, *Optical clocks in space*, Nuclear Physics B - Proceedings Supplements **166**, 300 (2007).

[44] H. Marion, F. P. D. Santos, M. Abgrall, S. Zhang, Y. Sortais, S. Bize, I. Maksimovic, D. Calonico, J. Grünert, C. Mandache, P. Lemonde, G. Santarelli, P. Laurent, and A. Clairon, *Search for variations of fundamental constants using atomic fountain clocks*, Phys. Rev. Lett. **90**, 150801 (2003).

[45] S. Bize, S. Diddams, U. Tanaka, C. Tanner, W. H. Oskay, R. E. Drullinger, T. Parker, T. Heavner, S. R. Jefferts, L. Hollberg, W. Itano, and J. Bergquist, *Testing the stability of fundamental constants with the $^{199}Hg^{+}$ single-ion optical clock*, Phys. Rev. Lett. **90**, 150802 (2003).

[46] E. Peik, B. Lipphardt, H. Schnatz, T. Schneider, C. Tamm, and S. G. Karshenboim, *Limit on the present temporal variation of the fine structure constant*, Phys. Rev. Lett. **93**, 170801 (2004).

[47] J. Webb, M. Murphy, V. Flambaum, V. Dzuba, J. D. Barrow, C. Churchill, J. Prochaska, and A. Wolfe, *Further evidence for cosmological evolution of the fine structure constant*, Phys. Rev. Lett. **87**, 091301 (2001).

[48] R. Srianand, H. Chand, P. Petitjean, and B. Aracil, *Limits on the time variation of the electromagnetic fine-structure constant in the low energy limit from absorption lines in the spectra of distant quasars*, Phys. Rev. Lett. **92**, 121302 (2004).

[49] R. Quast, D. Reimers, and S. A. Levshakov, *Probing the variability of the fine-structure constant with the VLT/UVES*, Astron. Astrophys. **415**, L7 (2004).

[50] H. Chand, R. Srianand, P. Petitjean, B. Aracil, R. Quast, and D. Reimers, *Variation of the fine-structure constant: very high resolution spectrum of QSO HE 0515-4414*, Astron. Astrophys. **451**, 45 (2006).

[51] A. Shlyakhter, *Direct test of the constancy of fundamental nuclear constants*, Nature **264**, 340 (1976).

[52] T. Damour and F. Dyson, *The Oklo bound on the time variation of the fine-structure constant revisited*, Nucl. Phys. B **480**, 37 (1996).

[53] Y. Fujii, A. Iwamoto, T. Fukahori, T. Ohnuki, M. Nakagawa, H. Hidaka, Y. Oura, and P. Möller, *The nuclear interaction at Oklo 2 billion years ago*, Nucl. Phys. B **573**, 377 (2000).

[54] S. K. Lamoreaux and J. R. Torgerson, *Neutron moderation in the Oklo natural reactor and the time variation of α*, Phys. Rev. D **69**, 121701 (2004).

[55] S. G. Karshenboim, *Fundamental physical constants: Looking from different angles*, Can. J. of Phys. **83**, 767 (2005).

[56] P. Lemonde, P. Laurent, G. Santarelli, M. Abgrall, Y. Sortais, S. Bize, C. Nicolas, S. Zhang, A. Clairon, N. Dimareq, P. Petit, A. G. Mann, A. Luiten, S. Cheng, and C. Salomon, *Frequency Measurement And Control Advanced Techniques And Future Trends*, chapter "Cold-atom clocks on Earth and in space", pages 131–152, Springer, Berlin, 2001.

[57] D. J. Wineland, J. C. Bergquist, T. Rosenband, P. O. Schmidt, W. M. Itano, J. J. Bollinger, D. Leibfried, and W. H. Oskay, *Ion optical clocks and quantum information processing*, in *Proceedings of the 2003 IEEE International Frequency Control Symposium and PDA Exhibition Jointly with the 17th European Frequency and Time Forum*, pages 68–71, 2003.

[58] M. A. Nielsen and I. L. Chuang, *Quantum Computation and Quantum Information*, Cambridge Univ. Press, Cambridge, 2000.

[59] N. Gisin, G. Ribordy, W. Tittel, and H. Zbinden, *Quantum cryptography*, Rev. Mod. Phys. **74**, 145 (2002).

[60] D. J. Wineland, J. J. Bollinger, W. M. Itano, and D. J. Heinzen, *Squeezed atomic states and projection noise in spectroscopy*, Phys. Rev. A **50**, 67 (1994).

[61] J. J. Bollinger, W. M. Itano, D. J. Wineland, and D. J. Heinzen, *Optimal frequency measurements with maximally correlated states*, Phys. Rev. A **54**, R4649 (1996).

[62] V. Giovannetti, S. Lloyd, and L. Maccone, *Quantum-Enhanced Measurements: Beating the Standard Quantum Limit*, Science **306**, 1330 (2004).

[63] V. Giovannetti, S. Lloyd, and L. Maccone, *Quantum metrology*, Phys. Rev. Lett. **96**, 010401 (2006).

[64] V. Meyer, M. A. Rowe, D. Kielpinski, C. A. Sackett, W. M. Itano, C. Monroe, and D. J. Wineland, *Experimental demonstration of entanglement-enhanced rotation angle estimation using trapped ions*, Phys. Rev. Lett. **86**, 5870 (2001).

[65] D. Leibfried, M. D. Barrett, T. Schätz, J. Britton, J. Chiaverini, W. M. Itano, J. D. Jost, C. Langer, and D. J. Wineland, *Toward Heisenberg-limited spectroscopy with multiparticle entangled states*, Science **304**, 1476 (2004).

[66] W. M. Itano, J. C. Bergquist, J. J. Bollinger, J. M. Gilligan, D. J. Heinzen, F. L. Moore, M. G. Raizen, and D. J. Wineland, *Quantum projection noise: Population fluctuations in two-level systems*, Phys. Rev. A **47**, 3554 (1993).

[67] P. O. Schmidt, T. Rosenband, C. Langer, W. M. Itano, J. C. Bergquist, and D. J. Wineland, *Spectroscopy using quantum logic*, Science **309**, 749 (2005).

[68] T. Schätz, M. D. Barrett, D. Leibfried, J. Britton, J. Chiaverini, W. M. Itano, J. D. Jost, E. Knill, C. Langer, and D. J. Wineland, *Enhanced quantum state detection efficiency through quantum information processing*, Phys. Rev. Lett. **94**, 010501 (2005).

[69] A. Widera, O. Mandel, M. Greiner, S. Kreim, T. W. Hänsch, and I. Bloch, *Entanglement interferometry for precision measurement of atomic scattering properties*, Phys Rev Lett **92**, 160406 (2004).

[70] D. Kielpinski, V. Meyer, M. A. Rowe, C. A. Sackett, W. M. Itano, C. Monroe, and D. J. Wineland, *A decoherence-free quantum memory using trapped ions*, Science **291**, 1013 (2001).

[71] D. A. Lidar, I. L. Chuang, and K. B. Whaley., *Decoherence-free subspaces for quantum computation*, Phys. Rev. Lett. **81**, 2594 (1998).

[72] C. F. Roos, G. P. T. Lancaster, M. Riebe, H. Häffner, W. Hänsel, S. Gulde, C. Becher, J. Eschner, F. Schmidt-Kaler, and R. Blatt, *Bell states of atoms with ultralong lifetimes and their tomographic state analysis*, Phys. Rev. Lett. **92**, 220402 (2004).

[73] C. F. Roos, *Precision frequency measurements with entangled states*, arXiv:quant-ph/0508148 (2005).

[74] B. K. Sahoo, M. R. Islam, B. P. Das, R. K. Chaudhuri, and D. Mukherjee, *Lifetimes of the metastable $^2D_{3/2,5/2}$ states in Ca^+, Sr^+, and Ba^+*, Phys. Rev. A **74**, 062504 (2006).

[75] J. Jin and D. A. Church, *Precision lifetimes for the Ca^+ 4p ^2P levels: Experiment challenges theory at the 1% level*, Phys. Rev. Lett. **70**, 3213 (1993).

[76] S.-S. Liaw, *Ab initio calculation of the lifetimes of 4p and 3d levels of Ca^+*, Phys. Rev. A **51**, R1723 (1995).

[77] R. Gerritsma, G. Kirchmair, F. Zähringer, J. Benhelm, R. Blatt, and C. F. Roos, *Precision measurement of the branching fractions of the 4p $^2P_{3/2}$ decay of Ca II*, Eur. Phys. J. D **50**, 13 (2008).

[78] Y. Ralchenko, A. E. Kramida, J. Reader, and N. A. Team, *NIST atomic spectra database (version 3.1.5)*, http://physics.nist.gov/asd3, 2008.

[79] S. Gulde, *Experimental realization of quantum gates and the Deutsch-Josza algorithm with trapped $^{40}Ca^+$–ions*, PhD thesis, Universität Innsbruck, 2003.

[80] M. Riebe, *Preparation of entangled states and quantum teleportation with atomic qubits*, PhD thesis, Universität Innsbruck, 2005.

[81] J. Benhelm, *Experimental quantum-information processing with $^{43}Ca^+$ ions*, PhD thesis, University of Innsbruck, 2008.

[82] D. J. Berkeland, J. D. Miller, J. C. Bergquist, W. M. Itano, and D. J. Wineland, *Minimization of ion micromotion in a Paul trap*, J. App. Phys. **83**, 5025 (1998).

[83] D. Leibfried, R. Blatt, C. Monroe, and D. Wineland, *Quantum dynamics of single trapped ions*, Rev. Mod. Phys. **75**, 281 (2003).

[84] C. F. Roos, *Controlling the quantum state of trapped ions*, PhD thesis, Universität Innsbruck, 2000.

[85] P. K. Ghosh, *Ion traps*, Oxford University Press, 1995.

[86] J. Vanier and C. Audoin, *The Quantum Physics of Atomic Frequency Standards*, IOP Publishing Ltd, 1989.

[87] R. Loudon, *The Quantum Theory of Light*, Oxford University Press, 3rd edition, 2000.

[88] R. Grimm, M. Weidemüller, and Y. B. Ovchinnikov, *Optical dipole traps for neutral atoms*, Molecular and Optical Physics **42**, 95 (2000).

[89] D. F. V. James, *Quantum dynamics of cold trapped ions with application to quantum computation*, Appl. Phys. B **66**, 181 (1998).

[90] H. S. Freedhoff, *Master equation for electric quadrupole transitions*, Journal of Physics B Atomic Molecular Physics **22**, 435 (1989).

[91] W. M. Itano, *External-field shifts of the $^{199}Hg^+$ optical frequency standard*, J. Res. Natl. Inst. Stand. Technol. **105**, 829 (2000).

[92] I. I. Sobelman, *Atomic Spectra and Radiative Transitions*, pages 74–88, Springer-Verlag, 1992.

[93] C. A. Blockley, D. F. Walls, and H. Risken, *Quantum collapses and revivals in a quantized trap*, Europhys. Lett. **17**, 509 (1992).

[94] E. T. Jaynes and F. W. Cummings, *Comparison of quantum and semiclassical radiation theories with application to the beam maser*, Proceedings of IEEE **51**, 89 (1963).

[95] B. W. Shor and P. L. Knight, *The Jaynes-Cummings model*, J. Mod. Opt. **40**, 1195 (1993).

[96] R. P. Feynman, F. L. Vernon, and R. W. Hellwarth, *Geometrical representation of the Schrödinger equation for solving the maser problem*, J. App. Phys. **28**, 65 (1957).

[97] T. Mayer-Kuckuk, *Atomphysik: Eine Einführung*, page 123, Teubner-Verlag, 1994.

[98] G. Tommaseo, T. Pfeil, G. Revalde, G. Werth, P. Indelicato, and J. Desclaux, *The* g_J*-factor in the ground state of* Ca^+, Eur. Phys. J. D **25**, 113 (2003).

[99] I. I. Sobelman, *Atomic Spectra and Radiative Transitions*, pages 189–199, Springer-Verlag, 1992.

[100] A. Bauch and R. Schröder, *Experimental verification of the shift of the cesium hyperfine transition frequency due to blackbody radiation*, Phys. Rev. Lett. **78**, 622 (1997).

[101] A. A. Madej, J. E. Bernard, P. Dubé, L. Marmet, and R. S. Windeler, *Absolute frequency of the* $^{88}Sr^+5s\,^2S_{1/2} - 4d\,^2D_{5/2}$ *reference transition at 445 THz and evaluation of systematic shifts*, Phys. Rev. A **70**, 012507 (2004).

[102] W. M. Itano, *Quadrupole moments and hyperfine constants of metastable states of* Ca^+, Sr^+, Ba^+, Yb^+, Hg^+, *and* Au, Phys. Rev. A **73**, 022510 (2006).

[103] C. Sur, K. V. P. Latha, B. K. Sahoo, R. K. Chaudhuri, B. P. Das, and D. Mukherjee, *Electric quadrupole moments of the d states of alkaline-earth-metal ions*, Phys. Rev. Lett. **96**, 193001 (2006).

[104] D. Jiang, B. Arora, and M. S. Safronova, *Electric quadrupole moments of metastable states of* Ca^+, Sr^+, *and* Ba^+, Phys. Rev. A **78**, 022514 (2008).

[105] J. Mitroy and J. Y. Zhang, *Long range interactions of the* Mg^+ *and* Ca^+ *ions*, Eur. Phys. J. D **46**, 415 (2008).

[106] D. Rotter, *Photoionisation von Kalzium*, Diploma thesis, Universität Innsbruck, 2003.

[107] H. Rohde, *Experimente zur Quanteninformationsverarbeitung in einer linearen Paulfalle*, PhD thesis, Universität Innsbruck, 2001.

[108] G. Kirchmair, *Frequency stabilization of a Titanium-Sapphire laser for precision spectroscopy on Calcium ions*, Diploma thesis, Universität Innsbruck, 2007.

[109] B. Young, F. Cruz, W. Itano, and J. Bergquist, *Visible lasers with subhertz linewidths*, Phys. Rev. Lett. **82**, 3799 (1999).

[110] M. Notcutt, L.-S. Ma, J. Ye, and J. L. Hall, *Simple and compact 1-Hz laser system via an improved mounting configuration of a reference cavity*, Opt. Lett. **30**, 1815 (2005).

[111] H. Stoehr, F. Mensing, J. Helmcke, and U. Sterr, *Diode laser with 1 Hz linewidth*, Opt. Lett. **31**, 736 (2006).

[112] A. D. Ludlow, X. Huang, M. Notcutt, T. Zanon-Willette, S. M. Foreman, M. M. Boyd, S. Blatt, and J. Ye, *Compact, thermal-noise-limited optical cavity for diode laser stabilization at 1×10^{-15}*, Opt. Lett. **32**, 641 (2007).

[113] G. P. Barwood, P. Gill, G. Huang, and H. A. Klein, *Observation of a sub-10-Hz linewidth $^{88}Sr^+$ $^2S_{1/2}$-$^2D_{5/2}$ clock transition at 674 nm*, IEEE Trans. Instr. Meas. **56**, 226 (2007).

[114] J. Alnis, A. Matveev, N. Kolachevsky, T. Udem, and T. W. Hänsch, *Sub-Hertz linewidth with diode lasers by stabilization to vibrationally and thermally compensated ULE Fabry-Pérot cavities*, Phys. Rev. A **77**, 053809 (2008).

[115] B. E. A. Saleh and M. C. Teich, *Fundamentals of Photonics*, Wiley, New York, 1991.

[116] T. W. Hänsch and B. Couillaud, *Laser frequency stabilization by polarization spectroscopy of a reflecting reference cavity*, Opt. Comm. **35**, 441 (1980).

[117] L.-S. Ma, P. Jungner, J. Ye, and J. L. Hall, *Delivering the same optical frequency at two places: accurate cancellation of phase noise introduced by an optical fiber or other time-varying path*, Opt. Lett. **19**, 1777 (1994).

[118] J. Benhelm, G. Kirchmair, U. Rapol, T. Körber, C. F. Roos, and R. Blatt, *Measurement of the hyperfine structure of the $S_{1/2}$-$D_{5/2}$ transition in $^{43}Ca^+$*, Phys. Rev. A **75**, 032506 (2007).

[119] F. Riehle, *Frequency Standards*, pages 50–54, Wiley-VCH,Weinheim, 2004.

[120] J. Reichert, M. Niering, R. Holzwarth, M. Weitz, T. Udem, and T. Hänsch, *Phase coherent vacuum-ultraviolet to radio frequency comparison with a mode-locked laser*, Phys. Rev. Lett. **84**, 3232 (1999).

[121] S. A. Diddams, D. J. Jones, J. Ye, S. T. Cundiff, J. L. Hall, J. K. Ranka, R. S. Windeler, R. Holzwarth, T. Udem, and T. W. Hänsch, *Direct link between microwave and optical frequencies with a 300 thz femtosecond laser comb*, Phys. Rev. Lett. **84**, 5102 (2000).

[122] T. Udem, J. Reichert, R. Holzwarth, and T. W. Hänsch, *Absolute optical frequency measurement of the cesium D1 line with a mode-locked laser*, Phys. Rev. Lett. **82**, 3568 (1999).

[123] M. Niering, R. Holzwarth, J. Reichert, P. Pokasov, T. Udem, M. Weitz, T. W. Hänsch, P. Lemonde, G. Santarelli, M. Abgrall, P. Laurent, C. Salomon, and A. Clairon, *Measurement of the hydrogen ^1S-^2S transition frequency by phase coherent comparison with a microwave cesium fountain clock*, Phys. Rev. Lett. **84**, 5496 (2000).

[124] M. Hentschel, R. Kienberger, C. Spielmann, G. A. Reider, N. Milosevic, T. Brabec, P. Corkum, U. Heinzmann, M. Drescher, and F. Krausz, *Attosecond metrology*, Nature **414**, 509 (2001).

[125] A. Baltuška, T. Udem, M. Uiberacker, M. Hentschel, E. Goulielmakis, C. Gohle, R. Holzwarth, V. S. Yakovlev, A. Scrinzi, T. W. Hänsch, and F. Krausz, *Attosecond control of electronic processes by intense light fields*, Nature **421**, 611 (2003).

[126] R. Kienberger, E. Goulielmakis, M. Uiberacker, A. Baltuska, V. Yakovlev, F. Bammer, A. Scrinzi, T. Westerwalbesloh, U. Kleineberg, U. Heinzmann, M. Drescher, and F. Krausz, *Atomic transient recorder*, Nature **427**, 817 (2004).

[127] G. Sansone, E. Benedetti, F. Calegari, C. Vozzi, L. Avaldi, R. Flammini, L. Poletto, P. Villoresi, C. Altucci, R. Velotta, S. Stagira, S. De Silvestri, and M. Nisoli, *Isolated Single-Cycle Attosecond Pulses*, Science **314**, 443 (2006).

[128] T. Fuji, J. Rauschenberger, C. Gohle, A. Apolonski, T. Udem, V. S. Yakovlev, G. Tempea, T. W. Hänsch, and F. Krausz, *Attosecond control of optical waveforms*, New J. Phys. **7**, 116 (2005).

[129] A. L. Cavalieri, N. Müller, T. Uphues, V. S. Yakovlev, A. Baltuška, B. Horvath, B. Schmidt, L. Blümel, R. Holzwarth, S. Hendel, M. Drescher, U. Kleineberg, P. M. Echenique, R. Kienberger, F. Krausz, and U. Heinzmann, *Attosecond spectroscopy in condensed matter*, Nature **449**, 1029 (2007).

[130] T. Steinmetz, T. Wilken, C. Araujo-Hauck, R. Holzwarth, T. W. Hänsch, L. Pasquini, A. Manescau, S. D'Odorico, M. T. Murphy, T. Kentischer, W. Schmidt, and T. Udem, *Laser Frequency Combs for Astronomical Observations*, Science **321**, 1335 (2008).

[131] H. Schnatz, B. Lipphardt, J. Helmcke, F. Riehle, and G. Zinner, *First phase-coherent frequency measurement of visible radiation*, Phys. Rev. Lett. **76**, 18 (1996).

[132] S. T. Cundiff and J. Ye, *Colloquium: Femtosecond optical frequency combs*, Rev. Mod. Phys. **75**, 325 (2003).

[133] T. Udem and F. Riehle, *Frequency combs applications and optical frequency standards*, in *Metrology and Fundamental Constants*, edited by T. W. Hänsch, S. Leschiutta, A. J. Wallard, and M. L. Rastello, Proceedings of the International School

of Physics "Enrico Fermi", Course CLXVI, pages 317–365, Amsterdam, 2007, IOS Press.

[134] R. Szipocs, K. Ferencz, C. Spielmann, and F. Krausz, *Chirped multilayer coatings for broadband dispersion control in femtosecond lasers*, Opt. Lett. **19**, 201 (1994).

[135] F. Salin, J. Squier, and M. Piché, *Mode locking of Ti:Ai$_2$O$_3$ lasers and self-focusing: a Gaussian approximation*, Opt. Lett. **16**, 1674 (1991).

[136] T. Brabec, C. Spielmann, P. F. Curley, and F. Krausz, *Kerr lens mode locking*, Opt. Lett. **17**, 1292 (1992).

[137] F. X. Kärtner and U. Keller, *Stabilization of solitonlike pulses with a slow saturable absorber*, Opt. Lett. **20**, 16 (1995).

[138] P. Russell, *Photonic Crystal Fibers*, Science **299**, 358 (2003).

[139] G. P. Agrawal, *Nonlinear Fiber Optics*, Academic Press, New York, 2006.

[140] H. R. Telle, G. Steinmeyer, A. E. Dunlop, J. Stenger, D. H. Sutter, and U. Keller, *Carrier-envelope offset phase control: A novel concept for absolute optical frequency measurement and ultrashort pulse generation*, Appl. Phys. B **69**, 327 (1999).

[141] R. Holzwarth, T. Udem, T. W. Hänsch, J. C. Knight, W. J. Wadsworth, and P. S. J. Russell, *Optical frequency synthesizer for precision spectroscopy*, Phys. Rev. Lett. **85**, 2264 (2000).

[142] J. K. Ranka, R. S. Windeler, and A. J. Stentz, *Visible continuum generation in air-silica microstructure optical fibers with anomalous dispersion at 800 nm*, Opt. Lett. **25**, 25 (2000).

[143] D. J. Jones, S. A. Diddams, J. K. Ranka, A. Stentz, R. S. Windeler, J. L. Hall, and S. T. Cundiff, *Carrier-envelope phase control of femtosecond mode-locked lasers and direct optical frequency synthesis*, Science **288**, 635 (2000).

[144] K. W. Holman, R. J. Jones, A. Marian, S. T. Cundiff, and J. Ye, *Intensity-related dynamics of femtosecond frequency combs*, Opt. Lett. **28**, 851 (2003).

[145] P. Schindler, *Frequency synthesis and pulse shaping for quantum information processing with trapped ions*, Diploma thesis, Universität Innsbruck, 2008.

[146] E. Peik, T. Schneiderl, and C. Tamm, *Laser frequency stabilization to a single ion*, J. Phys. B: At. Mol. Opt. Phys. **39**, 145 (2006).

[147] H. Häffner, S. Gulde, M. Riebe, G. Lancaster, C. Becher, J. Eschner, F. Schmidt-Kaler, and R. Blatt, *Precision measurement and compensation of optical Stark shifts for an ion-trap quantum processor*, Phys. Rev. Lett. **90**, 143602 (2003).

[148] P. A. Barton, C. J. S. Donald, D. M. Lucas, D. A. Stevens, A. M. Steane, and D. N. Stacey, *Measurement of the lifetime of the 3d $^2D_{5/2}$ state in $^{40}Ca^+$*, Phys. Rev. A **62**, 032503 (2000).

[149] A. Kreuter, C. Becher, G. P. T. Lancaster, A. B. Mundt, C. Russo, H. Häffner, C. Roos, W. Hänsel, F. Schmidt-Kaler, R. Blatt, and M. S. Safronova, *Experimental and theoretical study of the 3d ^2D–level lifetimes of $^{40}Ca^+$*, Phys. Rev. A **71**, 032504 (2005).

[150] H. Häffner, F. Schmidt-Kaler, W. Hänsel, C. F. Roos, T. Körber, M. Chwalla, M. Riebe, J. Benhelm, U. D. Rapol, C. Becher, and R. Blatt, *Robust entanglement*, Appl. Phys. B **81**, 151 (2005).

[151] W. M. Itano, L. L. Lewis, and D. J. Wineland, *Shift of $^2S_{1/2}$ hyperfine splittings due to blackbody radiation*, Phys. Rev. A **25**, 1233 (1982).

[152] B. Arora, M. S. Safronova, and C. W. Clark, *Blackbody-radiation shift in a $^{43}Ca^+$ ion optical frequency standard*, Phys. Rev. A **76**, 064501 (2007).

[153] T. Weinold, private communication, Institut für Geodäsie, Universität Innsbruck, 2007.

[154] G. D. Rovera, M. Abgrall, and P. Laurent, private communication.

[155] K. Matsubara, K. Hayasaka, Y. Li, H. Ito, S. Nagano, M. Kajita, and M. Hosokawa, *Frequency measurement of the optical clock transition of $^{40}Ca^+$ ions with an uncertainty of 10^{-14} level*, Appl. Phys. Express **1**, 067011 (2008).

[156] D. Leibfried, B. DeMarco, V. Meyer, D. Lucas, M. Barrett, J. Britton, W. M. Itano, B. Jelenković, C. Langer, T. Rosenband, and D. J. Wineland, *Experimental demonstration of a robust, high-fidelity geometric two ion-qubit phase gate*, Nature **422**, 412 (2003).

[157] F. Schmidt-Kaler, H. Häffner, M. Riebe, S. Gulde, G. P. T. Lancaster, T. Deuschle, C. Becher, C. F. Roos, J. Eschner, and R. Blatt, *Realization of the Cirac-Zoller controlled-NOT quantum gate*, Nature **422**, 408 (2003).

[158] J. Benhelm, G. Kirchmair, C. F. Roos, and R. Blatt, *Towards fault-tolerant quantum computing with trapped ions*, Nat. Phys. **4**, 463 (2008).

[159] D. Leibfried, E. Knill, S. Seidelin, J. Britton, R. B. Blakestad, J. Chiaverini, D. B. Hume, W. M. Itano, J. D. Jost, C. Langer, R. Ozeri, R. Reichle, and D. J. Wineland, *Creation of a six–atom 'Schrödinger cat' state*, Nature **438**, 639 (2005).

[160] H. Häffner, W. Hänsel, C. F. Roos, J. Benhelm, D. Chek-al-Kar, M. Chwalla, T. Körber, U. D. Rapol, M. Riebe, P. O. Schmidt, C. Becher, O. Gühne, W. Dür, and R. Blatt, *Scalable multiparticle entanglement of trapped ions*, Nature **438**, 643 (2005).

[161] J. J. . Bollinger, W. M. Itano, D. J. Wineland, and D. J. Heinzen, *Optimal frequency measurements with maximally correlated states*, Phys. Rev. A **54**, R4649 (1996).

[162] D. J. Wineland, J. J. Bollinger, W. M. Itano, F. L. Moore, and D. J. Heinzen, *Spin squeezing and reduced quantum noise in spectroscopy*, Phys. Rev. A **46**, R6797 (1992).

[163] T. Schneider, E. Peik, and C. Tamm, *Sub-Hertz optical frequency comparisons between two trapped $^{171}Yb^+$ ions*, Phys. Rev. Lett. **94**, 230801 (2005).

[164] N. Yu, X. Zhao, H. Dehmelt, and W. Nagourney, *Stark shift of a single barium ion and potential application to zero-point confinement in a rf trap*, Phys. Rev. A **50**, 2738 (1994).

[165] M. D. Barrett, J. Chiaverini, T. Schätz, J. Britton, W. M. Itano, J. D. Jost, E. Knill, C. Langer, D. Leibfried, R. Ozeri, and D. J. Wineland, *Deterministic quantum teleportation of atomic qubits*, Nature **429**, 737 (2004).

[166] P. J. Mohr, B. N. Taylor, and D. B. Newell, *CODATA recommended values for fundamental physical constants*, Rev. Mod. Phys. **80**, 633 (2008).

[167] E. Wigner, *Einige Folgerungen aus der Schrödingerschen Theorie für die Termstrukturen*, Z. Phys. **43**, 624 (1927).

[168] C. Eckart, *The application of group theory to the quantum dynamics of monatomic systems*, Rev. Mod. Phys. **2**, 305 (1930).

Danksagung

Die Erstellung dieser Arbeit wäre ohne die Unterstützung und Hilfe zahlreicher Kollegen nicht möglich gewesen, weshalb ich mich bei allen Beteiligten recht herzlich bedanken möchte.

An erster Stelle steht natürlich Prof. Rainer Blatt, der mir die Möglichkeit gegeben hat, nach der Diplomarbeit auch meine Dissertation in seiner Arbeitsgruppe und dem wunderbaren Umfeld für Quantenoptik an der Universität Innsbruck anfertigen zu können.

For the measurement involving the Cs fountain clock from LNE-SYRTE, I'd especially like to thank Michel Abgrall, Daniele Rovera and Philippe Laurent for their phenomenal effort in the realization of the absolute frequency measurement even though Hertz car rental and a hungry beech marten made the journey with the Cs clock from Paris to Innsbruck and back a lot more exciting than expected.

Bei Christian Roos möchte ich mich sowohl für die erfolgreiche Zusammenarbeit am Experiment, als auch für seine Hilfe bei theoretischen Problemen bedanken, allem voran seine Korrekturen zu meiner Doktorarbeit. Wolfgang Hänsel danke ich für unermüdliches, nächtelanges Programmieren an unserer Experiment-Steuerung und seine Hartnäckigkeit, ohne die so manche wichtige Messung unter den Tisch gefallen wäre. Ebenso danke ich Hartmut Häffner für erfolgreiche Messungen, aufregende Skitouren und kritische Kommentare sowie Piet Schmidt für zahlreiche Tips bei Frequenzmessung bzw. Laserstabilisierung, und für wertvolle Kommentare bei der Erstellung des PRL-Artikels.

Besonders großer Dank gilt den tapferen und unerschütterlichen Mit-Meßknechten am ^{40}Ca$^+$-Experiment Kihwan Kim, Thomas Monz, Mark Riebe, Philipp Schindler, Alessandro Villar sowie der ^{43}Ca$^+$ Crew mit Gerhard Kirchmair und Jan Benhelm, ohne deren Einsatz zu jeder Tages- und Nachtzeit der Arbeitsaufwand nicht zu bewältigen gewesen wäre. Die heiteren Gespräche, mit Tommy, Philipp und Mark weit nach Mitternacht am Laborrechner lümmelnd, werden mir in lebhafter Erinnerung bleiben. Mein erfürchtiger Respekt gebührt selbstverständlich auch Daniel Rotter, einem stolzen Träger der silbernen Mensa-Nadel mit Band.

Natürlich braucht eine erfolgreiche Arbeit ein entsprechendes privates Umfeld. Deshalb möchte ich mich an dieser Stelle bei meiner Familie und ganz besonders bei meiner Freundin Evi bedanken, die mir - nicht nur - in schwierigen Zeiten und während der zwei Wochen Marathonmessung für die ^{40}Ca$^+$ Absolutfrequenz immer zur Seite gestanden sind.

Schließlich ist auch die lästige Frage beantwortet, wann ich denn nun endlich fertig sei. . .